Human Serum Albumin Detection Using Aggregation Induced Emission Biosensors and Their Engineering Improvements for Screening and Monitoring Chronic Kidney Disease

By

Qi Hu
Master of Biomedical Engineering

Thesis
Submitted to Flinders University
for the degree of

Doctor of Philosophy
College of Science and Engineering
23/12/2024

TABLE OF CONTENTS

ABSTRACT

Chronic kidney disease (CKD) has become a medical problem that threatens public health across the world. Nowadays, the increasing prevalence of other diseases like diabetes, heart disease, and hypertension, along with factors like societal pressure, aging populations, and environmental pollution are all contributing to the global incidence of CKD. What is worrying is that symptoms are non-existent or minimal in the early stages of CKD until a significant amount of renal function loss. Therefore, screening and monitoring CKD becomes a crucial work in medical care with the highest priority at the initial stage. Human serum albumin (HSA) as an effective urinary biomarker is widely used to detect and determine the levels of albuminuria in CKD because it is utilized to define and measure the filtration capacity of the glomerulus in CKD owing to its concentration variation. At present, traditional techniques like colorimetry-based assays and immunoassays have mature standard operating procedures and extremely high popularity, but under the increasingly complex detection scenarios and the diverse requirements of different populations, there is still a need to develop other long-term and stable detection technologies. Fluorescence, as a rapidly emerging technology in recent decades, has attracted widespread attention on biological and chemical sensing, among which aggregation induced emission (AIE) based biosensors probably become a new solution for HSA detection in medical applications due to the advantages of simple operation, rapid response, high sensitivity, and cost efficiency. Certainly, despite researchers have reported numerous successful instances of HSA detection using AIE biosensors, this type of technique is still subject to many challenges, including external interference, restricted sensitivity, loss of FL signal, inconvenience of detection, high reagent consumption, reusability, etc. Given the aforementioned issues, it is great potential for AIE products to further modify their functionalities and achieve higher standard requirements in future medical research through engineering designs. In this work, novel AIE biosensors have been reported to achieve HSA detection and their corresponding applications in human urine at which experimental results demonstrate satisfactory FL behaviours. Afterwards, two different engineering designs, hydrogel platform and metasurface platform, are conducted to realize better performances on the basis of AIE biosensors. Ultimately, the results illustrate that some specific characterizations of HSA detection using AIE biosensors can be improved significantly via engineering designs, which means engineering improvement is a feasible and promising enhancement strategy of AIE biosensors for biomarker detection in the fields of fluorescence.

DECLARATION

I certify that this thesis:

1. does not incorporate without acknowledgment any material previously submitted for a degree or diploma in any university

2. and the research within will not be submitted for any other future degree or diploma without the permission of Flinders University; and

3. to the best of my knowledge and belief, does not contain any material previously published or written by another person except where due reference is made in the text.

Signed...........................Qi Hu................................

Date..........................23/12/2024.............................

ACKNOWLEDGEMENTS

LIST OF FIGURES

LIST OF TABLES

LIST OF APPENDIX FIGURES

LIST OF APPENDIX TABLES

INTRODUCTION

Research background

Kidney disease

Kidney disease is defined as the dysfunction of kidney due to the damage in some ways, resulting in impaired filtration (Levey et al., 2005), and it is divided into two branches (**Figure 1**): acute kidney injury (AKI) and chronic kidney disease (CKD). This is always a global public health problem across the world over centuries and it is currently the seventh most common cause of death worldwide due to its rising prevalence (Francis et al., 2024). The estimated global population with kidney disease is 850 million, the majority of whom reside in low-income and lower-middle-income countries (LICs and LMICs), and a significant fraction of these people do not have access to kidney disease diagnosis, prevention, or treatment (Jager et al., 2019; Stanifer et al., 2016). Furthermore, kidney disease prevalence is expected to further rise due to demographic trends, the obesity epidemic, and the effects of climate change. This will have a significant impact on quality of life, survival, and health care costs globally. More crucially, the burden of kidney disease is largest among historically marginalized people, who frequently lack access to the best treatments available for kidney disease (Gonzalez-Bedat et al., 2020). This significantly adds to the socioeconomic gaps in health outcomes that exist today.

As the top five non-communicable diseases (NCDs) causing premature mortality and disability, the WHO has identified heart disease, stroke, cancer, diabetes, and chronic lung disease (Organization, 2022). However, kidney disease, no matter which CKD or AKI, from this list is missing. It should be noted that CKD is more common in those with AKI and vice versa (Coca et al., 2012). In addition, renal illness frequently coexists with major NCDs and increases the risk of these conditions, including diabetes, cancer, peripheral vascular disease, ischemic heart disease, and stroke (Bikbov et al., 2020). Considering about the significant impaction of kidney disease, supported by three other regional nephrology societies, the joint statement from the International Society of Nephrology, European Renal Association, and American Society of Nephrology calls for kidney disease to be included in the current WHO statement on major non-communicable disease drivers of premature mortality (Francis et al., 2024).
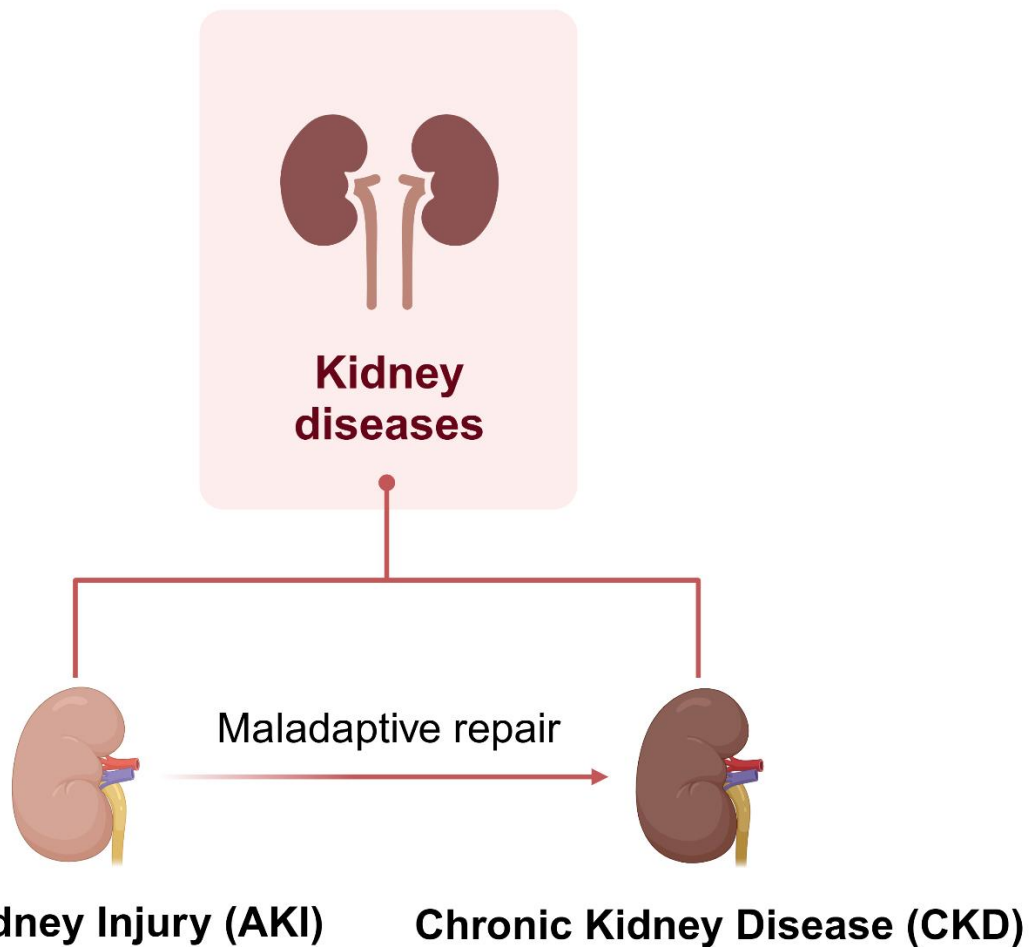
Figure 1 Illustration of kidney disease.

Chronic kidney disease

Generally, AKI will show more relatively obvious adverse symptoms due to its early pathogenesis, whereas CKD will present with few or no symptoms in the early stages, but severe signs emerged after losing the majority of kidney functionality (Kalantar-Zadeh et al., 2021). Due to the fact that many regions of the world lack early kidney disease identification and screening programs, CKD has a more significant impact on public health (Murphy et al., 2016). The number of patients requiring costly kidney replacement treatment (KRT) and experiencing renal failure would inevitably rise if CKD is mostly undiagnosed and treated as a result. According to statistics globally, an estimated 700 million people are thought to suffer from CKD (Jager et al., 2019). The mortality rate from CKD has been increasing compared to that from respiratory, cardiovascular, and stroke diseases (El Nahas & Bello, 2005). It is predicted that by 2040, CKD would rank as the world's fifth leading cause of years of life lost (YLL, **Figure 2**) (Foreman et al., 2018). Moreover, the Global Burden of Disease (GBD) research estimates that between 1990 and 2017, the prevalence of CKD rose by 33%

worldwide (Bikbov et al., 2020). Crucially, the majority of CKD patients—nearly one-third of them—live outside of high-income countries (HICs), with China and India alone accounting for the majority of the rise in CKD burden for prevalence and mortality simultaneously (Francis et al., 2024). The worldwide risk of kidney disease is elevated by a plethora of additional social, environmental, and economic factors beyond population dynamics. Besides, the most well-known factors influencing the development of CKD, particularly in areas with developed economies, are population increase, aging, and the rising prevalence of diabetes, heart disease, and hypertension (Jha et al., 2013). Hence, screening and monitoring CKD becomes a very crucial work in medical care.
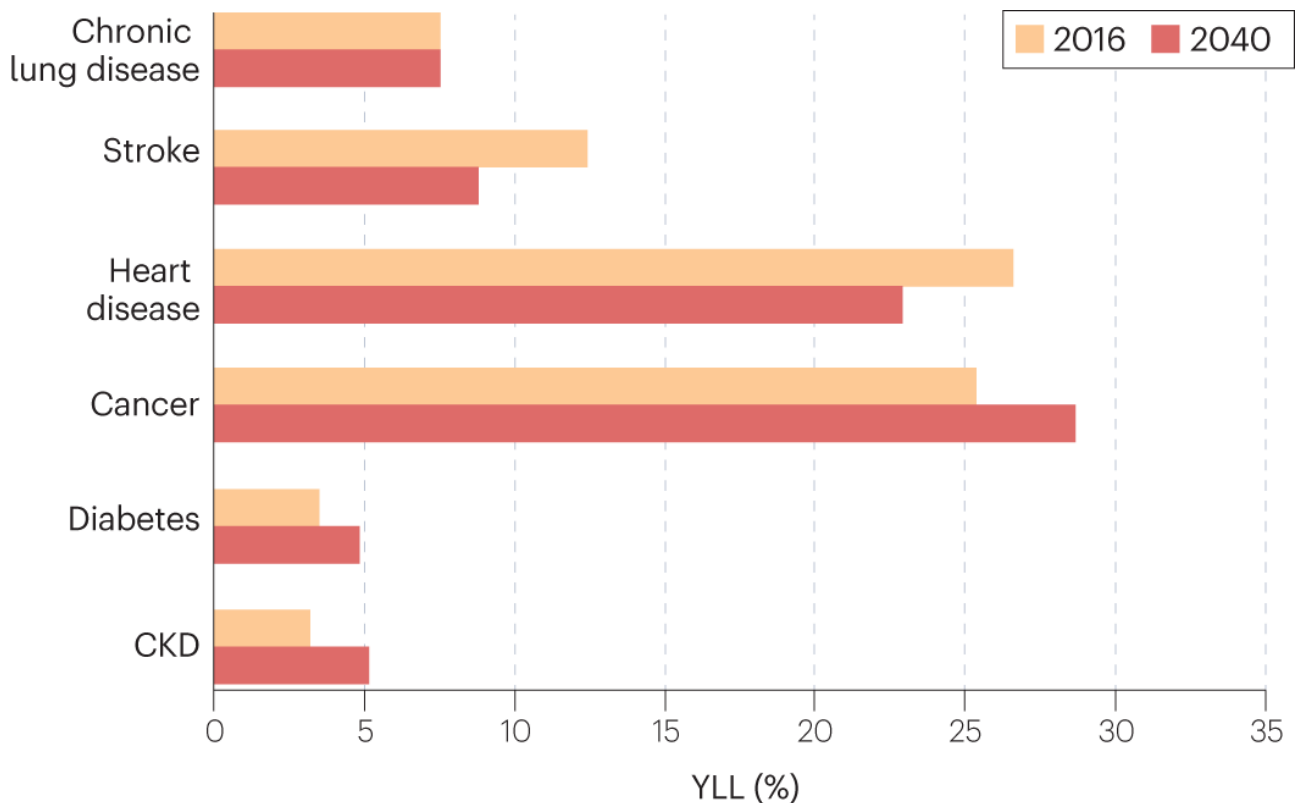
Figure 2 Predicted years of life lost from CKD by 2040 (Francis et al., 2024).

Proteinuria and albuminuria

Proteinuria is defined as the total amount of urinary protein excretion (≥150 mg/day) (Zhang & Huang, 2012). It is a typical symptom of CKD in pathophysiology where the mechanism is induced by enlarged permeability of glomerular capillary wall and Impaired reabsorption in proximal tubule epithelial cells, resulting in abnormal transglomerular passage of proteins (D'amico & Bazzi, 2003). Generally, normal persons excrete small amounts of proteins into urine (30-130 mg/day), whereas the existing large amounts of proteins in blood, such as albumin, globulins, mucoproteins, etc., leak into urine from proteinuria patients (**Figure 3A**) (Viswanathan & Upadhyay, 2011). The progression of kidney disease is highly positively correlated with the magnitude of proteinuria (Hemmelgarn et al., 2010). However, selecting total urine protein as the monitoring and screening biomarker is still

the source of controversy for CKD. Urinary proteins include many irrelevant proteins regarding CKD, which cannot be diagnosed accurately (Wu et al., 2012). Based on that, it is particularly crucial to locate the content of a specific component related to CKD within the scope of proteinuria.

Albuminuria is a reflection of CKD traditionally (GUH, 2010) and it is an associated symptom of proteinuria because the predominant urinary protein in kidney disease is HSA, which accounts for approximately 20% of total proteins (Kim, 1988). Concretely, albuminuria, as shown in **Figure 3B**, is defined as the total amount of urinary albumin excretion (≥30 mg/day) and it is invariably linked with clinical proteinuria (de Jong & Curhan, 2006). The percentage of urine albumin increased when urine total protein increased. Generally, individuals with albuminuria will excrete HSA with different extent. Therefore, HSA concentration is treated as the standard for evaluating the severity of albuminuria and albuminuria is highly correlated with proteinuria further to indicate the progression of CKD.
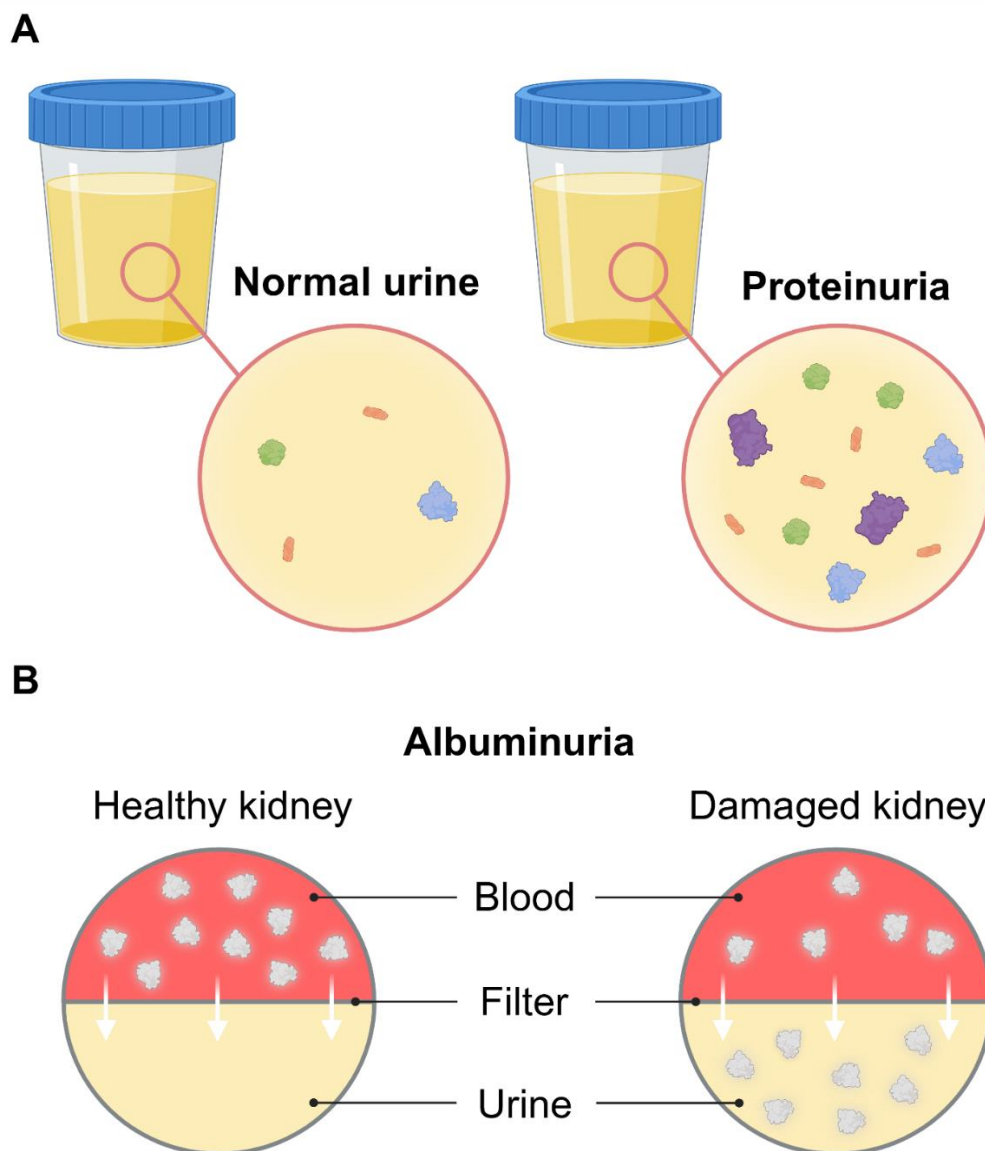
Figure 3 Illustration of (A) proteinuria and (B) albuminuria.

Research object

HSA as an important biomarker for CKD

Human serum albumin (HSA) is the most abundant protein in human blood plasma, accounting for 55–60% of the measured serum proteins (Nicholson et al., 2000). As the major soluble protein component in human serum, it has many physiological functions. For example, HSA maintains 80% of normal plasma colloidal osmotic activity. Besides, due to the existence of Gibbs-Donnan effect, it provides an attractive force for the retention of positively charged solutes in blood vessels (Nicholson et al., 2000; Prakash, 2017). Thanks to the existence of abundant reduced sulfhydryl groups, HSA also has good free radical scavenging ability (Levitt & Levitt, 2016). In terms of the structure of HSA, it is composed of three α-helical domains I, II and III, with each one contains two subdomains A and B (Fanali et al., 2012). Due to the different helical structures, the subdomains show different ligand binding affinity, endowing HSA with good binding capability towards various endogenous and exogenous ligands. As a result, HSA can bind with many substances including bilirubin, vitamin D, thyroxin, etc., and adjust their biologic activity, distribution, and rate of clearance (Kragh-Hansen, 2013; Lee & Wu, 2015; Tong et al., 2017; Yang et al., 2014).

Since certain diseases may alter the distribution of albumin between the intravascular and extravascular compartments (Nicholson et al., 2000), detecting HSA level in biological fluids is clinically used for the diagnosis of many diseases, such as cancer, diabetes, liver disease, inflammation, rheumatic disease, cardiovascular diseases, etc (Anraku et al., 2001; Rosenoer et al., 2014; Yao et al., 2021; X. Zhang et al., 2020). For example, urinary albumin is deemed as an important clinical indicator of CKD. For healthy people, very little albumin leaks through glomerulus into the urine, with a urinary albumin level less than 20 mg/L. However, in end-stage kidney failure (the last stage of CKD), a large amount of albumin will be spilled into the urine, resulting in a urinary albumin concentration greater than 200 mg/L. Therefore, screening and monitoring HSA in albuminuria accurately is critical to the diagnosis and treatment of CKD at the early stage.

Detection methodology

Fluorescence technology of HSA detection with aggregation induced emission features

Fluorescence method as a novel technology for detecting HSA has several unique advantages that is suitable in biological and chemical sensing. In the first place, the fluorescence emission is only induced by excitation, which is specific to a particular biomarker. Generally, different FL probes can be designed to adapt to biomarkers such as HSA to trigger its significant fluorescence. In the second place, FL reaction allows images and signal to have contrast. This is the key point to make the detection happen successfully. In the third place, the photostability of fluorescence signal can maintain accurate HSA detection results under different scenarios. This indicates that phenomena are reliable and reproducible in the same conditions. In the fourth place, the intensity of fluorescence can be linked with the concentration of HSA analyte. In other words, the establishment of standard curve provides an effective quantitative method to determine the concentration of HSA and to describe the correlation between fluorescence and analyte concentration. In the final place, the detection cost is inexpensive and the majority of expense is mainly focusing on FL bioprobes or biosensors (Ligler, 2008). Based on such background, fluorescence based strategies have attracted increasing attention from the biosensing field, due to the advantages of simple operation, rapid response, high sensitivity, and cost efficiency (Kobayashi et al., 2010; Jing Liang et al., 2015; Ju Mei et al., 2015). Among various fluorescent probes, the aggregation induced emission (AIE)-based fluorescent probe demonstrated outstanding performances, such as application to a broad concentration range, good photostability, low background noise, large Stokes shifts, etc (Xinggui Gu et al., 2017; Hong et al., 2009, 2011; Hong et al., 2012; Kwok et al., 2015). Unlike other FL phenomena, AIE phenomenon occurs through the restriction of intramolecular movement among FL molecules because of the introduction of HSA. FL molecules experience the process of energy absorption and release, thereby fluorescence is the end product during this process that can be observed and measured. The simplicity of the triggering circumstances is a benefit of the AIE biosensors. To be more specific, AIEgens exhibit non-emissive (normally no or little FL signal) in solutions when they are individuals, but they will emit intense fluorescence once interacting upon HSA as the aggregation state. Besides, biocompatibility and modifiability are characteristics of AIEgens to meet HSA detection (Duo et al., 2023). AIEgens and albumin can be connected successfully through electrostatic interaction, hydrogen bonding, non-covalent bonding, hydrophobic interaction, etc., while the activity of HSA is unchanged after reactions (Ding et al., 2013). Hence, fluorescence with AIE features has the ability to achieve HSA detection effectively.

Current situation of HSA detection using AIE FL biosensors

Most of AIE biosensors are derived from the typical framework tetraphenylethylene (TPE) and its derivatives (Würthner, 2020). For HSA detection, numerous researchers have chemically modified and changed on the basis of this structure to form a stable binding between HSA and AIE biosensors.

At present, biosensors with AIE features (Hong et al., 2009) become one of the most effective fluorescent methods for albumin detection due to its high sensitivity, rapid response, specific selectivity, operational simplicity, cost-efficiency and real-time & in-vitro sensing (Gao et al., 2019; Hong et al., 2010; Klymchenko, 2017; Liang et al., 2021). Numerous research focuses on the novel synthesis of AIE biosensors and the regular evaluation of their performance on fluorescent kinetics, thermodynamics, proteomics, imaging optics, etc (Ding et al., 2013; Lü et al., 2019; Wang et al., 2024). Depending on the purposes and designs of the experiment, there are certain differences in the test target and environment. HSA detection using AIE biosensors can be divided into the following categories (**Figure 4**). It is obvious that the majority of HSA detection is conducted in the deionized water because biospecimens of HSA are all aqueous solutions and there are no other interfering substances in the water. The data from water can intuitively reflect the detection performance of AIE biosensors under ideal conditions. Generally, the best FL response is obtained from pure water environments. As for buffers, the typical buffer systems are phosphate buffer, bicarbonate buffer, tris buffer and citrate buffer (Xie et al., 2019). They are another option to support HSA detection where the pH will not change dramatically on the introduction of external reagents or the function of dilution. More importantly, it can avoid the variation of the performance of AIE biosensors caused by pH change. Among these systems, PBS buffer system is the most popular choice of HSA detection for maintaining a neutral environment. Artificial urine contains the main chemical components of urine as simulated biological samples to further evaluate accuracy and limitation of AIE biosensors. The chemical ingredients added to artificial urine are constant meanwhile actual urine samples include too many unknown information (Sarigul et al., 2019). Therefore, the impact of the AIE biosensors' sensitivity towards primary urinary interferences is more easily identified in artificial urine. On the contrary, HSA detection becomes particularly complicated in biological samples. In serum samples, HSA content keeps an extremely high level of 35-50 g/L (Fanali et al., 2012), which masks the effects of other blood substances on AIE biosensors. Plasma detection of albumin focuses on detection stability, repeatability and biocompatibility rather than its sufficient sensitivity. In urine, due to its complex matrices and the very low HSA content in healthy individuals, the detection sensitivity of AIE biosensors becomes a crucial factor for achieving successful detection. Under such background, to evaluate the performance of AIE biosensors, researchers use not only HSA, but also BSA (75.8% endogenous structure of HSA) as a substitute for HSA considering about testing costs. A series of spiking testing is completed to establish a standard procedure, then are validated further in spiked/original samples. Based on current reported research on HSA detection using AIE biosensors, the number of studied cases decreases as the complexity of the solution matrix increases.
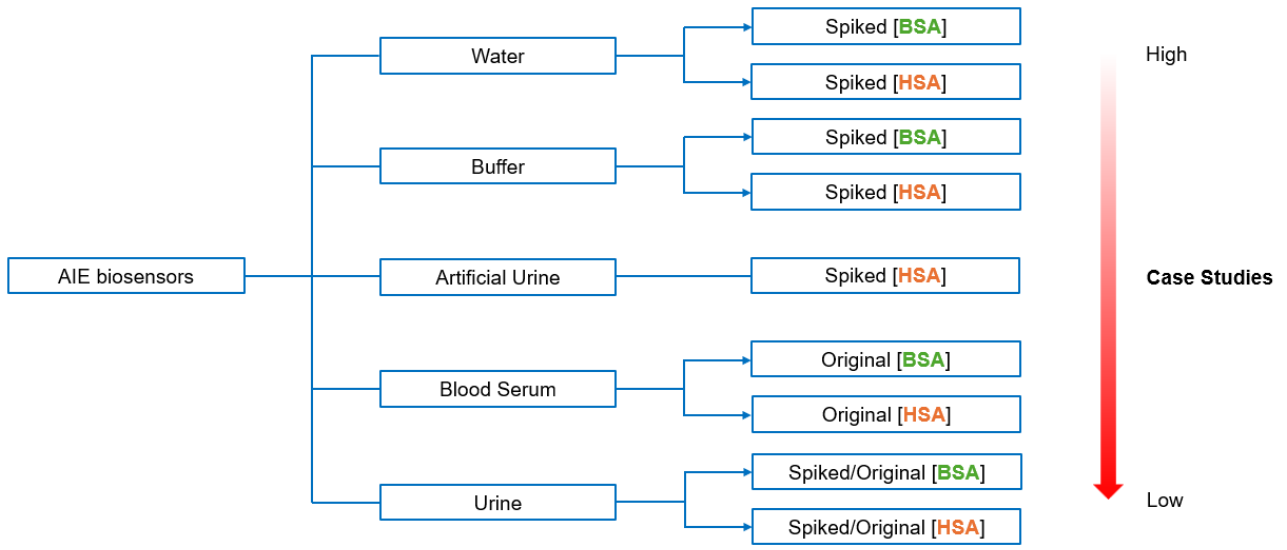
Figure 4 Differential HSA detections using AIE biosensors.

Gap and challenge

Considering the current status of HSA detection, there are still following gaps and challenges using AIE biosensors in this process. Firstly, protocols in most of research are designed under ideal solutions, and a few cases are extended on biological samples. One reason of this is that, with a comparatively straightforward experimental setup, fluorescence performance can be more readily verified. However, the complexity of biological samples itself places more requirements on the detection capabilities of AIE biosensors. Secondly, it is challenging to identify traces of albumin in urine samples, and urinary interferences will somewhat affect the AIE biosensors' sensitivity for HSA detection. It is a fact that most AIE fluorescent biosensors do not have significant ability to detect trace albumin in urine (Miller et al., 2009). Thirdly, the delivery system is not efficient enough because the reaction relies on traditional fluorescence titration (Mei et al., 2017). Fluorescence testing has a short window period, but manual preparation takes time. Additional techniques are needed to shorten the liquid delivery time. Fourthly, there is a delay in the test, which might lead to inconsistent findings. This delay results from the necessity to monitor the analyte delivery system and the fluorescence sensing& imaging using distinct equipment. In most FL setup, these terminals are not integrated together. Although FL signal remains stable during short-term detection, it is unavoidable to totally eliminate non-uniform background noise from transferring, artifacts, or other time-dependent phenomena like autofluorescence or fluorescence quenching in practical scenarios (Gao & Tang, 2017), which further leads to variations in trace HSA detection outcomes. Fifthly, the detection platform is one-time use and cannot be reused. This not only increases the cost of the test, but in some cases the samples need to be recalibrated before testing. Sixthly, large sample volume and long-term testing necessitate a high number of reagents of AIE biosensors, which substantially raises running costs. In many kinetic experiments, it is necessary to add an excess of fluorescent reagents to ensure that the protein is completely reacted. Seventhly, the majority of studies don't go beyond front-end research, which is limited to evaluating and testing biosensor itself. There is a gap of specific engineering design to extend and develop it onto the deeper applications. Eighthly, measurements can only be performed under laboratory equipment. This study aims to explore in situ detection as one of its development. Ninthly, biocompatibility and environmental friendliness are also important considerations for biological sample testing. Most current research still relies on a large number of disposable plastic or metal containers, which is bound to impose a burden on the environment. Tenthly, light signal can be improved by reducing light loss during measurement. Typically, most of optical instruments collect light signals from fixed light sources in a stable and controllable manner through preset optical paths and enclosed compartments. In that case, it is acceptable to lose some optical signal since the ratio of the output optical signal to the total optical signal can be set within a rational range. Nevertheless, light loss is difficult to be compensated because the default detection program has already excluded it.

Research route

Based on the above-mentioned research outline, the research routine has been illustrated in **Figure 5**. Chronic kidney disease has been modelled as the basis for this research, and albuminuria is its typical symptom where albumin is the most important biomarker to reflect the level of CKD. HSA detection is carried out using FL biosensors with AIE features. Through a systematic understanding of AIE biosensors, gaps and challenges during the detection process are defined in three categories: convenience, performance, and sustainability. Herein, two engineering designs, hydrogel platform and metasurface platform are introduced based on AIE biosensors to solve or optimize these issues.
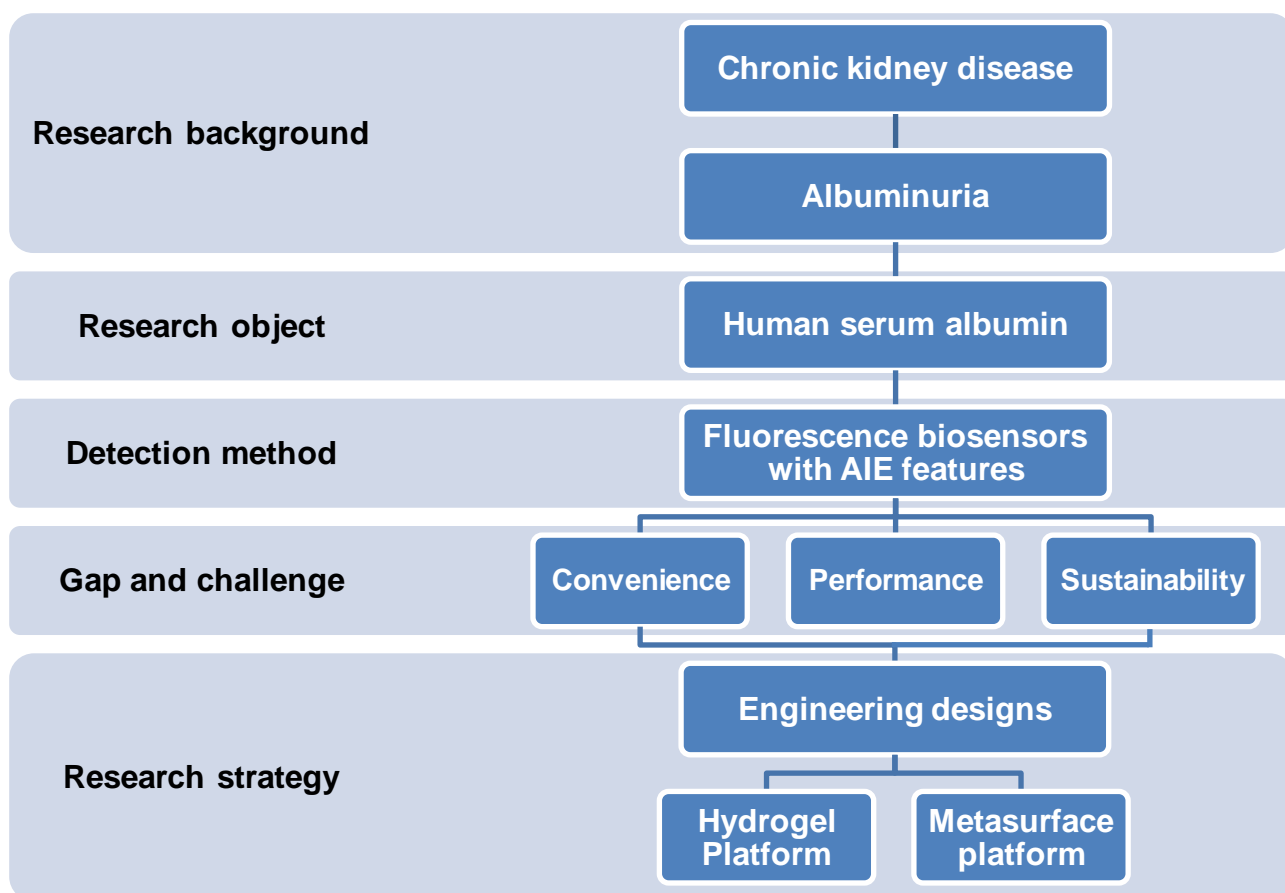
Figure 5 Research route for HSA detection using AIE FL biosensors incorporating with two engineering designs: hydrogel platform and metasurface platform.

In this work, the purpose of using engineering design can be summarized as follows:

- Engineering design provides the pathways of problem-solving and optimization by addressing current gaps and challenges of AIE biosensors in HSA detection.
- Engineering design offers competitive advantages for AIE products.
- Engineering design itself is an innovative process and it will further promote the development of AIE biosensors in more mature medical applications.

For two different engineering directions, combined with the subsequent literature review, the improvements that might be achieved by the hydrogel platform and the metasurface platform are summarized, as shown in **Figure 6**. Instead of relying solely on AIE biosensors, the research goal of engineering design 1 is to establish a portable hydrogel platform that is capable of being completely compatible with AIE biosensors. In addition to having superior aqueous phase distribution capabilities, the hydrogel network offers improved biocompatibility and environmental friendliness. This fully satisfied the design concept of the study. In terms of engineering design 2, customizable nanostructures have the ability to guide and amplify optical signals, and well-designed patterns provide efficient transmission of optical signal while minimizing light loss. Additionally, the consumption of chemical reagents can be greatly reduced by incorporating the microfluidic system into this platform. Importantly, metasurface platform is reusable through simple flushing, which dramatically saves running costs. Naturally, real-time setup is supplied for both normal and biological samples under these two platforms in order to ensure the consistent FL results.
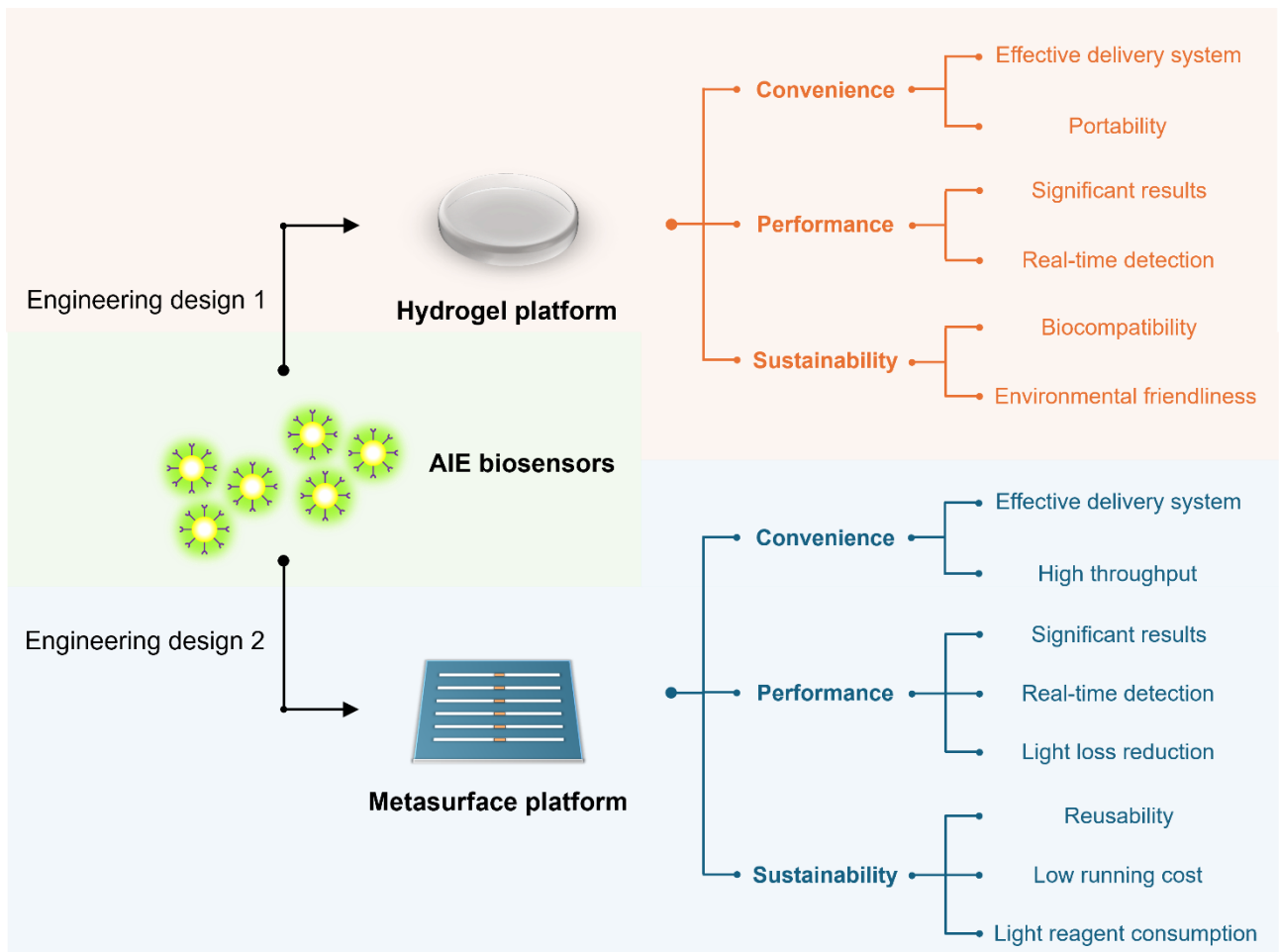
Figure 6 Research purpose of AIE biosensors in HSA detection using two engineering designs: hydrogel platform and metasurface platform.

LITERATURE REVIEW

Kidney and associated disease

Kidney functionality for filtration

Kidneys are very important bean-shaped organs in human body, which are located below the rib cage on the side of spine separately. The kidneys' primary function is to filter waste from blood and restore purified blood to the body. As indicated in **Figure 7**, The renal arteries allow approximately one liter of blood to pass into the kidneys every minute (Finco, 1997). The blood returns to the body through the renal veins after being cleansed. Kidney, as a powerful filter system, includes one million nephrons where tiny filters are assembled onto a tubule, which are called glomerulus (Pollak et al., 2014). Filtration of fluid and waste products occurs as blood flows through the nephron. When the waste products are concentrated in any excess fluid, such as urine, a large portion of the fluid is subsequently returned to the blood (Kassirer, 1971). After that, the bladder receives the urine through a tube known as the ureter. The urethra is the tube that the bladder uses to excrete urine from the body. Generally the kidneys produce one to two liters of urine every day (Borghi et al., 1998). It is worth noting that glomerulus plays a vital role in filtration. Once kidney disorders affect their normal physiological functions, substances in blood may leak into the urine depending on damage extent.
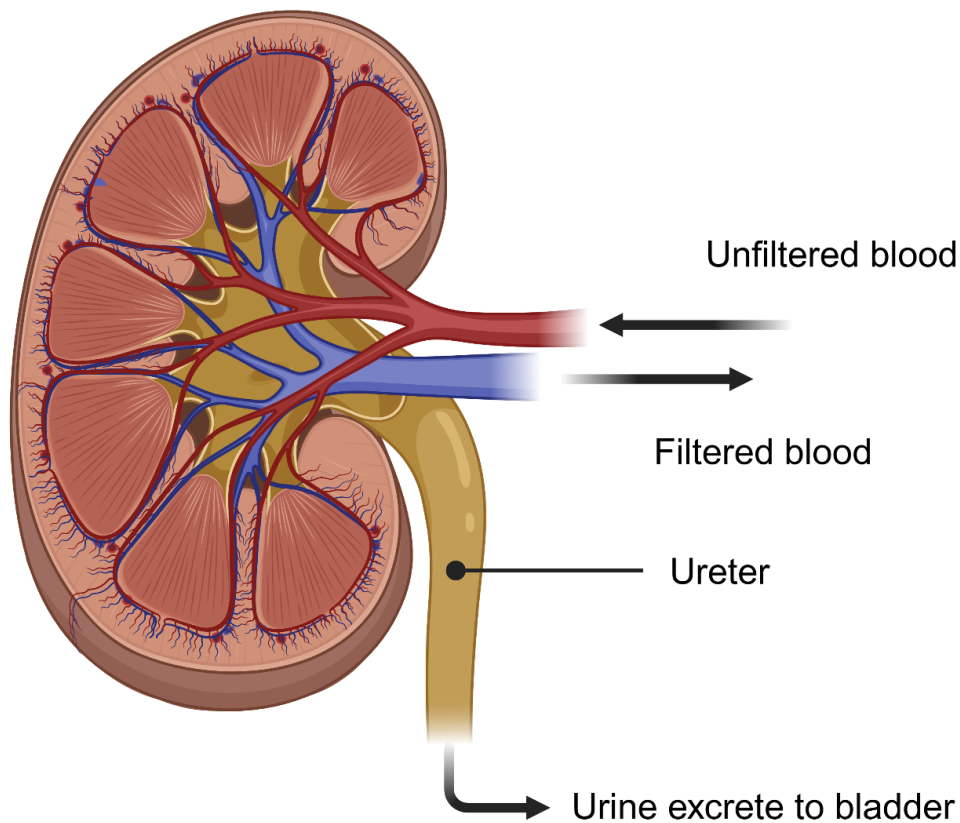
Figure 7 Schematic of kidney functionality for filtration.

Chronic kidney disease

Chronic kidney disease (CKD) is a typical instance of renal filtration imbalance. It refers to progressive kidney damage, resulting in disfunction and structural change due to various factors. Specifically, the standard definition of CKD is a decline in kidney function, an estimated glomerular filtration rate of less than 60 mL/min per 1·73 m², or indicators of kidney damage, such as albuminuria, haematuria, or abnormalities that have persisted for at least three months (Kalantar-Zadeh et al., 2021). It is estimated that 10% of individuals suffer from CKD globally, which accounts for 1.2 million fatalities every year (Y. Xie et al., 2018). With one of the biggest potential rises of all main causes of death, CKD is predicted to rank as the fifth most common cause of death globally by 2040 (Foreman et al., 2018). In developed countries, obesity, diabetes, hypertension, cardiovascular disease, etc. are typically linked to CKD in developed countries (Levey & Coresh, 2012). Significantly, the variation of glomerular filtration capacity is the most critical factor leading to CKD (Turin et al., 2013).

In order to determine the extent of renal damage, an estimated glomerular filtration rate (eGFR) and urinary albumin to creatinine ratio (uACR) are established to predict and diagnose CKD in pathophysiology. As shown in **Figure 8**, CKD has been classified into 5 stages from mild to severe symptoms: G1 is >90 mL/min per 1·73 m², G2 is 60-89 mL/min per 1·73 m², G3 is 30-59 mL/min per 1·73 m², G4 is 15-29 mL/min per 1·73 m² and G5 is <15 mL/min per 1·73 m². In the meanwhile, uACR reflects into 3 phases: A1 is 0-29 mg/g (Normoalbuminuria), A2 is 30-299 mg/g (Microalbuminuria) and A3 is >300 mg/g (Macroalbuminuria). Obviously, the thresholds of CKD are <60 mL/min per 1·73 m² and > 30 mg/g in these two categories, indicating the early stage of CKD diagnosis.

Figure 8 Prognosis of chronic kidney disease by GFR and albuminuria (Levey & Coresh, 2012). Different colour represents risk levels.

Human serum albumin as the CKD indicator

Based on above mentioned background, HSA, as one of the most effective indicators, is utilized to define and measure the filtration capacity of the glomerulus in CKD owing to its concentration variation. The relationship of HSA and GFR has been quantified in **Table 1**. In this case, the threshold range of urinary HSA concentration is >20 mg/L in albuminuria. The simulations of HSA content in this research can intuitively reflect onto pathophysiological significance of CKD.

	24 hours urine: Urinary Albumin Excretion, mg/24 hours	Urinary Albumin Concentration, mg/L	First Morning Void		
			Urinary Albumin Creatinine Ratio		
			Sex	mg/mmol	mg/g
Normoalbuminuria	<30	<20	Male	<2.5	<20
			Female	<3.5	<30
Microalbuminuria	30-300	20-200	Male	2.5-25	20-200
			Female	3.5-35	30-300
Macroalbuminuria	>300	>200	Male	>25	>200
			Female	>35	>300

Table 1 Cutoff value indicating Normoalbuminuria, Microalbuminuria and Macroalbuminuria (Lambers Heerspink et al., 2008).

Urine and urinary biomarkers

This part has already been published on "*Materials Chemistry Frontiers*, 2022, *6*(15), 2011-2033" under the title "**Inorganic–organic hybrid materials to detect urinary biomarkers: recent progress and future prospects**". Qi Hu is the primary author, while Dan Ding is the co-author and Youhong Tang is the correspondent author (**doi.org/10.1039/D2QM00213B**).

Urine and urinalysis

Biomarkers are changes in biological organisms that may be observed throughout physiological dynamic processes. Such variations are measurable, and their levels are linked to the disease, either directly or indirectly. Urine as the gathering places of various biomarkers is a very appealing bio-specimen for biomonitoring because it can be collected in relatively large volumes and on a regular basis using non-invasive procedures. They reflect an individual's metabolic and pathophysiologic status, which changes in the body, at a certain time point (Harpole et al., 2016), and urine is considered to be the most simple, efficient and cost-effective resources for identifying disease biomarkers in vitro (Decramer et al., 2008; Zhao et al., 2017). Therefore, identifying different biomarkers to pathophysiology of diseases in urine has long been a fundamental element of medical study. At present, the majority of urinary biomarker discoveries and research has focused on tracking variations in the morphology, contents, and properties of excretions in the urine caused by specific diseases (Pisitkun et al., 2006).

Specifically, the kidney produces urine, which permits the human body to remove waste items from the bloodstream. In addition to maintaining whole-body homoeostasis, the kidney where approximately 900 liters of plasma pass through it every 24 hours, with 150-180 liters being filtered generates hormones such as renin and erythropoietin. In fact, more than 99 percent of this primitive pee, on the other hand, is reabsorbed, and the remainder passes via the ureter and into the bladder. Ultimately, urine carries information from not just the kidney and urinary system, but also from other organs via plasma collected by glomerular filtration (Decramer et al., 2008). This is also why clinical diagnosis relies heavily on human urine. Besides that, urine has various properties that make it a favored choice for biomarker discovery when compared to other bodily fluids. For starters, non-invasive techniques can be used to acquire big amounts of pee, which allows for disease monitoring by sampling the same person multiple times. Next, urinary peptides and proteins with a smaller molecular mass are usually soluble (Marimuthu et al., 2011). More importantly, the urinary proteome did not change considerably when urine was held at 4 °C for a long period (Schaub et al., 2004). Conversely, the downsides of urine are quite clear certainly. It can be challenging to determine proteins and other constituents in urine since it is such a complex matrix. The following are some of the variables that make it challenging for researchers to analyze urine. To begin with, the urine matrix is complex, including a wide range of inorganic and organic components from low-molar mass molecules to polymers, and organisms in urine such as blood cells or bacteria can quickly change

the makeup of urine. Moreover, it's worth noting that the amount of contents in a patient's urine might vary significantly based on their diet, exercise, and the time of day they urinated (Aitekenov et al., 2021). As a result, the development of increasingly efficient and sensitive urine detection technologies is an unavoidable tendency.

Urinalysis is extremely useful in the clinical diagnosis, detection, and treatment of disorders such as urinary tract infections, renal disease, and diabetes. The amount (content, concentration, or color) of biological test's components in the urine might intuitively represent the body's health condition, and more meaningfully, abnormal urinalysis findings are closely correlated to various diseases (Gao, 2019). Typically, the comprehensive urinalysis usually include examining urine samples physically, chemically, and optically (Mahoney et al., 2019). Visual analysis of urine colour, odour, volume, quality and specific gravity is performed as part of the physical examination to determine whether urine is in normal condition. Chemical examinations are used to identify samples for pH value, chemical compositions, proteins and cells, etc (Strasinger & Di Lorenzo, 2014). Besides that, optical checking not only includes determination of urine components, also particle morphology and structure in urine samples (Cheng et al., 2020; Huang et al., 2019). To summarize the preceding, bilirubin, blood, glucose, ketones, leukocytes, nitrite, protein, creatinine, urobilinogen, RNA, pH and other biomarkers are included in this list (Rose et al., 2015; Simerville et al., 2005; Strasinger & Di Lorenzo, 2014), while dipsticks and point-of-care devices are the most common technologies for detecting urine in clinical settings (Simerville et al., 2005; Strasinger & Di Lorenzo, 2014). Based on these typical biomarkers and related pathologic causes (Fung et al., 2009; Lepowsky et al., 2017; Narayanan & Appleton, 1980; Papale et al., 2010; Patel, 2006; Salazar, 2014; Tsai et al., 2005; Wan et al., 2004), this part will introduce main biomarkers existing in urine (**Figure 9**).
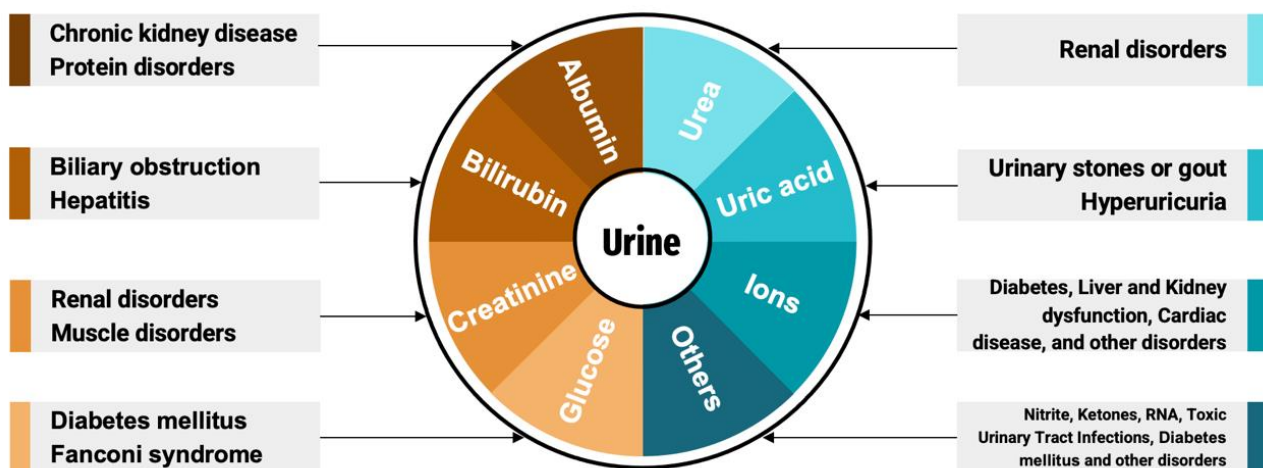
Figure 9 Major research components of urine and related diseases.

Urinary biomarkers

Urine is the end product of kidney filtration and contains numerous substances that reflect the biological information in bio-specimens. These substances can be utilized as typical biomarkers associated with different diseases to monitor and diagnose pathophysiological conditions. In addition to HSA, there are many major biomarkers in urine simultaneously as mentioned below.

Bilirubin

Bilirubin (BR) is a yellow-colored pathogenic pigment containing tetra pyrrole units that is produced as a by-product of the natural disintegration of aged red blood cells (Rahman et al., 2008) and the conjugated and unconjugated forms of BR circulate in the blood. Unconjugated BR interacts with albumin to generate water soluble BR, whereas conjugated BR forms compounds with glucoronic acid to form water soluble BR (Fevery, 2008). There is also a little amount of free BR, which is a significant signal of bilirubin toxicity, and hepatic or biliary tract dysfunction can be triggered by high free bilirubin levels. This unconjugated BR has a broad scope of toxicity, especially to neural cells, which is mitigated by its capacity to bind to albumin (Taurino et al., 2013). If left untreated, an increased BR level can lead to jaundice and liver damage where bilirubin enables to be detected in the environment of urine because of leaking. Clinically the BR test works by binding bilirubin to diazonium salts on a test pad in a highly acidic environment, resulting in colored compounds in tan or magenta colors. The urine dipstick test for conjugated bilirubin has a sensitivity of 0.5–1.0 mg/dL (Mundt & Shanahan, 2020).

Creatinine

Creatinine is a component of human blood and urine that is produced as a byproduct of creatine phosphate metabolism in muscles, and its levels in biological fluids are becoming a more relevant clinical indicator of renal failure, thyroid dysfunction, and muscle injury (Uchino, 2010). Human blood creatinine levels exceeding 140 µM are indicators for renal failure, whereas values below 40 µM are a signal for muscular illness (Lad et al., 2008), therefore measuring creatinine levels in bodily fluids can aid in the diagnosis and treatment of renal and muscle illnesses. The detection of creatinine is mainly based on the reaction with picric acid known as the Jaffe reaction where the change of color can dynamically display the level of creatinine in urine and tests based on the Jaffe reaction demonstrate a limit of 0.3 ppm (Falcó et al., 2001).

Glucose

Glucose is the main sugar in the blood that carries glucose to all cells in human's body for energy, and accurate measurement of glucose in body fluids such as urine, blood and interstitial fluid is a very common and necessary physiological indicator in clinical practice (Kubihal et al., 2021) since it is critical for the diagnosis and treatment of glucose-related disorders especially diabetes. More specifically, the presence of glucose in the urine is known as glucosuria under normal human settings, and the usual range is 0 mg/dL to 15 mg/dL. If the level is higher than the usual range, the blood glucose level is elevated, and blood glucose levels should be between 165 and 180 mg/dL.

Generally, the term "hypoglycemia" refers to blood glucose levels that are below 40 mg/dL, meanwhile "hyperglycemia" is defined as a blood glucose level of 270 mg/dL to 360 mg/dL (Robinson & Dhanlaksmi, 2017). Consequently, abnormal glucose levels in the urine or blood are indicative of diabetes, liver or kidney-related diseases. Glucose oxidase is required for the chemical reaction based on glucose-specific reagent strips because it oxidizes glucose to create gluconic acid and hydrogen peroxide, then peroxidase aids hydrogen peroxide's interaction with the chromogen, resulting in the color response seen on the test strip. Typically, the sensitivity of urine detection for glucose can be as low as 75-125 mg/dL (Pape et al., 2020).

Urea

Urea is a metabolite of nitrogenous compounds whose content has long been used to measure kidney and liver function by evaluating human excretory or blood samples (Dhawan et al., 2009). In the human body, urea production is the primary means of removing waste nitrogen created by protein and amino acid metabolism, and the urea cycle is used to carry out this function in the liver where urea is then taken from the bloodstream and discharged by the kidneys into the urine (Liu et al., 2012). The quantification of urea in urine and blood has important clinical implications. Specifically, the usual range of urea in human blood is 2.6 to 6.5 mM, but with substantial variance in human urine (daily excretion of 342 ± 67 mM in urine), it can be 50-fold more concentrated (Shaykhutdinov et al., 2009), thereby abnormal levels of urea as a biomarker are often indicators of renal disorders. The Berthelot reaction as specific response of urea, in which released ammonia combines with phenol and hypochlorite ions to generate a blue color, is dominant in the usage of urease in the estimation of urea clinically and the detection limit is as low as 5×10^{-4} M (Francis et al., 2002).

Uric acid

The ultimate product of purine metabolism in the organism is uric acid and the majority of tests detect for uric acid in the blood. However, the kidneys excrete 60-70% of uric acid therefore uric acid appears in human urine (Bobulescu & Moe, 2012; Devi & Pundir, 2014). It is an essential biomarker found in human fluids, whose levels in the blood are typically 0.13–0.46 mM (2.18–7.7 mg/dL) in serum and 1.49–4.46 mM (25–74 mg/dL) in urine excretion (Pundir, 2015; Raj & Ohsaka, 2003). Because elevated amounts of uric acid in urine increase the risk of disorders including leukocytosis, severe hepatitis, gout, cardiovascular and renal disease, a quick and accurate measurement of uric acid is critical for detecting hyperuricemia (Fathallah-Shaykh & Cramer, 2014). Clinical laboratories use the enzyme uricase reaction sequence as a routine method for uric acid determination, with reported cases showing a detection limit of 0.58 mM (Hamzah et al., 2013).

Ions

The major sources of different cations and anions in urine are various inorganic salts (such as chlorides, nitrates, and sulphates) generated by the body's metabolism. Sodium, potassium, magnesium, calcium, iron, chloride, nitrate and other dissolved ions are all common ions

(Ghaderinezhad et al., 2020) and these soluble ions are generally present at steady-state levels, but their presence can be aberrant in the context of impaired kidney and liver function, as well as other disorders like diabetes. Abnormal amounts of Na^+ ions in urine environment, for example, have been linked to renal illness (Bricker et al., 1957), and the enrichment of heavy metal ions such as mercury detected in urine can also suggest impaired health status. Ion chromatography with ion-selective electrodes are suitable clinical methods for measuring cations and anions in urine (Chapp et al., 2018).

Nitrite

Nitrates are derived from dietary metabolites, and nitrate to nitrite conversion is caused by the majority of bacteria colonizing the urinary tract (Christensen et al., 2007). Nitrite is created when bacteria convert nitrate in urine to nitrite, which is not normally detected in urine (Barratt, 2007). Certain groups of bacteria, especially gram-negative bacilli (e.g., E. coli) and some gram-positive bacteria are capable of this transformation to produce nitrite (Simerville et al., 2005). As a result, the amount of nitrite in urine is proportional to the number of bacteria in the urinary tract, and the proliferation of urinary tract pathogens typically results in urinary tract infections. The Griess reaction as the clinical method, in which nitrite combines in an acid medium with an aromatic amine (para-arsanilic acid or sulphanilamide) to make a diazonium salt, which then reacts with tetrahydrobenzoquinoline to produce a pink azo dye, is used to detect nitrite, and this test detects nitrite at concentrations as low as 0.1 μg/mL to give a positive result (Mambatta et al., 2015).

Ketones

Ketones mainly refers to 3-beta-hydroxybutyric acid (3HB), acetoacetate, and acetone, which are created in the mitochondria of liver cells by incomplete fatty acid metabolism and are utilised as an energy source when glucose is insufficient for body cells (Laffel, 1999; Umpierrez et al., 2002). The body normally uses glucose (sugar) as an energy source, however when cells don't absorb enough glucose, the body is forced to burn fat for energy, producing ketones in the process, which may be detected in your blood and urine. Ketone accumulation in the urine that are too high might suggest diabetic ketoacidosis (DKA) (Wallace & Matthews, 2004). When a ketone (most often acetoacetate, AcAc) is detected in the urine, it combines with sodium nitroprusside and glycine, resulting in a chemical reaction that detects ketones. The reaction produced a color change from dark pink to purple with positive results and ketone detection sensitivity can be as low as 5–10 mg/dL (Pape et al., 2020).

RNA

Ribonucleic acid (RNA) is a single-stranded molecule consisting of ribose and phosphate groups that carries genetic and regulatory information to reflect the state of cells (Truong et al., 2013). The utilization of extracellular RNA molecules is an effective means for early cancer diagnosis and tumour progression monitoring in body fluids such as serum and urine (Xi et al., 2017). In the current

study, miRNAs are good candidates as clinical biomarkers for exploring non-invasive early-stage disease due to homogeneity across individuals, restricted tissue distribution and their good stability in body fluids (Liang et al., 2007; Weber et al., 2010).

Toxic substances

Many components in the body come from external intake, and urine can reflect their physiological and biochemical parameters, with toxic substances attracting the most attention. Take toluene as an example, it is one of the common toxic substances, and urinary hippuric acid (HA), the final and major metabolite of toluene, is considered a biological indicator of toluene exposure (Zhao et al., 2011). This is due to the fact that roughly 80% of inhaled toluene is excreted in the urine as HA whose concentration in urine is proportional to the level of toluene exposure (Park et al., 2007). Therefore, the determination of the concentration of HA in biological fluids can better reflect the real toluene exposure and poisoning in humans.

Exosomes

Exosomes are extracellular nanoscale vesicles with a shape of sphere that range in size from 30 to 100 nm (Thongboonkerd, 2020). After endocytic vesicles fuse with the plasma membrane to create the multivesicular body (MVB), it is exocytosed and released from the cell into the extracellular space (Thongboonkerd & Kanlaya, 2022). Exosomes play a vital role in cell-cell communication through carrying various biomolecules such as proteins, nucleic acids, lipids and metabolites (Lee et al., 2021). It is worth noting that exosome exist in many biofluids (blood, saliva, urine, etc.) and research indicates the content of exosomes is highly linked to kidney diseases (Grange & Bussolati, 2022). When the kidney is functioning normally, the urine exosome serves as a carrier for bioactive molecules that efficiently transfer functional substances from the upstream renal tubular cells to the downstream tubular cells, which in turn affect the activities or functions of the effector cells (Thongboonkerd, 2020). The increase in urinary exosomes in CKD patients is negatively correlated with estimated glomerular filtration rate, and therefore can be used as a biomarker for early prediction of changes in renal function (Lange et al., 2019).

Human serum albumin

The Importance of HSA

Human serum albumin (HSA), a highly homologous primary structure, is the most abundant protein in human blood (accounting for 60% of the total plasma protein), which is synthesized only in the liver, with an average of about 12-25 g per day, accounting for 50% of the liver protein synthesis (Peters Jr, 1995). Serum albumin concentration is about 35-50 g/L (Fanali et al., 2012), and urine albumin concentration is usually less than 30 mg/L and the serum half-life is about 20 days (Miller et al., 2009). Excessive HSA in urine can lead to microalbuminuria, which is an early marker of cardiovascular disease (de Zeeuw et al., 2006) and kidney disease in diabetes mellitus and hypertension (Lin et al., 2016). However, low levels of HSA in the blood plasma, known as hypoproteinemia, may be a sign of liver cirrhosis, failure, and chronic hepatitis (Wen et al., 2022). HSA also has extremely important medical value and is commonly used clinically in the symptomatic treatment of hemorrhage, shock, burns, polycythemia and hypoalbuminemia (Mishra & Heath, 2021). Because of its low cost, BSA is widely used as an alternative to HSA in many biochemical and pharmacological applications. But actually, BSA has only 75.8% of the biological functions of HSA, hence it cannot replace HSA in many applications (Bujacz, 2012). Misuse of the two proteins will lead to fatal injury to patients. Therefore, accurate detection of HSA is of clinical importance in the aspects of high-specific selectivity and low limit of detection (LOD).

HSA structure and its ligand-binding sites

HSA is a single-chain protein that conforms a heart shape, which contains 585 amino acid residues with a molecular weight of 66.438 kDa (Ashraf et al., 2023). The mature secondary structure of HSA shows that it consists of a series of α-helix (67%), turns (10%) and random coils (23%) without β-sheets (Sahoo et al., 2024). A substructure domain is produced by every three α helices, while a structure domain is formed by two subdomains A and B. As shown in **Figure 10**, the entire structure of HSA includes following three homologous α -helical domains, I (residues 1–195), II (196–383) and III (384–585) (He & Carter, 1992). Six structural subdomains (IA, IB, IIA, IIB, IIIA, and IIIB) are distributed throughout the three globular domains that make up the whole HSA. Owing to its conformational adaptability, HSA has the ability to attach to a wide range of endogenous and exogenous substances, including fatty acids, metal ions, medicines, metabolites, etc (Sahoo et al., 2024). Three major strong ligand-binding sites are characterized and identified in analyte delivery. Binding site 1 (Sudlow site 1) is located in subdomain IIA where site mainly exhibits apolar interactions meanwhile possesses a few clusters of polar residues (Mishra & Heath, 2021). Tyr150, His242 and Ard222 are one set of polar residues, which are presented at the bottom of Sudlow site 1 (Ghuman et al., 2005). Another set is situated near the entrance of binding pocket including Lys195, Lys199, Arg218 and Arg222 (Ghuman et al., 2005). Specifically, warfarin, phenylbutazone, amantadine, azapropazone, azidothymidine, indomethacin, iodipamide, oxyphenbutazone, 2'indole sulfate, and 3'diflunisal are all accepted at Sudlow site 1 (Mishra & Heath, 2021). As for Binding site

2 (Sudlow site 2) in subdomain IIIA, it shows hydrophobicity with distinct electrostatic interactions and polar residues exist near the opening of binding pocket on one side. Moreover, three residues Arg410, Ser489 and Lys414 are highly involved in ligand interactions (Ghuman et al., 2005). This site 2 is particularly bound by a number of pharmacological molecules such as digitoxin, ibuprofen, benzodiazepine, halothane, propofol, and non-steroid anti-inflammatory medicines (Ghuman et al., 2005). In terms of binding site 3 in subdomain IB, high binding affinity for endogenous ligands and heterocyclic compounds is provided by four crucial residues Tyr138, Tyr161, Arg141 and Lys190 (Ascenzi et al., 2015). It has been demonstrated that Binding site 3 is capable of binding drugs such as lidocaine, bilirubin, warfarin, myristic acid, naproxen, indomethacin, and heme iophenoxic acid (Zsila, 2013).
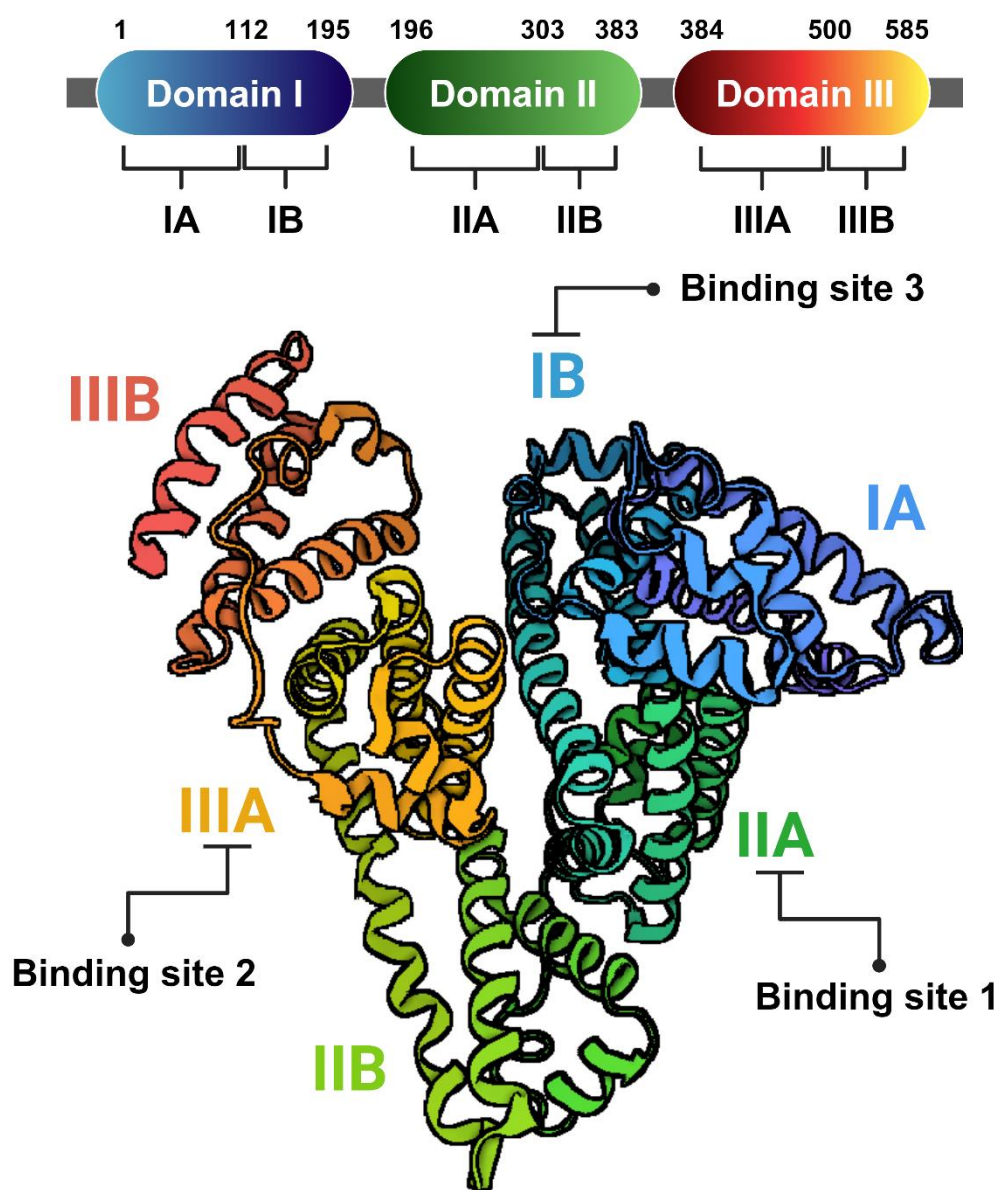
Figure 10 The tertiary structure and domains of HSA.

HSA detection methods

The best way to detect biomarkers would be using a straightforward, low-cost test that takes a non-invasive sample to be acquired. Primarily, the optimal biomarker needs to possess sensitivity and the ability to forecast a clinically significant outcome such as the advancement of end-stage renal disease (ESRD) or mortality (Nimse et al., 2016). Considering the economic cost and actual requirements of HSA detection among a large group of patients, the majority of HSA detection needs a qualitative/semi-quantitative testing rather than an accurate quantitative testing because the threshold of albuminuria localizes at a high concentration of HSA and the sensitivity of HSA detection are sufficient to diagnose the main pathological progress of CKD. Under such background, these effective methods must possess obvious features of reliable repeatability, significant phenomenon, simple operation, steady results and intuitive identification. Therefore, color and immune reactions as the typical biochemical response have the priority in this situation. With the expansion of medical applications, the detection of HSA at ultra-low concentrations, complex matrices or protein clearance has prompted continuous optimization of current detection methods or the emergence of new methods.

Traditional methods of HSA detection

Colorimetric and immunoassay as the common methods for HSA detection are very successful and mature analytical strategies with various forms. The schematic of them is illustrated as **Figure 11** shows and typical examples are mentioned below.
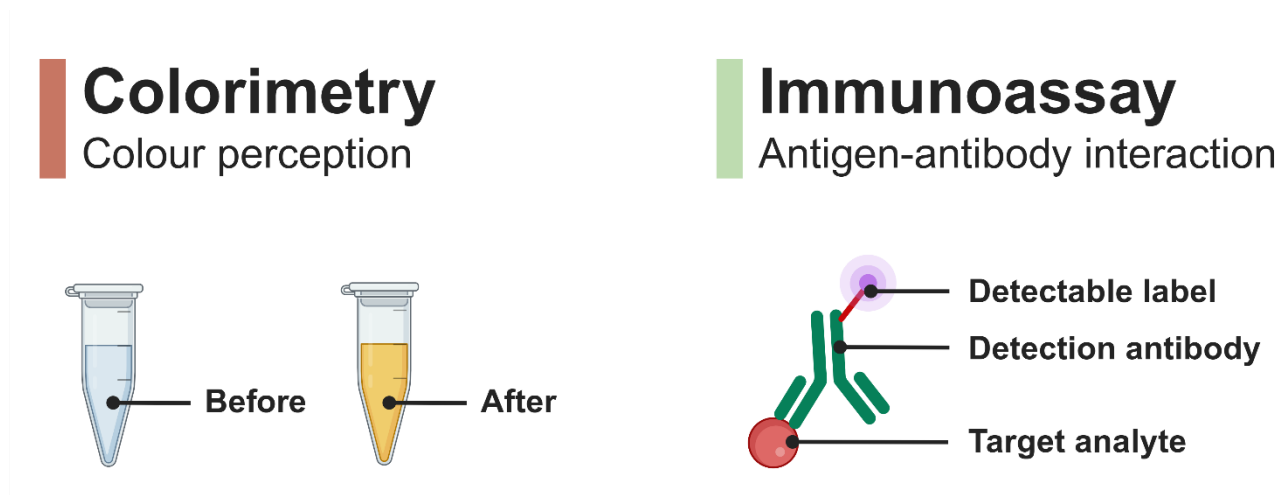
Figure 11 Schematic of colorimetry and immunoassay.

Colorimetric determination

Colorimetry is a type of photometry that is defined as colour matching and colour difference in the numerical descriptions of different samples by observation (Ohta & Robertson, 2006). Visual changes make it easy to distinguish variations in analytes on tracking chemical and physical reaction

before and after. The end products from the reaction of specific reagents and HSA change the light absorption directly based on the Beer-Lambert's Law (VS et al., 2017). With the fast development of imaging and sensing, the colour value can be read out directly from the results of HSA detection using intelligent instruments conveniently (Xu et al., 2022).

Reagent test strip

Reagent test strip is the most straightforward testing method of HSA in normal scenarios. It creates a semiquantitative detection on colour reaction through HSA and pH indicators. This phenomenon displays different colours in the presence/absence of HSA because HSA can serve as a hydrogen ion acceptor (ESTERASE et al.). Generally, the intensity of colour is positive correlated with the amount of HSA. The procedure is that when strip is dipped into samples, strip shows colour on read area within 60 seconds (Hohenberger & Kimling, 2008). After that, the provided colour map can be employed to match with our samples. Notably, test strip only produces approximate readings, which can help you distinguish the normal/abnormal concentration within a wide range. In terms of trace HSA, paper-based strip is not sensitive enough to identify it but provide a convenient operation to get HSA information.

Bromocresol green and bromocresol purple

The staining agent of bromocresol green (BCG) and bromocresol purple (BCP) are commonly used for determining HSA to form the chromophore. Although a few research found that the reaction between BCG and HSA are affected by globulins (Keay & Doxey, 1984; Ueno et al., 2016), they are still popular due to its simplicity, rapid response, obvious phenomenon and cost-efficiency. In most cases, the colour signal has a positive proportion to the amount of HSA. When BCG interact with HSA in acidic environment (pH = 4), the complex of BCG-HSA is formed, transforming from the colour of yellow into green (Duly et al., 2003). HSA concentration can be calculated indirectly through the readout of optical density (OD) or absorbance. Similarly, the purple-coloured BCP-HSA complex is formed at red emissions (Hinton et al., 1990).

Developed colorimetric biosensors

Gupta et al. have developed novel citric acid (CA) functionalized PtNi hollow nanospheres (CA@PtNi hNS) to achieve HSA colorimetric detection (Gupta et al., 2020). The enrichment of Pt on biosensor's surface, large surface area and heterogeneous interaction between Pt and Ni atoms massively improve peroxidase-like activities. CA@PtNi hNS shows a dynamic linear range of 0 to 400 ng mL^{-1} with limit of detection (LOD) 0.19 ng mL^{-1} and colour change of product from blue to yellow. It also exhibits 120% sensitivity compared to ELISA and high recovery results of HSA (around 110%) in human plasma samples. The above-mentioned results prove a good potential for the applications in HSA detection. Besides, Huang et al. have synthesized gold nanoparticles (Au NP) for HSA

colorimetric detection (Huang et al., 2015). When cross-linker melamine is introduced to induce the aggregation of nanoparticles, the citrate-capped AU NP produces a red to blue colour shift. Notably, HSA exhibits the function of anti-aggregation effect as colour change outputs. Melamine-induced aggregation does not occur in the presence of Au NP since tight junctions between adjacent gold particles are hindered by adsorption of HSA or cross-linking between Au NPs and melamine is inhibited by HSA fixation. The results illustrate a dynamic range from 0 to 500 nM with LOD of 1.4 nM and a good selectivity of HSA over amino acids, peptides, ions, and proteins. Moreover, good recovery rates of 96% to 103% are validated for HSA quantitative detection in artificial urine. Certainly, there are still many excellent colorimetric biosensors to achieve HSA detection which are not listed here.

Advantages and disadvantages of colorimetry in HSA detection

Colorimetry belongs to a quantitative and qualitative detection to measure coloured substances by using light wavelength as a function of colour. The outstanding performance focuses on its inexpensiveness, simple operation and fast response (Kangas et al., 2017). With the development and advancement of current technology, the sensitivity of colorimetric methods has been further improved (B. Liu et al., 2020). However, the measured reading of colorimetry has a strong time correlation (Shrestha & Shrestha, 2023). Colour difference and fading occur, thereby causing inaccurate reading. The limited throughput and short test windows are still big challenges so far (Shrestha & Shrestha, 2023). Moreover, some techniques involve certain degree of processing or modification on HSA structure, which may cause the colour response to disappear meanwhile colourless compounds cannot be analysed in colorimetry (Ohta & Robertson, 2006).

Immunoassay determination

In clinical and research scenarios, immunoassay is a commonly employed method for quantifying and qualifying macromolecules especially different proteins derived from organisms (Slagle & Ghosn, 1996). The underlying principle of immunoassay is the interaction between an antibody and an antigen, which occurs in vertebrates, including humans, as part of their adaptive immune system (Kapingidza et al., 2020). The complex conjugates of antibody-antigen are formed with very high selectivity where the analytes act as antigens in the meanwhile reagents act as antibodies. At present, immunoassay has been developed in numerous fields of pharmacokinetics, disease diagnosis, biomarker detection, optical sensing, etc (Findlay et al., 2000).

Immunonephelometry

The size, shape, and concentration of the scattering particles are ascertained by nephelometry, which define as the measurement of scattered light. The nephelometry-assisted immunoassays use the antigen-antibody complexes as the scatterers (Whicher et al., 1982). In the immunonephelometry approach of HSA detection, an antigen-antibody response is produced when HSA in the bio-

specimen comes into contact with an HSA antibody where an optometric analysis of the reaction's rise in light scatter yields HSA concentrations (Stamp, 1988). However, it is much more sensitive to noise from dust and occasional large aggregates of irrelevant antigen-antibody complex, which reduces the signal-to-noise ratio during the measurement (Ackerman & Rosevear, 1979) .

Immunoturbidimetry

The sample scatters and absorbs light in different proportions as it moves through the reaction solution, allowing the remaining portion of light to pass through the sample. By measuring the sample's light absorbance, the amount of protein antigen present in it may be ascertained (Teppo, 1982). The turbidity of samples increases due to blocking light from antigen-antibody complex. For example, HSA that has been coupled to latex particles competes with HSA in the urine sample for a monoclonal antibody that aggregates the latex particles in the immunoturbidimetry approach. As a result, the quantity of aggregation that occurs is inversely related to the amount of albumin present in the urine sample. Urinary albumin concentration is calculated from the aggregation quantity using optometric measurement (Shaikh et al., 2008).

Radioimmunoassay

Antibody-antigen binding and radioactive antigen are used in radioimmunoassay procedures. The competitive binding process, which occurs when analyte binds to fixed antibody or receptor binding sites in opposition to radio-labeled antigen, is the fundamental idea behind receptor-antigen competition. Antigen-antibody complex radioactivity is reduced when the unlabeled antigen binds to a fixed and limited quantity of antibody, displacing the radiolabeled antigen (Yalow, 1980). HSA in the bio-samples displaces isotopically tagged human albumin that has an antibody attached to it in the radioimmunoassay procedure. As a result, the quantity of tagged albumin that stays attached to the antibody is inversely proportional to the total amount of albumin present in the specimen. There are many methods for separating the albumin designated as "free" and "bound" in order to quantify radioactivity. HSA concentration is obtained by comparing radioactive counts to a standard curve or calibration (Brodows et al., 1986).

Developed immunoassay biosensors

In the past few decades, immunoassay achieved extraordinary development for improving its sensitivity, reducing analysis window time, simplifying operation procedure and automating design (Aitekenov et al., 2021). For instance, Zangheri et al. have synthesized the chemiluminescent (CL)-lateral flow immunoassay (LFIA) with integrated amorphous silicon (a-Si:H) photosensors array for quantitative HSA detection in urine samples. An indirect competitive immunoassay is designed where anti-HSA antibodies are competed for by HSA in urine and HSA immobilized on nitrocellulose membrane. Through the addition of the CL luminol/enhancer/hydrogen peroxide cocktail, detection

is carried out with secondary antibodies labeled with horseradish peroxidase (HRP). The results show a dynamic range up to 850 mg L^{-1} with LOD 2.5 mg L^{-1} in urine, which proves that the integration of the a-Si: H photosensors array and CL-LFIA technique is feasible applications for in-field and point-of-care bioanalyses (Zangheri et al., 2016). Del Valle and his team demonstrated a sandwich-type ultramicroELISA assay for HSA detection in urine (Del Valle et al., 2020). To guarantee the assay's specificity, solid phase is comprised of strips coated with a high affinity monoclonal antibody that is directed against albumin. It shows a wide dynamic range of 1.44×10^{-3} to 0.2 mg L^{-1} with LOD 1.44×10^{-3} mg L^{-1}. Depending on HSA concentrations examined, the intra- and inter-assay coefficients of variation were 3.98–4.35% and 7.59–8.92%, respectively. The recovery percentage varied from 98.50% to 94.26%. This test will enable low-income countries to get an affordable diagnostic kit for microalbuminuria in public health system. Based on the above and many reported examples, immunoassay is a very stable and effective HSA detection method.

Advantages and disadvantages of immunoassay in HSA detection

The immunoassay provides inherent specificity and high sensitivity for the analysis of a board range of HSA due to strong and stable immunobinding (Comper et al., 2004), which enable a wide range of applications in real scenarios. It is generally safe and environmentally friendly owing to the unnecessary use of radioactive substances and massive organic solvents, but the reagents and samples are protein-based, which demands refrigerated transport and storage (Sakamoto et al., 2018). Furthermore, preparation of antibodies, especially high-purity antibodies, is really expensive (Sakamoto et al., 2018). the specific ligand binding may be located on a group of compounds (aminoglycosides, pesticides, etc.) instead of an individual big biomolecule, resulting in false positive or negative readings (Darwish, 2006). Non-specific absorption/binding may occurs between antibody-antibody or antibody-matrix components (Darwish, 2006), which needs to be excluded during measurement. Besides, immunoassay requires costly equipment and long measurement time (Nie et al., 2020).

New possibilities of HSA detection

Fluorescence methods

Fluorescence, as a spectrochemical method, utilizes a specific light beam to excite analyte and then emit light with a longer wavelength. The produced emission light reflects the sample's information, which can be measured and identified by imparting light color and intensity changes. A variety of developed FL probes are capable of binding with HSA to form the complex of HSA-FL probes through chemical bond, physical interactions, optical effects, etc (Wang et al., 2024). Generally, the significant results are designed to two completely opposite phenomena: FL enhancement and FL quenching. Regardless of whether it is forward or reverse input, the difference in the output light signal can be quantified to determine the albumin content in the sample.

In recent years, researchers have synthesized a variety of FL sensors for the detection of HSA. In 2017, Chen et al. have developed a poly(thymine) (poly T)-templated copper nanoparticles (CuNPs) for quantitative detection of HSA (Chen et al., 2017). FL response will be quenched in the presence of HSA because HSA will absorb cupric ion to prevent the formation of CuNPs. The results indicate a strong linear relationship with LOD 8.2×10^{-8} mol L^{-1} and successfully apply it into 1% human serum to get 87%-101% recovery rates of HSA in biological system. Additionally, Ksenofontov and his team synthesized a water-soluble FL probe BODIPY (BP1) (sodium salt of 4,4-difluoro-1,3,7,8-tetramethyl-2,6-disulfo-4-bora-3a,4a-diaza-s-indacene) to measure HSA and BSA (Ksenofontov et al., 2022). BP1 forms stable supramolecular complex with HSA and BSA by specific interactions, resulting in strong FL quenching of BP1 due to fluorescence resonance energy transfer (FRET). The results showed that LOD of HSA and BSA were 0.05 and 0.26 mg L^{-1} and HSA detection in human urine demonstrated 90-96% accuracy that also proved a potential for early detection of microalbuminuria and concomitant diseases. Moreover, Liao et al. have reported a synthetic hybrid H1 of green fluorescent protein (GFP) chromophore and peptide for HSA detection through FL enhancement (Liao et al., 2016). FL response was produced by the combination of H1 and subdomain IIA cavity of HSA via non-covalent binding. Significant results illustrated good selectivity to HSA and a good linear relationship between 0 to 67 µg mL^{-1} with LOD as low as 198.6 ng L^{-1}. Importantly, a satisfactory recovery rates of 98.1-101.5% was obtained from health urine samples.

Fluorescence with aggregation induced emission

The phenomenon known as "aggregation-induced emission" (AIE) occurs where molecules exhibit intense fluorescence in an aggregation state but exhibit weak luminescence or no luminescence when they are dispersed (Hong et al., 2011).

The restriction of intra-molecular rotation (RIR) is the primary mechanistic concept that is currently being put forth to explain the AIE phenomena (Hong et al., 2009). Molecular rotors, such as rotatable aromatic rings, are found in a large number of AIE compounds. Excited state energy is consumed by the aromatic rotors of completely dissolved AIE molecules, causing the energy to decay quickly without being released. Intermolecular interactions cause the rotors' spinning to be limited when AIE molecules collect, which leads to the molecules' disintegration through the radiation channel (Zhao et al., 2020). In several molecular systems, the AIE has been explained by the RIR model. AIE features should also be present in polyphenylene rings with benzene rings strung together directly through single bonds without the need for olefin linkers, if the RIR process is the deciding element in evaluating whether a luminophore is AIE active (Chen et al., 2019). Nonetheless, it has been noticed that several systems display the AIE phenomena without a rotor as the family of AIE

molecules keeps expanding (Hong et al., 2011). For these systems, other characteristics or variables must be taken into account because the postulated RIR mechanism is insufficient to explain the AIE impact. In addition to rotational twist as a mechanism for dissipating excited state energy, in-plane/out-of-plane cluster oscillatory motion can also nonradiometrically decay excited state energy, according to an examination of theoretical calculations and experimental results. The restriction of these rotational and/or vibrational movements causing emission turn-on is arguably the most significant conclusion drawn from the data (Zhao et al., 2015). It is discovered that restriction of intramolecular vibrations (RIV) as well as restriction of intramolecular rotation (RIR) can both cause aggregation-induced emission(Hong et al., 2009). It may be seen that restricting excited state energy can increase emission more than limiting it, and that intramolecular rotation can be more effective in consuming excited state energy (Ju Mei et al., 2015). Therefore, AIE molecules can release excited state energy non-radiatively through two pathways of limitation: intramolecular rotation and vibration. This mechanism is collectively referred to as the restriction of intramolecular motion (RIM, **Figure 12**).
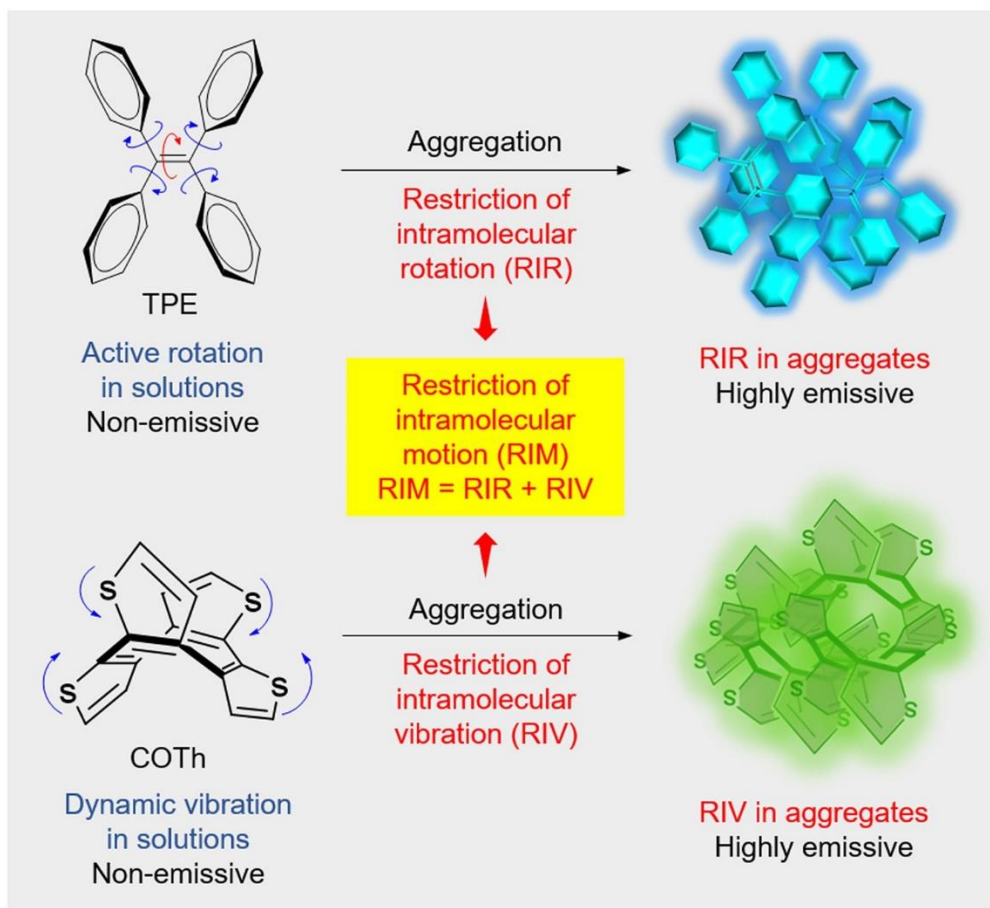
Figure 12 Mechanism of aggregation induced emission (Zhang et al., 2023).

The advantages of AIE

Firstly, High hydrophobicity is the typical properties of AIEgens in their emission centres, which leads to aggregation formation in physiological settings or aqueous media (Wang & Tang, 2019). These molecules are non-emissive in aqueous media, but their emission remarkably boost upon aggregation formation when interacting with reactive substrates. Secondly, AIEgens can constrain intramolecular movements by self-aggregation or accumulation in/on a matrix, which will further cause FL emission upon photoexcitation (Liu et al., 2011). This accumulation will show a more significant effect, especially when participating in the reaction of biological macromolecules, because the large steric hindrance of macromolecules creates a natural spatially restricted environment. Thirdly, AIEgens exhibit high sensitivity, fast response, easy operation and 'on-off' switchability in FL signalling systems due to efficient radiative transition and photosensitization in the aggregate state (De Silva et al., 1997; Feng & Liu, 2018). Above-mentioned features enable AIEgens to be developed as highly efficient FL 'turn-on' biosensors.

AIE biosensor examples for HSA detection

It is a fact that AIE-based techniques have the good potential to develop into a new detection methods for HSA in medical scenarios. In 2010, Tang and coworkers first reported an AIE probe, a tetraphenylethylene (TPE) derivative BSPOTPE for quantitative detection of HSA (Hong et al., 2010). This probe is non-fluorescent in PBS buffer but becomes emissive in the presence of HSA. The established fluorescent method exhibited a broad linear dynamic range (LDR) of 0-6.76 mg/L, a detection limit (LOD) as low as 0.0676 mg/L, and an excellent selectivity to HSA. Additionally, the sensing process was also demonstrated in artificial urine, showing great potential in real-life application. After this work, many AIE probes have been developed for HSA detection and quantification (Gao et al., 2020; Halder et al., 2019; J. Li et al., 2017; Wangyang Li et al., 2015; Zijie Luo et al., 2020; Yang Yu et al., 2016). Recently, Tu et al. reported another TPE derivative, TPE-4TA, for specific and quantitative detection of HSA (Tu et al., 2019). In this work, tetrazolate, which has a strong binding affinity toward HSA, was used as the targeting moiety. The HSA sensing performance was first evaluated in PBS buffer, showing a LOD down to 14.2 μg/L and a good LDR of 0.02-2500 mg/L. The feasibility of this probe for urinary albumin detection was further validated in clinical urine samples. All these results indicated that TPE-4TA is superior in HSA detection than other AIE-active HSA probes.

Current issues of AIE biosensors

Although AIE FL biosensors are generally stable in aqueous media, Strokes' shift is different among various AIE probes. Small Strokes' shift is not conducive to differential detection because of large areas of overlap (Hong et al., 2009). Synthesizing AIE FL biosensor with large Strokes' shift is always one of the challenges and directions for biomarker detection. Furthermore, aggregation-caused quenching (ACQ) may occur which produces the opposite phenomenon where reactants are extremely high or interact with some substances to form a planar structure occasionally in solvent

system and it favours the occurrence of π–π stacking in aggregation (Ma et al., 2016). Most reported AIEgens have a short absorption wavelength, which is frequently seen as a drawback. This is mostly due to their twisted molecule architectures, which can considerably lower the penetration depth in biomedical research, particularly for in vivo applications, but may not have an impact on their performance in electronics (Wu & Liu, 2021).

Engineering design

What is engineering design

Engineering design is a dynamic and systematic process that uses engineering knowledge, accumulated experience and rational creativity to solve the practical problems (Eggert, 2005). This process is divided into four steps. Firstly, engineering design requires well-defined problems and challenges that are fully or partially achievable within design constraints such as available resources, limited funds, limited time, safety issues, etc. Secondly, scientific and technical information should be investigated to generate several feasible solutions. This requires researchers to have sufficient knowledge accumulation or learn from the experience of others. It should be noted that the proposed solutions are only hypothesis for the problems and does not mean that they can be fully realized. After that, testing is a compulsory step by constructing models or prototypes to ensure whether the products meet the criteria (Hubka, 2015). The content items of the design have different priorities. The design can focus on realizing one or several functions while weakening some capabilities, but the premise is that the changes do not exceed the constraints. Finally, end product should be finalized and put into use.

The applications of engineering design for HSA detection

Hydrogel

What is hydrogel

Hydrogels, as 3D hydrophobic polymeric networks, are fabricated by water soluble polymer crosslinking, which possess the capability of retaining or absorbing a large amount of water (at least 20%) or biofluids in its network structure (Majcher & Hoare, 2019). The crosslinks of hydrogel are divided into two branches: chemical covalent bonds and physical non-covalent bonds (Deligkaris et al., 2010). Point crosslinks, or interactions between individual polymer chains over a certain length, do not result in junction zones. Hydrophilic and hydrophobic blocks are connected to produce a polymer amphiphile, which is one way that hydrophobic contact results in physical crosslinking (Xiao & Yang, 2006). In addition, polymers have the ability to connect through charge interaction or hydrogen bond formation, which creates a physical crosslink between them. Charge interaction can happen between two oppositely charged polymers or between a polymer and a tiny molecule. Bonds that aren't covalent, like hydrogen, are far weaker than those that are (Hennink & van Nostrum, 2012). In terms of chemical bonds, Covalent contacts offer superior mechanical stability since they are far stronger than non-covalent ones. Using enzymes, high intensity radiation, chemical reactions between complimentary groups, and radical polymerization are some techniques for creating chemical crosslinks (Hennink & van Nostrum, 2012).

The advantages of hydrogel

Hydrogel (**Figure 13**) is very popular for applying into the biomedical fields including sensing (Maruyama et al., 2008), fluid control (Richter et al., 2003), drug delivery (Hu et al., 2009), artificial materials (Bassil et al., 2008), biomarker detection (Ji et al., 2019), etc. The reason is that hydrogels exhibit very good characteristics such as biocompatibility, adjustable geometry, non-toxicity, non-biodegradability, flexibility, temperature sensitivity and low-cost (Revete et al., 2022; Tavakoli & Tang, 2017). These behaviors fulfill the biofunctionalized requirements to fully develop engineering applications of AIE FL biosensors. Hydrogels provide the platforms with porous structures and large internal surface for accommodating bioreceptors and achieving interactions of biological components. Designing strategies are mainly focusing on steady immobilization, bonding capacity, swelling kinetics, diffusion and environmental friendliness (Tavakoli et al., 2021).

The examples of AIE FL biosensors for HSA detection using hydrogels

Through looking up Google scholar, PubMed, ResearchGate, Web of science, etc., the key words such as "aggregation induced emission, hydrogels, HSA detection and fluorescence biosensors" are input and there is no work regarding AIE FL biosensors using hydrogels for HSA detection. After excluding the characteristics of AIE, several cases of FL hydrogels for HSA detection are found as reference attached. Liu et al. have synthesized an amphiphilic organic FL probe BCPB loading into hydrogels to achieve HSA detection as portable kits. The introduction of HSA triggers disassembly of BCPB aggregates then form conjugates of HSA and BCPB, resulting in FL ratio change and color shift. The results show a good linear dynamic range from 0 to 200 $\mu mol\ L^{-1}$ and LOD 2.1 $\mu mol\ L^{-1}$. The intensity of green and red channels (G/R value) fluctuated little, which proves the excellent stability of this hydrogel kit (Liu et al., 2024). Shikha et al. have reported FL encoded hydrogel microbeads to achieve protein detection including HSA. Upconversion nanoparticles are modified with carboxyl groups to impart functionality for conjugation of probe antibodies against target proteins. A wide range of 100 to 100000 $ng\ mL^{-1}$ and LOD 7 $\mu g\ mL^{-1}$ illustrates improved detection efficiency compared to ELISA (Shikha et al., 2018). To sum up, these instances demonstrate the good potential of applying hydrogel platform onto current AIE-based FL materials, thereby further improving the performance of HSA detection.

| Film | Soft | Amorphous | Stiff | Peelable |

Figure 13 Different prototypes of hydrogel models.

What is metasurface

Metasurface is two-dimensional versions of metamaterials that consist of periodic subwavelength metallic/dielectric structures. Unprecedented properties are exhibited by Its nanostructure coupled to the electric (E) and magnetic (M) fields of the incident EM waves (Ali et al., 2022). The customized unit cells (**Figure 14**), which is called meta-atoms, are designed under the full control to manipulate surface wave. The patterns of unit cells can guide, disperse and concentrate waves along designated directions (J. Hu et al., 2021). On the other hand, the geometry and periodicity of unit cells control the refractive index to adjust and change the optical performance (J. Hu et al., 2021). In general, metasurface is designed through four steps to develop feasible products (S. Zhang et al., 2020). Firstly, meta-atoms with subwavelength structures should be arranged carefully because the optical response, such as amplitude, polarization and phase, can be tuned by the selected materials, size, shape, etc. Secondly, the phase map should be decided based on fixed parameters. Adjusting diameters, periodicity and height of nanostructural arrays change the signal transmission value. Thirdly, phase profile can be created on the basis of phase map, which can describe the simulated phase of desired metasurface by a function of spatial position. Finally, the focal profile determines the full width of half maximum of the focused spot size, thus constructing the 3D model of metasurface.

The advantages of metasurface

In the past few decades, research on metasurface has attracted great attention on various applications in different fields. Notably, biosensing and bioimaging of biomarkers in metasurface platform provides a solution for high effective, high sensitivity, inexpensive and robust detection (S. Zhang et al., 2020). Firstly, the thickness of metasurface is in the nano-level that is roughly equal to the thickness on the order of wavelength (Li et al., 2018). By selecting the suitable nanostructures, the wave front can be arbitrarily regulated, in the meanwhile the components of nanostructures enable to adjust to meet the spectral and polarization response (Hsu et al., 2022). Secondly, all-dielectric metasurface based on silicon-on-insulator can fully use the advantages of Si optical properties including excellent refractive index, great optical transmission, low resonance loss, anti-interference, biocompatibility and low cost (Iwanaga et al., 2023b). Thirdly, light confined mode is achieved by beam shaping in both transmission and reflection (Brière et al., 2019). Furthermore, biofunctionalization is feasible to immobilize biomarkers onto the outermost of metasurface (Barulin et al., 2024; Yesilkoy et al., 2019). These features promote the applications of biomarkers detection and show the promising capabilities to enhance optical signal in real scenarios.

The examples of AIE FL biosensor for HSA detection using metasurface platform

Through looking up Google scholar, PubMed, ResearchGate, Web of science, etc., the key words such as "aggregation induced emission, metasurface, all-dielectric metasurface, HSA detection and fluorescence biosensors" are input and there is no current study regarding AIE FL biosensors using metasurface platform for HSA detection. After excluding the characteristics of AIE and fluorescence, several cases of metasurface for HSA detection are found as reference attached. Kuznetsova and his team have studied a metal-dielectric metasurface as microwave sensors for validating HSA detection. Resonance frequency shift of the wave reflection coefficient of the metal-dielectric metasurface allows researchers to calculate variations in HSA concentration in enzymatic reaction mixtures and water solutions. It shows a dynamic range from 0 to 100 mg/mL and detection sensitivity is 0.075 MHz/(mg/mL). Many industries, such as environmental monitoring, food and beverage production, and biomedical research and diagnostics, could benefit greatly from the use of this suggested metal-dielectric metasurface-based structure for protein concentration determination in various samples, including enzymatic protein hydrolysis reaction mixtures (Kuznetsova et al., 2024). Kuznetsova et al. also reported a multiwell plate metasurface to achieve HSA detection in the range of 0 to 100 mg/mL. The ability to customise the size of the metasurface to interact with electromagnetic waves at particular frequencies was demonstrated. Solutions in a range of frequency ranges may be tested thanks to the conventional multiwell plates' availability in different sizes (Kuznetsova et al., 2023).
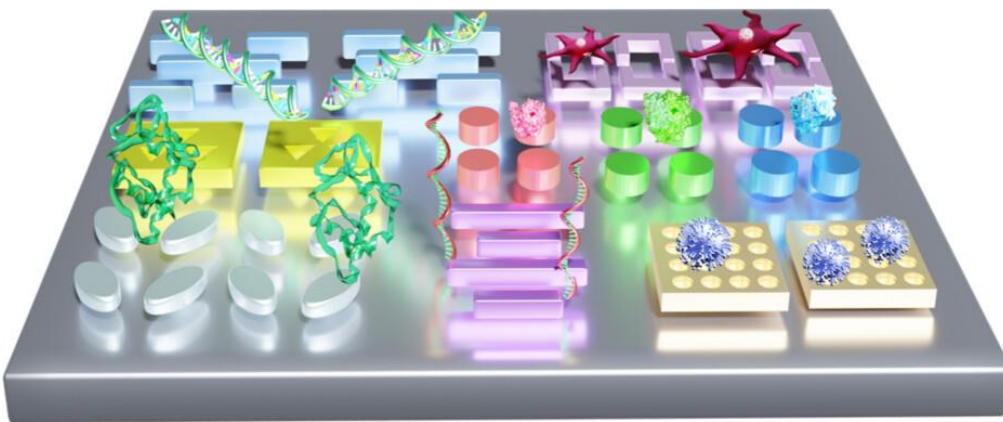
Figure 14 Illustration of metasurface with customized meta-atoms (Barulin et al., 2024).

AIE BIOSENSOR FOR HSA DETECTION

This chapter has already been published on "*Chemistry–An Asian Journal*, 2021, *16*(10), 1245-1252" under the title "**Detection of Urinary Albumin Using a Novel "Turn-on" Fluorescent Probe with Aggregation-Induced Emission Characteristics**". Qi Hu and Bicheng Yao are the primary authors, while Tze Cin Owyong, Sharon Prashanth, Changyu Wang, Xinyi Zhang and Wallace W. H. Wong are co-authors, and Youhong Tang and Yuning Hong are the correspondent authors (**doi.org/10.1002/asia.202100180**).

In this chapter, a novel fluorescent dye TC426 has been developed, which can be synthesized through a simple two-step synthetic route. This probe is non-fluorescent when molecularly dissolved in aqueous solution but shows strong emission upon aggregation or in a viscous medium, characteristic of typical AIE active molecules. Due to the unique chemical structure and photophysical property, TC426 can be applied in the detection of HSA, showing comparable results as previously reported HSA probes. To apply probe TC426 to albumin detection in real urine scenarios, the influence of pH and interfering substances present in urine are evaluated and the results demonstrated excellent stability and good selectivity towards HSA. Significantly, satisfactory recovery rates in spiked real human urine samples were obtained by using TC426 as the fluorescent probe. This indicates that AIE probe TC426 has great potential in practical urinary albumin analysis.

Introduction section

Human serum albumin (HSA) as the most abundant plasma proteins (55-60%) (Nicholson et al., 2000) is a significant biomarker for clinical diagnosis particularly on renal disease and proteinuria (Hu et al., 2022). It also plays vital roles in many aspects of physiological functions including maintenance of normal plasma colloidal osmotic activity (Fanali et al., 2012), the specific attractive force for the retention of positively charged solutes in blood vessels (Prakash, 2017), good scavenging ability towards free radical (Levitt & Levitt, 2016), etc. Therefore, HSA detection is of great importance in clinical sensing according to its biological effects and medical benefits. Additionally, α-helical domains of HSA structure where primary binding sites I and II located at subdomains IIA and IIIA prefer to react with larger heterocyclic compounds, dicarboxylic acid and small molecules allow numerous endogenous and exogenous substances to bind with HSA via varying ligand binding affinity (Kragh-Hansen, 2016; Lee & Wu, 2015; Tong et al., 2017). Current methods for identifying albumin take advantage of its characterized affinity, and immunoassay and colorimetry are very common measurements (Xu et al., 2022). Generally, immunoassay (Limit of detection, LOD: 2-10 mg/L) is undesirable for real-time HSA detection due to time-consuming, complicated processes and expensive costs, in the meantime low detection sensitivity and a small detection window in colorimetry (LOD: 150 mg/L) also make accurate detection difficult (Comper & Osicka, 2005; Gaitonde et al., 2017; Martin, 2011).

Fluorescence based strategies have attracted increasing attention from the biosensing field, due to the advantages of simple operation, rapid response, high sensitivity, and cost efficiency. Among various fluorescent probes, the aggregation induced emission (AIE)-based ones demonstrated outstanding performances, such as application to a broad concentration range, good photostability, low background noise, large Stokes shifts, etc.(X. Gu et al., 2017; Hong et al., 2009, 2011; Hong et al., 2012; Kobayashi et al., 2010; Kwok et al., 2015; J. Liang et al., 2015; J. Mei et al., 2015) As such, AIE-based techniques may be a good substitution for current test methods for HSA. In 2010, Tang and coworkers first reported an AIE probe, BSPOTPE for quantitative detection of HSA.(Hong et al., 2010) This probe is non-fluorescent in PBS buffer, but becomes emissive in the presence of HSA. The established fluorescent method exhibited a broad linear dynamic range (LDR) of 0-100 nM, a detection limit (LOD) as low as 1 nM, and an excellent selectivity to HSA. Additionally, the sensing process was also demonstrated in artificial urine, showing great potential in real-life application. After this work, many AIE probes have been developed for HSA detection and quantification.(Gao et al., 2020; Halder et al., 2019; J. Li et al., 2017; W. Li et al., 2015; Z. Luo et al., 2020; Y. Yu et al., 2016) Recently, Tu et al. reported a novel AIE probe TPE-4TA for specific and quantitative detection of HSA.(Tu et al., 2019) In this work, tetrazolate, which has a strong binding affinity toward HSA, was used as the targeting moiety. The HSA sensing performance was first evaluated in PBS buffer, showing a LOD down to 0.21 nM and a good LDR of 0.02-2500 mg/L. The feasibility of this probe for urinary albumin detection was further validated in clinical urine samples. All these results

indicated that TPE-4TA is superior in HSA detection than other AIE-active HSA probes. However, the synthesis of TPE-4TA requires harsh conditions, thereby the difficulty in synthesis may limit its further application.

Herein, a novel fluorescent probe TC426 with aggregation-induced emission (AIE) characteristics is reported as a sensitive and specific probe for HSA. This probe is non-emissive in aqueous solution, meanwhile it shows bright fluorescence upon interacting with HSA, which makes it applicable in detecting HSA with a high signal to noise ratio. Besides, the fluorescence of TC426 exhibits a high linear correlation with the concentration of albumin in the range of microalbumin (20-200 mg/L), which has a significant importance for the early diagnosis of glomerulus related diseases. Compared with previously reported HSA probes TPE-4TA and BSPOTPE, TC426 shows comparable anti-interference ability towards creatinine and other major components in urine. Moreover, probe TC426 can be excited at the visible light range, which can avoid the use of UV light for excitation like the previous dyes. Finally, with the established assay, TC426 shows excellent performance in detecting HSA in real human urine, indicating its great potential in practical urinalysis.

Experimental section

Materials and instruments

1,3-Propanesultone, inorganic salts (NaCl, KCl, $MgCl_2$, $CaCl_2$, NH_4Cl, Na_2CO_3, $NaHCO_3$, Na_2SO_4, and Na_2HPO_4), proteins (HSA, BSA, pepsin, ubiquitin, papain, and trypsin), RNA, GSH, PBS tablets, glycerol, uric acid, creatinine, glucose, and chromatographically pure solvents (DMSO, toluene, chloroform, etc.) were all purchased from Sigma-Aldrich. Hydrochloric acid and sodium hydroxide were obtained from Chem-supply. Urea was obtained from Chem-supply. 4-(Diethylamino)salicylaldehyde was obtained from AK Scientific. 1,3-Indanedione was obtained from Alfa Aesar. Probes BSPOTPE and TPE-4TA were synthesized according to previously publications (Hong et al., 2010; Tu et al., 2019). ^1H (400 MHz) & ^{13}C NMR (100 MHz) spectra were acquired on Agilent MR400 or Agilent DD2 instrument. The chemical shift data for each signal are given as $δ$. High-resolution mass spectra were acquired using a Thermo Scientific Q Exactive Plus Orbitrap LC-MS/MS instrument. Absorbance and fluorescence spectra were obtained on a Cary 300 UV-Vis spectrometer and Cary Eclipse fluorimeter (Agilent Technologies Inc., USA), respectively. Particle size distributions were measured in triplicate on Zetasizer Nano ZEN3600 (Malvern Instruments Ltd, Malvern, WR14 1XZ, United Kingdom). pH values were adjusted using HANNA HI208 pH meter. Data were plotted using Origin 2018 (OriginLab Corp., USA).

Synthetic procedures

Biosensors TPE-4TA (S. Xie et al., 2018) and BSPOTPE (Tong et al., 2007) were synthesized according to previous publications and supplied by AIEgen Biotech Co., Ltd, China. The synthetic route to TC426 was shown in Scheme 1 and detailed synthesis procedures were shown as following.

Synthesis of 2-(4-(diethylamino)-2-hydroxybenzylidene)-1H-indene-1,3(2H)-dione (**2**). 4-(Diethylamino)salicylaldehyde (1, 9.66 g, 50 mmol) was added to 1,3-indanedione (6.58 g, 45 mmol). A mixture of ethanol (100 mL) and water (50 mL) was then added. The reaction mixture was then stirred and heated at 75 °C for 3 h. Upon completion of the reaction, the reaction mixture was cooled to room temperature and 100 mL of water was added. The precipitates were filtered and washed with an ethanol: water mixture (1:1 x 1 and 1:5 x 2) to give the product as a dark red solid in 70% yield (11.2 g). ^1H NMR (400 MHz, DMSO-d_6) δ 10.71 (s, 1H), 9.21 (d, J = 9.4 Hz, 1H), 8.19 (s, 1H), 7.77 (s, 4H), 6.43 (d, J = 9.4 Hz, 1H), 6.18 (s, 1H), 3.76 – 3.14 (m, 4H), 1.15 (t, J = 7.0 Hz, 6H). ^{13}C NMR (101 MHz, DMSO-d_6) δ 191.54, 189.71, 163.94, 155.39, 141.74, 140.01, 139.37, 136.69, 134.86, 134.59, 122.18, 122.11, 118.84, 111.20, 105.81, 96.17, 44.91, 13.12. HRMS (ESI+): m/z. 322.14319 [$C_{20}H_{20}NO_3$ (M+H)$^+$, calcd 322.14322].

Synthesis of sodium 3-(5-(diethylamino)-2-((1,3-dioxo-1,3-dihydro-2H-inden-2-ylidene)methyl)phenoxy)propane-1-sulfonate (TC426). Intermediate compound **2** (500 mg, 1.56 mmol) was added with NaOH (74.9 mg, 1.87 mmol) and taken up in ethanol (20 mL) and stirred at

room temperature for 30 min. 1,3-propanesultone (419 mg, 3.43 mmol) was taken up in ethanol (10 mL), slowly added to the reaction mixture before heating at 75 °C for 12 h. Upon completion of the reaction, the reaction mixture was cooled to room temperature and poured into ethanol. The precipitate was then filtered and washed with ethanol (x3) to obtain the pure product as a red solid in 36% yield (258 mg). ^{1}H NMR (400 MHz, DMSO-d_6) δ 9.27 (d, J = 9.4 Hz, 1H), 8.20 (s, 1H), 7.78 (s, 4H), 7.58 (d, J = 5.6 Hz, 1H), 6.50 (d, J = 10.4 Hz, 1H), 6.24 (s, 1H), 4.28 (t, J = 6.6 Hz, 2H), 3.54 (q, J = 6.8 Hz, 4H), 2.60 (t, J = 7.1 Hz, 2H), 2.26 – 1.75 (m, 2H), 1.16 (t, J = 6.9 Hz, 6H). ^{13}C NMR (100 MHz, DMSO-d_6) δ 191.34, 189.61, 163.61, 155.57, 141.76, 139.56, 139.39, 136.99, 134.91, 134.66, 132.92, 122.25, 122.17, 120.80, 119.42, 111.69, 105.65, 93.96, 67.80, 48.07, 25.48, 13.16. HRMS (ESI-): m/z. 442.13161 [$C_{23}H_{24}NO_6S$ (M-Na)$^-$, calcd 442.13298].

Experimental protocols

Preparation of AIE FL biosensors

TC426 was dissolved in dimethyl-sulfoxide (DMSO) solution, the stock solution was made to 10 mM and kept at -20 °C in the dark for long term storage. Moreover, the recommended working solution of TC426 was prepared daily by suitable dilution of the stock solution with PBS buffer to 10 μM. TPE-4TA and BSPOTPE stock solution (10 mM) was prepared in PBS buffer and can be stored at 4 °C in the dark for further use.

Preparation of HSA samples in PBS buffer

HSA stock solution with a concentration of 1000 mg/L was first prepared in PBS buffer and stored under 0-4 °C. The stock solution was diluted stepwise to our desired concentrations including: 0.1, 0.5, 1, 5, 10, 20, 50, 75, 100, 125, 150, 175, 200, 500, 700 mg/L. Moreover, each concentration must have three parallel samples for three repeated fluorescence measurements.

Preparation of HSA-TC426 mixtures in PBS buffer for FL measurements

Pipette 1.998 mL of the above prepared HSA samples and 0.002 mL TC426 stock solution to an Eppendorf tube. Shake each mixture with vortex shaker violently for 10s to obtain HSA-TC426 samples with [TC426] = 10 μM and [HSA] = 0.1, 0.5, 1, 5, 10, 20, 50, 75, 100, 125, 150, 175, 200, 500, 700, and 1000 mg/L. Finally, the HSA-TC426 samples were transferred into a quartz cuvette for fluorescence measurement.

Study on pH influence

One PBS tablet was dissolved in 180 mL DDI water to afford the PBS buffer with pH value around 7.4. Afterward, 1 M hydrochloric acid and sodium hydroxide aqueous solutions were used to adjust the pH value to 4, 5, 6, 7 and 8, respectively. Finally, add DI water until the total volume of each solution reaches 200mL. For the study of pH influence, HSA solid powder was dissolved in PBS buffer with different pH values to give a final HSA concentration of 1000 mg/L. Then stock solution of TC426 was added, mixed using vortex shaker, incubated for 20 min, and measured using

fluorescence spectrometer. The fluorescence of PBS buffers with only probe TC426 added were also measured for comparison.

Study on selectivity

Certain amount of salt powders (sodium chloride, potassium chloride, magnesium chloride, calcium chloride, ammonium chloride, sodium bicarbonate, sodium sulfate, disodium hydrogen phosphate and sodium carbonate) were weighed and dissolved in the PBS buffer (pH 7.4), respectively, to give the ionic solutions with concentrations of 10 mM. Afterwards, 1.998 mL ion solutions, as well as PBS buffer and HSA solution (1000 mg/L), were added with 0.002mL TC426 stock solution to afford different samples for fluorescence measurement. Similarly, eight common biomolecules which are BSA, Pepsin, Ubiquitin, Papain, Trypsin, RNA, GSH and HSA were selected to explore the probe protein response at 1 mg/mL in PBS buffer. The fluorescence intensity of these samples was measured at room temperature according to the previous operation procedures.

Study on interference

Common urine components including uric acid, urea, creatinine and glucose, were dissolved in PBS buffer (pH = 7.4) at 10 mg/mL. Notably, due to the limited water solubility of uric acid, the concentration of uric acid applied is about 0.3 mg/mL. The concentration of HSA is 1000 mg/L. The concentration of bioprobes TC426, TPE-4TA and BSPOTPE after mixing with interferents were all 10 µM. During the whole measurement process, the three probe stock solutions were added separately into five urine components samples (v/v 1:999) to mix evenly. The excitation/emission maxima wavelength of TC426, TPE-4TA and BSPOTPE are 480/550 nm, 360/490 nm and 350/470 nm, respectively.

Mechanism study

Firstly, lyophilized powder of HSA was dissolved in PBS buffer (pH 7.4) with a concentration of 10 mg/L. Then, different amounts of urea were added to the as-prepared HSA solution to prepare samples with urea concentration ranging from 0 to 10 M. Afterward, 0.002 mL probe TC426 stock solution was added to each HSA/urea solutions and incubated for 1 hour to ensure that the protein denaturation fully occurred. At last, fluorescence spectra were recorded using a fluorescence spectrophotometer.

HSA detection in spiked human urine samples

Human urine samples were collected from healthy volunteers from Flinders University and tested following the guide from the Southern Adelaide Clinical Human Research Ethics Committee, Australia. First of all, based on the previously standard curve in PBS buffer, HSA samples with concentrations of 0, 0.1, 0.5, 1, 5, 10, 20, 50, 75, 100, 125, 150, 175 and 200 mg/L were similarly prepared in the urine samples of subjects and diluted ten times with PBS buffer. After that, 0.002 mL of TC426 stock solution was mixed with 1.998 mL of the (diluted) urine sample and was fully mixed

by vortex shaker for 10 seconds. The mixture was transferred to a cuvette and fluorescence spectra were recorded using a Cary Eclipse Fluorescence Spectrophotometer.

Recovery study

HSA solutions in human urine with different concentrations of 50, 125, 175 mg/L are prepared artificially. According to the obtained master curve in real human urine, the fluorescence intensity measured from these three samples were substituted into the master curve to calculate the recovered concentration and recovery rate.

Results and discussion section

Probe synthesis and structural characterization

The synthetic route to the albumin probe TC426 is shown in **Figure 15**. In short, the Knoevenagel condensation reaction between 4-(diethylamino)salicylaldehyde and 1,3-indandione yielded the intermediate compound **2**. Subsequent alkylation of the hydroxy group from compound **2** with 1,3-propanesultone allowed for the introduction of a sodium sulfonate group and formation of the final probe molecule TC426. The structure of both compound **2** and TC426 were characterized by ^{1}H NMR, ^{13}C NMR and HRMS and satisfying results were obtained (**Figure S1-S5**).
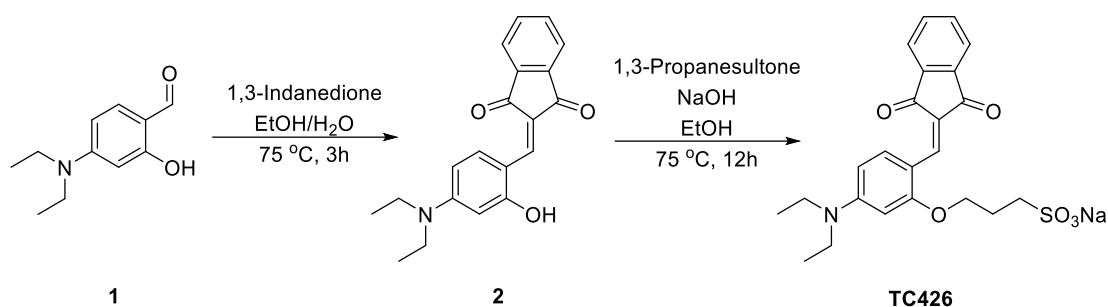
Figure 15 Synthetic route to probe TC426.

Photophysical property characterisation

As seen from Scheme 1, the conjugation of 1,3-indandione was extended after conjugated with 4-(diethylamino)salicylaldehyde through a carbon-carbon double bond. The presence of the electron acceptor 1,3-indanedione moiety, gives rise to an electron donor-acceptor (D−A) structure in TC426. Sodium sulfonate groups further endow TC426 with good water solubility. The first step was to measure the UV-vis absorbance spectra of TC426 in different solvents. As shown in **Figure 16A**, minimal differences in spectral character were observed for most of the solvents, with the absorbance maxima wavelength ranging from 494 nm to 512 nm. The spectra measured in toluene was an exception, with a slight blue-shifted absorbance maxima at ~450 nm and a shoulder peak at ~490 nm.

After that, the fluorescence emission behaviours of TC426 in these solvents were examined (**Figure 16B**). In most cases, when excited under the absorption maxima wavelength, the fluorescence emission spectra of TC426 does not change significantly, with all the peak wavelengths centred around 535 nm. With regards to the fluorescence emission intensity, some variances can be observed, and minimal emission intensity was recorded in PBS buffer. For the two exceptions measured in chloroform and toluene, new dominant fluorescence maxima were observed at ~ 655 nm, with only chloroform retaining the previously seen 535 nm peak. A possible explanation for this phenomenon is the formation of large emissive aggregates with red-shifted spectra in the low/non-polar solvents of chloroform and toluene. The particle sizes of TC426 in chloroform and toluene were

then measured using the Dynamic Light Scattering (DLS) technique. The results confirm that large particles of TC426 with average sizes of 107.2 nm and 175.6 nm were formed in chloroform and toluene respectively (**Figure S6–S7**).

Finally, relative fluorescence quantum yields (QYs) of TC426 in various solvents were measured using fluorescein as the reference. The results summarized in **Table S1** showed the highest QY value of 1.26% in chloroform and lowest QY values of 0.05% in water. Moreover, the QY value was plotted as a function of solvent Lippert-Mataga polarity parameter (**Figure S8**) and found that QY of TC426 decreases linearly with the increase of solvent polarity. The QYs in toluene, chloroform, DMSO and isopropanol are exceptions, which can be ascribed to the AIE characteristics of TC426 in poor solvents (toluene and chloroform) or viscous solvents (DMSO and isopropanol). This will be further explained in the next part. In summary, the QY of TC426 shows typical solvent polarity dependence.

As aforementioned, when molecularly dissolved in PBS buffer, TC426 is non-emissive under the excitation of 488 nm. However, it becomes highly fluorescent when aggregated into large particles or in solid state (**Figure S9**). This feature is completely in conformity with the definition of AIE, which inspired us to further study its AIE behaviour. The fluorescence of TC426 is measured in water/glycerol mixtures whose viscosity can be increased by adding more glycerol. As shown in **Figure 16C and 16D**, when the glycerol fraction is above 70 vol%, the fluorescence intensity of probe TC426 enhances dramatically with the increase of glycerol fractions. This phenomenon can be explained by the rigidification of the molecule structure resulting from the increasing solution viscosity, which blocks the non-radiative decay channels and enhances the fluorescence emission of TC426. Fluorescence spectra of TC426 in DMSO with increasing content of toluene, a poor solvent for TC426, were characterized (**Figure 16E and 16F**). When toluene fraction is below 70 vol %, fluorescence emission spectra peaked at 535 nm were obtained which can be ascribed to the monomeric emission of TC426. Affected by the electron D—A structure, the emission of TC426 monomer was slightly suppressed in polar solvent due to the twisted intramolecular charge transfer (TICT) effect (Sasaki et al., 2016), and enhanced when more non- polar solvent was added to weaken the TICT effect. Beyond 70 vol% of toluene, the fluorescence intensity at 535 nm began to decrease significantly, meanwhile a new peak belonging to the aggregates of TC426 emerged at 655 nm and increased with higher toluene fraction. This result indicates the transition of monomeric to aggregate emission species with the increase of toluene content. The formation of aggregates, instead of quenching fluorescence like traditional aggregation-caused quenching (ACQ) type fluorophores, exhibits fluorescence intensity enhancement, further manifesting the AIE-character of TC426.
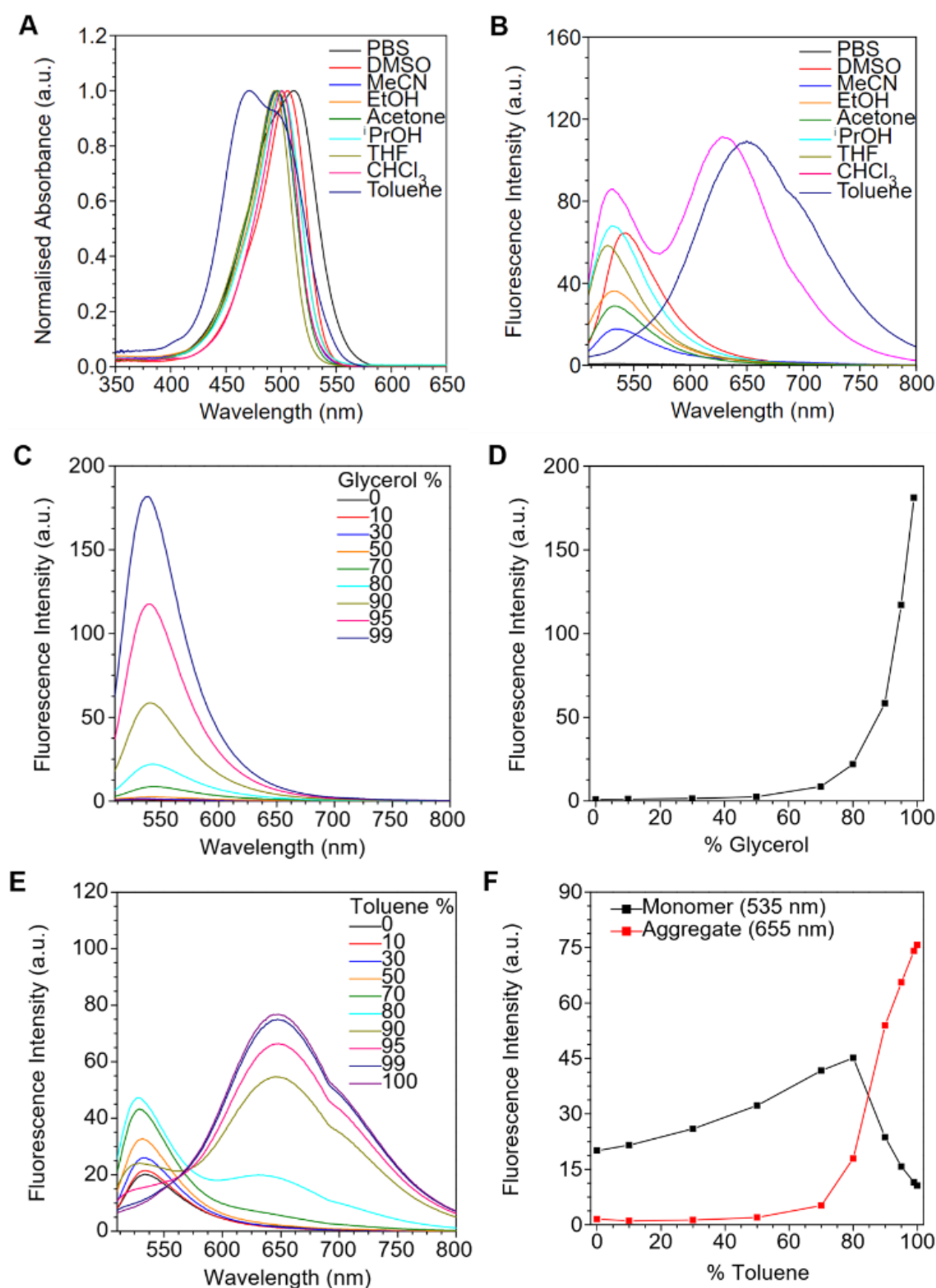
Figure 16 Absorbance and fluorescence emission spectra characterisation for TC426. (A) Normalised UV-Vis absorption spectra and (B) Fluorescence emission spectra of TC426 in different solvents. (C, D) Fluorescence spectra and plot of fluorescence intensity of TC426 in water/glycerol mixtures, with increasing fraction of glycerol from 0 to 99%. (E, F) Fluorescence spectra and plot of fluorescence intensity of TC426 in DMSO/toluene mixtures with increasing fraction of toluene from 0 to 100%. Plots were obtained by taking fluorescence emission intensity values at 535 nm and 655 nm for monomer and aggregate fluorescence emission, respectively. PBS was Na_2HPO_4 at 20 mM concentration. 10 µM dye concentration and 488 nm excitation wavelength were used for all measurements.

Quantitative detection of human serum albumin

Based on our previous research, AIE fluorogens (AIEgens) with periphery-charged groups including sulfonate, carboxylate, trialkyl-ammonium, pyridinium, and tetrazolium groups, may have fluorescence enhancements upon binding with HSA (Tu et al., 2019; Yao et al., 2021). These functional groups facilitate AIEgens to dissolve in water, thus exhibiting weak fluorescence. When bound to the hydro- phobic cavity of HSA, the RIM effect of AIEgens can occur and thus lead to the fluorescence enhancement effect. Since TC426 is AIE-active and has an alkyl sulfonate group, it may be applied in the detection of HSA. This research first studied the fluorescence response of TC426 towards HSA in PBS buffer (10 mM, pH = 7.4). The time-dependence of probe fluorescence intensity after adding the 1000 mg/L HSA sample was shown in **Figure S10**. Upon addition of HSA, an intense fluorescence signal at 550 nm can be detected. The fluorescence intensity reached equilibrium quickly and was stable within 60 min, indicating the fast response of probe TC426 towards HSA. In order to further explore its sensitivity, fluorescence titration of probe TC426 with various concentrations of HSA in PBS buffer was conducted. As shown in **Figure 17A**, the fluorescence intensity of probe TC426 at 550 nm increased gradually with the increase of HSA concentration. When HSA concentration reached to 1000 mg/L, the fluorescence intensity at 550 nm was enhanced approximately 450 times. Additionally, an excellent linear correlation between the fluorescence intensity and HSA con- centration was observed with $R^2 = 0.9954$ in the concentration range of 0–1000 mg/L (**Figure 17B**). This linear correlation can be further improved in the microalbuminuria range of 20 to 200 mg/ L as shown in **Figure 17C and 17D** (James et al., 2010; Narva, 2008). Finally, according to the IUPAC-based method, the limit of detection (LOD) of probe TC426 was calculated to be as low as 0.253 mg/L (3.74 nM). Both the linear dynamic range (LDR) and LOD of TC426 are comparable to those of other HSA probes, such as BSPOTPE (LOD: 0.0676 mg/L; LDR: 0–6.76 mg/L). In brief, probe TC426 shows good performance in the quantitative detection of HSA, which may find potential applications in urinalysis for kidney disease prediction.
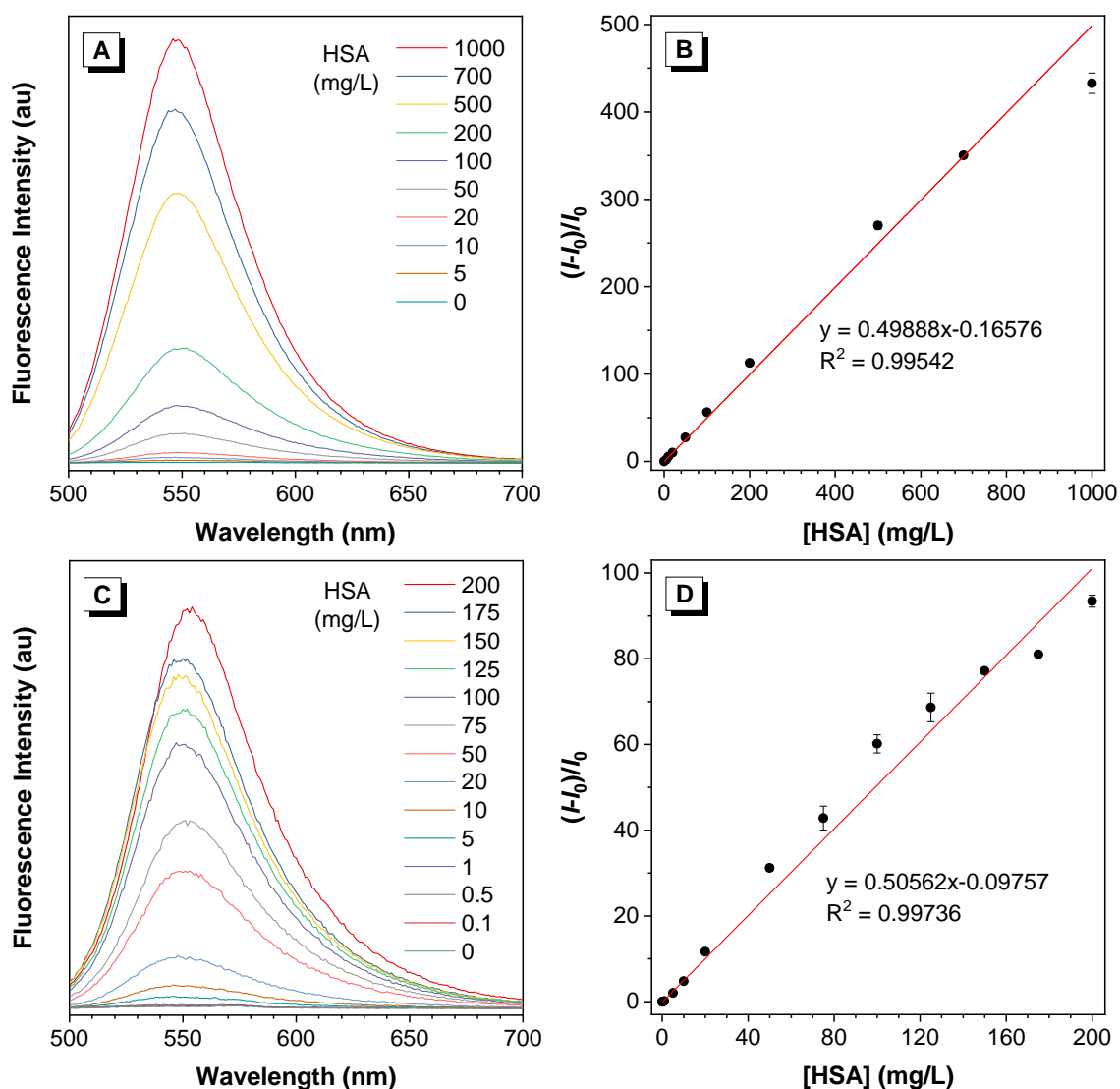
Figure 17 Fluorescence spectra of probe TC426 in the presence of HSA with concentration ranging from (A) 0–1000 mg/L and (C) 0–200 mg/L. Plot of fluorescence intensity increase fold at 550 nm versus the concentration of HSA ranging from (B) 0–1000 mg/L and (D) 0–200 mg/L. The fluorogenic detection were carried out in PBS buffer with pH= 7.4. [TC426] = 10 µM, λ_{ex} = 480 nm, I_0 equals the intensity of [HSA] = 0 mg/L.

Selectivity and interference study

Due to the chemical complexity of human urine, that includes a wide pH value (5.5–7.0) and various components (urea, uric acid, creatinine, inorganic salts, etc.), practical application of TC426 in urine should evaluate the environmental interferences first. Here, the effect of pH values was evaluated on the sensing process of TC426 towards HSA. As shown in **Figure 18A**, in the absence of HSA, no fluorescence can be detected. In contrast, after addition of 1000 mg/L HSA, the fluorescence intensity of TC426 increased markedly and remained stable in the pH range of 5.0–7.0. Even though the measured fluorescence intensity is slightly higher under extreme conditions (pH = 4.0 or 8.0), this impact may be reduced through diluting urine samples with PBS buffer. Based on the results, it can be concluded that probe TC426 is able to detect HSA in a wide range of pH values.

The specificity of probe TC426 toward HSA was then compared to a variety of ions, commonly found in biological fluids. As shown in **Figure 18B**, no fluorescence enhancement was observed after the addition of those ions. Proteins with different isoelectric points (ranging from 1 to 10) were then selected for study, including pepsin, BSA, ubiquitin, papain, and trypsin. Apart from a minor response from BSA, whose structure is similar to HSA, none of the other proteins were observed to elicit a large fluorescence intensity enhancement in TC426. Fluorescence responses of TC426 towards amino acid glutathione (GSH) and nucleic acid RNA were also examined and show minimal fluorescence variations under the same test conditions (**Figure 18C**). These results demonstrate the excellent selectivity probe TC426 has for HSA over other biomolecules or ions and can be applied in complex biological environments.

Since probe TC426 can be potentially applied in urinalysis, the influence of other major components in human urine on this detection was further evaluated. Some common organic components in urine include urea, uric acid, creatinine, and glucose were selected for testing. The experimental results shown in **Figure 18D** suggested that these urine interferents have limited influence on the fluorescence emission of TC426 in the presence or absence of HSA. Additionally, the influence of these components on TPE-4TA and BSPOTPE was compared. It can be seen that the fluorescence responses of both TC426 and TPE-4TA are more stable than that of probe BSPOTPE in the presence of interferents. In brief, the novel fluorescent probe TC426 shows great potential in detecting HSA in real urine samples.
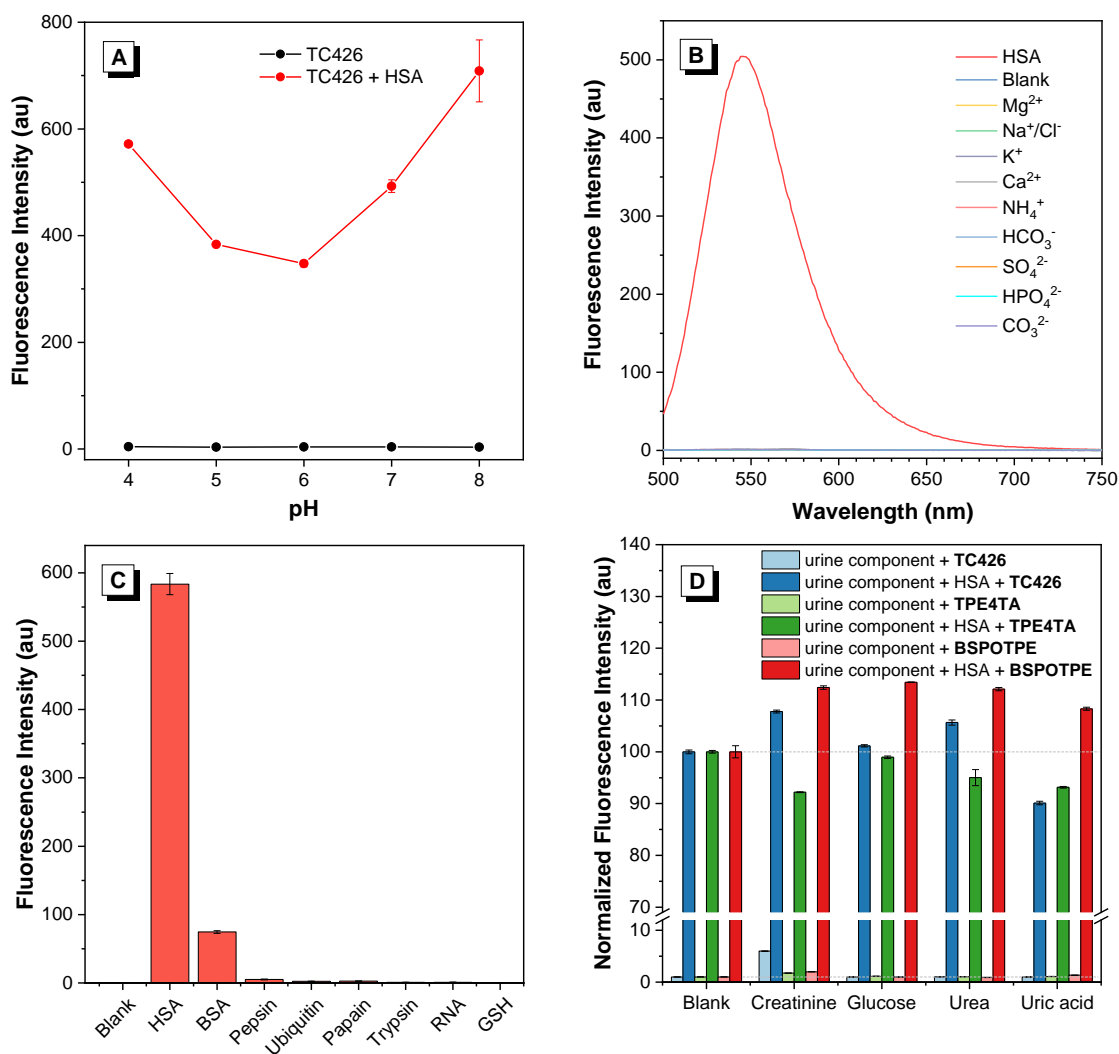
Figure 18 Study of the HSA sensing performance of TC426 at different conditions. (A) Fluorescence intensity variation of probe TC426 and HSA- TC426 mixture at 550 nm in a pH gradient. [HSA] = 1000 mg/L. (B) Fluorescence spectra of TC426 in the presence of various common cations and anions in PBS buffer (pH = 7.4). [HSA] = 1000 mg/L, [ions] - = 10 mM. (C) Fluorescence response of probe TC426 toward biomolecules in PBS buffer. [Biomolecules] = 1 mg/mL. (D) Interference of common components in urine on the fluorescence intensity of HSA probes TC426, TPE-4TA and BSPOTPE in the presence/absence of HSA in PBS buffer. [HSA] = 1000 mg/L, [urine component] = 10 mg/mL. For all the measurements, [TC426] = 10 μM, λ_{ex} = 480 nm.

Sensing mechanism

Since probe TC426 shows excellent performance in HSA detection, the sensing mechanism was further explored. Firstly, the Job plot analysis was performed to study the binding stoichiometry between TC426 and HSA. As shown in **Figure 19A**, the fluorescence intensity reached the maxima when the ratio of TC426 was among 0.3 to 0.4, which suggested that the binding ratio between TC426 and HSA is approx. 1 to 2. This observation suggested TC426 interacts with HSA as a monomeric species rather than as aggregates, which is in accord with the emission peak observed at ~ 550 nm (monomer). Secondly, the relationship between fluorescence intensity of TC426 and tertiary structure of HSA was investigated. As is known to all, HSA has two major drug binding sites,

site I and site II in subdomains IIA and IIIA, respectively. Most of the reported HSA probes interact with these drug binding sites mainly through hydrogen bonding, hydrophobic interaction, or electrostatic effects. Some literatures have reported strategies for studying HSA sensing mechanism, including using ligand displacement strategy, protein denaturation, isothermal titration calorimetry, and molecular docking calculation (Huang et al., 2020; Li et al., 2016; Luo et al., 2018; Muzammil et al., 2000; Zhu et al., 2019). Here the protein denaturation strategy was applied using urea denaturant which can break the stability of internal non-covalent bonds and destroy the tertiary structure of HSA under high concentrations (4–8 M). The fluorescence assay with urea concentration ranging from 0–10 M was carried out. As shown in **Figure 19B**, the whole process of HSA denaturation is a three-step process. When the concentration of urea is between 0–2 M, limited protein denaturation occurred, and albumin is still in its native state. The increase of fluorescence intensity maybe due to the swelling effect of HSA, which facilitates the dye molecule to get into the interior domain (Wangyang Li et al., 2015). With the increase of urea up to 2–4 M, HSA undergoes partial unfolding to reach an intermediate state, which provides a hydrophobic environment for the bound dye. As indicated in **Table S1**, the lower the solvent polarity, the higher the quantum yield. Therefore, at this stage, the fluorescence intensity further increases, mainly contributed from the hydrophobic effect. Afterwards, the continuous denaturation of albumin by higher concentration of urea, causing the loss of secondary structure, is manifested in the continuous decrease of fluorescence intensity, and finally reaches at a completely denatured state. This protein denaturation experiment proved that the sensing process is closely related to the tertiary and secondary structure of HSA. Additionally, since the QY of TC426 shows obvious polarity dependence, it can be concluded that the fluorescence enhancement during HSA detection is caused by the movement of probe TC426 from polar aqueous environment to the low polar cavities of HSA (**Figure 19C**). As such, TC426 acts as an environmentally sensitive probe for HSA detection.
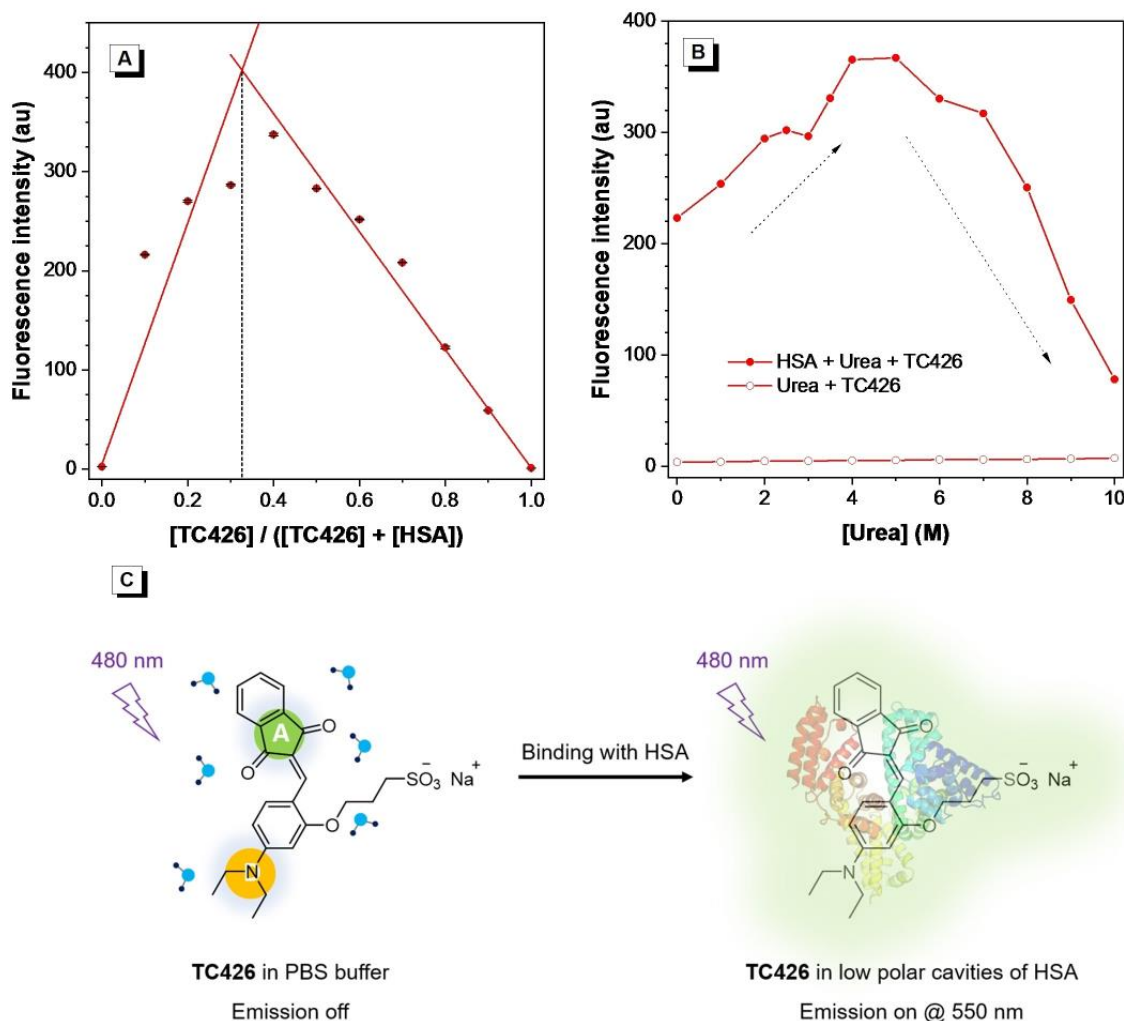
Figure 19 (A) Job plot for determination of the binding stoichiometry of TC426 and HSA. The total concentration of TC426 and HSA was kept constant as 10 μM in PBS buffer. (B) Variation in the fluorescence intensity of TC426 at 550 nm with concentration of urea in the presence or absence of HSA. [TC426] = 10 μM, [HSA] = 100 mg/L, λ_{ex} = 480 nm. (C) Schematic of the working mechanism of probe TC426 in HSA detection.

Detection of HSA in Real Human Urine

Due to its excellent performance in detecting HSA from PBS buffer, the feasibility of applying TC426 in real urine environment was further studied. Firstly, fluorescence titration in spiked human urine samples obtained from three healthy individuals was conducted to give an adjusted calibration curve which should be more suitable for practical applications (**Figure S11**). HSA spiked urine samples were diluted 10 times using PBS buffer (pH = 7.4) to eliminate the effect of pH values and autofluorescence from real urine. As shown in **Figure 20**, a good linear correlation between fluorescence intensity of TC426 and HSA concentration can be observed in the range of 0–200 mg/L. In order to simulate the application of probe TC426 to HSA detection in real scenarios, real human urine samples collected randomly from another two healthy people were spiked with certain amounts of HSA for recovery study. Since the diagnosis of microalbuminuria has significant importance in the early detection of CKD, the calculated concentrations of these urine samples are located in the microalbuminuria range, which are 50, 125, and 175 mg/L, respectively. With the newly established

fluorescence assay and adjusted calibration curve, the recovered HSA concentrations were measured and presented in **Table 2**. Satisfactory recovery rates in the range of 81.3–129.9% with standard deviations ranging from 1.5 to 10.7% were obtained. This indicates that probe TC426 can be applied to the detection of HSA in real urine samples.
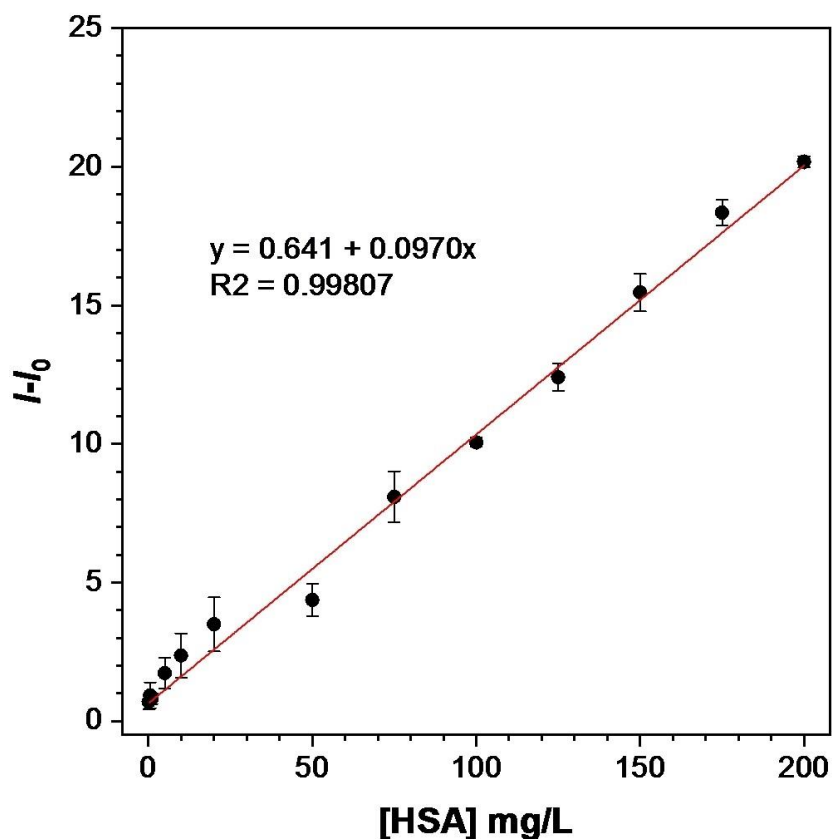
Figure 20 Plot of HSA concentration in real urine from health person versus the corresponding fluorescence intensity increase at 550 nm by the fluorescent assay using TC426 (Y-axis). I_0 equals to the fluorescence intensity at 550 nm of real urine without adding HSA. Three repeats for each concentration were conducted in urine from different healthy individuals [TC426] = 10 μM, λ_{ex} = 480 nm.

Sample	Spiked Concentration (mg/L)	Recovered Concentration $\pm$ SD (mg/L)	Recovery rate (%)
	50.0	40.7 $\pm$ 1.8	81.3 $\pm$ 3.5
Volunteer A	125.0	119.7 $\pm$ 2.1	95.8 $\pm$ 1.7
	175.0	204.7 $\pm$ 5.3	117 $\pm$ 3.0
Volunteer B	50.0	48.8 $\pm$ 5.3	97.7 $\pm$ 10.7

125.0	162.4 ± 2.6	129.9 ± 2.1
175.0	209.2 ± 2.7	119.5 ± 1.5

Table 2 Results of recovery study on the spiked HSA samples in human urine using biosensor TC426.

Conclusion

A novel 'turn-on' fluorescent probe TC426 is designed for the quantitative detection of HSA. This probe can be synthesized simply via a two-step reaction, and AIE characteristics were comprehensively investigated. Afterwards, probe TC426 was applied in the detection of HSA. The result of fluorescence titration shows a wide linear dynamic range (0-1000 mg/L) and a low detection limit 0.253 mg/L of probe TC426. Moreover, experiments proved that the sensing mechanism is through the environmental polarity response of TC426 in the tertiary structure of HSA. Before application in real urine samples, effect of pH value and common interferents from body fluids were evaluated, manifesting its high selectivity towards HSA and good stability in complex environments. Finally, the detection of HSA in real human urine by probe TC426 was validated, resulting in a satisfactory accuracy and recovery rate. Therefore, probe TC426 shows the promise to be further developed into an effective clinical method for quantitative detection of HSA in human urine.

AIE BIOSENSOR INCORPORATING WITH HYDROGEL PLATFORM

This chapter has already been published on "*Molecules*, 2023, *28*(7), 3244" under the title "**Hydrogel-Film-Fabricated Fluorescent Biosensors with Aggregation-Induced Emission for Albumin Detection through the Real-Time Modulation of a Vortex Fluidic Device**". Qi Hu is the primary author, while Xuan Luo, Damian Tohl, Anh Tran Tam Pham and Colin Raston are co-authors and Youhong Tang is the correspondent author (**doi.org/10.3390/molecules28073244**).

In this chapter, hydrogels have various promising prospects as a successful platform for detecting biomarkers, and human serum albumin (HSA) is an important biomarker in the diagnosis of kidney diseases. However, the difficult-to-control passive diffusion kinetics of hydrogels has always been a major factor affecting detection performance. This study focuses on using hydrogels embedded with an aggregation-induced emission (AIE) fluorescent probe TC426 to detect HSA in real time (**Figure 21**). Meanwhile, the technology of vortex fluidic device (VFD) as a rotation strategy is used to control the reaction kinetics and micro-mixing during measurement. The results show that the introduction of VFD can significantly accelerate its fluorescence response and effectively improve the diffusion coefficient, meanwhile VFD processing can regulate passive diffusion to active diffusion, opening up a new method for sensing research in the future.
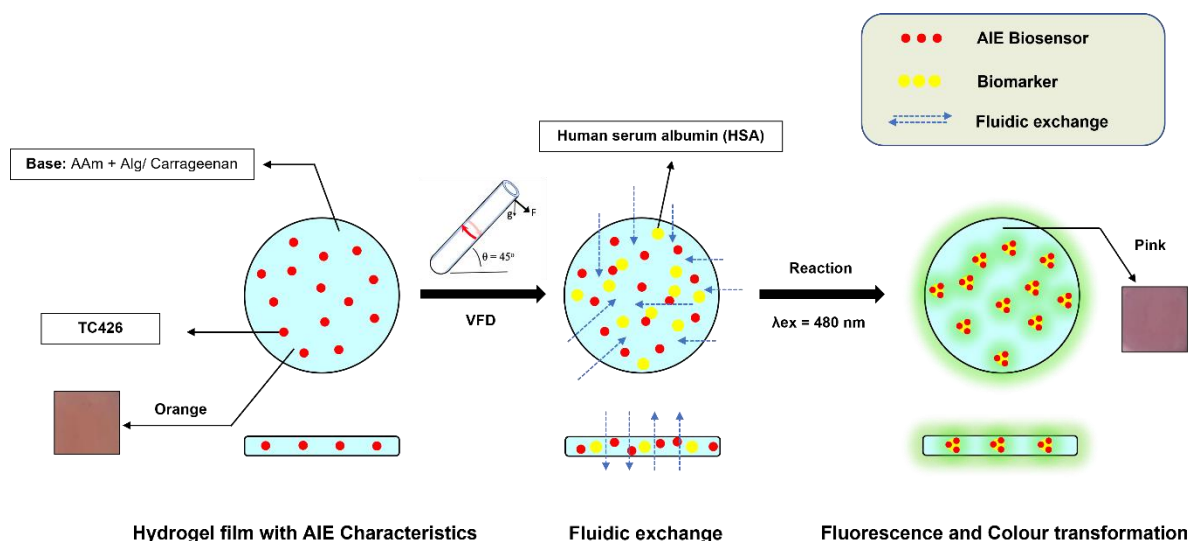
Figure 21 Illustration of AIE FL biosensor incorporating with hydrogel films under VFD control.

Introduction section

Hydrogels, as three-dimensional flexible materials, have been widely utilized due to the properties of non-toxicity, low cost, easily customizable structure & volume/shape variations, and good biocompatibility (Aswathy et al., 2020; Chai et al., 2017; Hoffman, 2012). The functional structure of its cross-linked hydrophilic network and high-water content can be manipulated for potential applications such as biomarker detection (Li, Ji, et al., 2020), drug delivery (Dreiss, 2020), shape support (Shang et al., 2019), etc. To date, some of research have paid attention to apply hydrogels in biomedical fields. Sun and his colleagues fabricated calcium alginate/polyacrylamide (CA/PAM) hybrid hydrogels with good mechanical characteristics through the combination of covalently cross-linked acrylamide (AM) and ionically cross-linked sodium alginate (SA) (Sun et al., 2012). This hydrogel has a fracture energy of roughly 9,000 Jm^{-2} and can be stretched more than 20 times of its original length even though possessing about 90% water content. The covalently crosslinked network's crack-bridging capability and the ionic crosslinked network's hysteresis contribute to the hydrogel's toughness as a whole. The adhesive properties of such hydrogels allow hydrophobic substances to be fixed stably inside through electrostatic interactions, covalent bonds or physical interpenetration. On the other hand, carrageenan is a class of polymers from natural origin that are widely used in the pharmaceutical and food industries as gelling agents, emulsifiers, thickeners or stabilizers (Kirsch, 2002). Mihaila *et al.* have developed Kappa carrageenan via physically and chemically cross-linking to achieve the demands of tissue engineering (Mihaila et al., 2013). By adjusting the degree of methacrylate and fabricating through the micromolding method, it exhibits good hydration, dissolution profile, morphology, mechanical and rheological properties, and achieves spatially controlled geometry and cell distribution patterns. The results show that the combination of its chemical and physical cross-linking procedures enables the formation of hydrogels with highly versatile physical and chemical properties, while maintaining the viability of encapsulated cells. Based on these evidence, these impressive hydrogel materials have the potential to serve as a matrix for the engineering construction of fluorescent hydrogel films.

A current research branch focuses on introducing AIE units into polymeric hydrogels to enhance the fluorescent properties owing to their surface adsorption, hydrophobic interaction, self-assembly, hydrogen bonding or other effects (Li, Wang, et al., 2020; Yang et al., 2021). Luminogens-based hydrogel films are final products that integrate the advantages of both AIE biosensors and hydrogels. First of all, the majority of AIEgens belong to hydrophobic organic molecules with non-planar propeller configurations that hardly fluoresce in the normal form but emit bright light when aggregated. The hydrophilic hydrogel matrix, where the spontaneous aggregation of AIEgens inhibits their intramolecular movements, can further amplify fluorescent effect (Lu et al., 2021). Furthermore, the encapsulation of AIE-based probe through a hydrophilic cross-linked structure is crucial to improve the environmental friendliness and biocompatibility of AIEgens in biomarker detection (Liow et al., 2017). However, the existence of some drawbacks in hydrogel films also need

to be paid attention to, which may have some impact on detection. Specifically, the sealed construction of hydrogel forces luminogens to react with the biomarker from outside to inside, thereby prolonging the detection time (Tavakoli & Tang, 2017). Additionally, the high swelling behavior may promote light scattering and increase internal structural clearance of hydrogels, resulting in weakened signal and reduced detection sensitivity, in the meantime diffusion kinetics are predominantly passive and difficult to control (Ghasemiyeh & Mohammadi-Samani, 2019). Improving these unfavourable factors is a vital first step in raising the performance of fluorescent hydrogels.

Vortex fluidic device (VFD) as a reported rotational system is a liquid thin film processing platform and has been intensively used for material synthesis (Britton, Dalziel, et al., 2016), micro-mixing (Britton, Meneghini, et al., 2016), chemical reactions (Yasmin et al., 2013), mechanical properties (He et al., 2021), etc. The mechanical energy generated from the VFD could be effectively applied to reactions, in precisely controlling the physical/chemical progress (Grzybowski et al., 2022). Accelerating reaction kinetics, modifying chemical reactivity, and enabling fast fluidic exchange are all significant effects of centrifugal or shear pressure provided by VFD (Britton & Raston, 2014; Sanders et al., 2022). More specifically, this microfluidic platform allows continuous flow operation with small sample volumes ($\leq$ 1 mL) while adjustable angle, rotational speed and steering produce dynamic thin films on the tube-wall surface and apply shearing stress during dynamic mixing. The liquid thin film offers many advantages including large surface area, high shear rates, rapid heat and mass transfer, micromixing, and fluid pressure waves (Britton et al., 2017). There have been several cases of hydrogel fabrication and optimization using VFD. Recently, Tavakoli *et al.* have achieved tuning surface morphology of fluorescent hydrogels using VFD (Tavakoli et al., 2020). The results show that the physically cross-linked hydrogels fabricated by the VFD technology have excellent fluorescence and self-adhesion as well as adjustable morphologies. VFD enables intense micro-mixing of the various ingredients, resulting in improved spatial distribution and more homogeneous end-products. Luo *et al.* have also reported silica hydrogels with embedded laccase nanoflowers (LNFs) for real-time biosensing under vortex fluidic-mediated fabrication (X. Luo et al., 2020). VFD significantly reduces LNFs production rate and further enhances LNF activity. Additionally, LNF@silica-coated VFD tubes could be used to track enzymatic processes, leading to a dramatic rise in catalytic activity (up to 16-fold).

Given to the above-mentioned characteristics of VFD, engineering designing using hydrogels expects to use the VFD technology (**Figure 22A**) to accelerate intra- and extra- film hydrodynamics in real time while enabling the AIEgens to be uniformly micro-mixed under shearing force, thus reducing the detection time, enhancing the fluorescence signal, and forming the active diffusion-controlled system. In this work, two hydrogel matrixes, acrylamide-alginate (AAm + Alg) and carrageenan, were employed in conjunction with AIE FL biosensor to detect HSA in real time to investigate their characterizations under VFD regulation. The results are anticipated that engineering hydrogel design onto AIE biosensor can meet the improved requirements of biomarker detection.

Experimental section

Materials

HSA and AIE FL biosensor

Albumin from human serum (A1653-5G) and dimethyl-sulfoxide (DMSO; 276855-2L) were purchased from Sigma-Aldrich, Australia, and bioprobe TC426 (Figure S3) was synthesised and characterised as previously reported (Q. Hu et al., 2021).

AAm-Alg-Ca^{2+} hydrogel film

For the PAAm/Alg–Ca^{2+} hydrogel, acrylamide (AAm; A8887) was the monomer used for the polyacrylamide (PAAm) networks; sodium alginate (SA; 2033; Pronova up LVM BP-1710-18) was the ionically cross-linkable biopolymer with calcium sulphate dehydrate (CaSO$_4$·2H$_2$O; C3771) as the ionic crosslinker for alginate; ammonium persulfate (APS; A3678) was used as the photo/thermal initiator for polyacrylamide; N,N-methylenebisacrylamide (MBAA; 146072) was used as a crosslinker for polyacrylamide; N,N,N',N'-tetramethyl-ethylenediamine (TEMED; T9281) was used as a crosslinking accelerator for polyacrylamide. All chemicals were purchased from Sigma-Aldrich, Australia unless otherwise stated, and they were of analytical grade and used without further purification. Solutions were prepared with deionised water unless otherwise noted. The fabricated hydrogels were stored at 4°C for 1 week and are ready for use when needed at room temperature.

Carrageenan hydrogel film

Carrageenan (GGOG, E407) was purchased from Sigma-Aldrich, Australia. The fabricated hydrogels were stored at 4°C for 1 week and are ready for use when needed at room temperature.

Instruments

A magnetic stirrer (Thermo Fisher Scientific Inc., Melbourne, VIC, Australia) was employed during hydrogel fabrication. Deionised water was produced from the Milli-Q Water Purification System (Merck Millipore Inc., Burlington, MA, USA). Laboratory Ovens (Labec Pty Ltd., Sydney, NSW, Australia) were equipped for heating. Fluorescence spectra were obtained on a Cary Eclipse Fluorescence Spectrophotometer (Agilent Technologies Inc., Santa Clara, CA, USA). A scanning electron microscope (SEM, FEI F50, Hillsboro, OR, USA) was employed to observe the microstructure. Optical imaging was performed with an Axio Imager 2 Upright microscope (Zeiss Inc., Oberkochen, Germany). Data were plotted using Origin 2019b (OriginLab Corp. Northampton, MA, USA).

Methods

Preparation of HSA and AIE FL biosensor solutions

2000 mg/L of an HSA solution in DI water was first prepared as the stock solution and stored it at 0–4 °C. Then, it was diluted stepwise to the required concentrations in the range of 0–2000 mg/L in

specific experiments for daily use. In addition, TC426 was dissolved in a DMSO solution to 10 mM as the stock solution and kept at 20 °C in the chemical cabinet for long-term storage.

Hydrogel fabrication of AAm-Alg-AIE FL biosensor

PAAm/Alg–Ca^{2+} hydrogel was synthesised on the basis of previously reported protocols with modifications (Yuk et al., 2016). 480 mg of AAm and 76.4 μL of $CaSO_4$ slurry (0.75 M) were dissolved into 1 mL of deionised water to prepare Solution A. Then, 80 mg of SA, 14.4 μL MBAA (2% w/v), 3.2 μL TEMED, and 90.4 μL APS (0.27 M) were dissolved in 3 mL of deionised water to prepare Solution B. Afterwards, 4 μL of the TC426 dye solution ([TC426] = 10 μM refers to working concentration) was added into Solution B. Under magnetic stirring, Solutions A and B were quickly mixed to obtain a uniform solution. The solution was then poured into a mould, sealed, and heated up to 80 °C for 20 min to achieve free-radical polymerisation. Afterwards, the mould had been taken out and left at room temperature overnight (24 h) before the hydrogel was removed from the mould.

Hydrogel fabrication of Carrageenan-AIE FL biosensor

First, 80 mg of carrageenan powder was dissolved in 4 mL of deionised water under magnetic stirring; then, 4 μL TC426 dye solution (TC426 = 10 μM refers to the actual working concentration) was added after powder had fully dissolved until the two were mixed well together. Similarly, the final solution had been poured into the mould and sealed at room temperature overnight (24 h) before the hydrogel was removed from the mould.

VFD operation

The film was placed at the bottom of the VFD tube against the wall of the tube. Then, 3–4 mL of the specific albumin solution was poured, ensuring that the film was completely submerged below the liquid surface (**Figure 22B** and **22C**). Rotational time was accurately controlled with a stopwatch, and one film was manipulated in each rotation.
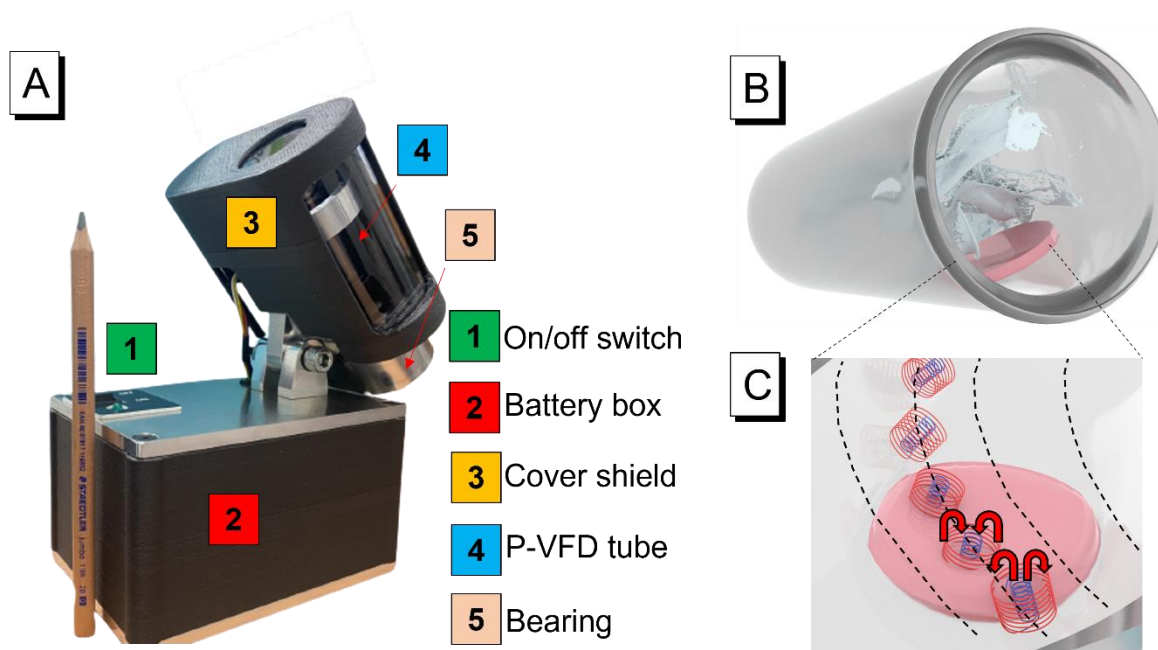
Figure 22 (A) Photo of portable-VFD used in this study; (B) The interaction process between the solution and hydrogel film adhered to the tube wall; (C) Spinning top flow mediated efficient transferring of the reactants into and out of the hydrogel matrix.

Protocols for AIE FL biosensor + AAm-Alg/Carrageenan hydrogels

The film had a fixed diameter of 25 mm and height of 2 mm under the mould fabrication (**Figure S12**), and the volume was 2 mL. Three random locations at each film were selected and tested as parallel control groups in every test; the excitation wavelength of TC426 was set at 480 nm. The VFD parameters for this study were 1500 rpm rotational speed, 45° tilt angle, clockwise (CW) rotation (looking down the tube), and rotational time was adjusted according to the specific experiment.

Kinetics of hydrogel swelling

The swelling ratio is one of the most important parameters to characterise the swelling behaviour of hydrogel samples. In this experiment, the swelling performance of two basements of AIE-embedded materials, AAm–Alg and carrageenan, with or without the influence of VFD, was evaluated. Samples were weighed every minute in a time span from 0 to 10 min in groups of three, and the results were averaged to simultaneously standardise the behaviour and reduce errors. Excess water on the sample surface was wiped off with absorbent paper before each measurement.

The real-time swelling ratio can be expressed with the following formula (Ganji et al., 2010):

$$Swelling\ ratio\ (\%) = \frac{M_t - M_e}{M_e} \times 100\% \tag{1}$$

where M_t is the actual film weight at t minutes, and M_e is the film weight when it is in equilibrium (kept ≥24 h).

Fraction of Swelling Power

The diffusion mechanism of hydrogels in aqueous solution is the primary element to study their swelling kinetics. Water diffusion motions induce a hydrogel to swell when hydrogels come into contact with water, which participates in the migration of water into pre-existing or dynamically formed spaces between the hydrogel chains. The fraction of swelling power can be derived from Fick's law (Karadağ & Saraydın, 2002):

$$Fraction \; _{swelling \; power} = \frac{M_t - M_0}{M_0} = Kt^n \tag{2}$$

where M_t is the mass of the swollen state at time t, and M_0 is the mass of the dry state at time 0. t is the time, K is the swelling constant, and n is the diffusional exponent. Equation (2) was only applied to the <60% stage in its swelling curve.

Transport determination

The solvent–polymer system is characterised by constants K and diffusional exponent n. The physical process of hydrogel film absorption or AIE release was defined, and Equation (2) could be further derived to obtain diffusional exponent (n) to decide which type of transport in hydrogels. Particularly, natural logarithms are applied on both sides of Equation (2):

$$\ln \left(\frac{M_t - M_0}{M_0}\right) = ln(Kt^n) \rightarrow \ln(F_{sp}) = ln(K) + n * \ln(t) \tag{3}$$

Therefore, diffusional exponent (n) can be calculated from the slopes of the lines of $\ln(F_{sp})$–$\ln(t)$ plots. For cylindrical films, Fickian behaviour is indicated by 0.45 < n < 0.5; non-Fickian diffusion is defined as 0.50 < n < 1.0; when n < 0.45, it is less-Fickian behaviour. Crucially, diffusion transport that is decided by n can be used to predict the relationship between the penetration rate of water and the relaxation rate of polymer chains in swollen systems (Ganji & VASHEGHANI, 2009). The information is displayed in **Table 3**.

Transport	Diffusional exponent (n)	Actual behaviours
Less-Fickian	n<0.45	$R_{water\ penetration} \ll R_{polymer\ chain\ relaxation}$
Fickian	0.45<n<0.5	$R_{water\ penetration} < R_{polymer\ chain\ relaxation}$
Non-Fickian	0.50<n<1.0	$R_{water\ penetration} > R_{polymer\ chain\ relaxation}$

Table 3 The definition of three types of diffusion transport and their corresponding factors

Diffusion coefficient

The diffusion coefficient (D) generally describes the amount of a certain substance that diffuses across a unit area in one standard time while being affected by a one-unit gradient (Elaloufi et al., 2003). Based on Equation (3), K and n are obtained from cylindrical models of AAm-Alg and carrageenan hydrogels, then the diffusion coefficient will be calculated as follows (Mathew et al., 2022):

$$D = \pi r^2 \left(\frac{K}{4}\right)^{1/n} \tag{4}$$

where r represents the radius of film at the swollen state, K is the swelling constant, and n is the diffusional exponent.

Dynamic loss

Fluorescence intensity loss is referred to as dynamic loss in this context. Since intensity is linearly positively associated with the quantity of TC426-HSA binding and TC426 biosensors all originate from film, hydrogel film is the source of all fluorescent signals and the ratio of the fluorescence intensity for current remaining films to the external solution recorded in the VFD tube can be expressed to reflect the actual leakage of TC426 in the delivery system. The equation is shown as follows:

$$Dynamic\ Loss(\%) = \frac{I_e}{I_f + I_e} \times 100\% \tag{5}$$

where I_e is the FL intensity of external HSA solution at different VFD time, and I_f is the FL intensity of currently existing hydrogel film.

Limit of detection

The limit of detection (LOD) represents the minimum fluorescence response of TC426-HSA aggregates in the presence of HSA. In this case, the LOD can be calculated by the following formula:

$$LOD = \frac{3\sigma}{k} \tag{6}$$

where σ is the standard deviation of the blank measurement, k is the slope of standard curve.

Results and discussion section

Kinetics of fluorescent response and VFD modulation

TC426 exhibited typical AIE characteristics in the hydrogel films (**Figure 28A**). **Figure 28B** shows that TC426 maintained a nonfluorescent state in both matrices: acrylamide–alginate and carrageenan. However, the introduction of HSA triggered green fluorescence that immediately produced an emission at the peaks of 530 and 545 nm. When HSA variation was in the range from 0 to 1000 mg/L, the ligand bonding of TC426–HSA remained concentration-dependent while also indicating positive proportional intensity in both matrices (**Figure 23A and 23B**). Additionally, a discrepancy of no more than 5.39% existed between the fluorescent intensity ranges presented with AAm–Alg and carrageenan.
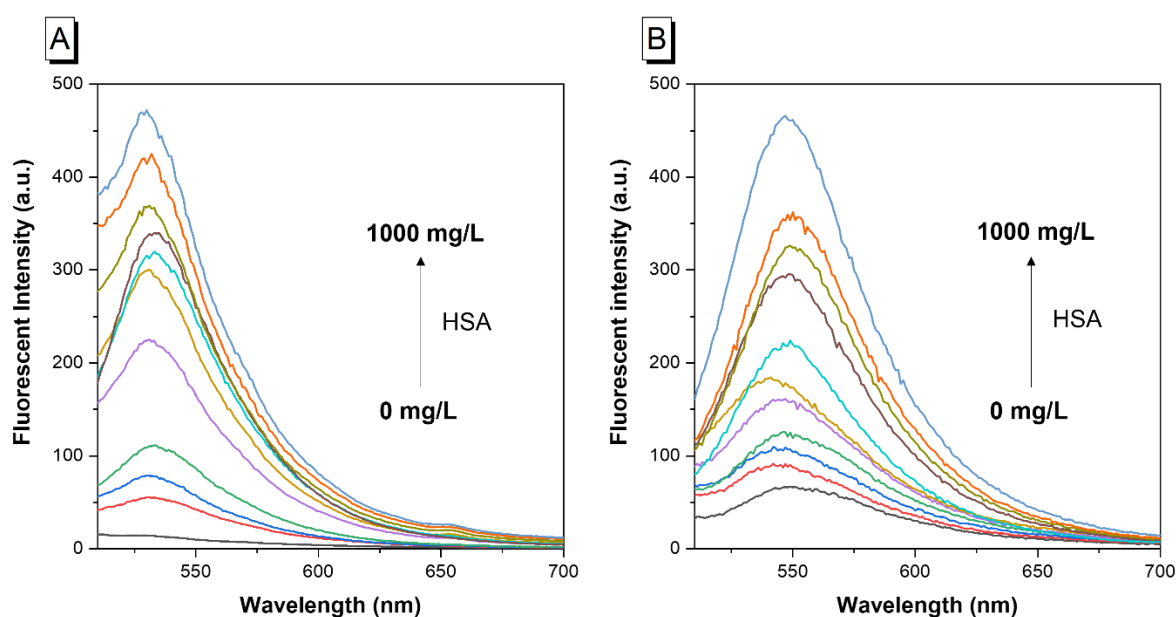
Figure 23 Hydrogel film with embedded AIE biosensor TC426 reacting with different concentrations of HSA solution. Fluorescence spectra of (A) AAm-Alg + TC426 and (B) Carrageenan + TC426 in the presence of HSA in the range of 0 to 1000 mg/L; [TC426] = 10 μM, λ_{ex} = 480 nm.

On this basis, a portable vortex fluidic device was further introduced to observe the influence of hydrogel films on photoluminescence behaviours in real time. In order to quantify the changes during time-varying rotation, multiple aspects, including colour shift, fluorescent intensity, swelling ratio, dynamic loss, and temporal stability as corresponding characterisations depict whether the AIE properties of the hydrogels were significant in the comparison between the normal condition and that with VFD support. First, the colour gradient progressively became a more pronounced indicator (**Figures 24** and **25**). The hydrogels containing TC426 initially appeared orange-red in AAm–Alg and carrageenan. The high concentration of HSA (2000 mg/L) in the external surroundings began to progressively permeate into the interior structure of the hydrogels over time due to the concentration differential between the inside and outside of the film, and water absorption caused swelling. During this process, the chance of albumin binding to TC426 was significantly boosted, resulting in an increase in the number and size of TC426–HSA aggregates. The Mie effect was triggered by size

changes and is reflected in the colour transformation from orange-red into pink, which was also consistent with the fluorescence spectrum. Colour change in AAm–Alg occurred at around 8 min in normal soaking (**Figure 24A**), but was advanced to the 2 min node under VFD support (**Figure 24B**). Similarly, a pink shift could be captured at 9 min without VFD (**Figure 25A**), and this phenomenon was accelerated for 5 min with a VFD (**Figure 25B**) in carrageenan. In this case, the time acceleration rates caused by the VFD were 60% and 50%.
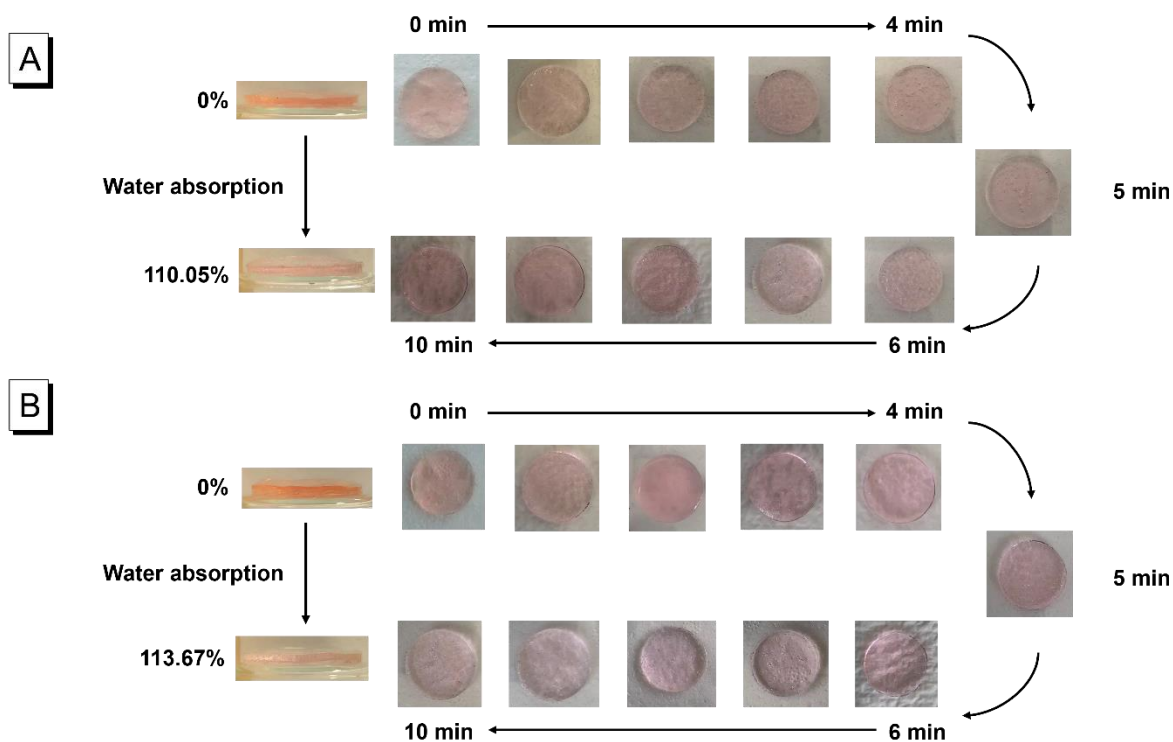
Figure 24 Acrylamide + Alginate + TC426 Hydrogel film for real observation. (A) Monitoring of colour change and swelling change from 0 to 10 min during normal soaking testing; (B) Monitoring of colour change and swelling change from 0 to 10 min during VFD testing. [TC426] = 10 μM, [HSA] = 2000 mg/L, λex = 480 nm, I0 equals the intensity of [HSA] = 0 mg/L.
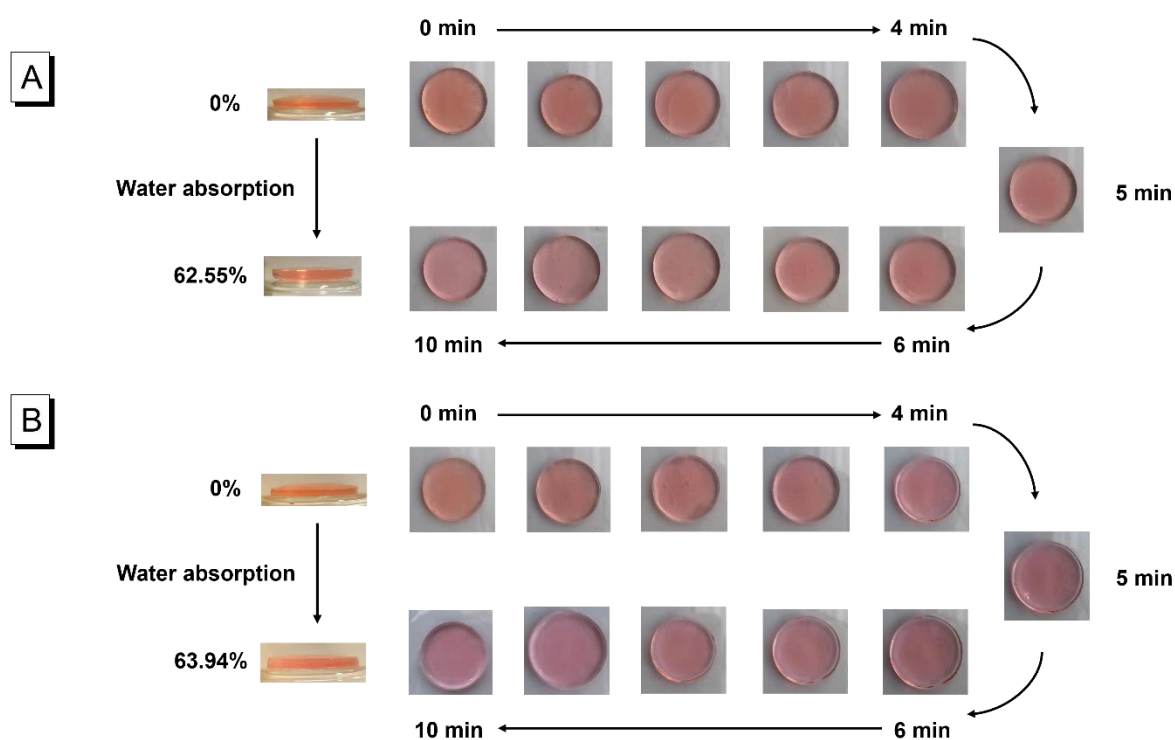
Figure 25 Carrageenan + TC426 Hydrogel film for real observation. (A) Monitoring of colour change and swelling change from 0 to 10 min during normal soaking testing; (B) Monitoring of colour change and swelling change from 0 to 10 min during VFD testing. [TC426] = 10 μM, [HSA] = 2000 mg/L, λ_{ex} = 480 nm, I_0 equals the intensity of [HSA] = 0 mg/L.

Afterwards, the real-time variations for VFD processing were also recorded, as shown in **Figure 26**. The fluorescent signal presented a stable rise and peaked in the normal AAm–Alg soaking test at around 10 min, 8.47 times the beginning level (**Figure 26A**). The difference in the same conditions was that the intervention of VFD accelerated the fluid exchange, reaching the maximum (11.67 times the initial samples) at 2 min earlier (**Figure 26B**). Following that, the shearing force from the VFD progressively detached TC426 molecules from the film surface, and they turned into a solution that accounted for the weakening of the fluorescence signal between 2 and 10 min. Similarly, the absorption and natural flow of water enabled the TC426 probe in carrageenan to relatively slowly bind with albumin until it had reached a 11.83-fold increase at 10 min (**Figure 26C**). Nevertheless, the same situation took only 4 min to complete under VFD processing (12.32-fold), and intensities remained in steady state from 4 to 10 min; lastly, they became as strong as 14.30-fold the starting value (**Figure 26D**). Regarding the dynamic performance of swelling during normal soaking and VFD processing, the swelling ratio (Equation (1)) of AAm–Alg–TC426 rose steadily from 0 to 110.05% in 10 min, in accordance with water absorption (**Figure 26A**). However, VFD altered this circumstance. To be more precise, the swelling ratio of AAm–Alg–TC426 immediately reached 79.37% in the first 2 minutes of rotation and climbed slowly during the following 8 minutes, only rising by a total of 34.29% (**Figure 26B**). Different from AAm–Alg–TC426, carrageenan–TC426 demonstrated a similar kinetic tendency and range, and both soaking (**Figure 26C**) and VFD rotation (**Figure 26D**) were

divided into two distinct trajectories: the rapid ascent phase (0–2 min) and the comparatively steady phase (2–10 min). At the first stage, they quickly rose to 43.45% and 50.26% respectively, and reached a plateau before rising to 62.55% and 63.94%, respectively.
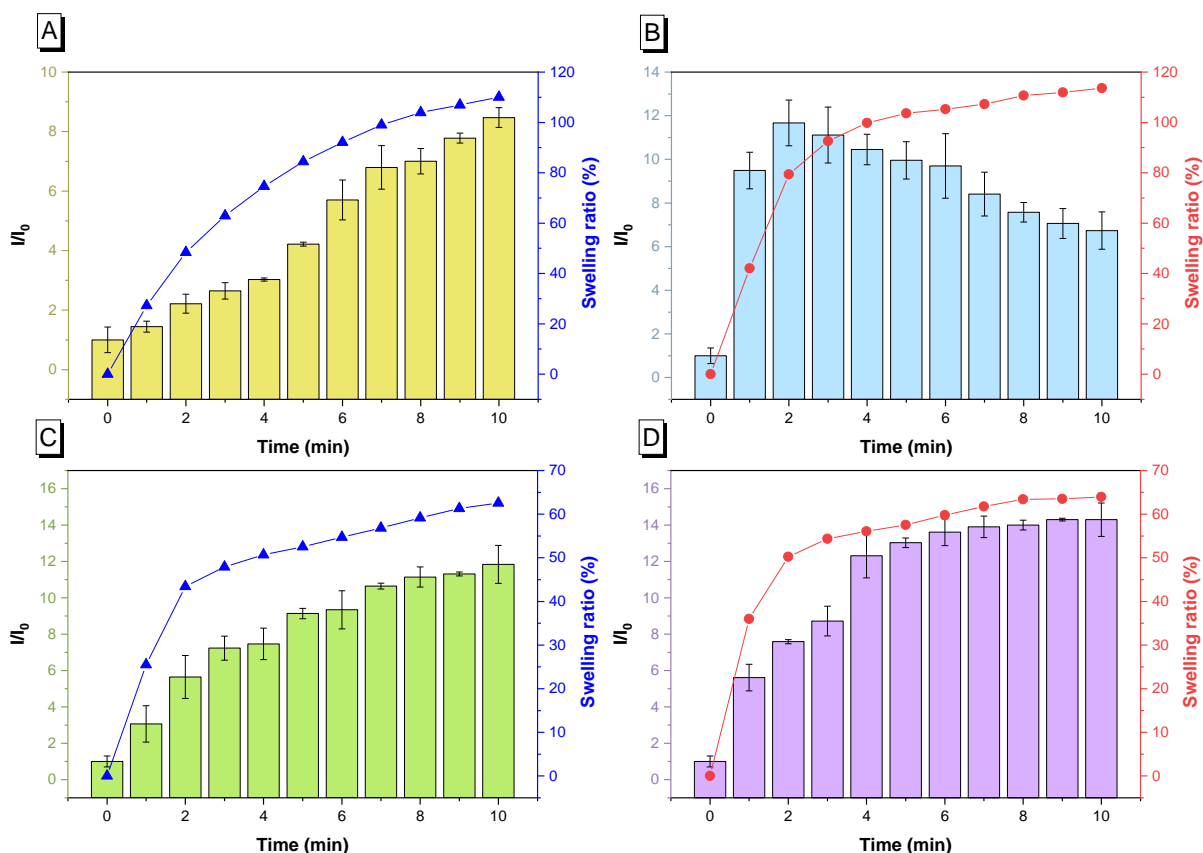
Figure 26 Hydrogel film for normal soaking testing and VFD processing testing. (A) Acrylamide + Alginate + TC426 and (C) Carrageenan + TC426 for time effect on variation of intensity and swelling ratio from 0 to 10 min during normal soaking testing; (B) Acrylamide + Alginate + TC426 and (D) Carrageenan + TC426 for time effect on variation of intensity and swelling ratio from 0 to 10 min during VFD testing. [TC426] = 10 μM, [HSA] = 2000 mg/L, λ_{ex} = 480 nm, I_0 equals the intensity of [HSA] = 0 mg/L.

Notably, a measurable decline in the fluorescent signal of AAm–Alg was observed in the previous VFD modulation (**Figure 26B**). The rotation of VFD unavoidably forced HSA into the hydrogel while transferring TC426 on the film surface into the external solution. Consequently, the determination of dynamic AIE loss is an essential step in realistically detecting quantitative biomarkers, optimising experimental outcomes, and comprehending the underlying fundamentals. Using Equation (5), the dynamic loss was found from 0 to 10 min during VFD for two different hydrogel basements (**Figure 27A**). The loss rate in AAm–Alg rapidly increased from 0 to 10.98% in the first 2 min and then steadily increased to 22.0% in the remaining 8 min. Moreover, the carrageenan film sharply increased by 5% within 1 min and eventually reached 13.3% at 10 min. Under the same experimental conditions, the loss ratio of carrageenan after 2 minutes was about half that of AAm–Alg, and its value was stable at around 10%. Moreover, the temporal stability of the fluorescent hydrogel film was assessed assuming that the dynamic loss was fully considered by modifying the rotational VFD time, as

illustrated in **Figure 27B**. The fluorescence responses of the two matrices still retained 92.32% (AAm–Alg) and 95.84% (carrageenan) of their maximal peaks after 3 h.
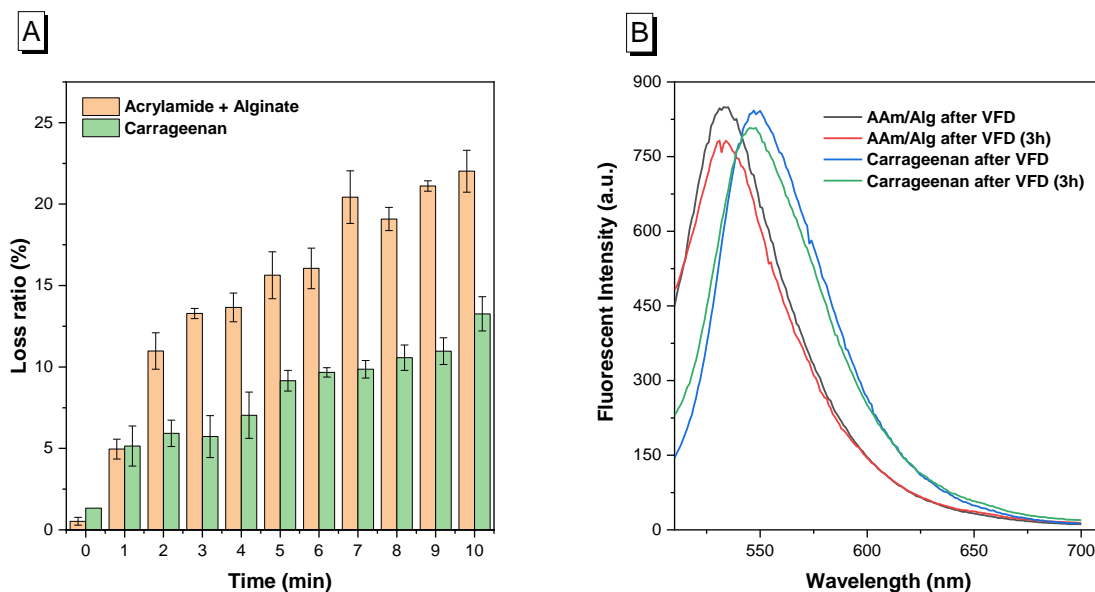
Figure 27 Comparison between AAm + Alg + TC426 film and Carrageenan + TC426 film. (A) Loss ratio from 0 to 10 min during VFD testing. (B) Time effect when VFD processing is immediately completed and 3 hours after the completion. [TC426] = 10 μM, [HSA] = 2000 mg/L, λ_{ex} = 480 nm, VFD was conducted for 2 minutes and 4 minutes, towards AAm + Alg + TC426 and Carrageenan + TC426 respectively.

The findings show that the intensity change of hydrogels was positively correlated with its colour shift. The orange-red of TC426 was contributed by the sodium sulfonate group in its chemical structure, and a pink transition occurred when the albumin macromolecules met the fluorescent dye as a result of the AIE molecules moving towards the Sudlow sites of albumin and the co-aggregates size expanding. With the development of water diffusion, the fluorescence enhancement phenomena also became increasingly clear. Although the bidirectional exchange of the HSA solution and hydrogels showed that the dynamic loss and the dynamic binding occurred simultaneously, the high level of temporal stability proved that an outward–inward flow was the dominant motion. Comparing the two different hydrogels, the overall fluorescence enhancement performance of carrageenan was better than that of AAm–Alg, and the corresponding FL enhancing efficiency of carrageenan was 39.66% (in normal soaking) and 5.57% (using VFD) higher than that of AAm–Alg. Correspondingly, AAm–Alg–TC426 was eventually stabilised at a swelling ratio of around 110%, and its increase was approximately 1.8 times that of carrageenan–TC426 (around 60%).

Lastly, **Figure 28C** shows that the utilisation of VFD technology boosted the fluorescence response by 5.27-fold on AAm–Alg and 1.71-fold on carrageenan compared to their original level. Furthermore, the dynamic ranges of both hydrogels were linearly distributed with/without VFD (**Figure 28D**, R_1^2 = 0.953, R_2^2 = 0.962, R_3^2 = 0.981, R_4^2 = 0.992). The limits of detection (LOD, Equation (6)) for AAm–Alg and carrageenan without VFD intervention were 74.77 and 53.87 mg/L, respectively, while VFD

further lowered these thresholds to 61.19 and 30.87 mg/L under the same conditions. The detection sensitivity of the standard curves under VFD control was 1.75 (AAm–Alg) and 2.56 (carrageenan) times higher than that of the non-VFD modulation.
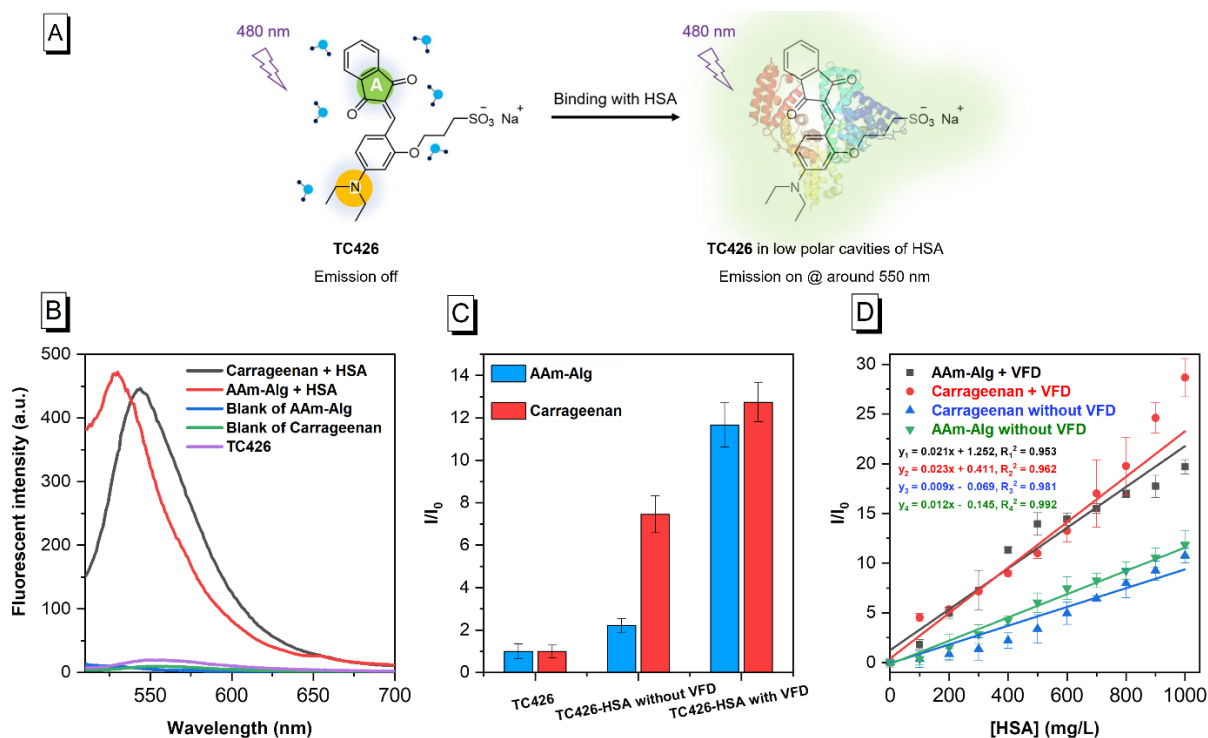
Figure 28 Characterisation of hydrogel films using TC426. (A) Schematic of the working mechanism of TC426 in HSA detection; (B) FL spectra of TC426 in two matrices: AAm−Alg and carrageenan under different conditions; (C) effect of TC426-based hydrogel films with and without VFD modulation; (D) standard curve of TC426-embedded hydrogel films under different HSA concentrations ranging from 0 to 1000 mg/L with/without VFD processing. TC426 = 10 μM, λ_{ex} = 480 nm, I_0 = intensity of HSA = 0 mg/L; VFD was used for 2 and 4 min in AAm–Alg + TC426 and Carrageenan + TC426, respectively.

Potential mechanisms

Diffusion characterisation

The above investigations show that the swelling ratios of AAm–Alg and carrageenan were different. Furthermore, this demonstrates how even while operating under the identical conditions, the hydrogel's dynamic diffusional process was distinct. The difference of the diffusion rate in the aqueous solution directly led to variation in the binding chance of TC426 in the film towards albumin in the solution. Hence, two crucial factors that govern whether TC426 and biomarkers continuously bind and persist in the film are the water diffusion rate (also referring to the albumin diffusion rate) and the polymer chain relaxation rate. In this case, the diffusion mechanism of the hydrogel system was studied according to Equations (2) and (3). The swelling power fractions versus time (**Figure S13A** and **S13B**) were plotted logarithmically to find the swell constant (K) and diffusional exponent (n). Diffusion information is summarised in **Table 4**. K was 0.012 (normal soaking) and 0.010 (VFD) in Aam–Alg, while n was 0.768 (normal soaking) and 0.917 (VFD). When the value of n was in the

interval from 0.5 to 1, the kinetics of diffusion belonged to non-Fickian behaviours in AAm–Alg. In this situation, the swelling rate was greater than the rate of the film collapse, which means that the polymer relaxation was the rate-limiting step in the TC426–HSA delivery system. The relaxation rate in the hydrogel network became an uncontrollable factor, and the faster water penetration rate passively accelerated the relaxation progress, eventually leading to built-in TC426 leakage in the internal structures. In the carrageenan model, K was 0.142 (normal soaking) and 0.055 (VFD), while n was equal to 0.247 (normal soaking) and 0.403 (VFD). Less-Fickian (n < 0.45) was the diffusive feature of carrageenan as a diffusion-controlled delivery system and it dominated the albumin release process (the water penetration rate was much lower than the polymer chain relaxation rate). Equation (4) was also utilised to calculate the diffusion coefficient (D). The D value of AAm–Alg was 437.38-fold greater than that of carrageenan in the natural absorption, and 67.99 times greater under VFD rotation. The calculated diffusion coefficients D were consistent with the transport behaviour of the two hydrogel models. More importantly, the diffusion coefficient (D) of VFD processing was greater than that of normal soaking under the same model (2.85 times greater in AAm–Alg and 18.31 times greater in carrageenan). In other words, VFD had the effect of increasing the diffusion coefficient without the need for other external factors (temperature, concentrations, etc.).

Material of hydrogels	Testing types	Diffusional exponent (n)	Type of transport	Behaviour	Diffusion coefficient ($D \times 10^{-10}$ / m^2 s^{-1})
AAm-Alg	Normal Soaking	0.768	Non-Fickian diffusion	$R_{\text{water penetration}} >$ $R_{\text{polymer chain relaxation}}$	3143.6
	VFD	0.917			8950.1
Carrageenan	Normal Soaking	0.247	Less-Fickian diffusion	$R_{\text{water penetration}} \ll$ $R_{\text{polymer chain relaxation}}$	7.187
	VFD	0.403			131.632

Table 4 Diffusional exponent (n), type of transport, actual behaviours, and diffusion coefficient (D) in normal soaking and VFD testing for hydrogel films of AAm–Alg and carrageenan.

Combined with the previous results, the template of non-Fickian diffusion was already at a high level of water penetration, and VFD further intensified it (D = 8950.06 $\times$ 10^{-10}/m^2 s^{-1}). The bonding tightness between TC426 and the hydrogels is loosened at a high flow rate, thereby simultaneously increasing its fluorescent loss rate. However, the relaxation rate of the hydrogel chain was not

significant in carrageenan due to Less-Fickian behaviour, and the diffusion coefficient (D = 131.63 × 10^{-10}/m^2 s^{-1}, an order of magnitude lower than that of AAm–Alg) and dynamic loss rate (51.53% less than AAm–Alg) still had a relatively low and stable status, even under the action of VFD. The difference in loss rate also indicated a distinction in the internal structure of the two basements, and the lower loss percentage of carrageenan facilitated TC426 being locked inside.

Microstructural analysis

As previously indicated, the swelling behaviours, fluorescence kinetics, and diffusion of the two hydrogel matrices were different under the same conditions, and variation was likely linked with their microstructures. Therefore, scanning electron microscopy (SEM) was employed to obtain and explain the surface and cross-sectional topography of the dried samples at a high magnification. For the AAm–Alg-based hydrogels, the surface and cross section had a typical cellular porous structure, and the pore was relatively dense and evenly distributed (**Figure 29A** and **29B**). The relatively loose network provided a sufficient adhering zone for the TC426 molecules and allowed for the aqueous solution of albumin to freely move within the film at a faster diffusion rate. A multilayer planar structure was characteristic of carrageenan on its surface and cross section (**Figure 29C** and **29D**). Each layer exhibited a flat, smooth surface, but a certain gap existed layer to layer where the flow of water penetration was mainly singular and along the cross-sectional direction. More importantly, the structural morphology was an important factor determining the properties of the hydrogels. The porous space tended to diffuse in three dimensions, while multilayered structures were predominantly two-dimensional. This can be explained by the fact that, under the accelerated process of VFD, the AAm–Alg hydrogels could reach their maximal fluorescence intensity within 2 min while maintaining a constant higher swelling ratio compared to that of carrageenan. Likewise, TC426 could escape the constriction of the film along the porous network path as a result of the impact of the flow, resulting in higher dynamic loss. Furthermore, the layered structure of carrageenan resulted in a lower swelling ratio and allowed for it to readily restrict TC426 movement to maintain lesser loss while maintaining higher intensity.
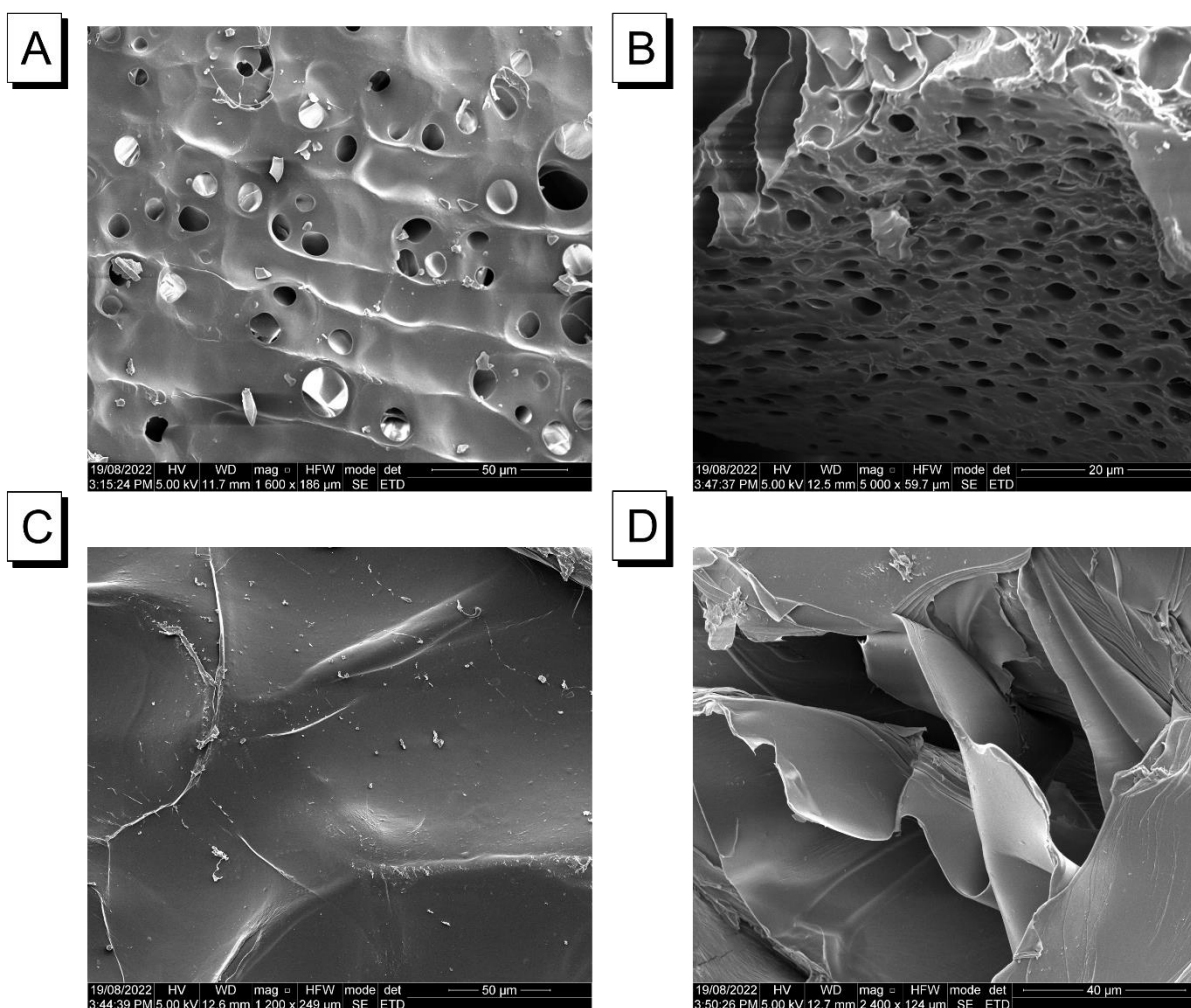
Figure 29 SEM images captured under 50 µm magnification from the surface of an (A) AAm–Alg + TC426 hydrogel film, (C) carrageenan + TC426 hydrogel film. SEM images captured under magnification 20 and 40 µm from the cross section of (B) AAm–Alg + TC426 hydrogel film, and (D) carrageenan + TC426 hydrogel film.

After comprehending the microstructural differences of hydrogels, optical imaging with and without VFD-mediated circumstances could be further analysed. **Figure S14A** shows the case where only the cross linking of AAm–Alg was contained in the film. Its surface layer was flat and smooth. When macromolecular HSA was introduced into the model of **Figure S14A**, a black spherical substance with a white core was clearly visible on the hydrogel surface (**Figure S14B**). Dense granular microparticles could be easily captured in the same model containing only TC426 (**Figure S14C**). When both TC426 and albumin were present in the system, several bright spots appeared around the periphery of HSA, each represented by a black globular substance (**Figure S14D**). Similarly, in carrageenan, the blank sample exhibited a flat and smooth surface (**Figure S15A**), and a black spherical substance with a white core represented only HSA existence (**Figure S15B**). The AIE-embedded film also displayed dense granules (**Figure S15C**), and both TC426 and HSA could be independently observed in the coexisting system (**Figure S15D**).

In the darkfield, HSA spheres were covered with TC426 microparticles on the external edge that were then lit up (**Figure 30A** and **30C**). Nevertheless, the strong green fluorescence was captured in the two matrices when VFD was applied during measurements (**Figure 30B** and **30D**). The forming opportunities of the TC426–HSA aggregates increased as a result of the rise in the diffusion coefficient due to VFD shearing forces, which caused free albumin in the external solution to continuously be injected into the hydrogel interstitial space. Particularly, numerous TC426 connected with the binding sites on the albumin surface owing to dense contacting, thus increasing the steric hindrance. The white circle parts coating on albumin spheres represented the enrichments of aggregation state.
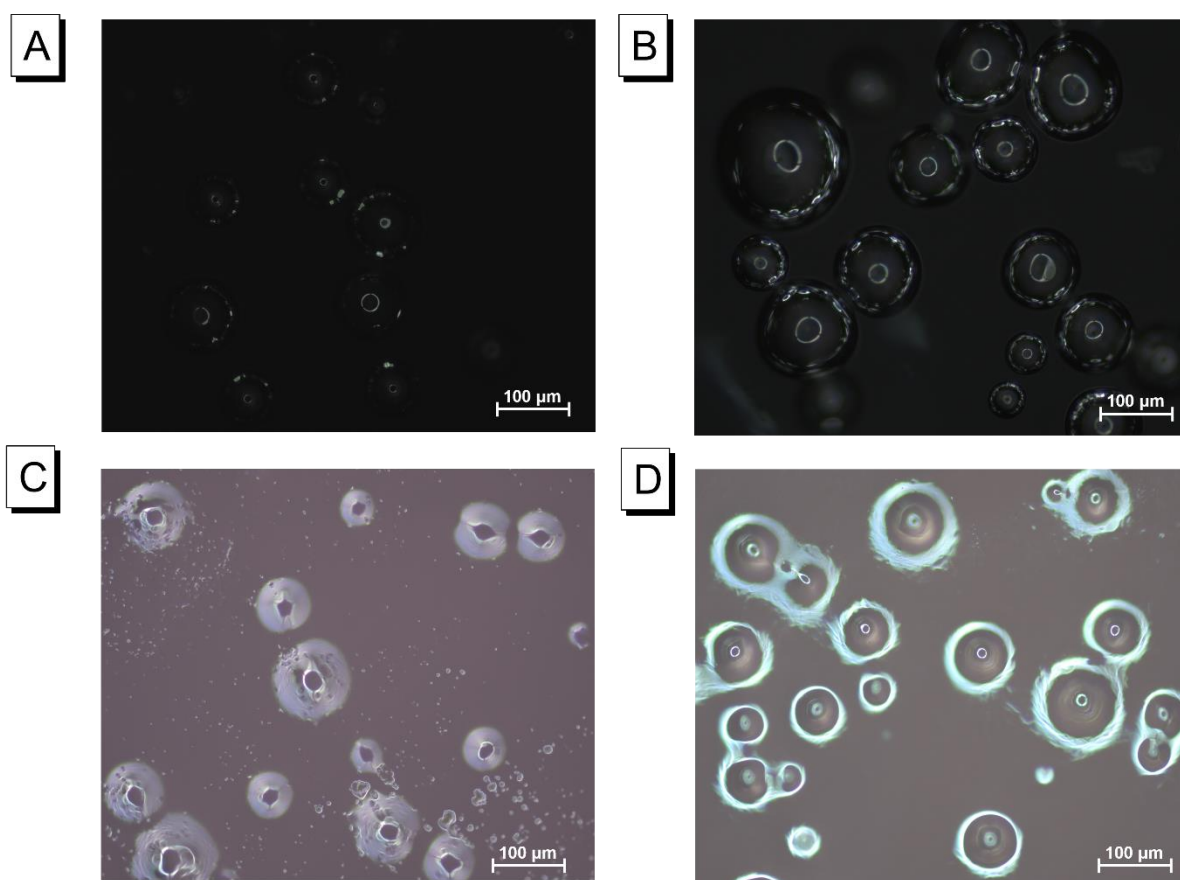
Figure 30 Optical microscopy images for the reflection mode in the darkfield. AAm–Alg hydrogel film + TC426: (A) without VFD; (B) with VFD, 100 µm; carrageenan hydrogel film + TC426: (C) without VFD; (D) with VFD, 100 µm; HSA = 2000 mg/L and TC426 = 10 µM, VFD was used for 2 and 4 min in AAm–Alg + TC426 and carrageenan + TC426, respectively.

Motion Analysis

The underlying mechanism (**Figure 31**) of the hydrogels became clear after investigating their fluorescence kinetics, swelling behaviours, diffusion, and microstructure throughout the whole process. Initially, anionic sulfonate dye TC426 with AIE properties was bound to biological macromolecule HSA through noncovalent interactions, especially electrostatic interactions and hydrophobic effects. When TC426 molecules were docked onto the surface of the biomacromolecule

and within the hydrophobic cavity of its folded structure, they clumped together by virtue of the strong electronic and hydrophobic interactions between their aromatic rings. Aggregation inhibited the intramolecular rotation of the TC426 molecules, thereby hindering their nonradiative transitions and activating their fluorescence emission processes. Subsequently, in the scenarios of hydrogel-based HSA detection with/without VFD, the porous network of AAm–Alg served as a fast-flow platform that enabled the albumin solution to simultaneously diffuse in multidimensional directions and further released the constraint of TC426 within the microstructure. Non-Fickian diffusion caused the relaxation rate of the AAm–Alg chain to become the delivery system's rate-limiting step, which is difficult to be quantified in hydrogel models. Furthermore, the difference was that carrageenan's layered structure provided only two-dimensional motion, while it affected diffusion to exhibit Less-Fickian behaviour, enabling the penetration rate of the HSA solution to dominate the transport process, and the passive diffusion-dominated delivery system to be regulated. More significantly, the introduction of VFD could artificially increase the diffusion rate under both models, and fluorescence intensity was greatly enhanced with the increased opportunity for a connection between HSA and TC426. By contrast, the diffusion-controlled delivery system of carrageenan was capable of boosting the diffusional rate while keeping dynamic losses constant. Without altering the original diffusion transport, the VFD acceleration procedure turned passive diffusion into active diffusion, which is a new control strategy for hydrogel studies.
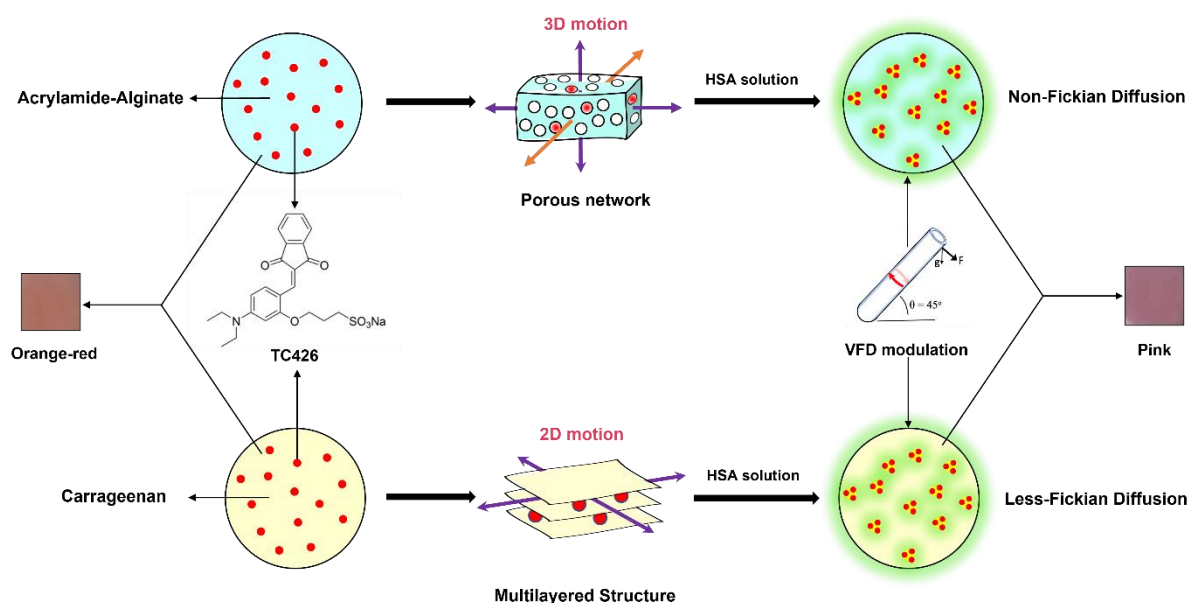
Figure 31 Potential mechanism of TC426-embedded AAm–Alg and carrageenan hydrogel film.

Application of portable device based on colorimetry

On the basis of our previously published studies (Pham, Tohl, Hu, et al., 2022; Pham, Tohl, Wallace, et al., 2022; Tohl et al., 2022), portable devices were developed for the quantitative detection of biomarkers. In this work, a colorimetric device (**Figure S16**) was developed for hydrogel films that

utilises a three-layer RGB image matrix to output intensity values. The advantages of this approach are its sensitivity to colour shifting and being robust to different noise sources that may affect the image, such as sensor noise and artefacts. Since an obvious colour change was captured in carrageenan under the action of VFD, six spiked data points (5 blue dots and 1 blank control) were set to plot the standard curve. As shown in **Figure 32**, the red dot with 100 mg/L HSA concentration was input into the built-in arithmetic circle and it yielded a recovery rate of 86% optical density. The experiments demonstrated that this device could effectively identify the colour response of hydrogels towards HSA in the microalbumin range.
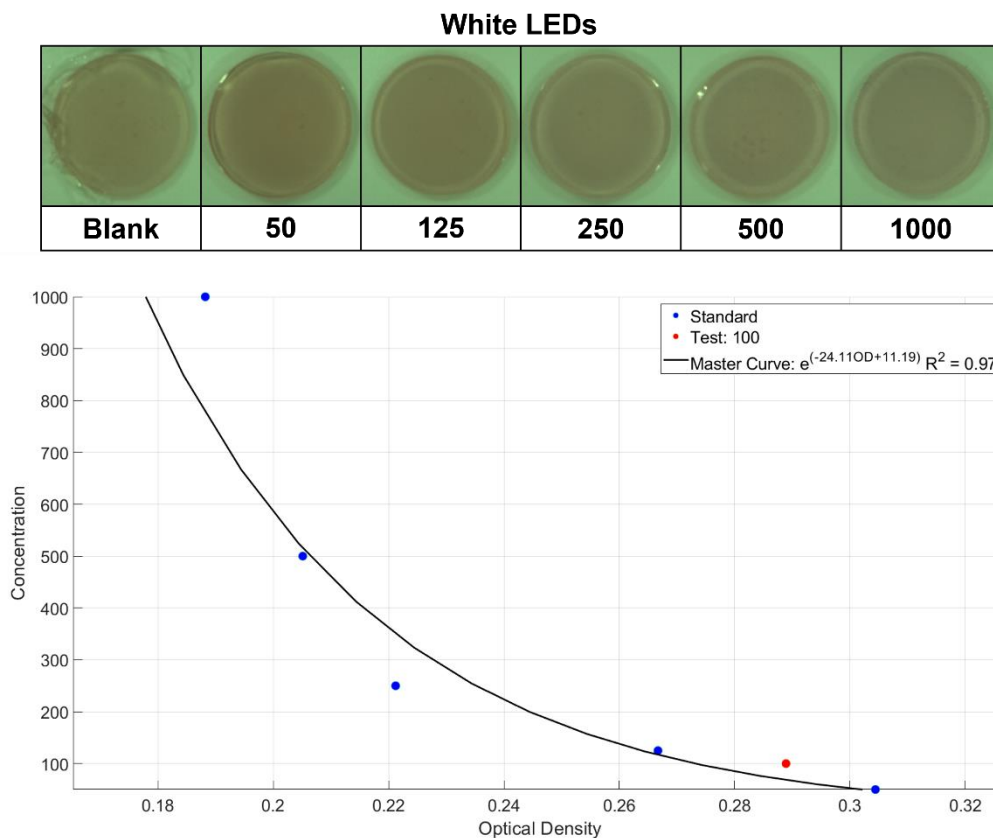
Figure 32 Correlations of HSA concentration and optical density in the range from 0 to 1000 mg/L under white LEDs. The black line represents the established master curve, R^2 = 0.97; the red dot represents the validated sample. TC426 = 10 μM.

Conclusion

In summary, two fluorescent TC426-embedded hydrogels, AAm–Alg and carrageenan, were investigated for HSA detection under 0–10 min of normal soaking and VFD modulation. The results indicated that the fluorescence responses of the two hydrogel matrices were enhanced by 5.27-fold and 1.71-fold, respectively, when VFD was involved. The detection sensitivity of the linear dynamic curves was increased by 1.75-fold and 2.56-fold, respectively, while the LOD was reduced to 61.19 and 30.87 mg/L. Through the explanation of the potential mechanism, the primary cause for the non-Fickian behaviour was the porous network of AAm–Alg, whose D was 3143.6×10^{-10}/m^2 s^{-1}, and the multilayered structure of carrageenan led to Less-Fickian behaviour under the same circumstances, resulting in a smaller diffusion coefficient (7.187×10^{-10}/m^2 s^{-1}). Significantly, VFD could speed up the diffusion rate without changing its initial transport mode (2.85-fold for AAm–Alg and 18.31-fold for carrageenan). After that, motion analysis showed that the movement of the HSA solution in three- or two-dimensional directions under the hydrogel microstructure was the rate-limiting factor that determined the transport system. The diffusion-dominated system led by carrageenan was more capable of increasing fluorescence intensity while maintaining the dynamic loss under VFD control. Furthermore, a recovery rate of 86% from the colorimetric device successfully validated that the colour change in the fluorescent hydrogels could be recognised in the microalbumin range after VFD processing. VFD could convert passive into active diffusion, which is a promising strategy for future hydrogel research.

AIE BIOSENSOR INCORPORATING WITH METASURFACE PLATFORM

This chapter has already been published on "*Advanced Optical Materials*, 2024, 2400868 " under the title "**Metasurface Platform Incorporating Aggregation Induced Emission Based Biosensor for Enhanced Human Serum Albumin Detection**". Qi Hu is the primary author, while Youhong Tang and Masanobu Iwanaga are the correspondent authors (**doi.org/10.1002/adom.202400868**).

In this chapter, metasurfaces exhibit excellent optical performance to enhance the light–matter interaction of target molecules in biosensing based on its well-optimized nanostructured unit cells. In the meantime, fluorescence (FL) biosensors with aggregation induced emissions (AIE) features also demonstrate outstanding performance in biomarker detection due to its fast response, high selectivity, and low background noise. Nevertheless, extremely low-level analytes are difficult to detect in practical applications since complex urine samples include a number of uncontrolled variables such as impurities, autofluorescence, other urine components, etc. At present, improving photosignal sensitivity of human serum albumin (HSA) detection is always a big challenge to overcome such interference in human urine scenarios. In this work, it is first to combine an AIE-based fluorescent biosensor TPE-4TA with an all-dielectric metasurface platform to achieve quantitative detection of trace HSA in urine by utilizing biofunctionalization protocols on the silicon nanostructures. The results indicate significant FL enhancement in metasurface platform that offers a promising pathway for improving biomarker detection in the future.

Introduction section

Metasurface is a two-dimensional version of metamaterials that consists of periodic/non-periodic subwavelength metallic/dielectric structures (Canet-Ferrer, 2019; J. Hu et al., 2021). It exhibits the capabilities of concentrating, inhibiting, absorbing, scattering or guiding waves by designing nanoscale cells to achieve dynamic modulation in optics, mechanics, electronics, etc (Ali et al., 2022; Hsiao et al., 2017). The strong wavefront manipulation is the remarkable characteristics where the unit cells of shape and size, diversified patterns and geometry are tunable and controllable (Ee & Agarwal, 2016; Gutruf et al., 2016; L. Li et al., 2017). It is precisely based on such characteristics that the attributes of incident light can be customised through light confined mode and localised surface plasmon (LSP) electromagnetic (EM) near-field, thus enhancing light–matter interactions of target molecules (Kabashin et al., 2009; Tseng et al., 2020).

To date, metasurface has been extensively developed in recent decades on the aspects of polarisation conversion (Zhu et al., 2013), wavefront shaping (Farmahini-Farahani & Mosallaei, 2013), controllable radiation (Bao et al., 2023). The advancement of metasurface platform has attracted marvelous attentions on the applications of biosensing and lead to a significant stride towards biomarker detection (R. Liu et al., 2020; S. Zhang et al., 2020). Oguntoye and his team designed a resonant dielectric photonic Si-nanoantenna metasurface to detect a tuberculosis biomarker CFP-10 peptide and this platform's cost was 87–96% lower than current assays with equivalent sensitivity. The results illustrated that a maximum sensitivity and limit of detection (LOD) was 0.1 µM and 10 pM, respectively (Oguntoye et al., 2022). Wang *et al.* reported an optofluidic silicon-on-insulator (SOI) metasurface that provided multiple nanoscale lateral flow channels to deliver ErbB2 breast cancer biomarkers to the sensor surface. This platform illustrated a resonance mode around 1550 nm wavelength and LOD for ErbB2 is 0.7 ng/mL (Wang et al., 2018). Negm *et al.* demonstrated a double-resonating metasurface with the characteristic of permittivity asymmetry and geometric asymmetry simultaneously to achieve a thin protein layer sensing. Germanium Antimony Telluride (GST326) ellipse-shaped nanopillars were sensitive to the analyte and show great robustness of phase transition losses from the amorphous to the crystalline state in the mid-infrared range (Negm et al., 2023). In our previous publications, Iwanaga *et al.* fabricated an effective all-dielectric metasurface fluorescence biosensor with periodic silicon (Si) nanorods array, which had also successfully detected several biomarkers such as immunoglobulin G (IgG) (Iwanaga, 2020), cancer biomarker (PSA and CEA) (Iwanaga, 2023), cell-free DNA (cfDNA) (Iwanaga et al., 2023a), *etc.* Specifically, Si or SOI-fabricated metasurfaces possess the tuning adaptability of their optical properties and provide high quality resonances (Cheung et al., 2012). When the target analyte enables immobilized or coated on Si-nanoscale matrices, high refractive index of Si facilitates light modulation (Ferrara et al., 2015; Van Laere et al., 2007), resulting in deep light–matter interactions, thereby reflecting on the analysed peaks. Collectively, these above-mentioned satisfactory results indicate the outstanding capability of metasurface on biomarker nanophotonic detection.

Aggregation-induced emission (AIE) fluorescence (FL) biosensors also exhibits excellent detection capabilities in biosensing where the intermolecular interactions restrict the movement of AIE molecules rotors, thus producing an extremely fast and bright FL response through the radiation channel (Hong et al., 2011; X. Zhang et al., 2020). However, HSA measurement using AIE FL biosensors has always faced considerable gaps and challenges in human urine scenarios owing to unpredictable reasons regarding the complexity of urinary excrement. For starters, it has been discovered that albumin excretion varies greatly across individuals, with a typical within-person coefficient of variation (CV) of 40–60% (Dyer et al., 2004), which leads to a board concentration extension of urinary HSA from extremely low to high depending on individual differences. In addition, urine matrix is made up of a variety of organic and inorganic compounds, ranging from low-molar mass molecules to polymers (Simerville et al., 2005). It could also contain cells and bacteria that have the ability to rapidly change the composition of urine (Simerville et al., 2005). On the basis of this background, undesirable FL enhancement or quenching will be further triggered because of the interference of numerous impurities (Bouatra et al., 2013), autofluorescence (Birková et al., 2020), other urine components (Patel, 2006; Simerville et al., 2005), etc. Consequently, it is inevitable to overestimate or underestimate HSA content, leading to inaccurate readings, especially at an extremely low-level (Aitekenov et al., 2021). Not only that, but the optical signal is also hardly detectable due to small amplitude of light absorption when HSA concentration is low, which requires the high detection accuracy by boosting sensitivity or reducing background noise. To address these issues with complex bio-samples in practical applications and evaluate the biomarker detection performance of metasurface in biosensing, herein, it is a first report nanophotonic all-dielectric metasurface platforms coupled with AIE featured FL biosensors for achieving the enhanced detection of HSA. This platform integrates a microfluidic system and a metasurface substrate to enable analyte delivery and the monitoring/detection of FL enhancement in real time with the outstanding characteristics of high throughput, good reusability and low reagent consumption, as shown in **Figure 33A**. Under the FL setup (**Figure 33B** and **Figure 33C**), the results from human urine samples show that this proposed engineering metasurface design has significant potential as a biomedical chip-based platform for providing a promising pathway of enhancing sensing and biomarker detection quantitatively.
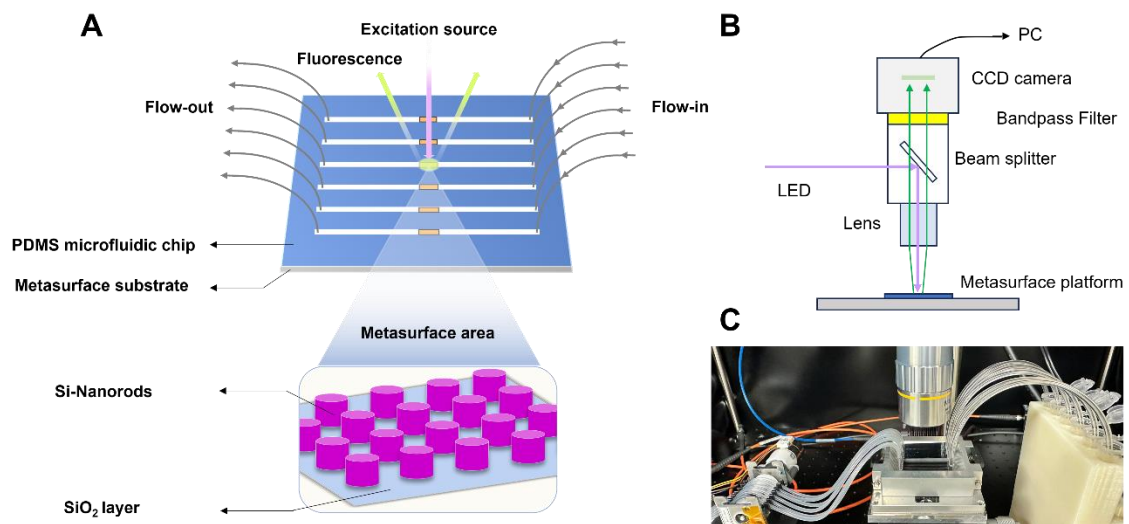
Figure 33 (A) Schematic diagram of metasurface platform. Inset figure magnifies the nanostructure of metasurface area; (B) The schematic diagram of FL setup for imaging; (C) Actual photograph of experimental configuration for HSA detection. Sample liquids flow on metasurface platform through inlet (right) and outlet tubes (left) controlled by rotary pump and FL is collected by setup in (B).

Experimental section

Materials and instruments

The FL biosensor TPE-4TA had been synthesized according to previous publications (Tu et al., 2019). Human serum albumin (HSA) was purchased from Sigma-Aldrich (A1653-500MG, Germany). Biotin labelled HSA antibody (Biotin-HSA Ab) was purchased from Abcam (ab27632, purified, UK). Cys-streptavidin (Cys-SA) was purchased from Click Biosystems (PRO1005, Richardson, USA). Raw human urine samples were purchased from LEE BioSolutions (991-03-S, USA). Phosphate-buffered saline (PBS) and PBS-Tween 20 (PBS-T) were purchased from Fujifilm Wako Pure Chemical, Japan (164-25511 and 163-24361, respectively). Nanosep Centrifugal devices were purchased from Pall Life Sciences (OD300C34, USA). HiLyte Fluor^{TM} 555 (HL555) Labeling Kit was purchased from Dojindo Molecular Technologies (LK14, Japan) and the labelling operation was done according to standard protocols. Human Albumin SimpleStep ELISA® Kit was purchased from Abcam (ab227933, UK) and the operation procedure followed the standard instructions in manual.

An all-dielectric metasurface manufacturing procedure was carried out through the use of electron-beam lithography and dry etching on SOI wafers according to our previous publication (Iwanaga, 2020, 2021). The six metasurface regions in this investigation were distributed in the middle of each substrate with the dimension of 45×45 mm^2, corresponding to six microfluidic flow in-out channels, as seen in Figure 1A. Notably, the metasurface substrates could be reused after being washed with a complex acid solution ($H_2SO_4 + H_2O_2$).

The FL setup had been illustrated in Figure 1B. Light-emitting device was acquired from Thorlabs (M365FP1, USA). 10× objective lens was acquired from Mitsutoyo (M Plan Apo, Japan). 16-bit FL images were recorded by an uncooled CCD camera (Infinity-3S, Teledyne-Lumenera, Canada). FL spectra was measured by Spectrofluorometer (FP-8500, Jasco International, Japan). The binding affinity was obtained from the surface plasmon resonance instrument (SPR, BIACORE-X100, General Electric Healthcare, USA).

Methods

Preparation of samples

1000 µg mL^{-1} of AIE FL biosensor TPE-4TA solution as the stocking solution was dissolved in PBS buffer and stored at 4 °C in the dark environment. Stocking solution would be diluted freshly with PBS buffer to 20 µg mL^{-1} in every experiment unless otherwise noted. The freshly made HSA solution was formulated to 1000 µg mL^{-1} in PBS buffer and diluted to the required concentration of 0–1000 µg mL^{-1} with a specific concentration gradient. 200 µg mL^{-1} of Cys-SA stocking solution and 1 mg mL^{-1} of Biotin-HSA Ab were diluted to 20 µg mL^{-1} and 5 µg mL^{-1} with PBS buffer for daily use, respectively. PBS-T buffer was diluted with PBS buffer (pH = 7.4) 3 times for rinsing use. Mixing solutions of HSA and TPE-4TA were incubated for 10 minutes before use.

In the results section of 2.2, in order to ensure that all components were fixed tightly on the gold thin film, Cys-SA, Biotin-HSA Ab, HSA and TPE-4TA were all formulated to relatively high working concentration of 20 µg mL^{-1} during the experiments of binding response. For non-specific absorption, HL555- HSA antibodies were set to 0–5 µg mL^{-1}.

In human urine testing, raw urine samples (991-03-S, Lot. 18-06-615, Lee Biosolutions, MO, USA) would be thawed from -20 °C to room temperature. Afterwards, centrifugal filters with 300K Omega film were used to centrifuge for 10 minutes with the rotation speed of 120 × 100g and this operation must be repeat three times for each experiment until a sufficient amount of treated urine was collected for further use. Finally, the treated urine could be prepared into different urine samples through specific dilution factors with PBS. The mixing solutions of urine samples and TPE-4TA were incubated for 10 minutes before measurement.

Preparation of three platforms

Metasurface platform

The metasurface platform was a dynamic measurement that composed of a self-absorbed pair of a metasurface substrate and a polydimethylsiloxane (PDMS) microfluidic chip (thickness = 2 mm) that had six flow-in and flow-out independent microfluidic channels. These microfluidic paths (height = 30 µm) connected with tubes and the flowing speed could be controlled by rotary pump (RP-6R01S-5A-DC3V, Takasago Fluidic Systems, Japan). In the meanwhile, this metasurface substrate was a three-layer planar structure (from top to bottom) consisting of the Si-nanocolumns array (with a diameter of 220 nm, a height of 200 nm, and a period of 300 nm), a 375 nm SiO$_2$ layer and a 675 µm base Si wafer (Figure 2A).

Microplate platform and Microfluidic platform

Microplate platform was based on the conventional transparent 96-wells plate (P96F03N, Sansho, Japan) for static measurement. Microfluidic platform was assembled by a PDMS microfluidic chip and a normal substrate (a SiO$_2$ layer and a base Si wafer without the Si-nanocolumns array) for dynamic detection. Microfluidic configuration remained consistent across microfluidic platform and metasurface platform.

Microfluidic flowing program

The microfluidic flowing program was divided into the following steps: control of reagent flow time and rate, multiple reagents switching, FL imaging and system cleaning and drying. In order to achieve the multiple immobilizations on Si-nanorods, different sample liquids needed to be injected step by step through stainless-steel pins connected to the external inlet and outlet tubes for passing over six metasurface regions where flowing variation among different channels was approximately 5%. First, PBS buffer was prepared for 3 min preflow with the flowing rate of 102.8 µL/min to fill the

microfluidic paths. Secondly, Cys-SA was flowed at 10.9 μL/min on metasurface area for 11 min and PBS rinse was performed at the flowing rate of 18 μL/min for around 7 min. Afterwards, FL background measurements were recorded in PBS environment. Next, biotin labelled HSA Ab was also performed to flow at 10.9 μL/min for 11 min then PBS rinsing at 18 μL/min for 7 min. The same step was repeated when the prepared mixture solution of FL biosensor TPE-4TA and HSA flowed on the Si-nanocolumn array (using PBS-T buffer for rinsing instead of PBS buffer). Ultimately, actual FL images were captured then analysed by deducting the preceding background effects. Besides, system cleaning would be carried out with neutral washing solutions and pure water for two sections (rinse cleaning of tubes and ultrasonic cleaning of microfluidic chips & metasurface substrates) after FL measurement. Overall, this microfluidic flowing program required about 70 min flowing process, 30 min FL measurement and 50 min cleaning & drying, respectively.

FL measurement

In FL setup, ultraviolet LED emitted 360 nm excitation light, which focused on the metasurface through an objective lens of numerical aperture (NA) 0.28. After that, beam splitter filtered out the reflected light with the wavelength less than 409 nm, meanwhile emissive FL was collected by objective lens, and transmitted toward a 529–571 nm bandpass filter, then was detected eventually by an uncooled CCD camera. The exposure time was appropriately adjusted according to different platforms and the gain was fixed at 10 during every experiment. The excitation wavelength was set to 360 nm and the emission wavelength was detected within the range of 529–571 nm.

Results and discussion section

Optical properties of metasurface platform

The optical optimization of the metasurface has a history, which was reported in previous publications [1–3] (Choi et al., 2015; Iwanaga, 2018; Iwanaga et al., 2016). In principle, fluorescence (FL)-intensity enhancement is a consequence from multiple control of photoexcited states (Choi et al., 2015; Iwanaga, 2018; Iwanaga et al., 2016); that is, FL enhancement factor is equal to the product of excitation efficiency, inner quantum yield, and FL-emission efficiency (namely, Purcell factor). One of the keys is to the FL-emission efficiency, which was optimized by adjusting a particular resonant mode of the metasurface (i.e., a reflectance peak in Figure 2B) to the wavelength of FL. This was conducted by tuning the diameter and height of the Si nanocolumns (Iwanaga, 2018). Besides, the periodicity of the metasurface was set to a reasonable value, in accordance with the diameter of the Si nanocolumns. Thus, the present metasurface has a set of optimized structural parameters, based on the previous studies (Iwanaga, 2018, 2020). In this case, the optical structural design of metasurface is suitable for AIE FL biosensor TPE-4TA to achieve FL signal enhancement at green wavelengths around 530 nm. **Figure 34A** shows that the dimension parameters of SOI-nanorod metasurface with the thickness of a base Si wafer 675 μm and SiO_2 layer 375 nm, respectively. Si nanocolumns consisting of diameter 220 nm and height 200 nm forms a square lattice of 300 nm periodicity. Normal incident light propagates from the air to the metasurface, ensuring that the vector of the electric field is perpendicular to the incidence plane. Furthermore, the reflectance spectrum, as shown in **Figure 34B**, was numerically computed in the configuration of Figure 2A, exhibiting reflection peaks or dips according to the resonances of metasurface. A reflectance band of 30% is generated at 360 nm that is excitation wavelength for TPE-4TA, whereas reflection response at 530 nm reaches up to 70% with a single sharp peak significantly. A high reflectance exceeding 90% also observes between 700–800 nm, which is originated from the magnetic dipole resonance (**Figure S17**). **Figure S18** shows simulated and measured reflectance spectra, respectively. Overall, the two spectra agree with each other in the spectral shapes. Since the spectrometer allowed us to measure reflectance at 5 degrees and more, we set the incident angle to be 5 degrees, which is close to the normal incidence, and, indeed, verified that the simulated spectrum in (A) is approximately the same with the spectrum in Figure 2B. Importantly, the main feature regarding reflectance peaks at 360 and 530 nm, which was related to the FL enhancing effect in this study, was reproduced in the measured reflectance spectrum (B). The incident polarization was set to s polarization, which means that, when plane of incidence is the *xz* plane, the incident electric-field vector is parallel to the *y* axis. Besides, we mention that some interference signatures at 840—1050 nm came not from the metasurface itself but from the optical configuration in the spectrometer. Afterwards, to visualize the underlying mechanism of the FL enhancement induces by the Si nanocolumns, resonant EM field distributions are investigated in Figure 2C–2F. The intensities of electric fields ($|\mathbf{E}|^2$, **Figure 34C**) and magnetic fields ($|\mathbf{H}|^2$, **Figure 34D**) excited at 360 nm are reinforced to 54.9 and 6.1, respectively, in comparison with the incident field intensity of 1.0. These

EM-field distributions are dark inside the Si nanocolumns and indicate that the incident light was absorbed in the Si nanocolumns. However, the electric field at the outermost surface is highly enhanced at the sidewall of the Si nanocolumns and is not significantly reduced at the top of the Si nanocolumns. At the wavelength of 530 nm, the electric field intensity decreases at 41.9 slightly but this strong electric field distributions shift towards the upper part of the Si nanocolumns on which the majority of FL-labelled HSA analytes tend to be immobilized (**Figure 34E**). Notably, the magnetic fields are significantly enhanced up to 115.3 inside Si nanocolumns as **Figure 34F** shown, which indicates that this resonance is a magnetic mode (specifically, a higher magnetic mode than magnetic dipole mode), corresponding to the high-reflectance resonance at 530 nm in Figure 2B. The reinforced resonant EM fields is advantageous to transit electric dipole in FL molecules (Iwanaga, 2018), thus contributing to enhanced FL emission at the outermost surface of the Si nanocolumns. The numerical calculation was based on rigorous coupled-wave analysis and scattering matrix algorithm (Iwanaga, 2016).
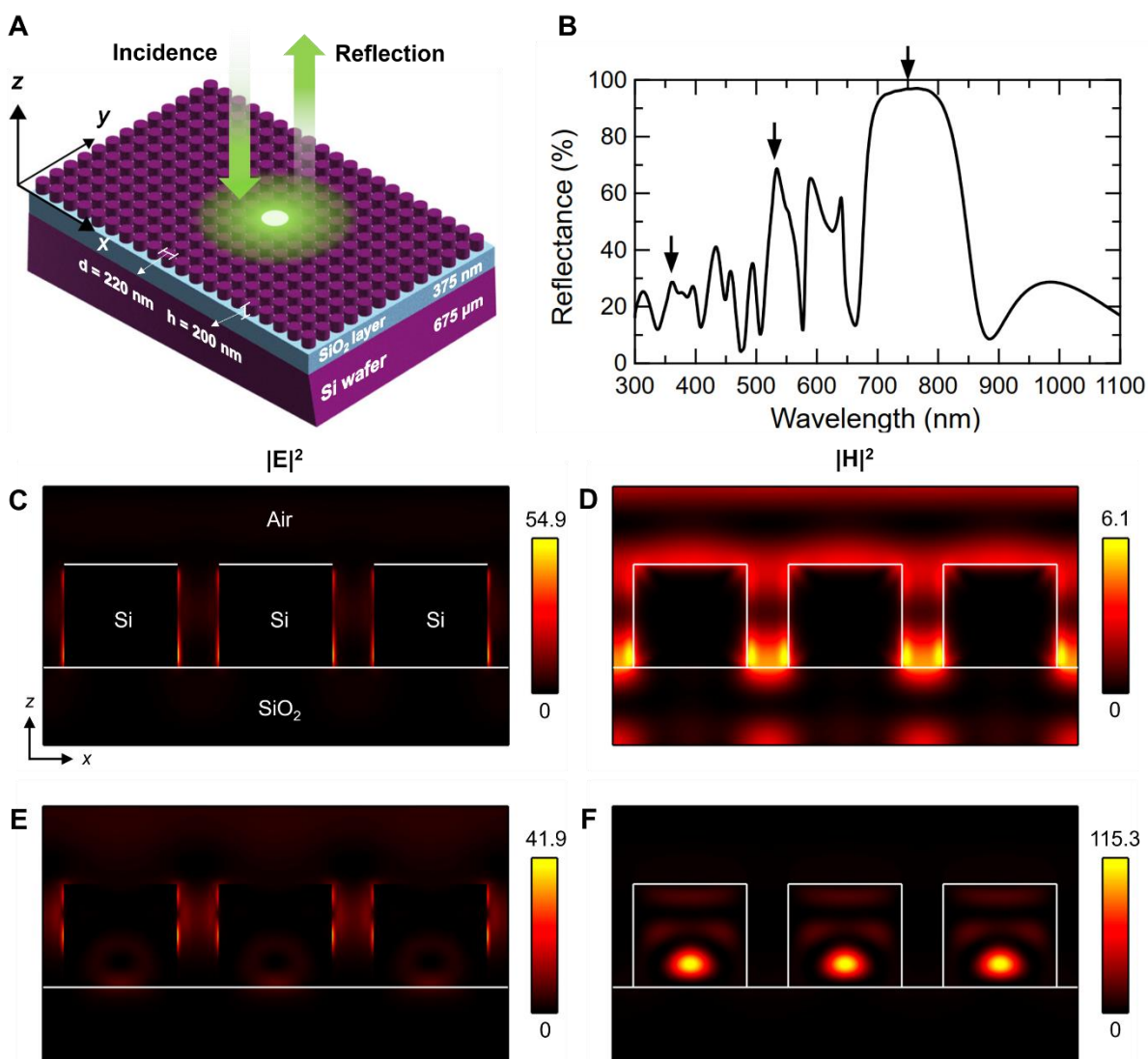
Figure 34 (A) 3D illustration of metasurface of Si nanocolumn (diameter d = 220 nm, height h = 200 nm) array forming a square lattice of periodicity 300 nm. (B) Simulated reflectance spectrum at the normal incidence in

a wide wavelength range from the ultraviolet to the near infrared. (C) and (D) Electric and magnetic field intensities ($|E|2$ and $|H|2$), respectively, excited at 360 nm, which is indicated by an arrow in Figure 2B. This xz-section was set to cut through the centre of the Si nanocolumns. (E) and (F) Electric and magnetic field intensities, respectively, shown in the xz-section view similar to (C) and (D) and excited at 530 nm, indicated by an arrow in Figure 2B. Incident field was set to be unity, that is, $|Ein|2 = 1$ and $|Hin|2 = 1$. Colour bars indicate the field intensities. White lines show the interfaces of the Si nanocolumns with air and the underlying SiO2 layer.

Detection strategy and binding affinities on metasurface platform

The detection strategy is to utilise biofunctionalization protocols of binding molecules, labelled antibody (Ab) and target analyte for achieving multi-level immobilizations on metasurface (**Figure 35A**). After initial phosphate-buffered saline (PBS) flow, the binding molecules of Cys-streptavidin (Cys-SA) flows through the microfluidic paths onto the metasurface regions where a uniform and stable physiosorbed layer is formed directly by the interaction between streptavidin and the silica shell of nanocolumns (Irrera et al., 2018). Next, HSA antibodies labelled with biotin (Biotin-HSA Ab) are bound to the Cys-SA through the fast and strong non-covalent protein-ligand interactions, and this formed complex biolayer provides a good high-density binding platform for HSA. Furthermore, when tetrazolate nitrogens from FL biosensors TPE-4TA bind with polar dominant-contacting lysine residues (Lys) in HSA binding conformation through hydrogen bonding and electrostatic interactions, triggered restriction of intramolecular movement effect lights up HSA (Tu et al., 2019). Afterwards, pre-bound products of HSA and TPE-4TA can be captured persistently through antibody-antigen reaction. Notably, PBS rinsing is compulsory to remove unbound parts after immobilization at each level. Besides, the results in **Figure S19** demonstrate that binding sequence of TPE-4TA affects final FL response. Two pre-bound products ([HSA+TPE-4TA] and [HSA Ab+HSA+TPE-4TA]) possess the strongest FL intensities in this protocol compared to the case where TPE-4TA is individually immobilized on HSA in the last step. The potential reason for the FL-intensity differences is the inward orientation of HSA as big biological molecules when immobilized. The binding sites of endogenous and exogenous substances are mainly located in subdomain IIA and IIIA on HSA tertiary structure (Huang et al., 2020; Luo et al., 2018; Zhu et al., 2019) where Immunoglobulin G (IgG) binding positions of ligands on HSA are localized precisely in Domain III (Fasano et al., 2005; Zorzi et al., 2019). Nevertheless, the favourable binding positions of ligands between HSA and TPE-4TA are found in the intersection of Domain I and Domain III (Tu et al., 2019). Once HSA immobilizes onto its Ab successfully, Domain I and III of HSA mainly face the surface of Si nanocolumns. The presence of steric hindrance may limit TPE-4TA movement by crossing directly into the interface of Domain I and III, thereby the binding opportunities between HSA and TPE-4TA will be further reduced due to immobility of adaptive spatial conformation of HSA-HSA Ab (**Figure S20**). However, prepared mixing solution of HSA and TPE-4TA beforehand can be fully reacted to completely avoid this binding loss. In short, the whole designed biofunctionalization protocol indicates that the detection strategy is feasible and optimal on binding identification, stability, and intensity, which has been validated from subsequent experimental results.

In order to ensure that the preset immobilizations can proceed as the desired protocols, the surface plasmon resonance (SPR) measurement was conducted to evaluate the effectiveness of immobilization quantitatively as shown in **Figure 35B**. The measurement was conducted on flat gold surface where SPR is induced. Initial flow of PBS at 10 µL min^{-1} for 10 min is the highest priority step to clean the gold film surface and maintain unobstructed microfluidic paths. Next, Cys-SA, Biotin-HSA Ab and the mixing solutions of HSA and TPE-4TA are flowed at 10 µL min^{-1} for 10 min, respectively. Furthermore, each binding stage contains a standard rinse with PBS for 10 min to remove residual reagents of previous step. The results at the steady state indicate that binding affinity reflects on a quantity, ΔRU, defined as absorbent mass per unit area in the scale of pg mm^{-2}. As the sequential immobilizations accomplishes, ΔRU continues to increase with three binding stages, which are 1303.8 of Cys-SA immobilization (Molecular weight, M_{Cys-SA} = 17.9 kDa), 1694.2 of Biotin-HSA Ab immobilization ($M_{Biotin-HSA Ab}$ = 69 kDa) and 281.5 conjugates of HSA and TPE-4TA ($M_{HSA+TPE-4TA}$ = 67 kDa), respectively. Inset figure in Figure 3B represents the difference of HSA with/without TPE-4TA in binding response. Compared with HSA solution only, the binding ratio of HSA+TPE-4TA increases by 34%, which is attributed to the ligands binding of TPE-4TA through hydrogen bonding and electrostatic interactions. Based on analysis of BIACORE, the theoretical binding capacity of TPE-4TA as small molecules on gold surface can be calculated using the following equation (1):

$$R_{TPE-4TA} = \frac{M_{TPE-4TA} \times R_{HSA} \times S_r}{M_{HSA}} \text{ (RU)} \tag{1}$$

where $M_{TPE-4TA}$ and M_{HSA} represent the molecular weight of TPE-4TA and HSA, respectively; R_{HSA} represents the binding capacity of immobilized HSA and S_r refers to the stoichiometric ratio between TPE-4TA and HSA.

The result indicates that 95.7 of the measured binding response of TPE-4TA is 24 times more than the theoretical estimate. This increase could be explained by the AIE phenomenon since numerous FL molecules of TPE-4TA aggregate into the structural cavity of HSA.

Moreover, the immobilized molecular density is evaluated by the equation (2):

$$D_A = \frac{M_A}{R_A \times N_A} \text{ (1 molecule for nm}^2\text{)} \tag{2}$$

where D_A represents the immobilized molecular density of analyte; M_A represents the molecular weight of analyte; R_A represents the binding capacity of analyte and N_A is the constant of Avogadro.

The result shows that one molecule of Cys-SA, Biotin-HSA Ab and conjugates of HSA and TPE-4TA are situated on an average square surface area of 4.61 × 4.61 nm^2, 8.20 × 8.20 nm^2 and 19.9 × 19.9 nm^2, respectively, indicating this multi-level immobilization strategy is feasible and can be also applied in our platform effectively.

The indirect verification of immobilization is also carried out through non-specific Ab-Ab absorption as shown in **Figure 35C**. In this case, the same species of HSA Abs have been labelled individually with two different moieties: biotin and FL-label HyLite Flour 555 (HL555). The flowing order of samples is as follows: Cys-SA, Biotin-HSA Ab, HSA, and HL555-HSA Ab then rinse is performed after each sample flow. Concretely, HL555 labelled HSA Abs emit FL at the peak of 570 nm and they will be absorbed onto Biotin-HSA Abs in metasurface area that has not reacted with HSA yet, hence being forced to dock on the metasurface likewise. When different concentrations of HSA are already fixed on 2 μg mL^{-1} biotin-labelled HSA Abs, FL quenching effect occurs as HSA concentration increases upon extra introduction of 5 μg mL^{-1} HL555 labelled HSA Ab into the microfluidic paths, which proves that antibody-antigen reactions with higher priority interrupt Ab-Ab nonspecific absorption (Inset graph of Figure 3C). The results illustrate that FL intensities reaches the strongest value in the absence of HSA meanwhile it descends by 68.1% when HSA concentration reaches at 1000 ng mL^{-1}. **Figure S21** reveals that the concentration of HL555-labeled HSA Ab is positively correlated with its FL efficiency under this non-specific absorption. Inset figure in Figure S21 indicates that the introduction of HSA is the primary factor for this FL quenching effect. Consequently, multi-level immobilization can also be confirmed indirectly.

Figure 35 (A) Schematic diagram of multiple immobilizations on Si nanocolumns; (B) Binding response of immobilizations on an Au-film sensor chip using surface-plasmon-resonance instrument. Inset: the difference of binding ratio between HSA and the mixture of HSA + TPE-4TA in the final immobilization step; (C) Non-specific absorption between 2 μg mL-1 Biotin-HSA Ab and 5 μg mL-1 HL555-HSA Ab with HSA concentration varying. Inset: the change of FL efficiency with different concentrations of HL555-HSA Ab.

FL kinetics on metasurface platform

The FL kinetics behaviour of AIEgen TPE-4TA in HSA detection under the modulation of metasurface platform are evaluated in this section. TPE-4TA has excellent FL response towards HSA and its concentration effect has been optimised (**Figure S22** and **Figure S23**). Its good selectivity towards HSA excludes potential interference from biomolecules over various proteins with isoelectric points ranging 1–10 in buffer solution (Tu et al., 2019). **Figure 36A** shows an excellent photostability of HSA+TPE-4TA conjugate within 2 hours, which allows multi-level immobilizers to

generate FL persistently on the metasurface. Moreover, FL intensity is positively related to HSA concentration as displayed in **Figure 36B**. FL enhancement in the microalbumin range is divided into two phases: a sharp phase (0 to 20 µg mL^{-1}) and a slow phase (20 to 160 µg mL^{-1}). Slowing trend indicates binding capabilities of Biotin-HSA Ab are approaching its maximum limitation. The steady FL intensities near 160 µg mL^{-1} describe that the fixed amount of HSA and TPE-4TA conjugates has been regionally saturated on metasurface. Significantly, the metasurface platform remains ultra-sensitive towards the trace of HSA (< 20 µg mL^{-1}) where FL signal climbs rapidly 82% of maximum response when HSA content jumps towards 20 µg mL^{-1}. To further explore the extent to which the metasurface platform contributes to FL amplification, two other platforms (that is, microplate platform and microfluidic platform) are also established for horizontal comparison and the corresponding linear fittings of three platforms are plotted in **Figure 36C**, **Figure S24** and **Figure S25**. The microplate platform composes of the conventional transparent polystyrene materials and microfluidic platform possesses the same construction as metasurface platform without Si-nanocolumns. In **Figure 36D**, 39% and 136% FL enhancement of HSA detection are observed in microplate platform and microfluidic platform respectively, however, emitted FL boosts up to 1001% under the light-confined mode in the metasurface platform. Through comparison of three platforms (**Figure 36E**), FL signal of the metasurface platform and the microfluidic platform are 7.93-fold and 1.70-fold stronger than that of the microplate platform respectively. Obviously, FL regulation of metasurface is superior to the other two platforms. We also note that numbers of the FL molecules involved in these measurements are the least in the metasurface platform because the PBS rinse removed the unbounded FL molecules. Thus, net FL-detection efficiency is far superior in the metasurface platform to the other microplate and microfluidic platforms.

On top of that, the practical evaluation in the application of human urine is investigated among three platforms to verify feasibility of sensing augmentation. In urinary FL analysis, autofluorescence is induced inevitably under UV light and leads to FL overlap within the detection scope of 529–571 nm (**Figure S26**). Hence, treated urine samples diluted 80 times with PBS buffer are employed as the standard to eliminate the impact of auto-FL as efficiently as possible (**Figure S27**). PBS buffer also maintains diluted urine samples into a neutral environment avoiding the potential impact of changes in urinary pH on FL measurements. Additionally, the robustness of TPE-4TA has already been proved in slightly acidic environment and main urinary components, such as urea, uric acid, creatinine, etc., do not interference assay sensitivity of HSA (Tu et al., 2019). Validation from the commercial kit shows HSA level of 45.8 µg mL^{-1} in the urine samples and this concentration can be calculated independently by referring to the standard curves established in three platforms to obtain 40.7, 41.9 and 43.8 µg mL^{-1} with recovery rate of 88.9%, 91.5% and 95.6% respectively (**Table S2**). Through systematic measurements presented in **Figure 36F**, FL retention rate refers to the percentage variations in detectable FL signals from intense to dimmed at extremely low HSA concentrations as the dilution ratio increases. First, the FL retention rates of three platforms are 100% in the initial phase (80x diluted urine samples) and drop towards 80% with doubling of the

dilution ratio (160x). When the dilution ratio is adjusted to 320x, the microfluidic and metasurface platforms retains their 70%, while the microplate platform experiences a dramatic decline to 29%. At this time, the FL retention rate of the microplate is less than half of that of the other two platforms. Next, 7%, 18% and 38% FL retention rates are recorded under the dilution ratio of 640x where metasurface platform is 2.1 folds and 5.4 folds more intense than the microfluidic and microplate, respectively. After that, the metasurface maintains 27% of FL signal with further dilution (1280x) whereas the microplates and microfluidics almost lose it completely (2%). Similar circumstance still persists until the final phase of 2560x with near 10% retention rate in metasurface. Moreover, microplate, microfluidic and metasurface platforms have 300 ng mL^{-1} (LOD1), 150 ng mL^{-1} (LOD2) and 18.75 ng mL^{-1} (LOD3) as their respective detection limits, corresponding to the FL retention rate of 80%, 70% and 9% respectively. The above results of FL retention rate change are consistent with the performance of LODs in three platforms. Finally, the sensitivity level is expressed as: metasurface > microfluidic > microplate. The metasurface platform can effectively amplify the FL signal at extremely low concentrations of HSA in human urine environment. FL retention rate is still detectable even if urine specimens are diluted by 2560 times, which fully illustrates that Si-nanocolumn matrices which enables HSA to immobilize are the primary reason for producing FL enhancement.
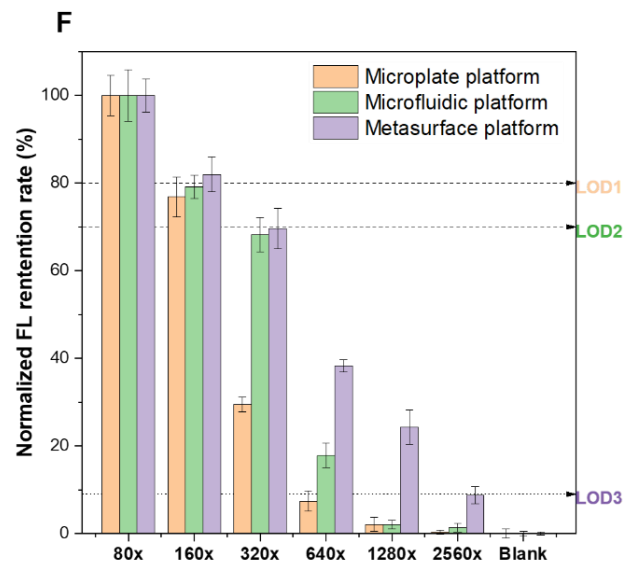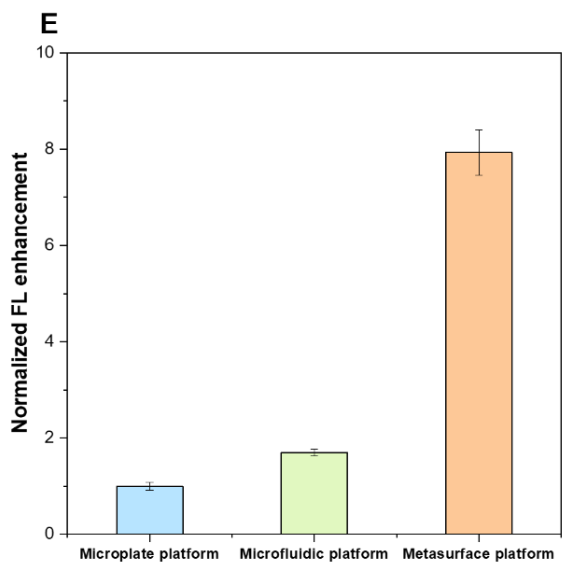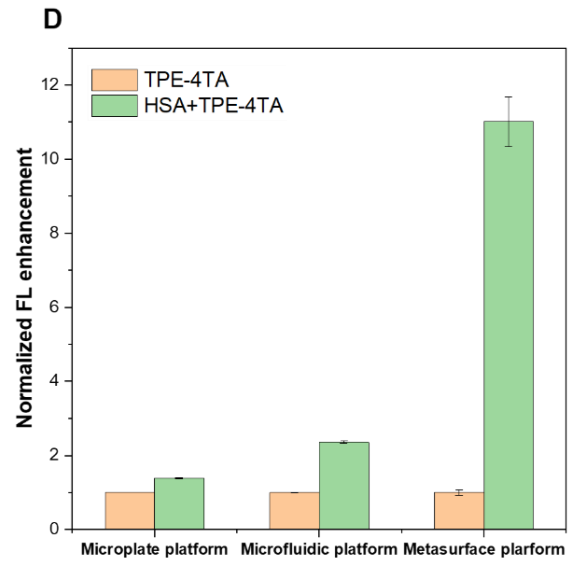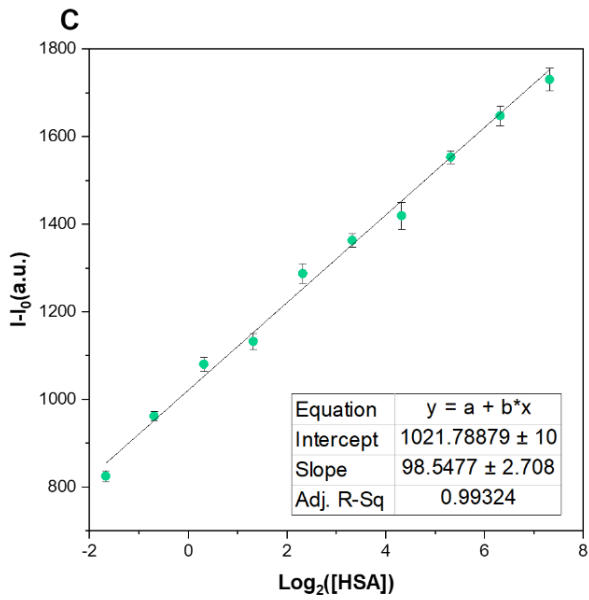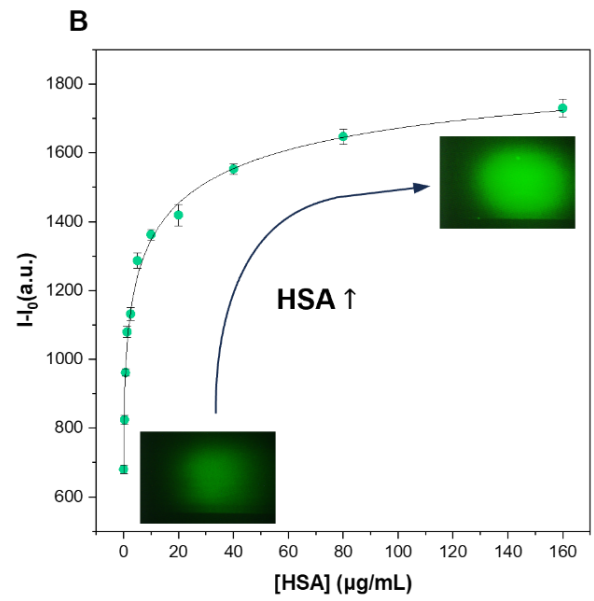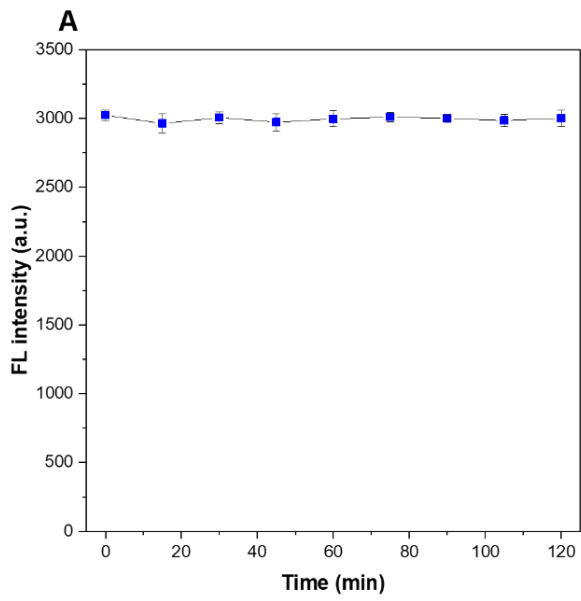
Figure 36 (A) Stability of FL in HSA detection within 2 hours using the metasurface platform; (B) The correlation of HSA and TPE-4TA from 0 to 160 µg mL^{-1} using the metasurface platform. Inset graphs are change in FL images at 0 and 160 µg mL^{-1}; (C) The corresponding standard curve of TPE-4TA for HSA detection in the range of 0–160 µg mL^{-1} using the metasurface platform based on (B); (D) The difference of FL response with/without HSA in each of platform; (E) The comparison of FL enhancement among the microplate platform, the microfluidic platform and the metasurface platform; (F) FL retention rate between three platforms in urine scenarios with different dilution ratios where dilution ratios refer to total volume/treated urine volume with PBS buffer as diluent. Three broken horizontal lines represent corresponding LODs in different platforms (LOD1: the microplate platform (orange), LOD2: the microfluidic platform (green), LOD3: the metasurface platform (purple)).

Underlying mechanisms on metasurface platform

After understanding optical properties, binding affinities, and FL kinetics of metasurface platform throughout the dynamic sensing process, the potential mechanism can be explained as **Figure 37** displayed with the comparison of three models. Initially, large-scale wells located on microplate platform enable numerous conjugates of HSA and TPE-4TA to freely move in multi-dimensional directions. Uniformly dispersed FL molecules are hardly restrained in camera zone, resulting in the limited FL signal in large liquid dimensions. Remarkably, microfluidic and metasurface platforms further compress the scope of FL activities along the height direction, thus enabling us to acquire the focused FL images, which aligns with the results presented in Figure 4E. More significantly, the Si nanocolumns allow FL molecules to be stacked in a non-uniform manner within an extremely small area and local enrichment state occurs, thus enhancing FL output. Particularly, the reinforced effect of resonant EM fields further amplifies FL emission of HSA+TPE-4TA from the outermost surface of Si nanocolumns through multi-level immobilizations. Moreover, the results from FL kinetics (**Figure 36B**) reveal that FL enhancement is subject to the total fixed number of conjugates of HSA and TPE-4TA in metasurface area. FL molecules immobilization reaches its saturation when the concentration of HSA is excessive (> 160 µg mL^{-1}). Amplifying effect can only occurs on the bound sections and does not cause promotion with HSA concentration continues to increase any longer. Conversely, the microalbumin or trace range do not have the saturation effect, which is the reason why metasurface is more significant for it.
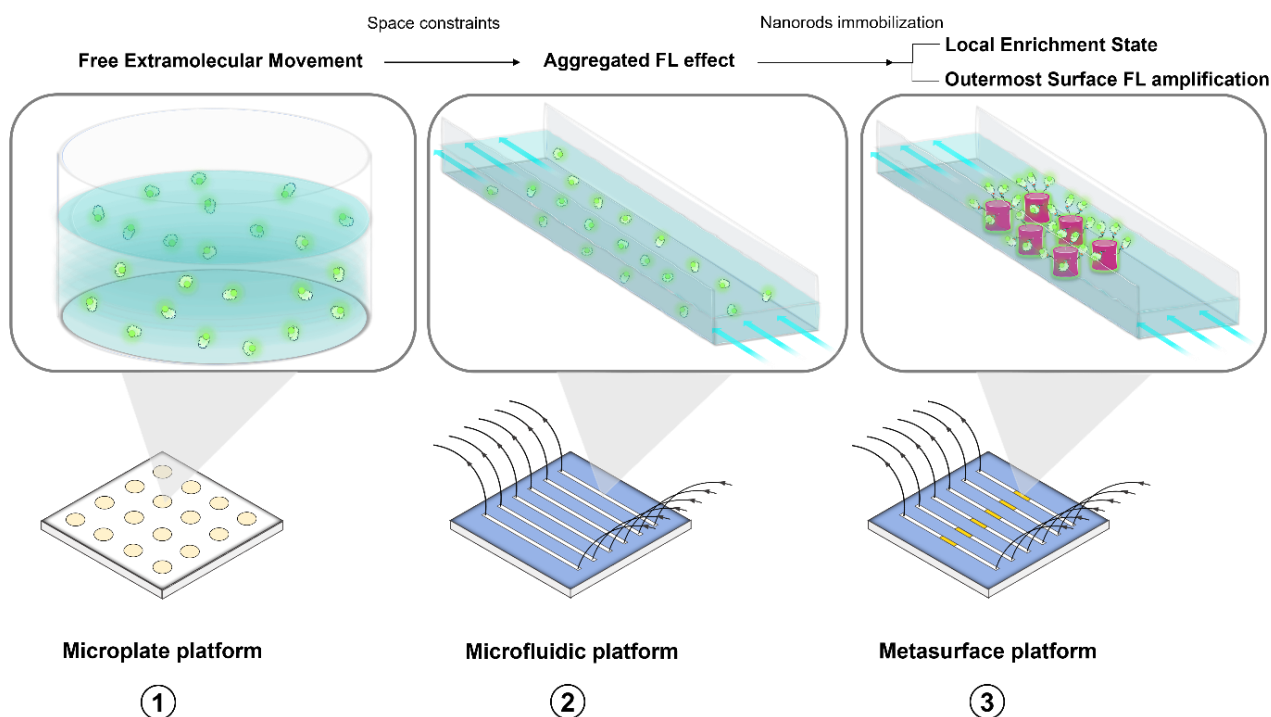
Figure 37 Potential mechanism of the metasurface platform compared to the microplate and microfluidic platforms under their nanostructures.

Future prospects on metasurface platform

This research offers a feasible strategy to achieve enhanced HSA detection using AIE FL biosensor incorporating with metasurface platform. Through the reinforced resonant EM fields of Si nanocolumns, photosignal sensitivity of analytes can be amplified, which is particularly significant in the presence of many interferences in the urine scenarios. Improved LOD meets the higher standard requirements of HSA detection at a low level. Besides that, the removal of HSA from human urine for enhancing sample loading capabilities in analytical methods becomes a promising pathway to identify low-abundant proteins and improve their detection sensitivity. To be more specific, urine contains thousands of different types of proteins, while HSA is one of main proteins as the high-abundant proteins. At present, more than 3400 individual proteins have been found in urine that could become potential biomarkers for different diseases and the majority of them belong to low-abundant proteins (Marimuthu et al., 2011; Santucci et al., 2015). The masking effect of HSA poses an impeding factor in urine for discovery/screening less-abundant proteins. Si nanocolumns enable to deplete existing HSA content efficiently to act as the function of filtration. The superior optical properties provided by the metasurface platform are apparently beneficial for monitoring in downstream process analysis of HSA removal.

This metasurface platform also provides a universal microfluidic design to be biofunctionalized for targeted biomarker detection via the combination of standard streptavidin-biotin model, immunobinding and fluorescence labelling, which is fully capable of applying onto other biomarkers.

Firstly, the array of Si-nanocolumns constructed on SOI substrate has a larger surface area on which biomolecules are allowed to immobilize. Secondly, this platform can achieve high reflectance in a visible wavelength range to be compatible with optical properties of target objects by tuning radius and periodicity. Thirdly, FL molecules specific with target biomarkers are selected carefully to ensure that steady output of optical signal will be turned on only after multi-level immobilization is completed successfully. More significantly, the running cost can be reduced dramatically because our metasurface substrates are reusable by washing.

All-dielectric metasurface platform has been illustrated on biomarker detection in biosensing with extraordinary optical characteristics that may lead to better sensitivity, higher throughput and more significant specificity for extremely low-level analytes in the future. The performance of several instances of all-dielectric metasurface platforms based on microfluidic FL sensing is summarized in this section as shown in **Table 5**. As metasurface platform become better explored, it will have a potential promotion on biomarker detection in the medical diagnosis criterion to be a higher standard.

No.	FL component	Biomarker	Performance		Reference
			Dynamic range	LOD	
1	TPE-4TA	HSA	0–160 µg mL^{-1}	18.75 ng mL^{-1}	This work
2	AF555	IgG	5–2000 pg mL^{-1}	5 pg mL^{-1}	(Iwanaga, 2020)
3	HL555	PSA and CEA	0.16–1000 ng mL^{-1}; 0.002–25 ng mL^{-1}	1 ng mL^{-1}; 0.002 ng mL^{-1}	(Iwanaga, 2023)
4	HL555	COVID-19 glycoprotein peptide and corresponding Ab	0.16–100 ng mL^{-1}; 6.25–100 ng mL^{-1}	0.64 pg mL^{-1}; 1.56 ng mL^{-1}	(Iwanaga & Tangkawsakul, 2022)
5	HEX	cfDNA	0-2 fM	0.488 aM	(Iwanaga et al., 2023a)
6	HEX	SARS-CoV2	5-4000 aM	5.86 aM	(Iwanaga, 2022)

Table 5 Summary of FL detection of biomarkers on the metasurface platform. AF555 denotes Alexa Flour 555, HL555 HyLite Flour 555, and HEX a fluorescent probe on DNA.

Conclusion

This designed all-dielectric metasurface platform shows a resonance of 70% reflection response at 530 nm and can enhance FL emission at the outmost surface of Si nanostructures owing to the significant amplification of its resonant EM field. Subsequently, the multi-level immobilization as detection strategy successfully implements strong high-density bindings of FL molecules on metasurface area. FL kinetics results prove its good photostability and a good dynamic range of 0–160 μg mL^{-1} especially ultra-sensitive to the trace HSA. In the comparison of three platforms, metasurface platform is superior to microplate and microfluidic platforms, which exhibits 1001% FL enhancement, and its FL signal is 7.93-fold and 4.69-fold stronger than the others. Furthermore, the results in urine testing demonstrate the highest recovery rate (96%), the lowest LOD (18.75 ng mL^{-1}) and the biggest FL retention rate (9%) in urine up to 2560 times diluted among three platforms. The underlying mechanism concludes that a local enrichment state on the metasurface area and space constraints from microfluidic paths are the main reasons for enhancing FL emission. In summary, the AIE-based FL biosensor incorporating metasurface platform can effectively achieve FL enhancement in HSA detection. The combination of AIE fluorogens and metasurface platform opens up a new route for biosensing in real scenarios.

FUTURE PROSPECTS

The improvements of AIE biosensors

Inorganic-organic hybrid materials are novel biological and chemical modifications as the potential improvements of AIE FL biosensors for biomarker detection. These contents have already been published on "*Materials Chemistry Frontiers*, 2022, *6*(15), 2011-2033" under the title "**Inorganic–organic hybrid materials to detect urinary biomarkers: recent progress and future prospects**". Qi Hu is the primary author, while Dan Ding is the co-author and Youhong Tang is the correspondent author (**doi.org/10.1039/D2QM00213B**).

To be more specific, inorganic-organic hybrid materials are constructed by combining inorganic and organic building elements at the molecular or nanoscale level. Their attributes are determined not only by the type and proportion of the ingredients, but also by their dispersion (Schubert, 2011). Different forms of hybrid materials have been reported, each with its unique structural features. To date, inorganic-organic hybrids have attracted extensive attention as a new type of material, exhibiting a great diversity of material characteristics including mechanical, chemical, optical, and biological capabilities (Sharp, 1998). As for inorganic-organic hybrid forms, protein-inorganic and non-protein-inorganic hybrid materials are two main orientations of worthy. Proteins are macromolecular substances with outstanding activity and specificity, but their application is restricted by a number of drawbacks, including high sensitivity to the environment, low repeatability of experimental results, and the need for lengthy purification (Lee et al., 2015). The stability of proteins is often enhanced by interactions through charge affinity, covalent bonds, and structural coupling to immobilize on inorganic surfaces such as metals (Ge et al., 2012). Hence, protein-inorganic hybrids compounds have emerged to surpass the constraints of pure protein applications to facilitate their use in biomarker detection systems. In reality, unlike the technical route of hybrid protein assembly, inorganic modification in the framework of classical organic compounds is simpler to perform to improve the properties of products of polymer, hence most hybrid materials choose the non-protein synthesis pathway. Non-protein hybrid materials take specific organic compounds as the basic framework, and further chemically modify organic ligands by introducing a series of inorganic components such as metals, oxides, and polyoxometalates. Structural tunability and functional diversity are embodied by the highly free organic moieties' ability to build 1D, 2D, and 3D spatial frameworks as needed, while structural modifications can reflect in varying porosity and alter the thermal stability of hybrid species (Cui & Jia, 2017).

With the advancement of technology and marketing need, optics, electronics, biology and chemical sensing are one of main fields for inorganic-organic hybrid materials. Hybrid materials not only provide the material properties of different inorganic and organic components, but also can change their material features by adjusting the composition at the molecular level to create smart materials

(Sanchez et al., 2005). Cross-cutting techniques that synergistically combine molecular engineering and processing allow for precise control over size, composition, functioning, and morphology in complex hybrid systems of varied forms (Mir et al., 2018). in the optical field, materials that satisfy essential needs for wafer-scale optical systems include inorganic–organic hybrid polymers (Streppel et al., 2003). It possesses appropriate optical features such as reduced attenuation and a refractive index that can be accurately adjusted. Excellent surface planarization and long-term environmental stability are very impressive in reliability testing. The hybrid structure improves mechanical and thermal stability while keeping the capabilities of traditional polymers as compared to pure organic polymers (Houbertz et al., 2003). Chemical and biological sensing technologies also have evolved owing to the synergistic features of organic-inorganic hybrid materials. A typical aspect is by attaching molecules to the electrode surface (adsorption, covalent binding, self-assembled monolayers, etc.) (Walcarius, 2001). Electrodes are able to be hybridized by immobilizing multilayer films on electrodes (mainly polymers) and by designing heterogeneous and spatially defined layers and microstructures on the electrode surface or within the bulk of the electrode material to catalyze new performance (Walcarius, 2001). Additionally, biocatalytic processes can benefit significantly from inorganic-organic nanocomposites created by immobilizing biomolecules such as enzymes, proteins, antibodies, DNA or RNA in tailored nanoscale structures. When compared to free enzymes, hybrid materials have a large surface area, increased enzymatic activity, improved stability, and superior grabbing ability (Zhu et al., 2018). Its excellent prospects are also due to improved biocompatibility, increased catalytic activity, and label-free characteristics. At present, there are plenty such instances where inorganic-organic hybridization of materials corresponding protein-inorganic and non-protein-inorganic are effective means to assemble biological macromolecules or employ characteristic chemical reactions to detect biomarkers of different diseases directly or indirectly. Biomarkers are underlying molecular or cellular processes that relate certain environmental exposures to certain health consequences and it is crucial in determining the link between exposure to environmental toxins and the development of chronic illness in individuals, as well as identifying disease-prone subpopulations (Califf, 2018). Subsequently, biomarkers drive the development of biomarker-disease ecological detection systems in chemical and biosensing with this non-negligible importance. Due to these considerations, novel detection routes based on inorganic-organic hybrid modalities hold tremendous promise for the needs of chemical and biological sensing in disease diagnosis and monitoring compared with traditional detection methods (Lei et al., 2018).

Fluorescence detection tracks the change of optical properties to sense the physical/chemical reaction between biomarkers and FL biosensors. Based on the above introduction, the inorganic-organic hybridization can play a positive role in biomarker detection and the unique response of AIE biosensors for HSA detection is completely in line with this background. The pathway to make it brighter is to use non-protein-inorganic hybridization. the fluorescence properties of AIE molecules are completely dependent on whether intramolecular motion is restricted in their aggregated state.

In other words, the FL efficiency of AIE molecules will be greatly enhanced if a spatially constrained framework is made available, hence amplifying AIE properties will promote the sensitivity of HSA detection. In order to achieve this goal, choosing an appropriate inorganic architecture has become an important part of building a non-protein-inorganic hybrid material. Based on current reported research on inorganic-organic hybrid materials, graphene oxide (GO), silicon dioxide (SiO_2) and metal ions are the most three promising inorganic candidates that are suitable for AIE biosensors. Graphene, which exhibits unique mechanical, electronic, and optical characteristics including a large theoretical specific surface area, high intrinsic mobility, high Young's modulus, high thermal conductivity, high light transmittance, and strong electrical conductivity, has attracted extensive attention in many fields (Chung et al., 2013; Zhu et al., 2010). Chemically derived graphene oxide (GO) inherits graphene's intrinsic properties and is rich in oxygen-containing functional groups. Excitation wavelength-dependent fluorescence is exhibited by GOs, which are inexpensive, nontoxic, photostable, water-soluble, biocompatible, and ecologically benign (Zheng & Wu, 2017). Moreover, strong non-covalent interactions can be formed between its 2D structured surface and the adsorbed biomolecules through π-π interactions, electrostatic force or hydrogen bonding, which provides a chemically tunable platform for bioconjugation (Loh et al., 2010). Typically, GO is well dispersed in solution, which makes it easy to modify. In most studies, GO is an effective fluorescence quencher for many optical species because molecular aggregation caused by π-π stacking or hydrophobic interactions usually reduces the brightness of the fluorophore, which is also the source of GO's quenching ability (Ling et al., 2010). However, under certain concentration conditions, especially low GO concentrations, there are still studies demonstrating the enhanced aggregation-induced emission of AIE fluorophores in the presence of GO (Liu et al., 2010). Owing to its characteristics, GO has been widely employed as an adjustable fluorescence enhancer or an efficient fluorescence quencher in fluorescence sensing. As a result, the introduction of GO as an inorganic moiety into the structure of AIE biosensors is a potential improvement strategy. Taking GO as an instance, the illustration of AIE biosensors and GO is displayed in **Figure 38**. The expectation is to utilize the underlying physical or chemical mechanism such as space folding, embedding, π-π interactions, electrostatic force, hydrogen bonding to form inorganic-organic hybrid materials using AIE biosensors as the organic moiety and graphene oxide (GO) as the inorganic framework. It is very likely that AIEgens-GO hybridization of this combination significantly enhances the detection performance through the synergistic effect of two different components compared to AIE biosensors only. After that, the introduction of VFD can tune the morphology of AIE molecules in this process to promote the fluorescence effect. Similarly, SiO_2 possesses good biocompatibility and facile surface modification (Bonacchi et al., 2011). AIE biosensors are capable of being coated by silica shells directly through covalent chemical bonding (Geng et al., 2014). As for metal ions, good stability and efficient sensitization is advantageous to form a rigid matrix on which AIE biosensors can be anchored via covalent bonding (Cui et al., 2012; Shustova et al., 2011). All in all, inorganic-organic hybrid materials, where AIE FL biosensors are employed as an organic component, while GO, SiO_2,

and metal ions are employed as inorganic components under VFD acceleration, is a feasible alternative of improvements.
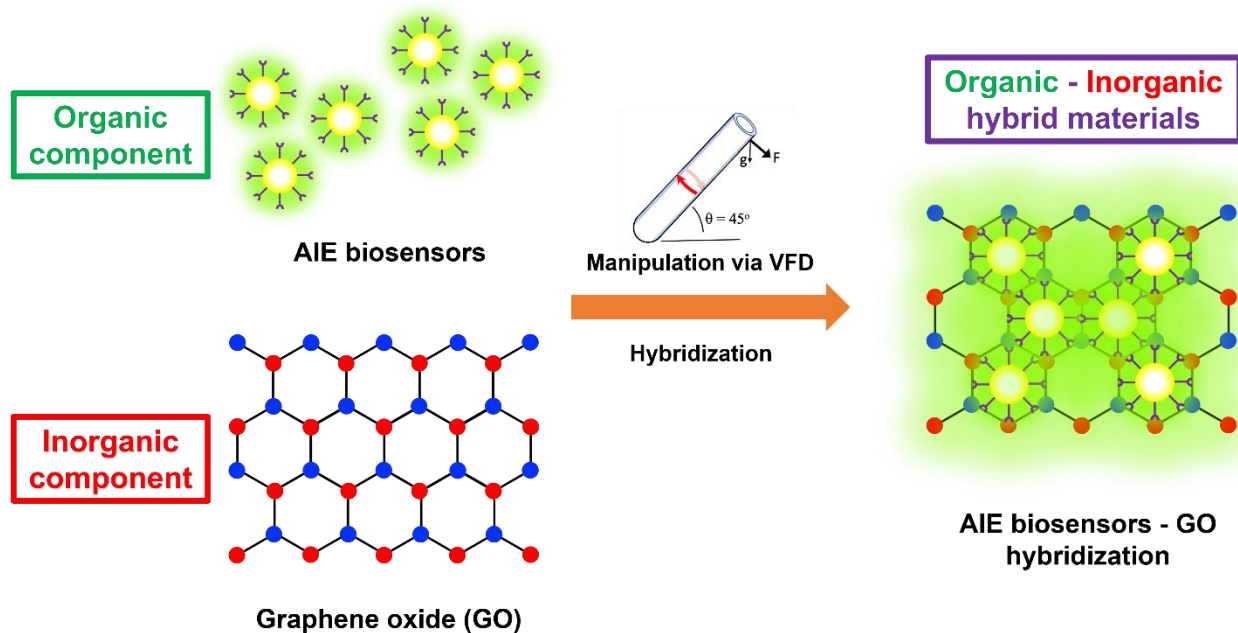
Figure 38 The hypothesis of the illustration of AIE biosensors – GO hybridization by the concept of organic-inorganic hybrid improvements.

The development of new biomarkers for CKD

Proteinuria is the most sensitive marker for detecting CKD progression in clinical settings (Fassett et al., 2011). However, the pathophysiological process behind CKD progression is far more complicated than imagined. Patients with impaired renal function are at risk of multiple complications or cardiovascular diseases (CVD), which may make detection more difficult or miss the best time for treatment (Levey & Coresh, 2012). Currently, many studies have reported new potential biomarkers for early detection of CKD, which may help to better understand the underlying pathogenesis and identify new therapeutic targets.

Adiponectin is a multifunctional cytokine (30 kDa) that plays a role in regulating inflammation (Halvorsen et al., 2000). Plasma adiponectin levels depend on renal function and are significantly elevated in patients with renal insufficiency (Cantarin et al., 2013). In patients with chronic kidney disease (CKD), adiponectin levels are elevated and positively predict disease progression. Yamakado and his team has developed an ELISA-based combined thionicotinamide-adenine dinucleotide cycle to detect urinary adiponectin (Yamakado et al., 2019). By measuring the urinary adiponectin level in 59 patients with diabetes mellitus (DM) and 24 non-diabetic subjects, the results showed that the urinary adiponectin level in patients with diabetes was 14.88±3.16 (ng/mg creatinine, mean±SEM), and the urinary adiponectin level in normal people was 3.06±0.33 (ng/mg creatinine). Urinary adiponectin levels increased with the increase of CKD risk. In addition, Song et al. studied the adiponectin levels of 2238 patients with chronic kidney disease (divided into the following categories based on concentration levels: initiation of dialysis or transplantation, a two-fold increase in baseline serum creatinine levels, or a 50% decline in the estimated glomerular filtration rate (eGFR)) and used the cox proportional hazard ratio model to analyse the relationship between the comprehensive renal outcomes and serum adiponectin levels (Song et al., 2020). The results showed that serum adiponectin levels were negatively correlated with eGFR ($p < 0.001$) and positively correlated with urine albumin-creatinine ratio. The highest quartile of serum adiponectin levels was associated with an increased risk of adverse renal outcomes (HR, 1.39; 95% CI, 1.05-1.84; p=0.021) Therefore, adiponectin can be suggested as a biomarker for CKD.

Liver-type fatty acid binding protein (L-FABP) is a 15 kDa soluble protein and they are present in large amounts in the cytoplasm of liver cells (Wang et al., 2015). Not only that, this protein is also present in the kidneys (Fassett et al., 2011). Studies have shown that L-FABP expression and urinary excretion are increased in CKD (Devarajan, 2010). Kamijo et al. evaluated the clinical significance of urinary L-FABP as a biomarker for detecting CKD (Kamijo et al., 2006). Comparing the results of non-CKD patients (n=48) and CKD patients (n=73), significantly poorer renal function degradation was seen in patients (n=36) with high levels of L-FABP in urine compared to those (n=12) with low levels of L-FABP in urine. Urinary L-FABP excretion rises with deteriorating renal function and L-FABP in urine did not change in response to L-FABP in serum. Urinary L-FABP is one potential

example of a clinical biomarker for CKD monitoring. To confirm the clinical efficacy of urinary L-FABP measurement in CKD, this team conducted a clinical trial in which they divided CKD patients into a progression group (n=32) and a non-progression group (n=16) (Kamijo et al., 2005). The experimental results showed that under similar creatinine clearance rates (Ccr), the urinary L-FABP concentration in the progression group was significantly higher than that in the non-progression group (111.5 vs 53 μg/g creatinine, $P < .001$), and urinary L-FABP is more sensitive than urine protein in predicting CKD progression (93.8% vs 68.8%) but less specific than urine protein (62.5% vs 93.8%). The trial also found that the progression of CKD is associated with changes in L-FABP in urine ($r = − .32$, $P < .05$). These studies all illustrate that urinary L-FABP excretion is an effective clinical biomarker for monitoring CKD progression.

N-acetyl-β-d-glucosaminidase (NAG) is a mesophilic hydrolase expressed by proximal tuble (Liangos et al., 2007). In many kidney diseases, the excretion of N-acetyl-β-D-glucosaminidase (NAG) in urine is abnormally high because it is an indicator for renal tubular dysfunction (Gluhovschi et al., 2012). Kuo et al. explored whether NAG could predict renal function progression in the end stage of CKD (Kuo et al., 2018). In this experiment, the urinary NAG concentration of 30 patients with stage 3-4 CKD was continuously tracked. Findings indicated that patients in all stratified CKD stages had significant differences between the different NAG groups (P = 0.005 for stage 3A, P = 0.001 for stage 3B, and P = 0.004 for stage 4). Higher urine NAG levels are linked to a higher likelihood of renal function loss occurring quickly in people with end-stage CKD. In clinical practice, urinary NAG is a helpful biomarker for identifying individuals with a faster rate of GFR decrease and for diagnosing continuing renal damage. Furthermore, Sheira et al. evaluated the potential of urine NAG as an early biomarker for detecting diabetic nephropathy (Sheira et al., 2015). Fifty patients with DM were divided into three groups (normoalbuminuria, microalbuminuria, and macroalbuminuria) to measure urine NAG content. The results showed that urine NAG levels were significantly elevated in all patients and NAG values increased in parallel with the severity of kidney involvement.

These three biomarkers provide new developments for detecting CKD and clinical data confirmed the positive correlations between their content and CKD. However, their physiological mechanism is still unclear. It is generally believed that the increase in biomarker levels is due to the damage of renal filtration function, resulting in reduced clearance rate or the counter-regulatory response of complex metabolic disorders in CKD patients. However, it should be noted that the sample size provided by these clinical studies is not sufficient to replace the current mature urine protein detection system, and long-term research and observation are still needed to determine its clinical significance. Certainly, multi-channel verification with the selection of multiple CKD biomarkers as reference can further improve the accuracy of CKD diagnosis. This requires the simultaneous development of multiple AIE biosensors that can detect targeted biomarkers. From a design perspective, proteins (macromolecules) promote the AIE phenomenon. A large number of amino groups can provide

natural hydrogen bonding targets, and the swelling effect of proteins can further compress the activity space of AIE molecules. However, adiponectin, L-FABP and NAG are low-abundance proteins under normal physiological conditions. The shielding effect from high-abundance proteins will greatly affect their identification, which undoubtedly puts higher requirements on the sensitivity of AIE biosensors. The metasurface platform proposed in this study that can improve detection sensitivity is a good direction for improving this barrier.

SUMMARY

In this research, there are 6 chapters totally: Introduction, Literature review, AIE biosensor for HSA detection, AIE biosensor incorporating with hydrogel platform, AIE biosensor incorporating with metasurface platform and future prospects, which are demonstrated to explain novel AIE biosensors and their engineering improvements in achieving HSA detection for screening and monitoring CKD.

In the chapter of Introduction, it has 5 parts including research background, research object, detection methodology, gap and challenge, and research route. The research background describes a public health issue in which kidney disease has become the seventh leading cause of death worldwide. With changes in population trends, disease epidemic changes, induction of complications, climate changes, environmental pollutions and other external factors, the prevalence of kidney disease will still significantly increase and have a negative impact that cannot be ignored on human quality of life, medical costs, and socioeconomic disparities. Therefore, it is necessary to improve the detection and monitoring of kidney diseases. Generally, kidney diseases are divided into two types: acute kidney injury (AKI) and chronic kidney disease (CKD). Acute kidney disease has an early onset and obvious adverse symptoms, while chronic kidney disease is just the opposite. It has few symptoms in the early stages but becomes more severe after losing the majority of the kidney functions. Due to the lack of early identification and screening capabilities for chronic kidney disease in many regions around the world, CKD patients are unable to receive timely diagnosis and treatments, resulting in continued increases in prevalence and mortality. Proteinuria is a typical symptom of CKD, and the progression of kidney disease is highly positively correlated with the protein content in proteinuria. However, urinary protein includes many proteins that are irrelevant to CKD. On this basis, it becomes particularly important to find specific components related to CKD within the scope of proteinuria. Clinically, albuminuria is used as a more specific classification to reflect the level of CKD because albumin is the main content of urinary protein. Because of this, albumin is treated as the main object of this research. Human serum albumin (HSA), as the most abundant protein in human plasma (accounting for 55-60% of the total serum proteins), has three alpha helical domains and each domain contains two subdomains. Due to the different ligand binding affinities exhibited by the subdomains, HSA can provide multiple binding sites for reacting with substances in its different structural domains where HSA possesses different binding abilities to endogenous and exogenous ligands. The impairment of glomerular filtration function in CKD disrupts the concentration balance of HSA in body fluids, causing it to leak from blood into urine (>20 mg/L). Therefore, accurate screening and monitoring of HSA in albuminuria is crucial for early diagnosis and treatment of CKD. As a new technology in the field of biosensing, fluorescence has attracted more and more attention on detecting HSA due to many unique advantages, including simple operation, obvious phenomena, fast response, high sensitivity, low cost, etc. Among various fluorescence technologies, FL biosensors based on aggregation-induced emission (AIE) features

show excellent performance, such as a wide range of applicable concentrations, good photostability, low background noise, and large Stokes shift. In particular, AIE FL biosensors are non-emissive in solutions individually, but once they interact with HSA, strong fluorescence will be triggered since they form an aggregation state. The binding between AIE molecules and HSA can be activated through electrostatic interactions, hydrogen bonds, non-covalent bonds, hydrophobic interactions, etc., and the activity of HSA remains unchanged after the reaction. Hence, fluorescence will AIE characteristics can be utilized to detect HSA effectively. At present, the flexible modifiability of AIE molecules has enabled many researchers to successively design FL biosensors that can specifically detect HSA. However, depending on the targets and designs of differential studies, there will be certain differences in the test objects and environments. Most HSA detections are carried out in simple deionized water, while buffer system is another option to support HSA detection by avoiding pH variation. Additionally, in order to further evaluate the accuracy and limitations of AIE biosensors, some studies have selected artificial urine as a simulated biological sample. Predictably, according to the existing issues of complexity of biological samples, the biocompatibility of biosensors, etc., there are less studies that focus on HSA detection in serum and urine samples. Owing to the limited research funds, some studies also use BSA (75.8% endogenous structure of HSA) instead of HSA for conducting lab tests. From the currently reported situation on the detection of HSA using AIE FL biosensors, the number of research cases decreases as the complexity of the solution matrix increases. As far as the current status of HSA detection is concerned, some gap and challenges still exist in the detection process of AIE biosensors and they are summarized on the aspects of extension to biological sample applications, trace biomarker detection in urine, insufficient delivery efficiency, delayed detection, reusability, high running costs, lack of back-end research, limitations of laboratory use, biocompatibility&environmental friendliness, and optical signal loss. According to the above research outline, the gaps and challenges are divided into three categories: convenience, performance, and sustainability. These issues tend to be improved by using engineering designs. The purpose of engineering design is focusing on problem-solving and the optimization of HSA detection, the development of competitive advantage for AIE products, and functionalization in more mature medical applications. Two feasible engineering designs are proposed after literature review: hydrogel platform and metasurface platform as research strategies to improve the performance of AIE biosensors in HSA detection. The hydrogel platform not only has good portability and excellent liquid phase distribution ability, but also has better biocompatibility and environmental friendliness. As for the metasurface platform, it can achieve guidance and amplification during the transmission of optical signals while minimizing light loss. Crucially, it is reusable, and by being equipped with a microfluidic system, the consumption of chemical reagents is greatly reduced. Of course, these two platforms provide real-time settings for normal samples and biological samples to ensure consistent FL results.

In the chapter of literature review, it focuses on 5 parts including kidney and associated disease, urine and urinary biomarkers, human serum albumin, HSA detection methods and engineering

design. The first part is for reviewing the relevant information of kidneys. First, kidneys are very important organs in the human body and their main function is to filter waste from the blood and return the purified blood to the body. Once kidney disease affects its normal physiological function, substances in the blood may seep into urine depending on the degree of damage. CKD is a typical manifestation of imbalance in renal filtration function. Changes in glomerular filtration capacity are the most critical factor leading to CKD. In order to determine the extent of renal damage, eGFR and uACR are established clinically to predict and diagnose the pathophysiology of CKD. The thresholds of early CKD are <60 mL/min/1·73 m² and >30 mg/g in these two categories. Among these parameters, changes in HSA concentration are one of the indicators that are directly used to define and measure the glomerular filtration capacity in CKD. The threshold range of urinary HSA concentration is defined as albuminuria >20 mg/L by quantifying the relationship between HSA and GFR/uACR. As we all know, urine is a very complex matrix. Before conducting HSA detection in urine, other major urinary components are investigated in the second part, including bilirubin, creatinine, glucose, urea, uric acid, ions, ketones, nitrites, RNA and other substances. After that, HSA as the target biomarker is reviewed in the third part. It is a heart-shaped single-chain protein and its overall structure includes three homologous α-helical domains I, II and III, each of which contains two subdomains A and B, where three major binding sites are located at IIA, IIIA and IB. By utilizing these binding sites, HSA detection methods are reviewed in fourth part. Considering the economic costs and practical requirements of HSA testing in large numbers of patients, most conventional methods of HSA detection are qualitative/semi-quantitative tests because the threshold for albuminuria lies in the range of high concentrations of HSA, whereas conventional methods like immunoassays and colorimetry exhibit obvious reaction results and are sufficient to meet daily detection needs. Colorimetry is a photometric method. By tracking the chemical and physical reactions before and after, the visual changes can easily distinguish the changes in the analyte. Common detection methods of HSA based on the colorimetric principle include test strips, bromocresol green and bromocresol purple, as well as many new colorimetric biosensors. The fundamentals of immunoassay are the interaction between antibodies and antigens. The antibody-antigen complex is formed with very high selectivity, in which the analyte acts as the antigen and the reagent acts as the antibody. Common immunoassays for HSA detection are divided into Immunonephelometry, Immunoturbidimetry, Radioimmunoassay and developed immunoassay biosensors. Compared to these traditional methods, new possibilities of detection methods based on AIE phenomenon have also been reviewed. Restriction of intramolecular motion is the fundamental reason for producing fluorescence. A typical characteristic of AIE molecules is that their luminescent centres are highly hydrophobic and therefore prone to aggregate formation in physiological environments or aqueous media. In addition, the large steric hindrance of protein macromolecules will form a natural spatially restricted environment, then the fluorescence accumulation effect will be more significant. Through reviewing the current research on this, many AIE biosensors have been developed for HSA quantitative detection. In the final part, engineering

design is a dynamic and systematic process that uses engineering knowledge, accumulated experience, and rational creativity to solve practical problems. In terms of biomarker detection, hydrogels are widely used because they exhibit very good properties such as biocompatibility, adjustable geometry, non-toxicity, non-biodegradability, flexibility, temperature sensitivity, and low cost. Hydrogels provide a platform with a porous structure and a large internal surface to accommodate bioreceptors and enable the interaction of biological components. The design strategy mainly focuses on stable immobilization, bonding ability, swelling kinetics, diffusion, and environmental friendliness. HSA detection using AIE biosensors is a liquid-based form. Hydrogels have the ability to retain or absorb large amounts of water or biofluids in their network structure. In addition, hydrogel polymers have the ability to form connections through charge interactions or hydrogen bonds, thereby creating physical crosslinks between analytes and hydrogels. These behaviours meet the requirements of biofunctionalization of AIE biosensors, making it possible to improve their performance. After reviewing the literature, no cases of AIE biosensors using hydrogel as a platform to detect HSA were found, which meets the innovative ideas of engineering design. Similarly, the detection of biomarkers on metasurface platforms has also attracted great attention because it can provide an efficient, highly sensitive, inexpensive and robust solution. The nanostructure of the metasurface can achieve wavefront manipulation, and the fluorescence generated in this area can take advantage of this property. On the other hand, the all-dielectric metasurface based on silicon-on-insulator can fully take advantage of the outstanding of silicon optical properties, including excellent refractive index, good optical transmission, low resonance loss, anti-interference, biocompatibility and low cost. Furthermore, light confinement mode is achieved through beam shaping in transmission and reflection. Significantly, biofunctionalization is achievable through biomarkers immobilization on the outermost layer of the metasurface. These properties show a new engineering direction that fits and promotes HSA detection using AIE biosensors. Through searching the current studies of this, it is also the first work regarding AIE FL biosensors using metasurface platform for HSA detection.

In the chapter of AIE biosensor for HSA detection, a novel AIE biosensor TC426 is first reported for HSA detection. It was obtained through a two-step synthesis. 4-(diethylamino) salicylaldehyde and 1,3-indandione underwent Knoevenagel condensation to yield the intermediate compound 2. The hydroxyl group in compound 2 was then alkylated with 1,3-propanesultone to introduce a sodium sulfonate group to form the FL molecule TC426. This periphery-charged groups facilitate TC426 to dissolve in water. The spectral properties of TC426 exhibit modest variations when tested with different solvents and its maximum absorption wavelength range is 494-512 nm. The fluorescence emission spectra of TC426 remains relatively constant when stimulated at the wavelength of maximal absorption, with all peak wavelengths being clustered around 535 nm. The QY of TC426 shows typical solvent polarity dependence. When the molecule is dissolved in PBS buffer, TC426 does not emit under excitation at 488 nm. However, when it aggregates into large particles or is in a solid state, it becomes highly fluorescent. In the quantitative detection, a strong fluorescence signal

was detected at 550 nm after the addition of HSA, and the fluorescence intensity quickly reached equilibrium and stabilized within 60 min. There was a good positive linear correlation between the fluorescence intensity and the HSA concentration in the dynamic range of 0-1000 mg/L, R2 = 0.9954. When the HSA concentration reached the maximum, the FL intensity at 550 nm increased by about 450 times. LOD of TC426 was as low as 0.253 mg/L based on measurements. The fluorescence response of TC426 remains stable over the pH range 5.0–7.0. In selectivity studies, no changes in fluorescence intensity were observed in TC426 caused by any other substances except for a slight reaction with BSA. Even in the presence of urine interferences, TC426 remained an excellent stability. The sensing mechanism demonstrated that the binding ratio between TC426 and HSA is approximately 1 to 2, and this results prove that TC426 interacts with HSA in the form of monomers rather than aggregates. Moreover, protein denaturation experiments demonstrated that the sensing process was closely related to the tertiary and secondary structures of HSA. The fluorescence enhancement during HSA detection results from the movement of TC426 from the polar water environment to the low polarity cavity of HSA. Finally, the validation in the urine scenario showed a satisfactory recovery rate of 81.3–129.9%, with a standard deviation ranging from 1.5% to 10.7%, which shows that AIE biosensor TC426 can be applied to the detection of HSA in the actual microalbuminuria range.

In the chapter of AIE biosensor incorporating with hydrogel platform, this study concentrates on using hydrogels embedded with AIE biosensor TC426 to achieve HSA detection. As a three-dimensional flexible material, hydrogels are widely employed due to their non-toxicity, low cost, easily customizable structure & volume/shape changes, and good biocompatibility. The functional structure and high-water content of their cross-linked hydrophilic networks can be manipulated for potential applications such as biomarker detection, drug delivery, and shape support. Acrylamide-alginate (AAm + Alg) and carrageenan are both hydrogels that have been proven to have highly versatile physical and chemical properties. Their adhesive properties enable hydrophobic substances to be stably fixed inside through electrostatic interactions, covalent bonds, or physical interpenetration. They have the potential to serve as the engineering construction of fluorescent hydrogel platforms under this study. One current research branch is to introduce AIE units into hydrogel polymers to improve their fluorescence properties by utilizing hydrogels' surface adsorption, hydrophobic interactions, self-assembly, hydrogen bonding or other effects. The principle of hydrogel platform engineering is that most AIE molecules are hydrophobic organic molecules with non-planar propeller structures, which emit almost no fluorescence in their normal form, but emit bright light when aggregated. In the hydrophilic hydrogel matrix, the spontaneous aggregation of AIE molecules inhibits their intramolecular motion, thereby further amplifying the fluorescence effect. In addition, encapsulating AIE biosensors through hydrophilic cross-linking structures plays an important role in improving the environmental friendliness and biocompatibility in biomarker detection. However, there are also some disadvantages in hydrogel platform, such as the sealed structure of hydrogels forces the luminophore to react with biomarkers from the outside to the inside, thereby prolonging the

detection time. High swelling behaviour may promote light scattering and increase the internal structural gaps of hydrogels, resulting in signal attenuation and reduced detection sensitivity, while the diffusion dynamics are mainly passive and difficult to control. Improving these unfavourable factors is the primary goal of realizing the hydrogel platform. Vortex fluidic device (VFD) is a reported rotating system for liquid film processing. Physical/Chemical processes can be accurately controlled by applying the mechanical energy produced by a VFD to reactions. The mechanical energy generated by a VFD can be effectively applied to reactions to precisely control physical/chemical processes. The VFD's centrifugal or shear forces have a number of significant impacts, including accelerating reaction kinetics, altering chemical reactivity, and facilitating fast fluid exchange. VFD has been used to regulate the surface morphology of fluorescent hydrogels. The results show that physically cross-linked hydrogels prepared using VFD technology have excellent fluorescence and self-adhesion properties as well as adjustable morphology. VFD enables intensive micro-mixing of various components, resulting in improved spatial distribution and a more uniform final product. In view of VFD characteristics, this study employed hydrogel platform for engineering design in the expectation of using VFD technology to accelerate the fluid dynamics inside and outside the membrane in real time, while allowing AIE biosensors to be uniformly micromixed under shear force, thereby reducing detection time, enhancing fluorescence signals, or forming an active diffusion control system. Specifically, this study used AIE FL biosensors in conjunction with two hydrogel platforms, carrageenan and acrylamide-alginate (AAm + Alg) respectively, to detect HSA in real time and evaluate their characteristics under VFD regulation. The hydrogel of AAm+Alg with strong stability and mechanical properties was synthesized using a two-step method to form dual chemical/physical networks through chemical cross-linking, which was compatible with many bio-substances. The hydrogel of carrageenan was a natural polymer that was prepared normally. It was first observed that colour gradient became a more pronounced indicator for AIE hydrogels. AAm-Alg and Carrageenan appeared orange-red initially and transferred into pink by HSA absorption under VFD acceleration at 2 min node and 4 min node, respectively. the intensity change of the hydrogels was positively correlated with their colour change. The orange-red of TC426 is due to the sodium sulfonate group in its chemical structure, while when the albumin macromolecules encounter TC426, a pink transition occurs due to the movement of the AIE molecules toward the Sudlow sites of HSA and the expansion of the size of the coaggregates. For FL kinetics, TC426 remained non-fluorescent in AAm-Alg and carrageenan under the normal conditions, but introduction of HSA triggered green fluorescence, with immediate emission peaks at 530 and 545 nm. When HSA was varied from 0 to 1000 mg/L, ligand binding of TC426-HSA remained concentration-dependent, also showing proportional intensity in both hydrogels. The fluorescence behaviours under VFD modulation showed that fluorescence of AAm-Alg rose steadily in HSA solution and reached a peak value at 10 minutes (8.47 times), while it only took two minutes (11.57 times) under the intervention of VFD that accelerated fluid exchange. Similarly, intensity in Carrageenan under normal flow reached the maximum (11.83 times) at 10 minutes, but it only took 4 minutes under VFD processing (12.32 times).

Additionally, the experiments of FL stability illustrated that the fluorescence responses of the two AIE hydrogels still retained 92.32% (AAm-Alg) and 95.84% (carrageenan) of their maximum peaks after 3h. Comparing the two different hydrogels, the overall fluorescence enhancement performance of carrageenan was better than that of AAm-Alg, and the corresponding fluorescence enhancement efficiency of carrageenan was 39.66% (normal immersion) and 5.57% (using VFD) higher than that of AAm-Alg. Correspondingly, AAm-Alg-TC426 finally stabilized at an expansion rate of about 110%, and its increase was about 1.8 times that of carrageenan-TC426 (about 60%). Compared with the original level, the use of VFD technology can increase the fluorescence response of AAm-Alg by 5.27 times and that of carrageenan by 1.71 times. In addition, the dynamic range of both AIE hydrogels is linear with/without VFD. For diffusion characterisation, the kinetics of diffusion belonged to non-Fickian behaviours ($0.5 < n < 1$) in AAm–Alg. In this case, the swelling rate was greater than the hydrogel collapse rate, implying that polymer relaxation was the rate-limiting step in the TC426-HSA delivery system. On the contrary, carrageenan was Less-Fickian ($n < 0.45$), and it dominated the release process of HSA (the water permeation rate was much lower than the polymer chain relaxation rate). The above differences were all related to the microstructures of the two hydrogels. The surface and cross section of AAm-Alg had a typical honeycomb porous structure, and the relatively loose network provided sufficient adhesion area for TC426 molecules and allowed the aqueous solution of albumin to move freely in the internal structure at a faster diffusion rate. The multilayer planar structure is a characteristic of the surface and cross section of carrageenan. The flow of water infiltration is mainly singular and along the cross-sectional direction. Therefore, the potential mechanism could be described that HSA reacted with the AIE biosensors embedded in the hydrogel platform through diffusion movement from outside to inside. The porous network of AAm-Alg acted as a fast flow platform, enabling the albumin solution to diffuse in multiple dimensions simultaneously and further releasing the constraints of TC426 within the microstructure. Non-Fickian diffusion made the relaxation rate of the AAm–Alg chain become the rate-limiting step of the delivery system, which was difficult to quantify in the hydrogel model. Moreover, the difference was that the lamellar structure of carrageenan only provided two-dimensional movement, while its effect on diffusion exhibited Less-Fickian behavior, making the permeation rate of the HSA solution dominant transport process, thereby regulating the delivery system dominated by passive diffusion. More importantly, in both models, the introduction of VFD could artificially increase the diffusion rate, and the fluorescence intensity was greatly enhanced as the contact opportunities between HSA and TC426 increase. In contrast, the diffusion-controlled delivery system of carrageenan was able to increase the diffusion rate while keeping the dynamic loss unchanged. The VFD acceleration process transformed passive diffusion into active diffusion without changing the original diffusion transport, which is a new control strategy for hydrogel research. Afterwards, the recovery rate using the colorimetric device was 86%, successfully verifying that the AIE hydrogels could be identified with color changes within the microalbumin range after VFD treatment. Finally, the schematic of AIE biosensor incorporating with hydrogel platform is summarized as illustrated in **Figure 39.**
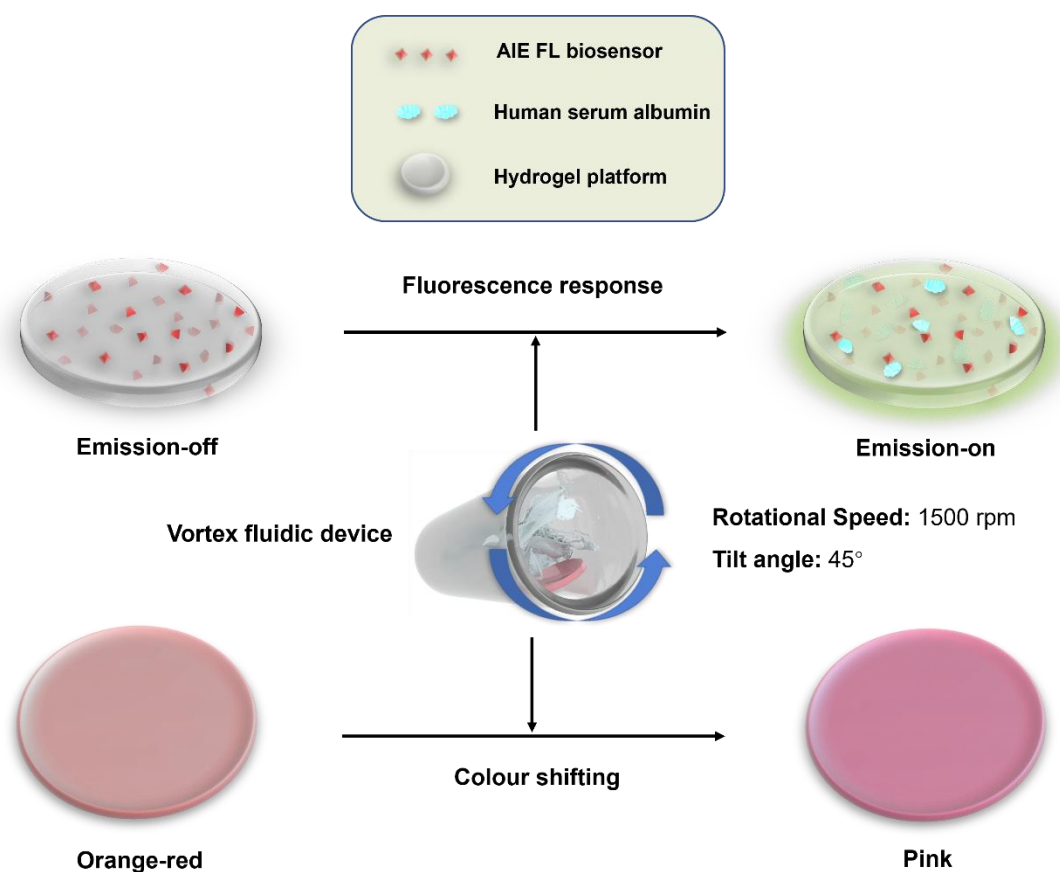
Figure 39 Schematic of AIE FL biosensor incorporating with hydrogel platform for HSA detection.

In the chapter of AIE biosensor incorporating with metasurface platform, this study focuses on using the conjugates of HSA and AIE biosensors immobilized on nanostructure to observe FL behaviours. First of all, two-dimensional metamaterials known as metasurfaces are made of metal/dielectric periodic or non-periodic subwavelength structures. They demonstrate the capacity to concentrate, inhibit, absorb, scatter or guide waves by creating nanoscale unit cells that enable dynamic manipulation in the fields of optics, mechanics, electronics, etc. One of the unique features is its powerful wavefront manipulation, which allows for the control and adjustment of the cell's diversified patterns, geometries, and sizes. Metasurfaces also provide light confinement modes and localized surface plasmon (LSP) electromagnetic (EM) near-fields to modify the incident light's properties, improving the target molecules' light-matter interaction. At present, the metasurface platform has been successfully applied in biomarker detection. Fluorescent biosensors based on all-dielectric metasurfaces have already detected a variety of biomarkers, such as IgG, cancer PSA and CEA, and cfDNA, because the metasurfaces made of Si or SOI have the tunable adaptability of their optical properties and provide high-quality resonance. When the target analyte can be immobilized or coated on a silicon nanoscale matrix, the high refractive index of silicon is conducive to light modulation, resulting in deep light-matter interactions, which are reflected in the analytical peaks. these reported cases demonstrate the superior capabilities of metasurfaces in nanophotonic

detection of biomarkers. Nevertheless, individual differences in albumin excretion, impurities in urine, autofluorescence, interference from other urinary components, etc. will further induce undesirable FL enhancement or quenching. It is inevitable that the HSA content will be overestimated or underestimated, resulting in inaccurate readings, especially at very low levels. When the HSA concentration is low, the optical signal is also difficult to detect due to the small light absorption amplitude, which requires improving the detection accuracy by increasing sensitivity or reducing background noise. To address these issues of HSA measurement using AIE biosensors in human urine scenarios and evaluate the performance of metasurfaces for biomarker detection in FL sensing, this study first reports the integration of a nanophotonic all-dielectric metasurface platform with an AIE biosensor TPE-4TA to achieve improved detection of HSA. This platform consisted of a pair of self-absorbed metasurface substrates and a PDMS microfluidic chip (thickness = 2 mm). The metasurface substrate was fabricated using electron beam lithography and dry etching on an SOI wafer, and the microfluidic chip had six independent microfluidic channels for inflow and outflow. The flow rate could be controlled by a rotary pump. Meanwhile, the metasurface substrate was a three-layer planar structure (from top to bottom) consisting of a silicon nanopillar array (diameter 220 nm, height 200 nm, period 300 nm), a 375 nm SiO_2 layer, and a 675μm base Si wafer. Next, the optical structure design of the metasurface was applied to the AIE biosensor TPE-4TA to achieve FL signal enhancement at green wavelengths around 530 nm. A 30% reflection band was generated at the excitation wavelength of 360 nm for TPE-4TA, while the reflection response at 530 nm reached 70% with a single sharp peak. Importantly, the main features of the reflection peaks at 360 and 530 nm related to the FL enhancement effect in this study were reproduced in the measured reflection spectrum. Furthermore, the resonant electromagnetic field distribution showed that the intensity of the electric and magnetic fields excited at 360 nm was enhanced to 54.9 and 6.1, respectively. These electromagnetic fields were distributed darker inside the Si nanocolumns, indicating that the incident light was absorbed by the Si nanocolumns. However, the electric field at the outermost surface was highly enhanced at the sidewalls of the Si nanocolumns without significantly weakening at the top of the Si nanocolumns. At a wavelength of 530 nm, the electric field strength decreased slightly at 41.9, but this strong electric field distribution shifted toward the upper part of the nanocolumns, where most FL-labelled HSA analytes tended to be immobilized. Notably, the magnetic field inside the Si nanocolumns was significantly enhanced to 115.3, indicating that this resonance was a magnetic mode. The enhanced resonant electromagnetic field was beneficial to the transmission of electric dipoles in FL molecules, thereby helping to enhance the fluorescence emission on the outermost surface of the silicon nanocolumns. The detection strategy was to achieve multi-level immobilization on the metasurface using a biofunctionalization scheme of binding molecules, labelled antibodies, and target analytes. First, a uniform and stable physical adsorption layer was directly formed through the interaction between streptavidin and the silica shell of the nanocolumns. Next, the HSA antibody labelled with biotin bound to Cys-SA through a fast and strong non-covalent protein-ligand interaction, and the formed composite biolayer provided a good high-density binding platform for HSA. In

addition, when the tetrazolate nitrogens in TPE-4TA bound to the polar dominant contact lysine residue (Lys) in the HSA binding conformation through hydrogen bonding and electrostatic interactions, the induced intramolecular motion restriction effect made HSA emissive. Subsequently, the pre-binding products of HSA and TPE-4TA could be continuously captured by antibody-antigen reactions. The experiments of binding affinities proved that 95.7% of the binding response measured by TPE-4TA was 24 times higher than the theoretical estimate, in the meanwhile one molecule of Cys-SA, Biotin-HSA Ab, and the conjugates of HSA and TPE-4TA were located on an average square surface area of 4.61 × 4.61 nm^2, 8.20 × 8.20 nm^2, and 19.9 × 19.9 nm^2, respectively, indicating that this multi-level immobilization strategy was feasible and could also be effectively applied to this platform. Fluorescence kinetic studies under the metasurface platform not only showed excellent photostability within 2 h, but also demonstrated that the FL intensity was positively correlated with the HSA concentration. The FL enhancement in the range of trace albumin was divided into two stages: a sharp stage (0 to 20 μg mL^{-1}) and a slow stage (20 to 160 μg mL^{-1}). The slowing trend indicates that the binding capacity of Biotin-HSA Ab is approaching its maximum limit. The metasurface platform is still ultrasensitive to traces of HSA (< 20 μg mL^{-1}), and the FL signal rises rapidly to 82% of the maximum response when the HSA content jumps to 20 μg mL^{-1}. In order to further explore the contribution of the metasurface platform to FL amplification, two other platforms (microplate platform and microfluidic platform) were established for horizontal comparison. The results showed that 39% and 136% FL enhancement of HSA detection was observed on the microplate platform and microfluidic platform, respectively. However, in the light confinement mode of the metasurface platform, the emission FL enhancement was as high as 1001%. By comparing the three platforms, the FL signals of the metasurface platform and the microfluidic platform were 7.93 times and 1.70 times stronger than those of the microplate platform, respectively. Obviously, the FL regulation of the metasurface is better than that of the other two platforms. On this basis, the actual evaluation of the three platforms in human urine applications was also studied. The validation of the commercial kit showed that the HSA level in the urine sample was 45.8 μg mL^{-1}, which can be independently calculated by referring to the standard curves established by the three platforms, which are 40.7, 41.9 and 43.8 μg mL^{-1}, respectively, with recoveries of 88.9%, 91.5% and 95.6%, respectively. The detection limits of the microplate, microfluidics and metasurface platforms were 300 ng mL^{-1}, 150 ng mL^{-1} and 18.75 ng mL^{-1}, respectively, and the final sensitivity level was expressed as: metasurface>microfluidics>microplate. The metasurface platform could effectively amplify the FL signal of extremely low concentration HSA in the human urine environment. Even if the urine sample was diluted 2560 times, the FL retention rate can still be detected, which fully demonstrates that the silicon nanocolumn matrix that could fix HSA is the primary reason for the FL enhancement effect. The mechanism of enhanced HSA detection by the metasurface platform could be explained in two aspects. Firstly, the extremely small size of the microfluidic channels further compressed the range of fluorescence activity along the height direction, allowing camera to obtain focused fluorescence images. Secondly, Si nanocolumns allowed fluorescent molecules to be

stacked in a very small area in a non-uniform manner and locally enriched, thereby enhancing the fluorescence output. In particular, the enhancement effect of the resonant electromagnetic field further amplified the fluorescence emission of HSA+TPE-4TA from the outermost surface of the Si nanocolumns through multi-level immobilization. In summary, AIE biosensors combined with the metasurface platform can effectively achieve fluorescence enhancement in HSA detection. The combination of AIE biosensor and metasurface platforms opens up a new path for engineering design in practical scenarios. The schematic of AIE biosensor incorporating with metasurface platform is summarized as illustrated in **Figure 40.**
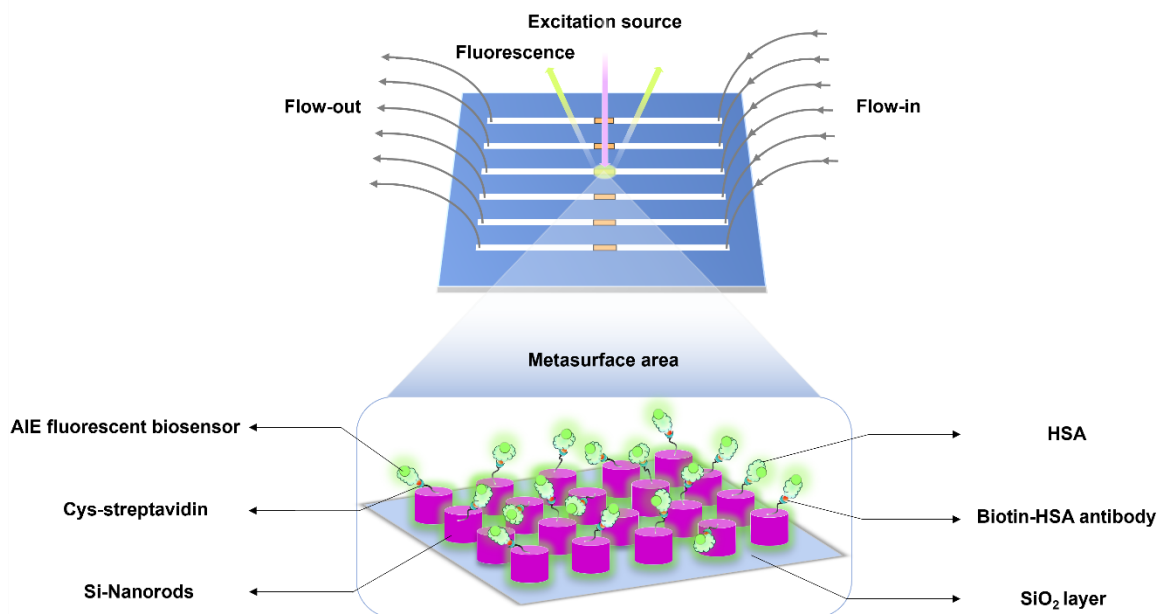
Figure 40 Schematic of AIE biosensor incorporating with metasurface platform.

In the chapter of future prospects, it extends to 2 parts: the improvements of AIE biosensors and the development of new biomarkers for CKD. The first part mentions about positive impacts of inorganic-organic hybridization in AIE biosensors. Non-protein-inorganic hybrid approaches can provide a spatially constrained framework for AIE molecules. Therefore, their fluorescence efficiency will be greatly enhanced, thereby further improving the sensitivity of HSA detection. According to the currently reported research on inorganic-organic hybrid materials, GO, SiO_2 and metal ions are the three most promising inorganic candidate materials for AIE biosensors. The two-dimensional structure surface of GO can form strong non-covalent interactions with adsorbed biomolecules through π-π interactions, electrostatic forces, or hydrogen bonds, providing a chemically tuneable platform for biological binding. Similarly, SiO_2 has good biocompatibility and easy surface modification. AIE biosensors can be directly coated with a silica shell through covalent chemical bonds. For metal ions, good stability and effective sensitization facilitate the formation of a rigid matrix on which AIE biosensors can be immobilized via covalent bonds. This combination of AIE

biosensors + one of inorganic parts is likely to significantly improve detection performance through the synergistic effect of the two different components. The introduction of VFD during this process can further adjust the morphology of AIE molecules, thus promoting the FL effect. The second part discusses on three new biomarkers for CKD: adiponectin, L-FABP and NAG. Clinical data confirm that their content is positively correlated with CKD. However, due to the insufficient number of samples, long-term observation and research are still needed. However, selecting multiple CKD biomarkers as references for multi-channel verification can further improve the accuracy of CKD diagnosis, which requires the simultaneous development of multiple AIE biosensors that can detect targeted biomarkers. During this process, the high-sensitivity detection of the metasurface platform can reduce the difficulty of AIE biosensors in detecting low-abundance proteins.

In a nutshell, this research proposes two feasible engineering designs of AIE biosensors and the results show significant improvements and provides a promising development in biomarkers detection for screening and monitoring CKD.

PUBLICATION AND AWARD LIST

In this chapter, the other research work and honour I have been involved are listed here during my PhD period.

Publications:

- In Situ Monitored Vortex Fluidic-Mediated Protein Refolding/Unfolding Using an Aggregation-Induced Emission Bioprobe (**doi.org/10.3390/molecules26144273**). This article is published on "*Molecules*, 2021, *26*(14), 4273 ". Qi Hu and Haozhen Hu are the first authors, while Xinyi Zhang, Kyle Fan, Yuning Hong and Colin L. Raston are co-authors, and Youhong Tang is the correspondent author.

- Aggregation-induced emission biomarkers for early detection of orthopaedic implant failure (**doi.org/10.1002/agt2.645**). This article is published on "*Aggregate*, 2024, e645". Javad Tavakoli is the first author, while Qi Hu and Joanne L. Tipper are co-authors, and Javad Tavakoli and Youhong Tang are the correspondent authors.

- Developing a fluorescent sensing based portable medical open-platform - a case study for albuminuria measurement in chronic kidney disease screening and monitoring (**doi.org/10.1016/j.sbsr.2022.100504**). This article is published on "*Sensing and Bio-Sensing Research,* 2022, *37, 100504*". Anh Tran Tam Pham is the first author, while Damian Tohl, Angus Wallace, Qi Hu, Jordan Li and Karen J. Reynolds are co-authors, and Youhong Tang is the correspondent author.

- Portable Colorimetric Device with Commercial Microplates for Quantitative Detection of Urine Biomarkers: Design, Development, and Clinical Evaluation (**doi.org/10.3390/bios12090723**). This article is published on "*Biosensors,* 2022, *12(9), 723*". Anh Tran Tam Pham is the first author, while Damian Tohl, Qi Hu, Jordan Li and Karen J. Reynolds are co-authors, and Youhong Tang is the correspondent author.

- Synthesis of a β-Arylethenesulfonyl Fluoride-Functionalized AIEgen for Activity-Based Urinary Trypsin Detection (**doi.org/10.1021/acsabm.2c00513**). This article is published on "*ACS Applied Bio Materials,* 2022*, 5(9), 4321-4326*". Marie-Claire Giel is the first author, while Shouxiang Zhang, Qi Hu, Dan Ding and Youhong Tang are co-authors, and Yuning Hong is the correspondent author.

Awards:

- *WILEY*: Top Cited Article 2021-2022 for the article of Detection of Urinary Albumin Using a "Turn-on" Fluorescent Probe with Aggregation-Induced Emission Characteristics.

- Journal cover of issues for *Materials Chemistry Frontiers*: ISSN 2052–1537 CODEN MCFAC5 6(15) 2003–2144 (2022).

APPENDICES

AIE fluorescent biosensor for HSA detection
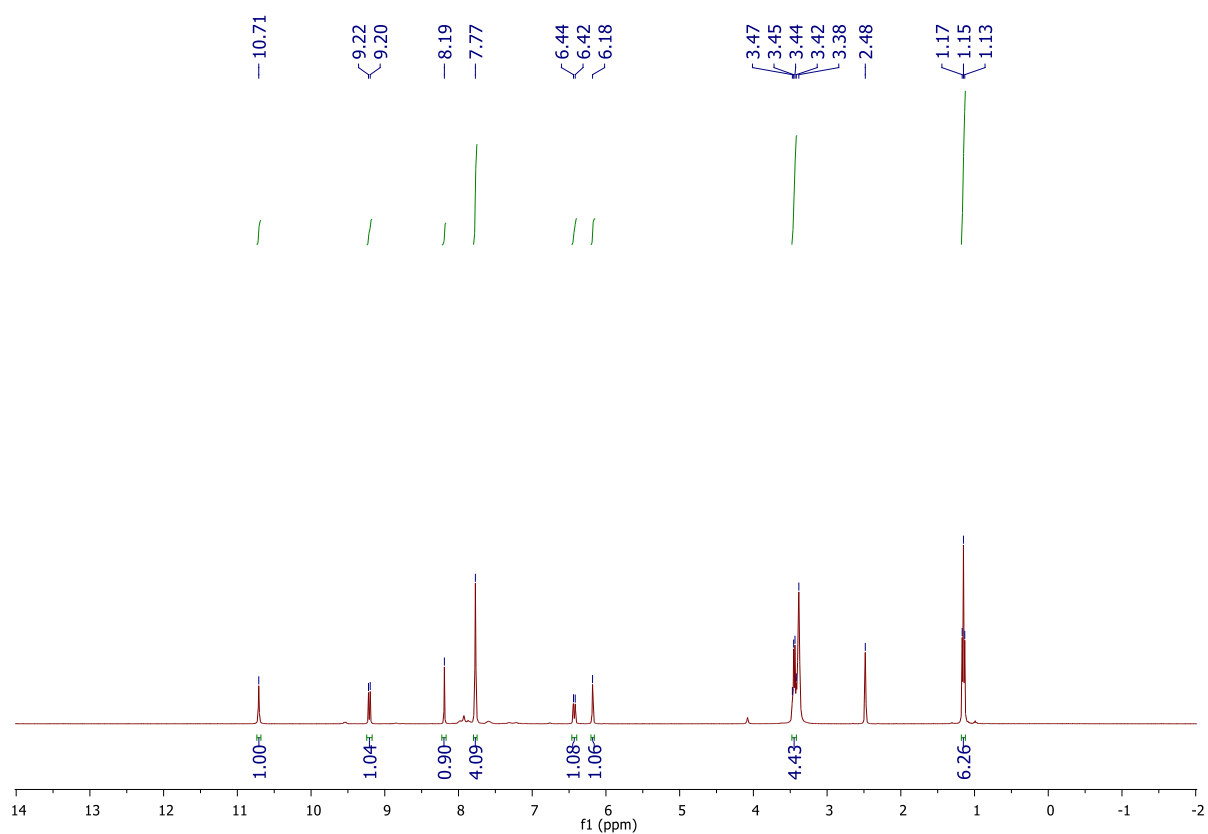
Figure S1 ^{1}H NMR in DMSO for precursor compound 2.
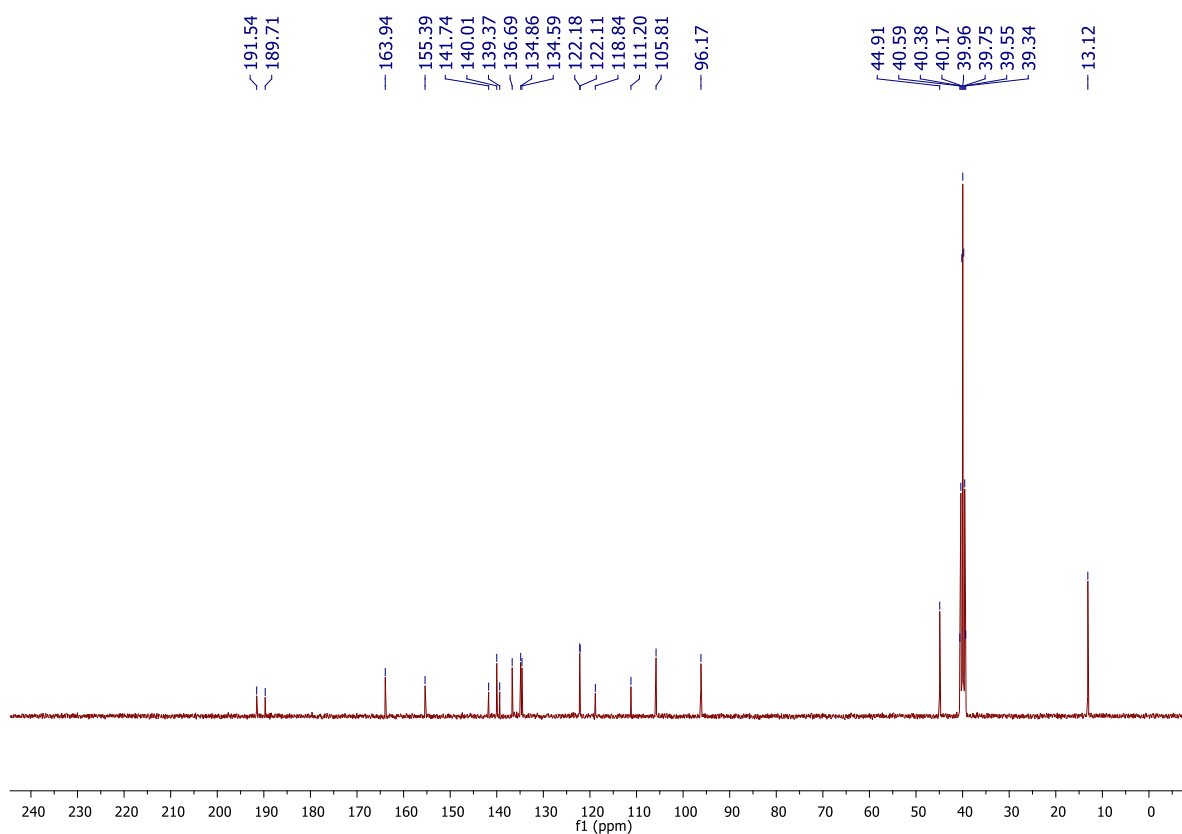
Figure S2 ^{13}C NMR in DMSO for precursor compound 2.
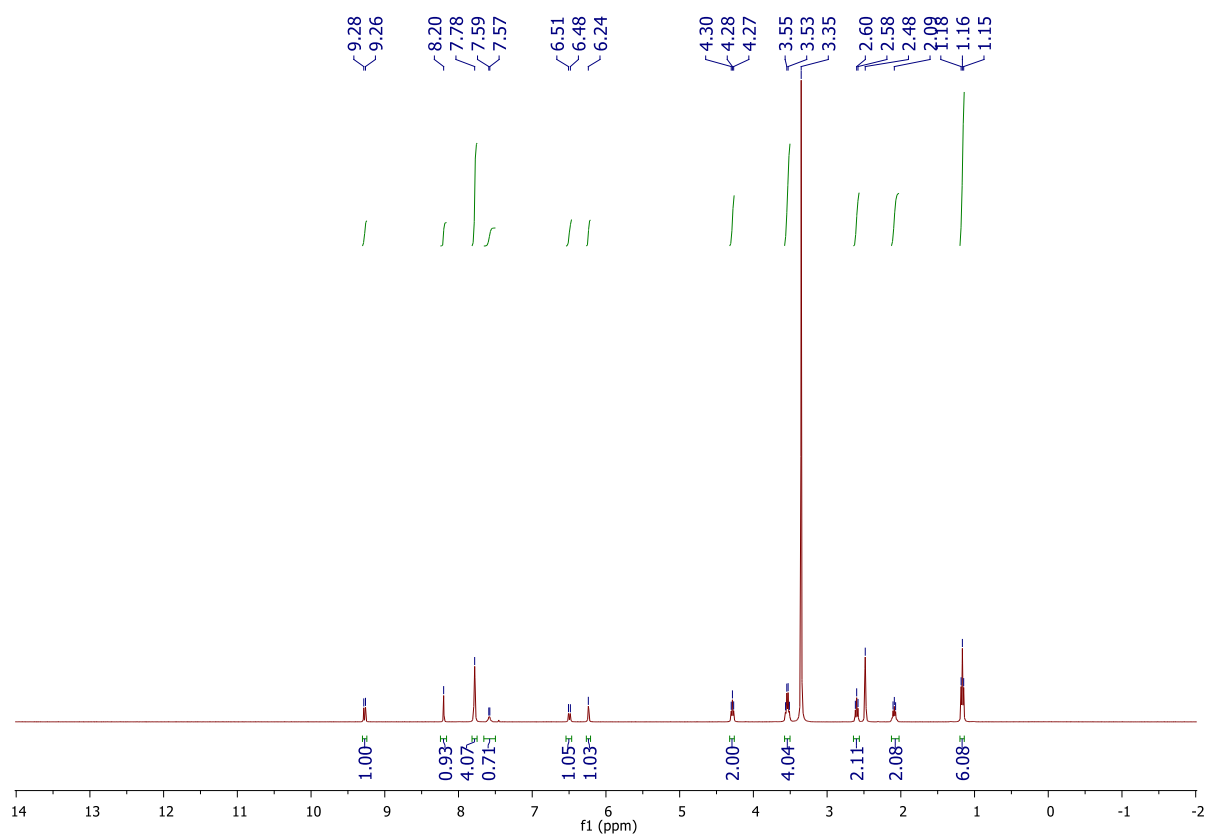
Figure S3 ^{1}H NMR in DMSO for TC426.

118

240 230 220 210 200 190 180 170 160 150 140 130 120 110 100 90 80 70 60 50 40 30 20 10 0
f1 (ppm)

191.34 189.61 163.61 155.57 141.76 139.56 136.99 134.91 122.56 122.25 122.17 120.80 119.42 111.69 105.65 93.96 67.80 44.97 40.59 40.38 40.17 39.96 39.75 39.54 35.48 25.34 13.16
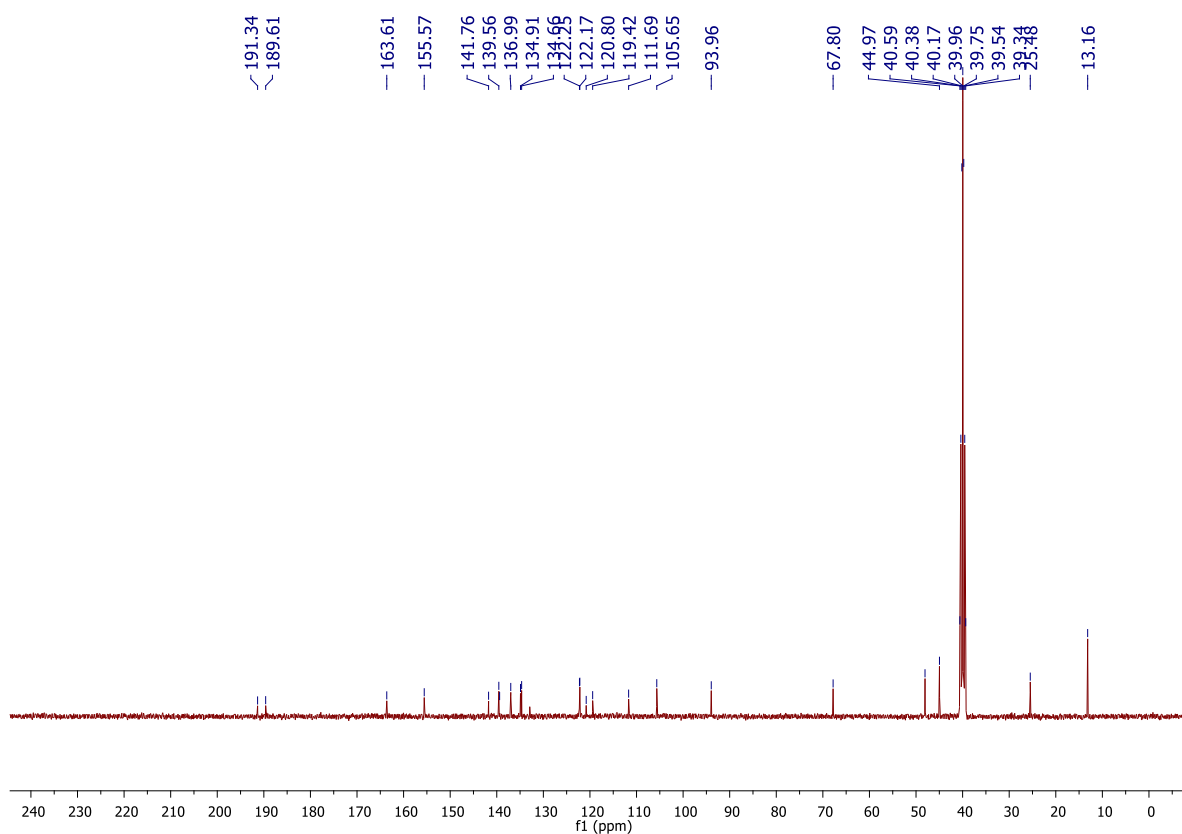
Figure S4 ^{13}C NMR in DMSO for TC426.
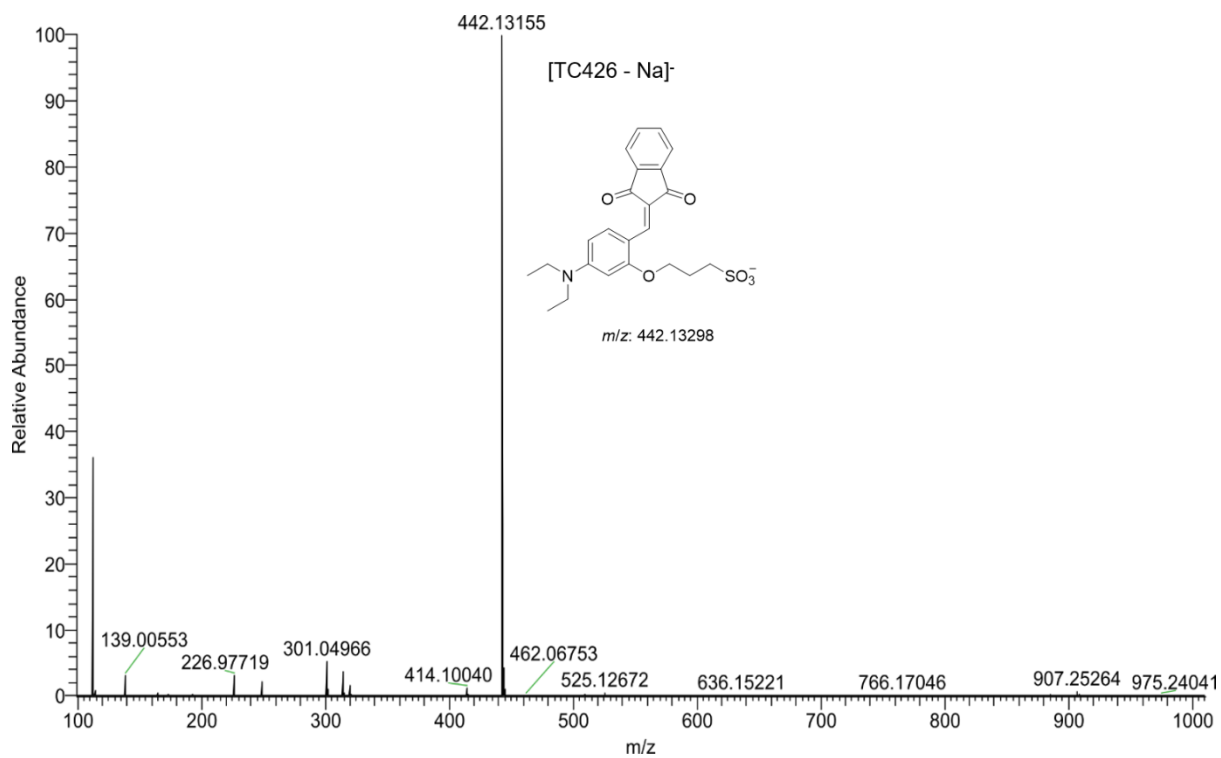
Figure S5 HRMS spectrum of compound TC426.

119
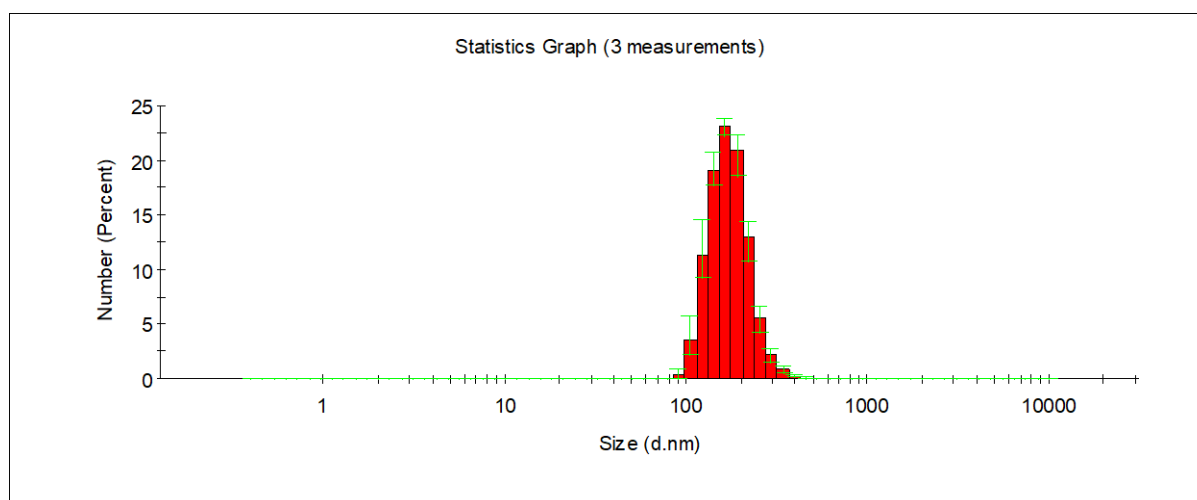
Figure S6 DLS in toluene.
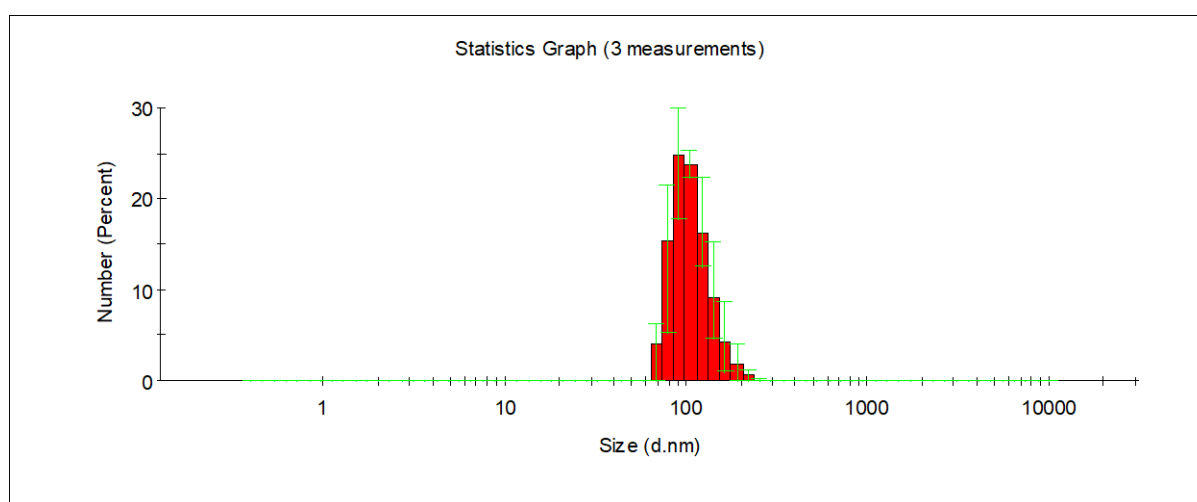
Figure S7 DLS in chloroform.

Solvent	λ_{abs} (nm)	λ_{em} (nm)	ΦF (%) [a]	Lippert-Mataga polarity [c]
Toluene	496	635	0.86	0.016
1,4-Dioxane	493	526	0.69	0.021
Chloroform	502	530, 638	1.26	0.148
THF	495	524	0.31	0.208

DMSO	505	545	0.34	0.263
Isopropanol	501	531	0.42	0.272
Acetone	497	530	0.23	0.284
Ethanol	499	546	0.21	0.289
Acetonitrile	496	525	0.16	0.305
Methanol	500	524	0.12	0.308
Water	513	– [b]	0.05	0.320

Table S1 Photophysical properties of probe TC426 in different solvents. [a] Relative fluorescence quantum yields ΦF were measured using fluorescein in 0.01 M NaOH aqueous solution (ΦF = 90%) as the standard. [b] The fluorescence intensity is too weak to identify its peak wavelength. [c] The Lippert-Mataga polarity parameters were calculated from the Lippert-Mataga solvent polarity functions.
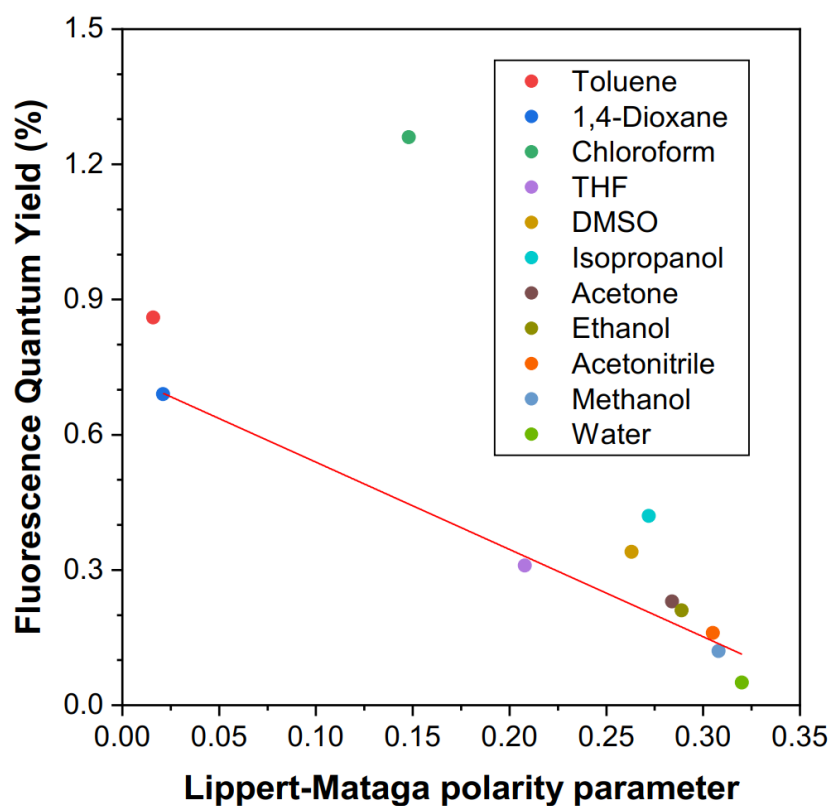
Figure S8 Plot of fluorescence quantum yield of probe TC426 as a function of solvent polarity measured by Lippert-Mataga polarity parameter.
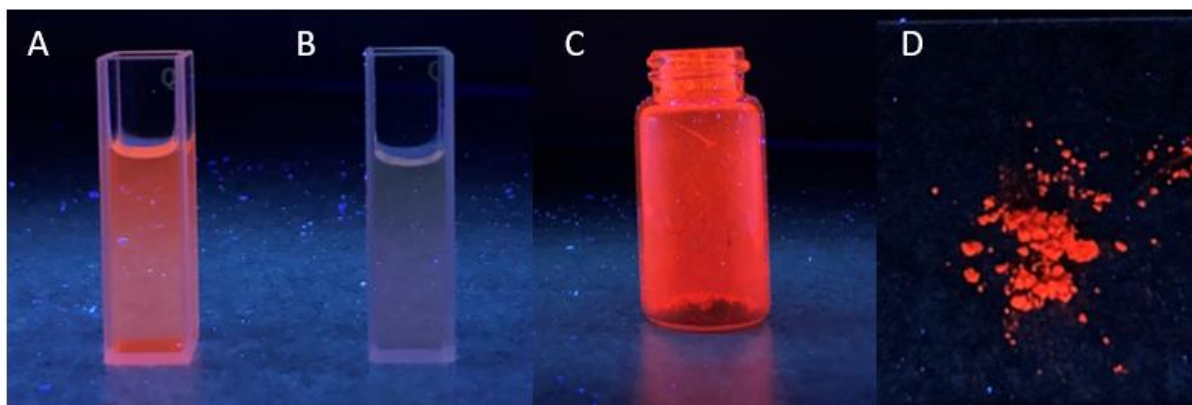
Figure S9 Fluorescent images of compound TC426 in different states including (A) aggregates in toluene, (B) solution in DMSO, (C) powder in glass vial, and (D) powder on glass slide. The images were taken under a 365 nm handheld UV lamp. Concentration of TC426 is 10 µM for both sample (A) and (B).
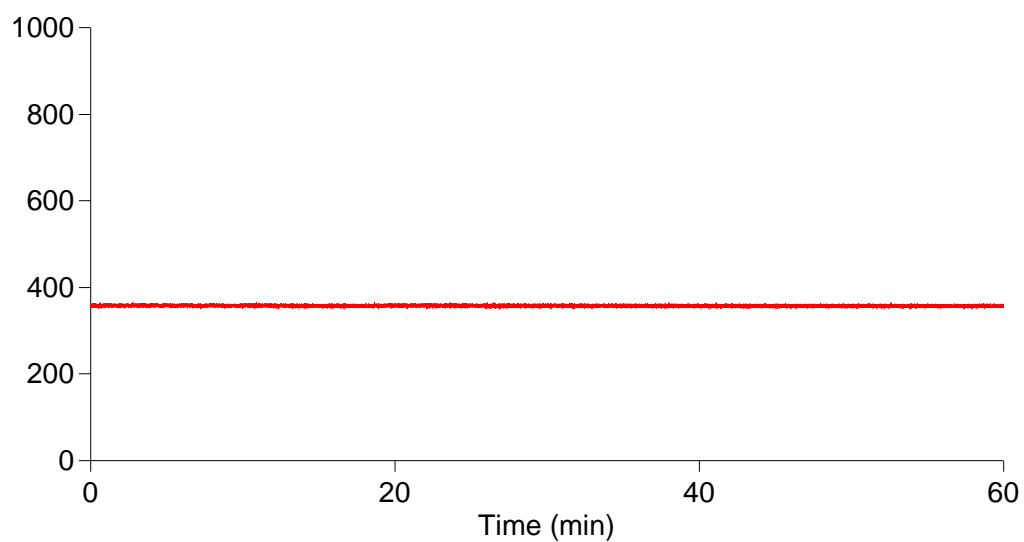
Figure S10 Reaction time in real urine sample: an equal amount of 1000 mg/L albumin solution and TC426 are mixed evenly. [TC426] = 10 μM, λex = 480 nm, and λem = 545 nm.
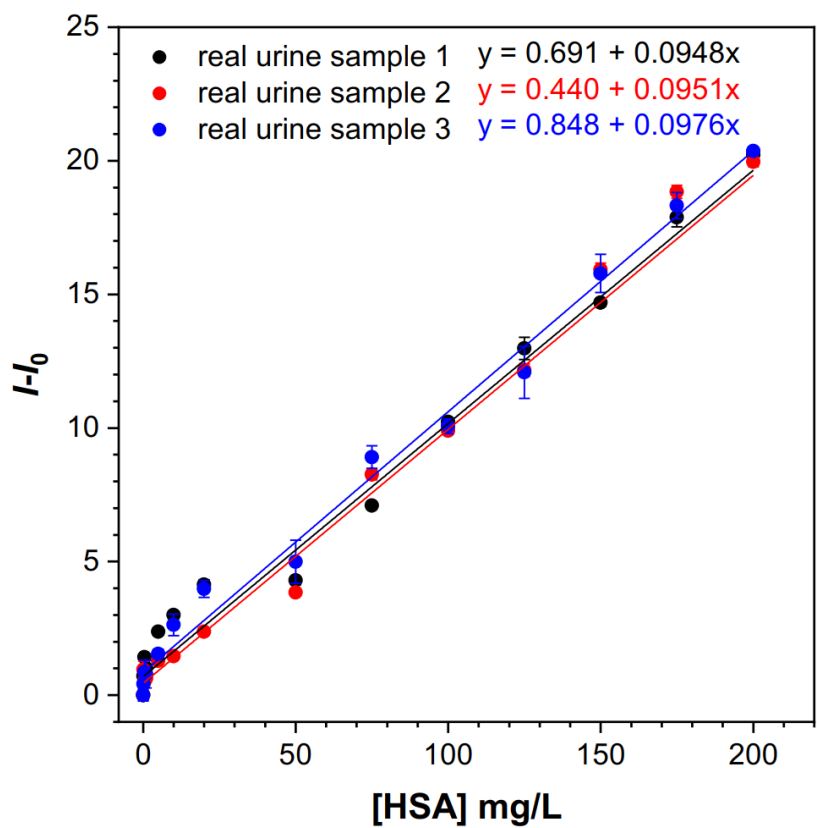
Figure S11 Calibration curves of probe TC426 measured in real human urine samples collected from three individuals.

AIE FL biosensor incorporating with hydrogel platform
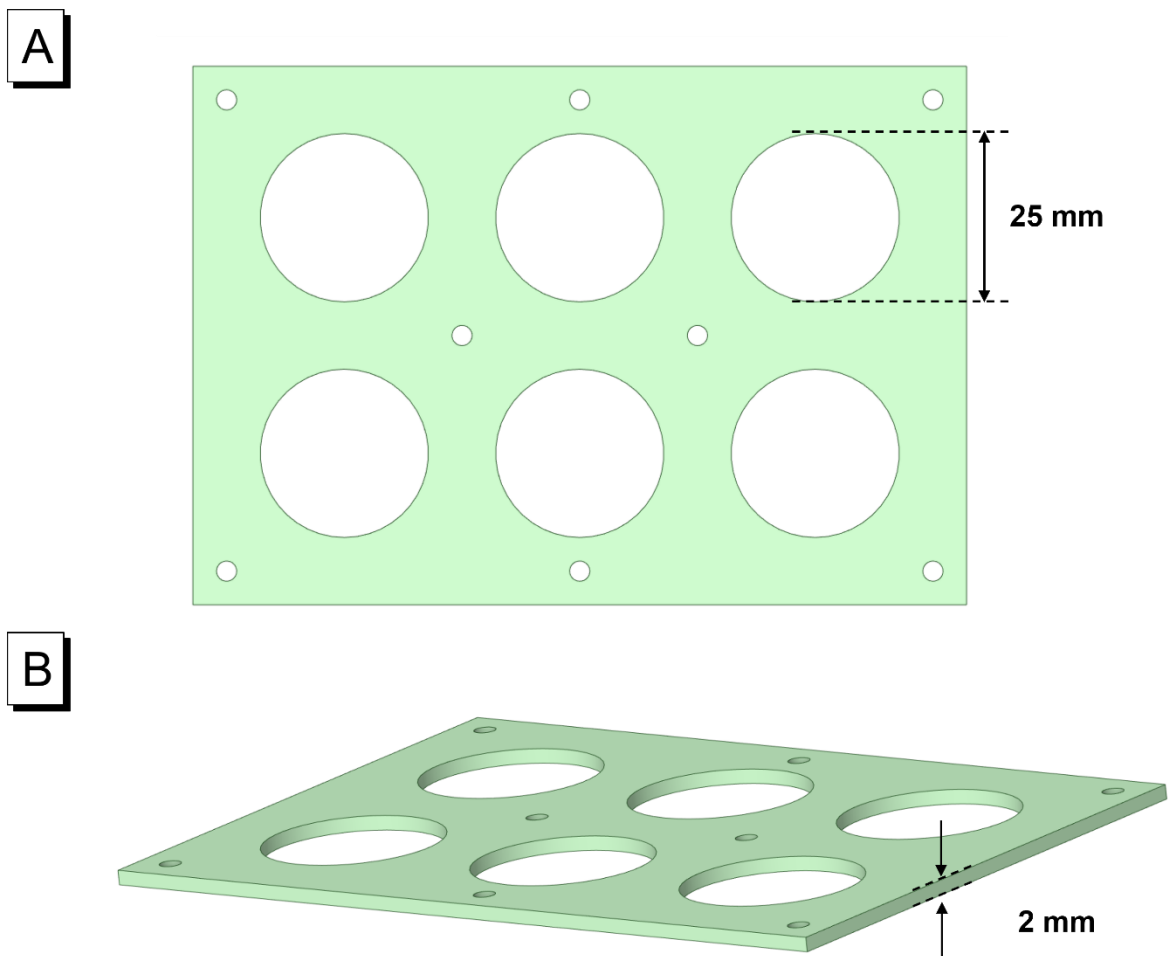
Figure S12 The mould of hydrogel film. (A) Template of flat design illustration and the diameter is 25 mm; (B) Template of spatial design illustration and thickness is 2 mm.

In panel A:

$Ln (F_{sp}) = 0.40335 * Ln(t) - 2.90379$ (VFD processing)

$Ln (F_{sp}) = 0.24679 * Ln(t) - 1.95043$ (Normal soaking)

In panel B:

$Ln (F_{sp}) = 0.91709 * Ln(t) - 4.62156$ (VFD processing)

$Ln (F_{sp}) = 0.76819 * Ln(t) - 4.43366$ (Normal soaking)
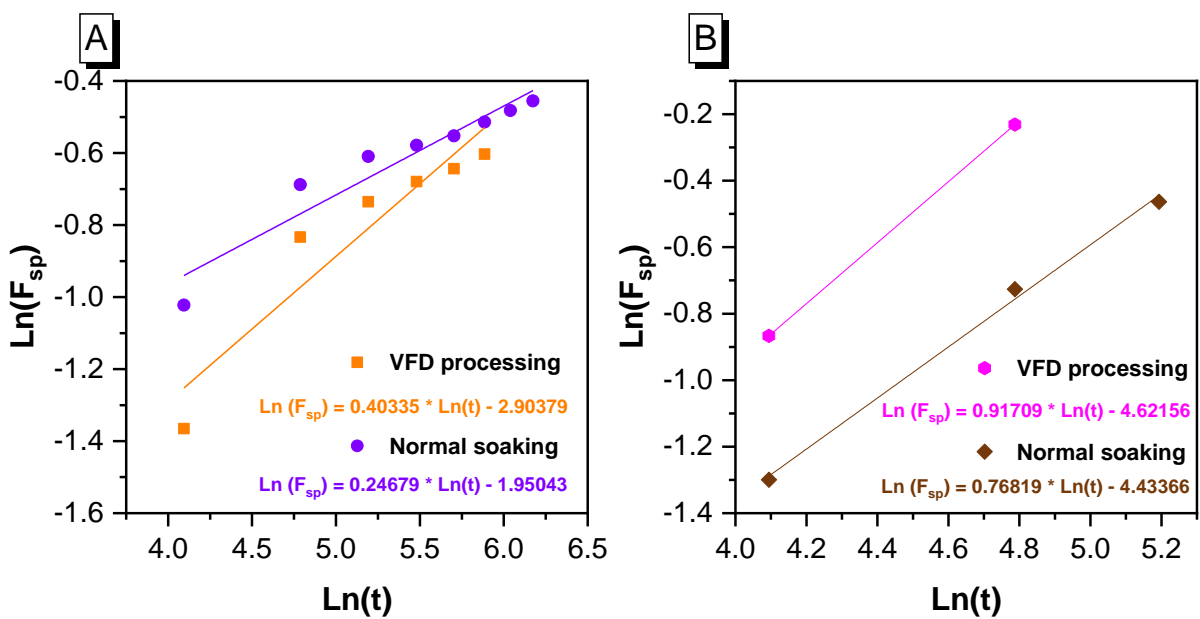
Figure S13 Change in the fraction of swelling power (F_{sp}) vs. time to identify the diffusion mechanism in normal soaking and VFD tests of (A) Carrageenan + TC426 film and (B) AAm + Alg + TC426 film.
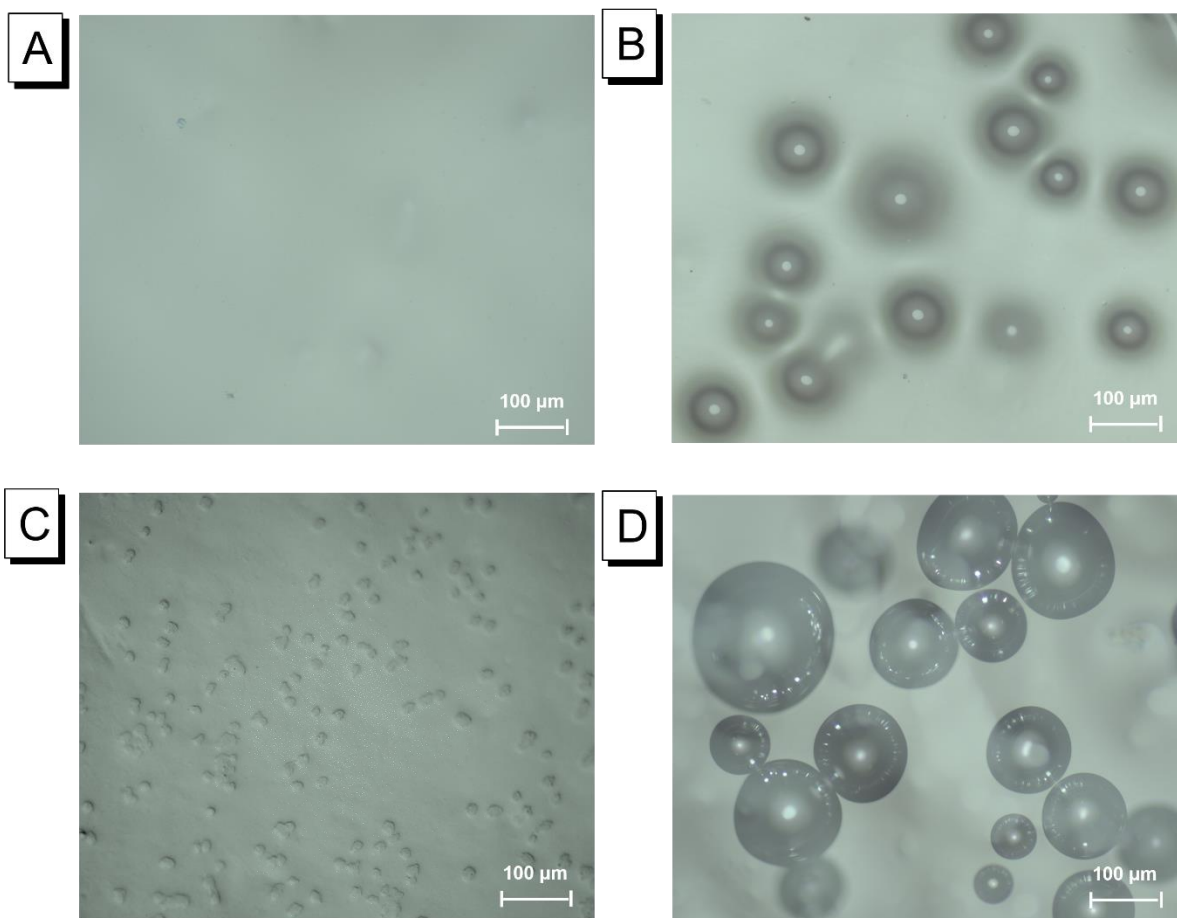
Figure S14 The images of optical microscopy in reflected light. (A) AAm + Alg hydrogel film only, 100 μm; (B) AAm + Alg hydrogel film + HSA, [HSA] = 2000 mg/L, 100 μm; (C) AAm + Alg hydrogel film + TC426, [TC426] = 10μM, 100 μm; (D) AAm + Alg hydrogel film + HSA + TC426, [HSA] = 2000 mg/L and [TC426] = 10μM, 100 μm.
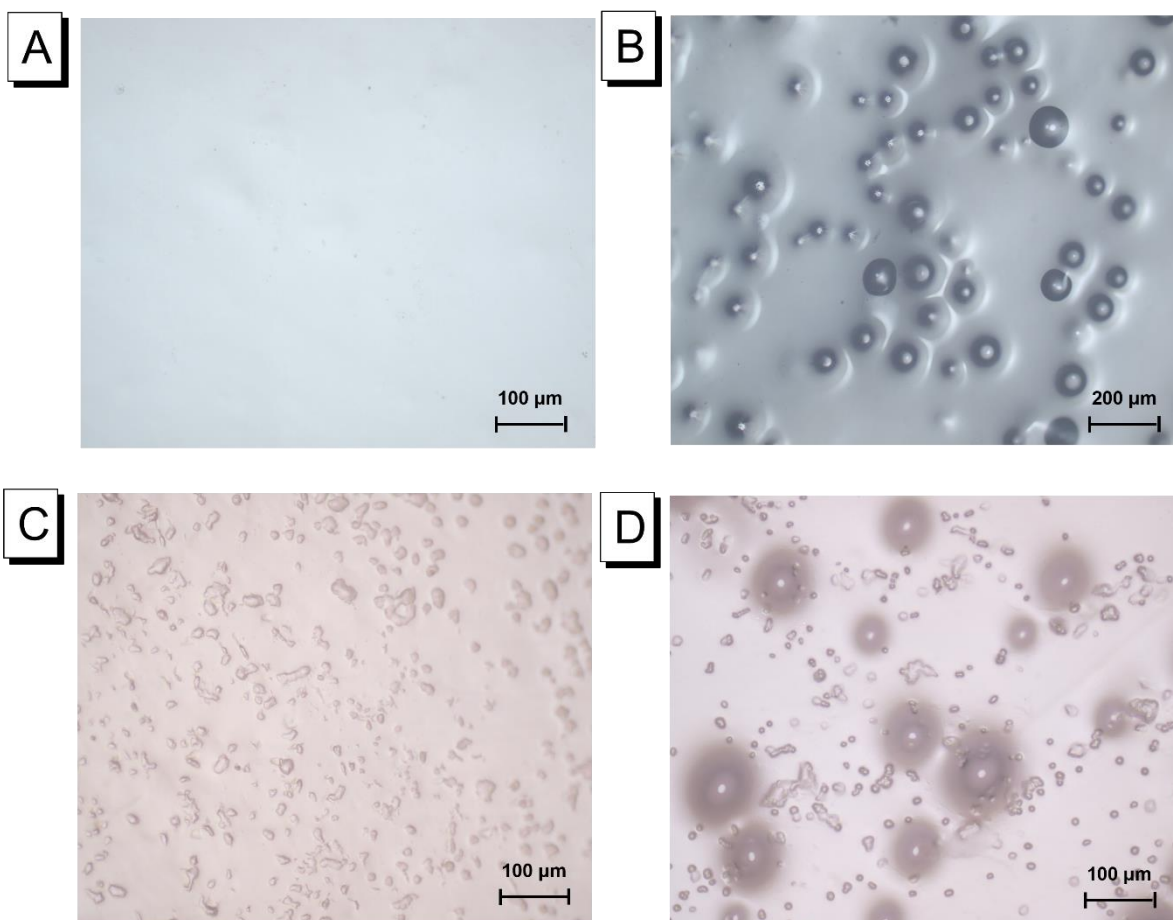
Figure S15 The images of optical microscopy in reflected light. (A) Carrageenan hydrogel film only, 100 µm; (B) Carrageenan hydrogel film + HSA, [HSA] = 2000 mg/L, 200 µm; (C) Carrageenan hydrogel film + TC426, [TC426] = 10µM, 100 µm; (D) Carrageenan hydrogel film + HSA + TC426, [HSA] = 2000 mg/L and [TC426] = 10µM, 100 µm.
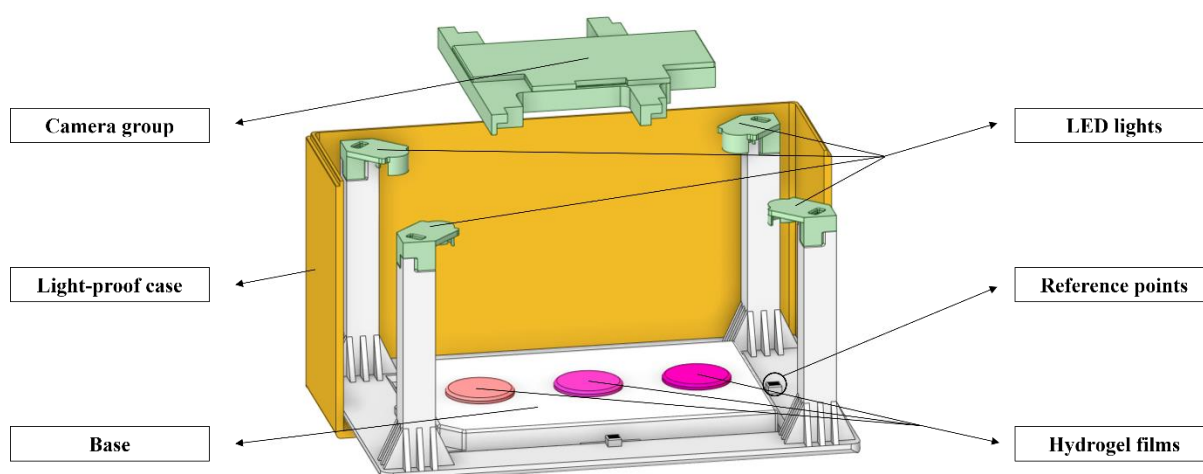
Figure S16 The 3D structure of Portable Colorimetric Device for optical imaging analysis; Components illustration including camera group, environmental light-proof case, base, 4 LED modules and 4 reference points.

AIE FL biosensor incorporating with metasurface platform
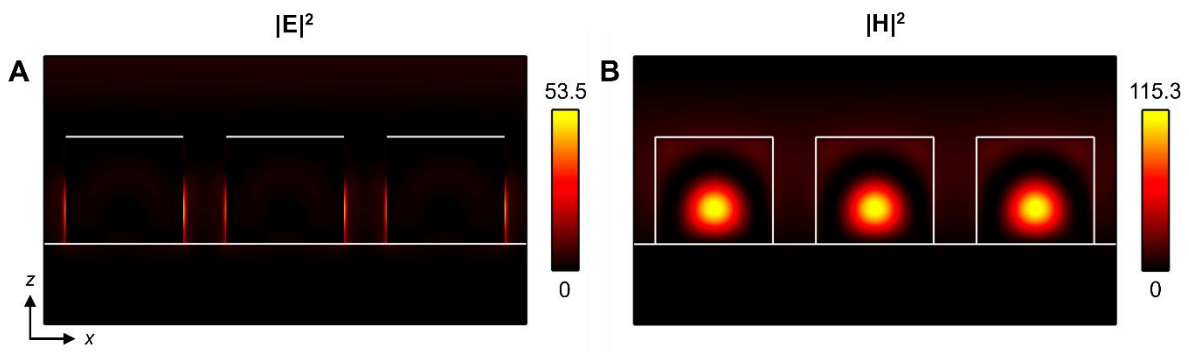
Figure S17 (A) and (B) Electric and magnetic field intensities ($|E|^2$ and $|H|^2$), respectively, induced at 750 nm, which is indicated by an arrow in Figure 2B. This *xz*-section was set to cut through the centre of the Si nanocolumns. Incident field was set to be unity, that is, $|E_{in}|^2 = 1$ and $|H_{in}|^2 = 1$. Colour bars indicate the field intensities. White lines show the interfaces of the Si nanocolumns with air and the underlying SiO_2 layer.

Figure S18 (A) and (B) Simulated and measured reflectance spectra, respectively.
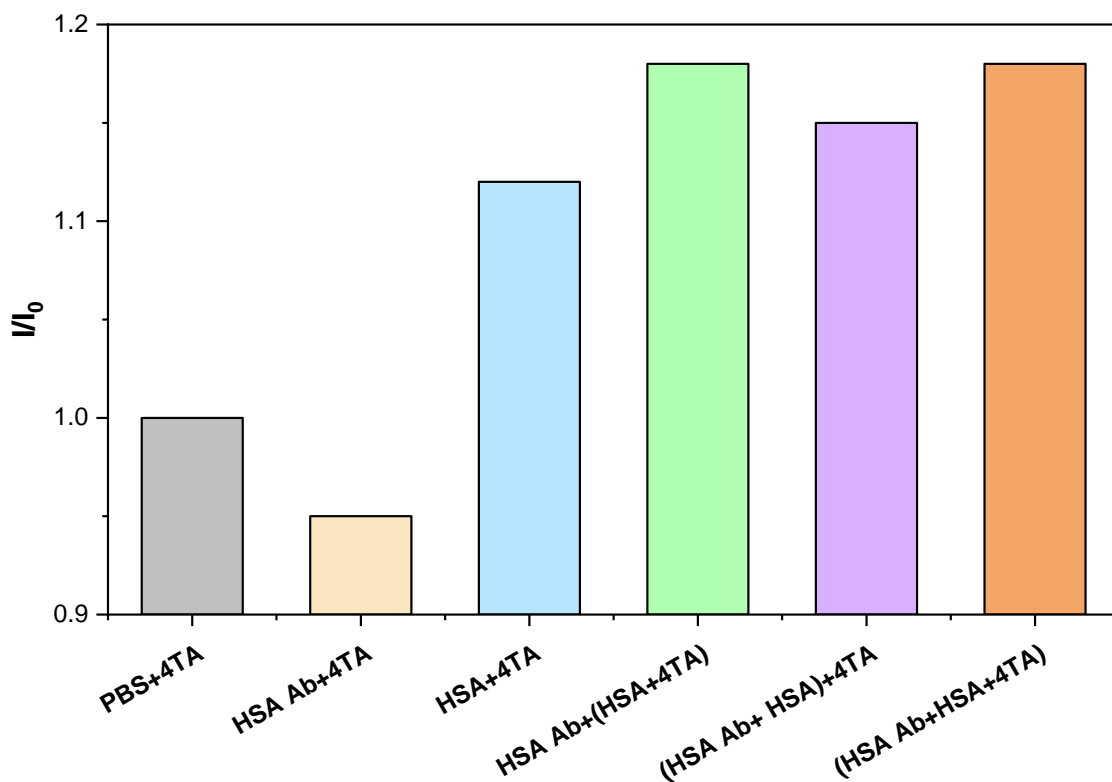
Figure S19 The effect of reaction sequence between different combinations among biotin-HSA antibody (HSA Ab), HSA, and TPE-4TA (4TA); Brackets represent a well-mixed solution that have been fully reacted and incubated in advance with these components. [HSA] = 5 µg mL^{-1}, [Biotin-HSA antibody] = 5 µg mL^{-1}, [TPE-4TA] = 20 µg mL^{-1}, Exposure time: 6000 ms, Gain: 10.
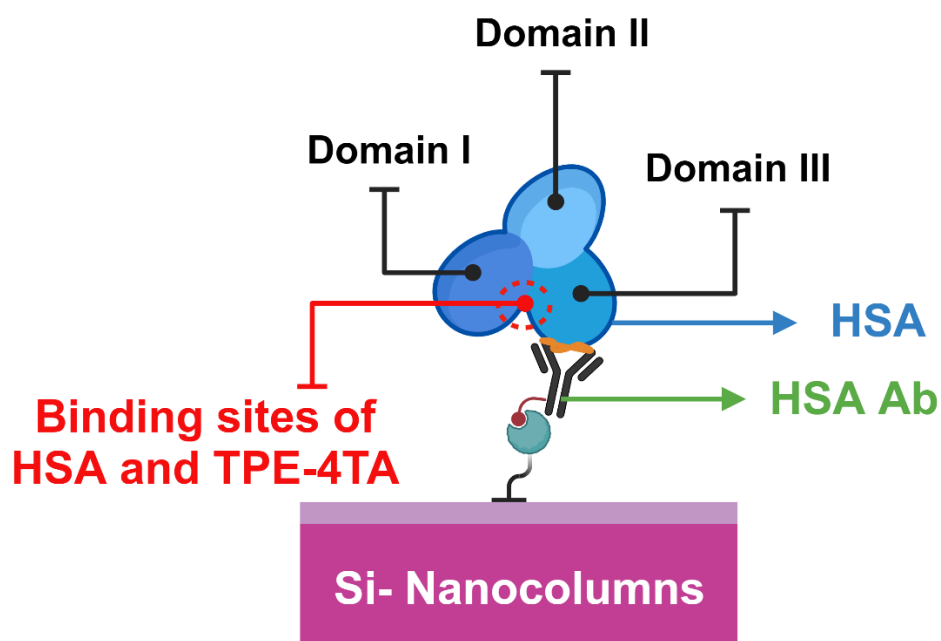
Figure S20 Explanation for FL quenching effect.
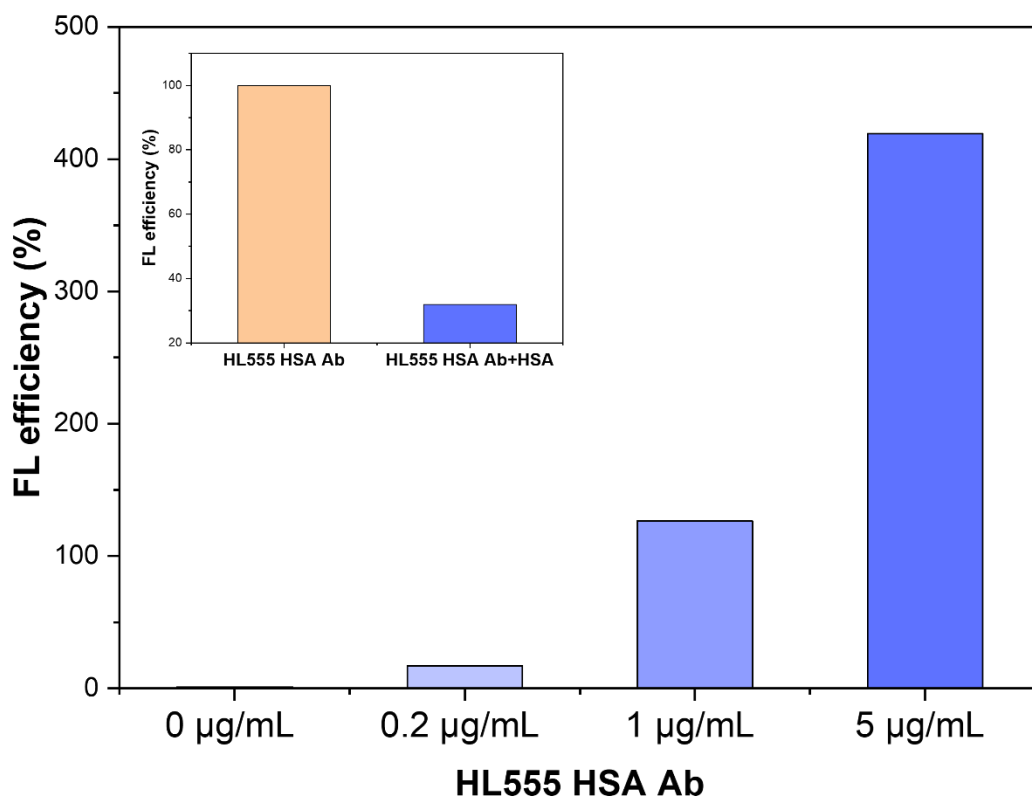
Figure S21 The change of FL efficiency with different concentrations of HL555-HSA Ab; [Biotin-HSA Ab] = 2 µg mL^{-1}, Exposure time: 3000 ms, Gain: 10. Inset figure represents FL quenching before and after adding HSA. [Biotin-HSA Ab] = 2 µg mL^{-1}, [HL555-HSA Ab] = 5 µg mL^{-1}, Exposure time: 3000 ms, Gain: 10.
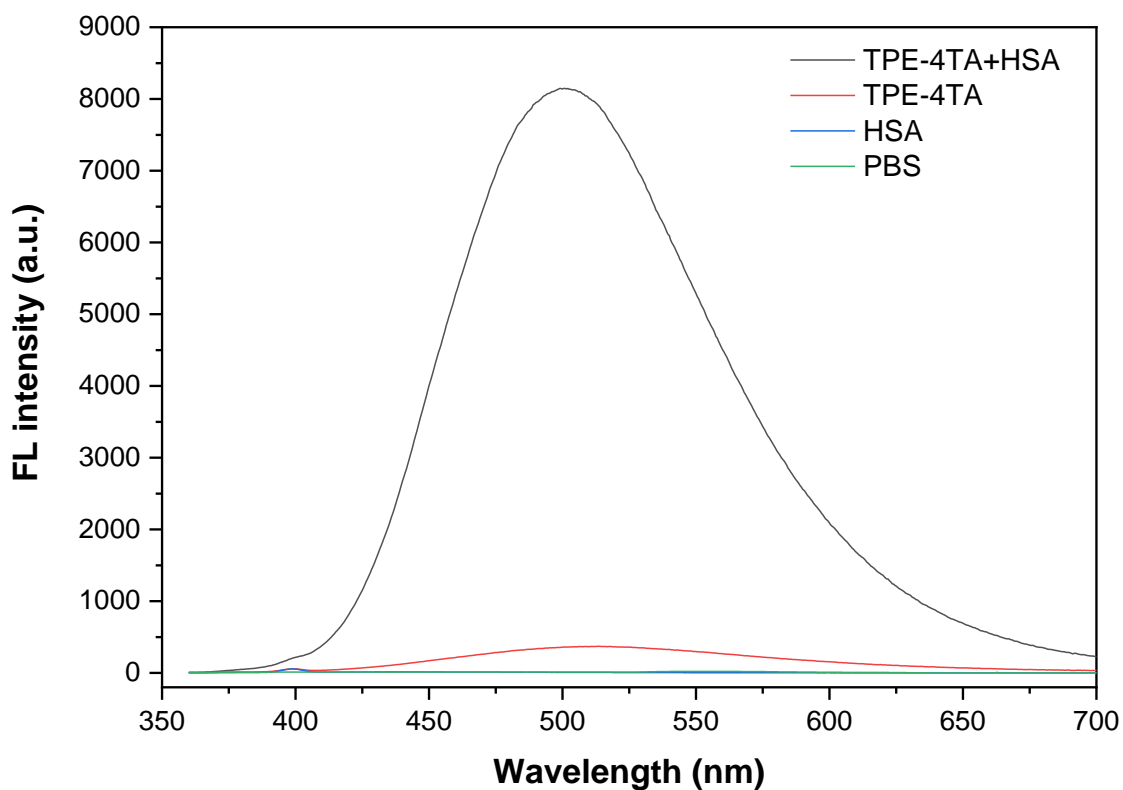
Figure S22 The FL spectra of TPE-4TA+HSA (black), TPE-4TA (red), HSA (blue) and PBS (green). λ_{ex} = 350 nm, [HSA] = 100 µg mL^{-1} and [TPE-4TA] = 10 µg mL^{-1}.
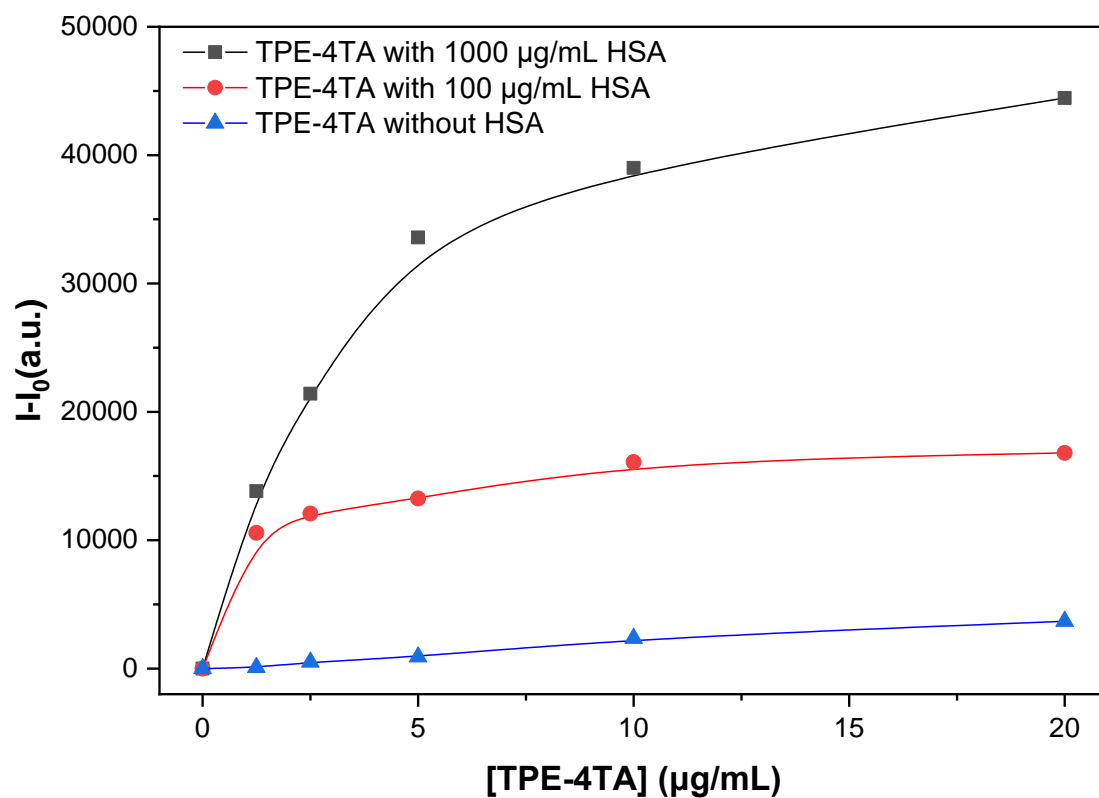
Figure S23 TPE-4TA concentration effect with or without HSA; [TPE-4TA] = 0-20 µg mL^{-1}, [HSA] = 0, 100, 1000 µg mL^{-1}, Exposure time: 3000 ms, Gain: 10.
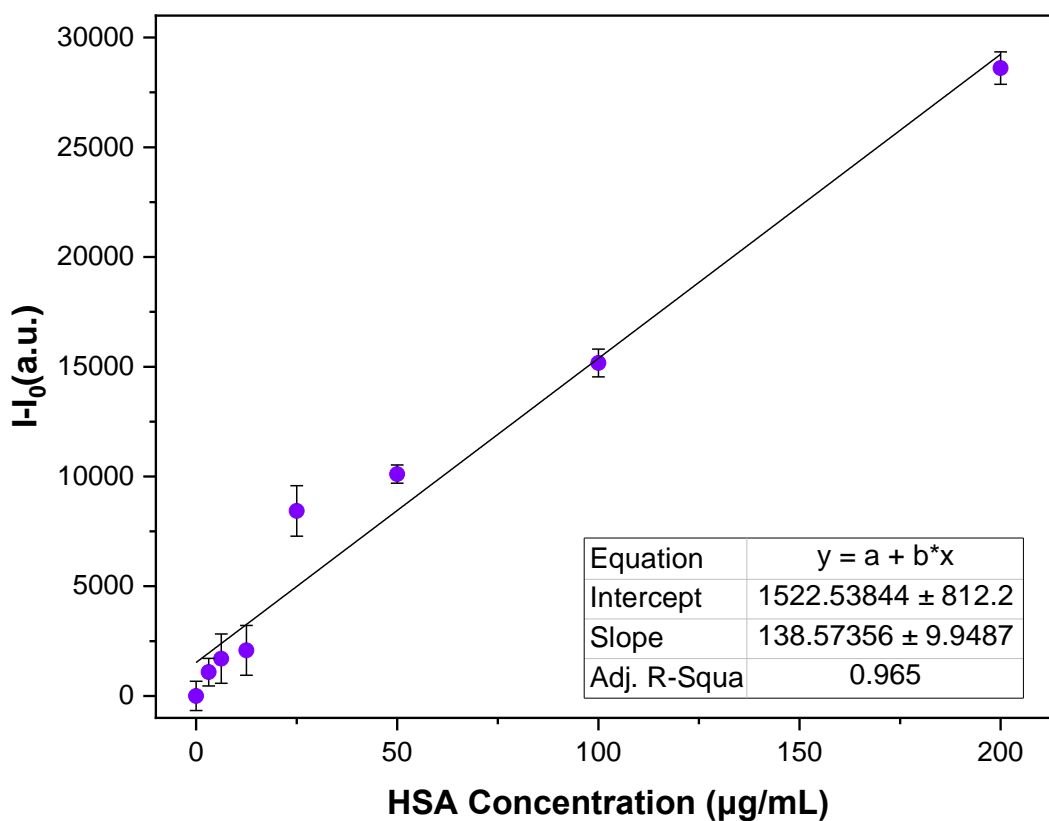
Figure S24 The standard curve of TPE-4TA for HSA detection using the microplate platform. λ_{ex} = 360 nm, [HSA] = 0-200 μg mL^{-1} and [TPE-4TA] = 20 μg mL^{-1}, Exposure time: 3000ms, Gain: 10.
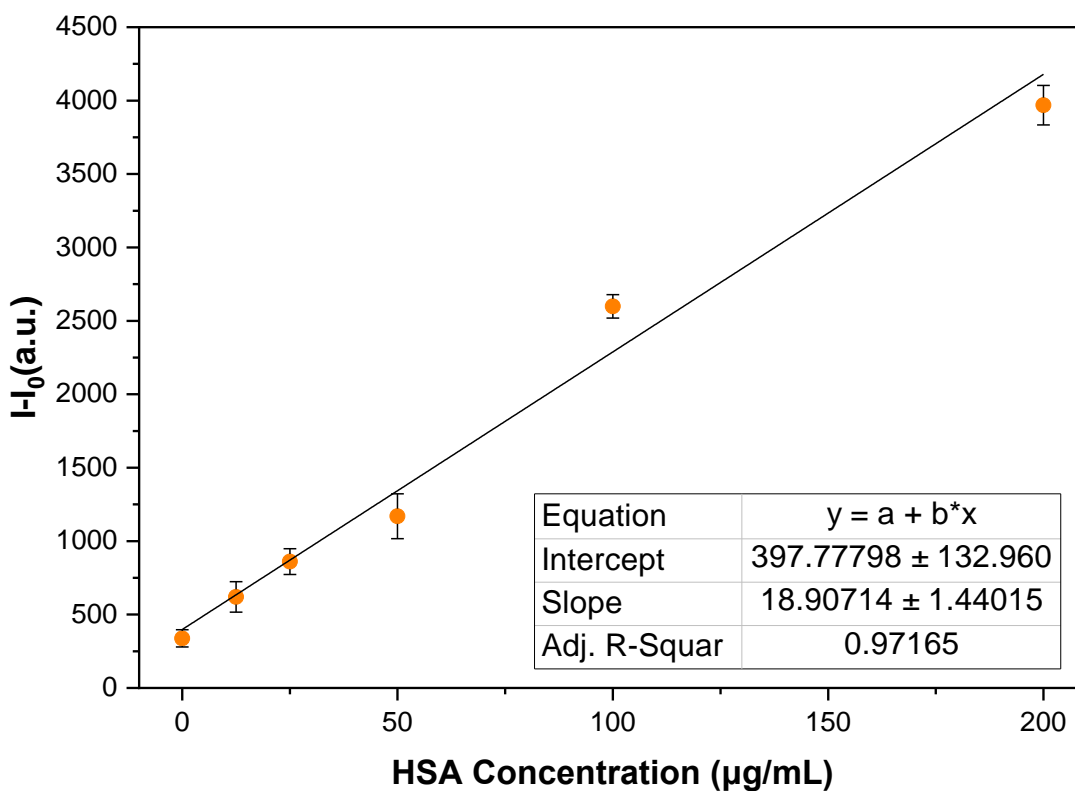
Figure S25 The standard curve of TPE-4TA for HSA detection using the microfluidic platform. λ_{ex} = 360 nm, [HSA] = 0-200 μg mL^{-1} and [TPE-4TA] = 20 μg mL^{-1}, Exposure time: 3000ms, Gain: 10.
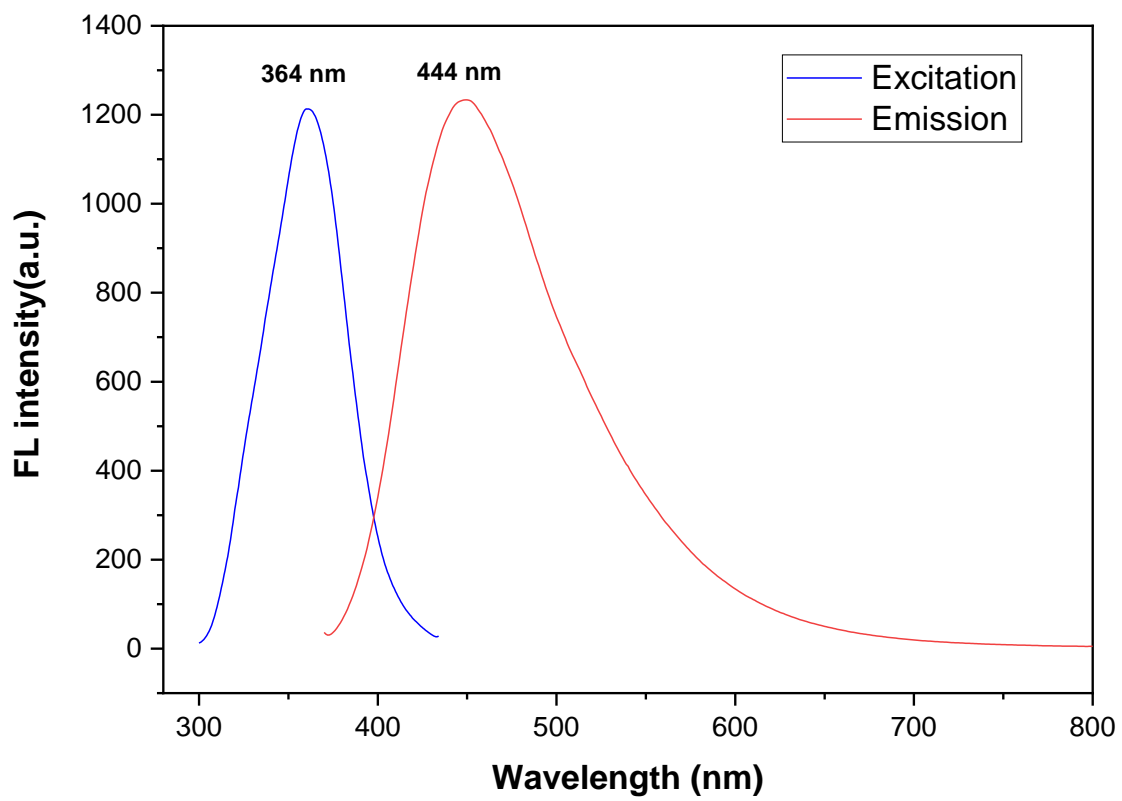
Figure S26 Spectrum of untreated urine.
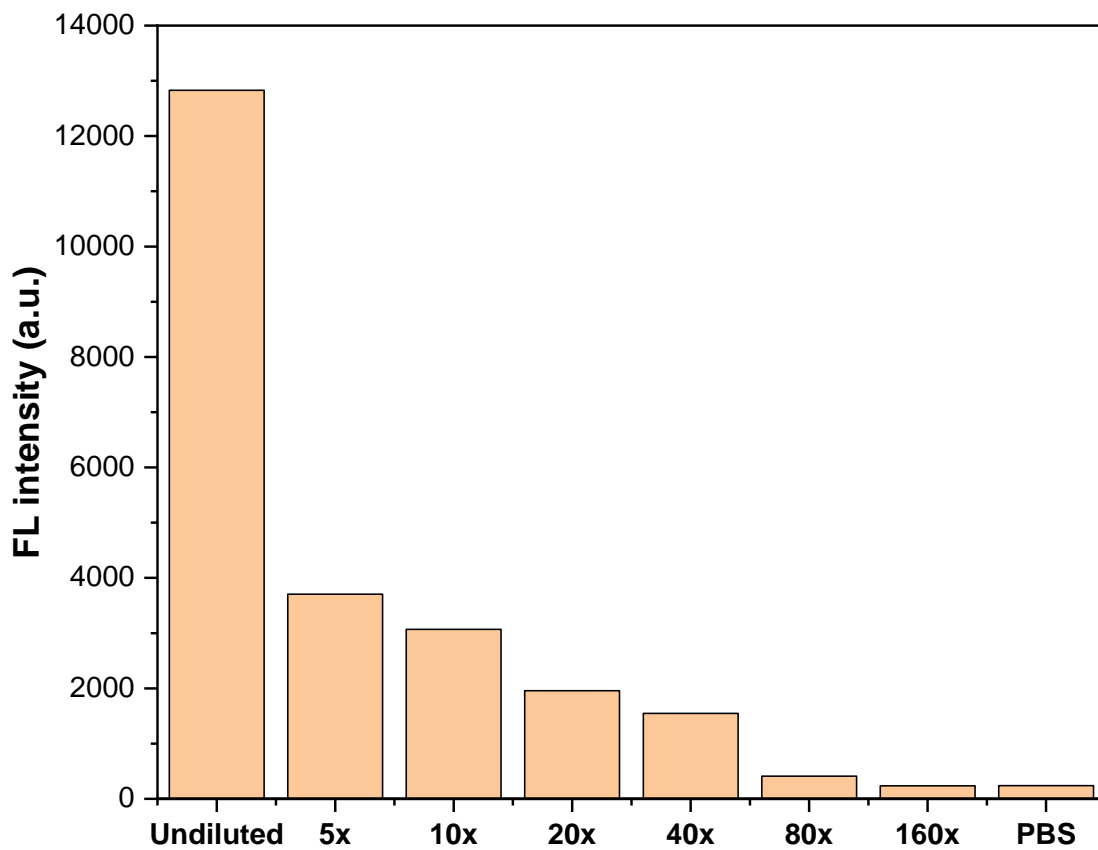
Figure S27 The effect of urine dilution where dilution ratios refer to total volume/treated urine volume with PBS buffer as diluent. λ_{ex} = 360 nm, Exposure time: 3000ms, Gain: 10.

Content	Commercial kits	Microplate wells system	Microfluidic system	Metasurface platform
Measured concentration	45.828 µg mL^{-1}	40.720 µg mL^{-1}	41.917 µg mL^{-1}	43.832 µg mL^{-1}
Recovery rate	——	88.85%	91.47%	95.64%

Table S2 The measurement of HSA concentrations and corresponding recovery rates in urine among microplate, microfluidic and metasurface platforms.

REFERENCE

Ackerman, E., & Rosevear, J. (1979). Immunonephelometric assays. *Medical Progress Through Technology*, *6*(2), 81-90.

Aitekenov, S., Gaipov, A., & Bukasov, R. (2021). Detection and quantification of proteins in human urine. *Talanta*, *223*, 121718.

Ali, A., Mitra, A., & Aïssa, B. (2022). Metamaterials and metasurfaces: A review from the perspectives of materials, mechanisms and advanced metadevices. *Nanomaterials*, *12*(6), 1027.

Anraku, M., Yamasaki, K., Maruyama, T., Kragh-Hansen, U., & Otagiri, M. (2001). Effect of oxidative stress on the structure and function of human serum albumin. *Pharmaceutical research*, *18*, 632-639.

Ascenzi, P., Di Masi, A., Fanali, G., & Fasano, M. (2015). Heme-based catalytic properties of human serum albumin. *Cell death discovery*, *1*(1), 1-7.

Ashraf, S., Qaiser, H., Tariq, S., Khalid, A., Makeen, H. A., Alhazmi, H. A., & Ul-Haq, Z. (2023). Unraveling the versatility of human serum albumin–A comprehensive review of its biological significance and therapeutic potential. *Current Research in Structural Biology*, 100114.

Aswathy, S., Narendrakumar, U., & Manjubala, I. (2020). Commercial hydrogels for biomedical applications. *Heliyon*, *6*(4), e03719.

Bao, Y., Ren, X., Liao, S., & Xue, Q. (2023). Controlling Radiation Beams by High-Efficiency Metasurfaces with Enhanced Refractive Index Elements. *ACS Applied Materials & Interfaces*, *15*(33), 40022-40031.

Barratt, J. (2007). What to do with patients with abnormal dipstick urinalysis. *Medicine*, *35*(7), 365-367.

Barulin, A., Nguyen, D. D., Kim, Y., Ko, C., & Kim, I. (2024). Metasurfaces for Quantitative Biosciences of Molecules, Cells, and Tissues: Sensing and Diagnostics. *ACS Photonics*.

Bassil, M., Davenas, J., & Tahchi, M. E. (2008). Electrochemical properties and actuation mechanisms of polyacrylamide hydrogel for artificial muscle application. *Sensors and Actuators B: Chemical*, *134*(2), 496-501.

Bikbov, B., Purcell, C. A., Levey, A. S., Smith, M., Abdoli, A., Abebe, M., Adebayo, O. M., Afarideh, M., Agarwal, S. K., & Agudelo-Botero, M. (2020). Global, regional, and national burden of chronic kidney disease, 1990–2017: a systematic analysis for the Global Burden of Disease Study 2017. *The lancet*, *395*(10225), 709-733.

Birková, A., Oboril, J., Kréta, R., Čižmárová, B., Hubková, B., Šteffeková, Z., Genči, J., Paralič, J., & Mareková, M. (2020). Human fluorescent profile of urine as a simple tool of mining in data from autofluorescence spectroscopy. *Biomedical Signal Processing and Control*, *56*, 101693.

Bobulescu, I. A., & Moe, O. W. (2012). Renal transport of uric acid: evolving concepts and uncertainties. *Advances in chronic kidney disease*, *19*(6), 358-371.

Bonacchi, S., Genovese, D., Juris, R., Montalti, M., Prodi, L., Rampazzo, E., & Zaccheroni, N. (2011). Luminescent silica nanoparticles: extending the frontiers of brightness. *Angewandte Chemie International Edition*, *50*(18), 4056-4066.

Borghi, L., Meschi, T., Schianchi, T., Briganti, A., Guerra, A., Allegri, F., & Novarini, A. (1998). Urine volume: stone risk factor and preventive measure. *Nephron*, *81*(Suppl. 1), 31-37.

Bouatra, S., Aziat, F., Mandal, R., Guo, A. C., Wilson, M. R., Knox, C., Bjorndahl, T. C., Krishnamurthy, R., Saleem, F., & Liu, P. (2013). The human urine metabolome. *PloS one*, *8*(9), e73076.

Bricker, N. S., Shwayri, E. I., Reardan, J. B., Kellog, D., Merrill, J. P., & Holmes, J. H. (1957). An abnormality in renal function resulting from urinary tract obstruction. *The American journal of medicine*, *23*(4), 554-564.

Brière, G., Ni, P., Héron, S., Chenot, S., Vézian, S., Brändli, V., Damilano, B., Duboz, J. Y., Iwanaga, M., & Genevet, P. (2019). An etching-free approach toward large-scale light-emitting metasurfaces. *Advanced Optical Materials*, *7*(14), 1801271.

Britton, J., Dalziel, S. B., & Raston, C. L. (2016). The synthesis of di-carboxylate esters using continuous flow vortex fluidics. *Green Chemistry*, *18*(7), 2193-2200.

Britton, J., Meneghini, L. M., Raston, C. L., & Weiss, G. A. (2016). Accelerating enzymatic catalysis using vortex fluidics. *Angewandte Chemie International Edition*, *55*(38), 11387-11391.

Britton, J., & Raston, C. L. (2014). Continuous flow vortex fluidic production of biodiesel. *RSC Advances*, *4*(91), 49850-49854.

Britton, J., Stubbs, K. A., Weiss, G. A., & Raston, C. L. (2017). Vortex fluidic chemical transformations. *Chemistry–A European Journal*, *23*(54), 13270-13278.

Brodows, R. G., Nichols, D., Shaker, G., & Kubasik, N. P. (1986). Evaluation of a new radioimmunoassay for urinary albumin. *Diabetes care*, *9*(2), 189-193.

Bujacz, A. (2012). Structures of bovine, equine and leporine serum albumin. *Acta Crystallographica Section D: Biological Crystallography*, *68*(10), 1278-1289.

Califf, R. M. (2018). Biomarker definitions and their applications. *Experimental Biology and Medicine*, *243*(3), 213-221.

Canet-Ferrer, J. (2019). *Metamaterials and metasurfaces*. BoD–Books on Demand.

Cantarin, M. P. M., Waldman, S. A., Doria, C., Frank, A. M., Maley, W. R., Ramirez, C. B., Keith, S. W., & Falkner, B. (2013). The adipose tissue production of adiponectin is increased in end-stage renal disease. *Kidney international*, *83*(3), 487-494.

Chai, Q., Jiao, Y., & Yu, X. (2017). Hydrogels for biomedical applications: their characteristics and the mechanisms behind them. *Gels*, *3*(1), 6.

Chapp, A. D., Schum, S., Behnke, J. E., Hahka, T., Huber, M. J., Jiang, E., Larson, R. A., Shan, Z., & Chen, Q. H. (2018). Measurement of cations, anions, and acetate in serum, urine, cerebrospinal fluid, and tissue by ion chromatography. *Physiological reports*, *6*(7), e13666.

Chen, M., Xiang, X., Wu, K., He, H., Chen, H., & Ma, C. (2017). A novel detection method of human serum albumin based on the poly (thymine)-templated copper nanoparticles. *Sensors*, *17*(11), 2684.

Chen, Y., Lam, J. W., Kwok, R. T., Liu, B., & Tang, B. Z. (2019). Aggregation-induced emission: fundamental understanding and future developments. *Materials Horizons*, *6*(3), 428-433.

Cheng, P., Miao, Q., Huang, J., Li, J., & Pu, K. (2020). Multiplex optical urinalysis for early detection of drug-induced kidney injury. *Analytical chemistry*, *92*(8), 6166-6172.

Cheung, S., Guan, B., Djordjevic, S., Okamoto, K., & Yoo, S. (2012). Low-loss and high contrast silicon-on-insulator (SOI) arrayed waveguide grating. 2012 Conference on Lasers and Electro-Optics (CLEO),

Choi, B., Iwanaga, M., Miyazaki, H. T., Sugimoto, Y., Ohtake, A., & Sakoda, K. (2015). Overcoming metal-induced fluorescence quenching on plasmo-photonic metasurfaces coated by a self-assembled monolayer. *Chemical Communications*, *51*(57), 11470-11473.

Christensen, R. L., Creekmore, F. M., Strong, M. B., & Lugo, R. A. (2007). The predictability of urinary pathogens based on the urinalysis nitrite test in hospitalized patients. *Hospital Pharmacy*, *42*(1), 52-56.

Chung, C., Kim, Y.-K., Shin, D., Ryoo, S.-R., Hong, B. H., & Min, D.-H. (2013). Biomedical applications of graphene and graphene oxide. *Accounts of chemical research*, *46*(10), 2211-2224.

Coca, S. G., Singanamala, S., & Parikh, C. R. (2012). Chronic kidney disease after acute kidney injury: a systematic review and meta-analysis. *Kidney international*, *81*(5), 442-448. https://www.ncbi.nlm.nih.gov/pmc/articles/PMC3788581/pdf/nihms504360.pdf

Comper, W. D., Jerums, G., & Osicka, T. M. (2004). Differences in urinary albumin detected by four immunoassays and high-performance liquid chromatography. *Clinical biochemistry*, *37*(2), 105-111.

Comper, W. D., & Osicka, T. M. (2005). Detection of urinary albumin. *Advances in chronic kidney disease*, *12*(2), 170-176.

Cui, J., & Jia, S. (2017). Organic–inorganic hybrid nanoflowers: A novel host platform for immobilizing biomolecules. *Coordination Chemistry Reviews*, *352*, 249-263.

Cui, Y., Yue, Y., Qian, G., & Chen, B. (2012). Luminescent functional metal–organic frameworks. *Chemical reviews*, *112*(2), 1126-1162.

D'amico, G., & Bazzi, C. (2003). Pathophysiology of proteinuria. *Kidney international*, *63*(3), 809-825.

Darwish, I. A. (2006). Immunoassay methods and their applications in pharmaceutical analysis: basic methodology and recent advances. *International journal of biomedical science: IJBS*, *2*(3), 217.

de Jong, P. E., & Curhan, G. C. (2006). Screening, monitoring, and treatment of albuminuria: Public health perspectives. *Journal of the American Society of Nephrology*, *17*(8), 2120-2126.

De Silva, A. P., Gunaratne, H. N., Gunnlaugsson, T., Huxley, A. J., McCoy, C. P., Rademacher, J. T., & Rice, T. E. (1997). Signaling recognition events with fluorescent sensors and switches. *Chemical reviews*, *97*(5), 1515-1566.

de Zeeuw, D., Parving, H.-H., & Henning, R. H. (2006). Microalbuminuria as an early marker for cardiovascular disease. *Journal of the American Society of Nephrology*, *17*(8), 2100-2105.

Decramer, S., de Peredo, A. G., Breuil, B., Mischak, H., Monsarrat, B., Bascands, J.-L., & Schanstra, J. P. (2008). Urine in clinical proteomics. *Molecular & cellular proteomics*, *7*(10), 1850-1862.

Del Valle, R., Cazanave Mora, J. M., Carrazana San Martín, N. L., Hernández Pérez, L., Legrá Torres, M. E., López Cisneros, R., Ordaz Ramos, R. P., Rodríguez, A. M., & Valdivia Álvarez, I. (2020). An enzyme immunoassay for determining albumin in human urine samples using an ultra-microanalytical system. *Journal of Immunoassay and Immunochemistry*, *41*(5), 896-912.

Deligkaris, K., Tadele, T. S., Olthuis, W., & van den Berg, A. (2010). Hydrogel-based devices for biomedical applications. *Sensors and Actuators B: Chemical*, *147*(2), 765-774.

Devarajan, P. (2010). The use of targeted biomarkers for chronic kidney disease. *Advances in chronic kidney disease*, *17*(6), 469-479.

Devi, R., & Pundir, C. (2014). Construction and application of an amperometric uric acid biosensor based on covalent immobilization of uricase on iron oxide nanoparticles/chitosan-g-polyaniline composite film electrodeposited on Pt electrode. *Sensors and Actuators B: Chemical*, *193*, 608-615.

Dhawan, G., Sumana, G., & Malhotra, B. (2009). Recent developments in urea biosensors. *Biochemical Engineering Journal*, *44*(1), 42-52.

Ding, D., Li, K., Liu, B., & Tang, B. Z. (2013). Bioprobes based on AIE fluorogens. *Accounts of Chemical Research*, *46*(11), 2441-2453.

Dreiss, C. A. (2020). Hydrogel design strategies for drug delivery. *Current Opinion in Colloid & Interface Science*, *48*, 1-17.

Duly, E., Grimason, S., Grimason, P., Barnes, G., & Trinick, T. (2003). Measurement of serum albumin by capillary zone electrophoresis, bromocresol green, bromocresol purple, and immunoassay methods. *Journal of clinical pathology*, *56*(10), 780-781.

Duo, Y., Xiang, Z., Gao, G., Luo, G., & Tang, B. Z. (2023). Biomedical application of aggregation-induced emission luminogen-based fluorescent sensors. *TrAC Trends in Analytical Chemistry*, 117252.

Dyer, A. R., Greenland, P., Elliott, P., Daviglus, M. L., Claeys, G., Kesteloot, H., Ueshima, H., & Stamler, J. (2004). Evaluation of measures of urinary albumin excretion in epidemiologic studies. *American journal of epidemiology*, *160*(11), 1122-1131.

Ee, H.-S., & Agarwal, R. (2016). Tunable metasurface and flat optical zoom lens on a stretchable substrate. *Nano letters*, *16*(4), 2818-2823.

Eggert, R. J. (2005). *Engineering design*. Pearson/Prentice Hall Upper Saddle River.

El Nahas, A. M., & Bello, A. K. (2005). Chronic kidney disease: the global challenge. *The lancet*, *365*(9456), 331-340.

Elaloufi, R., Carminati, R., & Greffet, J.-J. (2003). Definition of the diffusion coefficient in scattering and absorbing media. *JOSA A*, *20*(4), 678-685.

ESTERASE, L., INDICATORS, P. E. O., & STRIP, R. Chemical Analysis of Urine.

Falcó, P. C., Genaro, L. T., Lloret, S. M., Gomez, F. B., Cabeza, A. S., & Legua, C. M. (2001). Creatinine determination in urine samples by batchwise kinetic procedure and flow injection analysis using the Jaffé reaction: chemometric study. *Talanta*, *55*(6), 1079-1089.

Fanali, G., Di Masi, A., Trezza, V., Marino, M., Fasano, M., & Ascenzi, P. (2012). Human serum albumin: from bench to bedside. *Molecular aspects of medicine*, *33*(3), 209-290.

Farmahini-Farahani, M., & Mosallaei, H. (2013). Birefringent reflectarray metasurface for beam engineering in infrared. *Optics letters*, *38*(4), 462-464.

Fasano, M., Curry, S., Terreno, E., Galliano, M., Fanali, G., Narciso, P., Notari, S., & Ascenzi, P. (2005). The extraordinary ligand binding properties of human serum albumin. *IUBMB life*, *57*(12), 787-796.

Fassett, R. G., Venuthurupalli, S. K., Gobe, G. C., Coombes, J. S., Cooper, M. A., & Hoy, W. E. (2011). Biomarkers in chronic kidney disease: a review. *Kidney international*, *80*(8), 806-821.

Fathallah-Shaykh, S. A., & Cramer, M. T. (2014). Uric acid and the kidney. *Pediatric nephrology*, *29*(6), 999-1008.

Feng, G., & Liu, B. (2018). Aggregation-induced emission (AIE) dots: emerging theranostic nanolights. *Accounts of Chemical Research*, *51*(6), 1404-1414.

Ferrara, J., Yang, W., Zhu, L., Qiao, P., & Chang-Hasnain, C. J. (2015). Heterogeneously integrated long-wavelength VCSEL using silicon high contrast grating on an SOI substrate. *Optics express*, *23*(3), 2512-2523.

Fevery, J. (2008). Bilirubin in clinical practice: a review. *Liver International*, *28*(5), 592-605.

Finco, D. R. (1997). Kidney function. In *Clinical biochemistry of domestic animals* (pp. 441-484). Elsevier.

Findlay, J. W., Smith, W., Lee, J., Nordblom, G., Das, I., DeSilva, B., Khan, M., & Bowsher, R. (2000). Validation of immunoassays for bioanalysis: a pharmaceutical industry perspective. *Journal of pharmaceutical and biomedical analysis*, *21*(6), 1249-1273.

Foreman, K. J., Marquez, N., Dolgert, A., Fukutaki, K., Fullman, N., McGaughey, M., Pletcher, M. A., Smith, A. E., Tang, K., & Yuan, C.-W. (2018). Forecasting life expectancy, years of life lost, and all-cause and cause-specific mortality for 250 causes of death: reference and alternative scenarios for 2016–40 for 195 countries and territories. *The lancet*, *392*(10159), 2052-2090.

Francis, A., Harhay, M. N., Ong, A. C., Tummalapalli, S. L., Ortiz, A., Fogo, A. B., Fliser, D., Roy-Chaudhury, P., Fontana, M., & Nangaku, M. (2024). Chronic kidney disease and the global public health agenda: an international consensus. *Nature Reviews Nephrology*, 1-13.

Francis, P. S., Lewis, S. W., & Lim, K. F. (2002). Analytical methodology for the determination of urea: current practice and future trends. *TrAC trends in analytical chemistry*, *21*(5), 389-400.

Fung, K.-K., Chan, C. P.-Y., & Renneberg, R. (2009). Development of a creatinine enzyme-based bar-code-style lateral-flow assay. *Analytical and bioanalytical chemistry*, *393*(4), 1281-1287.

Gaitonde, D. Y., Cook, D. L., & Rivera, I. M. (2017). Chronic kidney disease: detection and evaluation. *American family physician*, *96*(12), 776-783.

Ganji, F., & VASHEGHANI, F. E. (2009). Hydrogels in controlled drug delivery systems.

Ganji, F., Vasheghani, F. S., & Vasheghani, F. E. (2010). Theoretical description of hydrogel swelling: a review.

Gao, L., Lin, X., & Chen, X. (2020). Ionic liquid decorated AIE luminogen for selective detection of HSA in biofluids and early disease screening. *Talanta*, *212*, 120763. https://doi.org/10.1016/j.talanta.2020.120763

Gao, M., & Tang, B. Z. (2017). Fluorescent sensors based on aggregation-induced emission: recent advances and perspectives. *ACS sensors*, *2*(10), 1382-1399.

Gao, S., Wei, G., Zhang, S., Zheng, B., Xu, J., Chen, G., Li, M., Song, S., Fu, W., & Xiao, Z. (2019). Albumin tailoring fluorescence and photothermal conversion effect of near-infrared-II fluorophore with aggregation-induced emission characteristics. *Nature communications*, *10*(1), 1-15.

Gao, Y. (2019). *Urine: Promising Biomarker Source for Early Disease Detection*. Springer.

Ge, J., Lei, J., & Zare, R. N. (2012). Protein–inorganic hybrid nanoflowers. *Nature nanotechnology*, *7*(7), 428-432.

Geng, J., Goh, C. C., Tomczak, N., Liu, J., Liu, R., Ma, L., Ng, L. G., Gurzadyan, G. G., & Liu, B. (2014). Micelle/silica co-protected conjugated polymer nanoparticles for two-photon excited brain vascular imaging. *Chemistry of Materials*, *26*(5), 1874-1880.

Ghaderinezhad, F., Koydemir, H. C., Tseng, D., Karinca, D., Liang, K., Ozcan, A., & Tasoglu, S. (2020). Sensing of electrolytes in urine using a miniaturized paper-based device. *Scientific reports*, *10*(1), 1-9.

Ghasemiyeh, P., & Mohammadi-Samani, S. (2019). Hydrogels as drug delivery systems; pros and cons. *Trends in Pharmaceutical Sciences*, *5*(1), 7-24.

Ghuman, J., Zunszain, P. A., Petitpas, I., Bhattacharya, A. A., Otagiri, M., & Curry, S. (2005). Structural basis of the drug-binding specificity of human serum albumin. *Journal of molecular biology*, *353*(1), 38-52.

Gluhovschi, C., Velciov, S., Kaycsa, A., Gluhovschi, G., Petrica, L., Marian, R., Bozdog, G., Gadalean, F., Bob, F., & Cioca, D. (2012). The dynamics of urinary N-acetyl-β-d-glucosaminidase (NAG), a marker of renal tubular dysfunction, in patients with lupus nephritis undergoing oral prednisone therapy. *Immunopharmacology and Immunotoxicology*, *34*(1), 163-169.

Gonzalez-Bedat, M. C., Rosa-Diez, G., Ferreiro-Fuentes, A., Douthat, W., Cueto-Manzano, A., & Fernandez-Cean, J. M. (2020). Burden of disease: Closing the gaps in the burden of end-stage kidney disease in Latin America. *Clin Nephrol*, *93*(1), 55-59.

Grange, C., & Bussolati, B. (2022). Extracellular vesicles in kidney disease. *Nature Reviews Nephrology*, *18*(8), 499-513.

Grzybowski, B. A., Sobolev, Y. I., Cybulski, O., & Mikulak-Klucznik, B. (2022). Materials, assemblies and reaction systems under rotation. *Nature Reviews Materials*, *7*(5), 338-354.

Gu, X., Kwok, R. T., Lam, J. W., & Tang, B. Z. (2017). AIEgens for biological process monitoring and disease theranostics. *Biomaterials*, *146*, 115-135.

Gu, X., Kwok, R. T. K., Lam, J. W. Y., & Tang, B. Z. (2017). AIEgens for biological process monitoring and disease theranostics. *Biomaterials*, *146*, 115-135. https://doi.org/10.1016/j.biomaterials.2017.09.004

GUH, J. Y. (2010). Proteinuria versus albuminuria in chronic kidney disease. *Nephrology*, *15*, 53-56.

Gupta, P. K., Son, S. E., & Seong, G. H. (2020). One-pot synthesized citric acid-modified bimetallic PtNi hollow nanospheres as peroxidase mimics for colorimetric detection of human serum albumin. *Materials Science and Engineering: C*, *116*, 111231.

Gutruf, P., Zou, C., Withayachumnankul, W., Bhaskaran, M., Sriram, S., & Fumeaux, C. (2016). Mechanically tunable dielectric resonator metasurfaces at visible frequencies. *ACS nano*, *10*(1), 133-141.

Halder, S., Samanta, S., & Das, G. (2019). Exploring the potential of a urea derivative: an AIE-luminogen and its interaction with human serum albumin in aqueous medium. *Analyst*, *144*(8), 2696-2703. https://doi.org/10.1039/c9an00102f

Halvorsen, Y.-D. C., Wilkison, W. O., & Briggs, M. R. (2000). Human adipocyte proteomics-a complementary way of looking at fat. *Pharmacogenomics*, *1*(2), 179-185.

Hamzah, H. H., Zain, Z. M., Musa, N. L. W., Lin, Y.-C., & Trimbee, E. (2013). Spectrophotometric determination of uric acid in urine based-enzymatic method uricase with 4-aminodiphenylamine diazonium sulfate (variamine blue RT salt). *J. Anal. Bioanal. Tech. S*, *7*, 1-6.

Harpole, M., Davis, J., & Espina, V. (2016). Current state of the art for enhancing urine biomarker discovery. *Expert review of proteomics*, *13*(6), 609-626.

He, S., Vimalanathan, K., Su, P., Jellicoe, M., Luo, X., Xing, W., Cai, W., Gibson, C. T., Chen, Y., & Wong, J. W. C. (2021). Upsized Vortex Fluidic Device Enhancement of Mechanical Properties and the Microstructure of Biomass-Based Biodegradable Films. *ACS Sustainable Chemistry & Engineering*, *9*(43), 14588-14595.

He, X. M., & Carter, D. C. (1992). Atomic structure and chemistry of human serum albumin. *Nature*, *358*(6383), 209-215.

Hemmelgarn, B. R., Manns, B. J., Lloyd, A., James, M. T., Klarenbach, S., Quinn, R. R., Wiebe, N., Tonelli, M., & Network, A. K. D. (2010). Relation between kidney function, proteinuria, and adverse outcomes. *Jama*, *303*(5), 423-429.

Hennink, W. E., & van Nostrum, C. F. (2012). Novel crosslinking methods to design hydrogels. *Advanced drug delivery reviews*, *64*, 223-236.

Hinton, R., Mallon, B., Morris, K., Miller, J., Atkinson, T., Hammond, P., & Price, C. (1990). Colorimetric determination of human albumin. *Journal of clinical pathology*, *43*(7), 610.

Hoffman, A. S. (2012). Hydrogels for biomedical applications. *Advanced drug delivery reviews*, *64*, 18-23.

Hohenberger, E., & Kimling, H. (2008). Compendium urinalysis: urinalysis with test strips. *Germany: Roche Diagnostics*.

Hong, Y., Feng, C., Yu, Y., Liu, J., Lam, J. W. Y., Luo, K. Q., & Tang, B. Z. (2010). Quantitation, visualization, and monitoring of conformational transitions of human serum albumin by a tetraphenylethene derivative with aggregation-induced emission characteristics. *Analytical chemistry*, *82*(16), 7035-7043.

Hong, Y., Lam, J. W., & Tang, B. Z. (2009). Aggregation-induced emission: phenomenon, mechanism and applications. *Chemical Communications*(29), 4332-4353.

Hong, Y., Lam, J. W., & Tang, B. Z. (2011). Aggregation-induced emission. *Chemical Society Reviews*, *40*(11), 5361-5388.

Hong, Y., Meng, L., Chen, S., Leung, C. W. T., Da, L.-T., Faisal, M., Silva, D.-A., Liu, J., Lam, J. W. Y., & Huang, X. (2012). Monitoring and inhibition of insulin fibrillation by a small organic

fluorogen with aggregation-induced emission characteristics. *Journal of the American Chemical Society*, *134*(3), 1680-1689.

Houbertz, R., Domann, G., Cronauer, C., Schmitt, A., Martin, H., Park, J.-U., Fröhlich, L., Buestrich, R., Popall, M., & Streppel, U. (2003). Inorganic–organic hybrid materials for application in optical devices. *Thin Solid Films*, *442*(1-2), 194-200.

Hsiao, H. H., Chu, C. H., & Tsai, D. P. (2017). Fundamentals and applications of metasurfaces. *Small Methods*, *1*(4), 1600064.

Hsu, W.-L., Chen, Y.-C., Yeh, S. P., Zeng, Q.-C., Huang, Y.-W., & Wang, C.-M. (2022). Review of metasurfaces and metadevices: advantages of different materials and fabrications. *Nanomaterials*, *12*(12), 1973.

Hu, J., Bandyopadhyay, S., Liu, Y.-h., & Shao, L.-y. (2021). A review on metasurface: from principle to smart metadevices. *Frontiers in Physics*, *8*, 586087.

Hu, Q., Ding, D., & Tang, Y. (2022). Inorganic-organic hybrid materials to detect urinary biomarkers: Recent progress and future prospective. *Materials Chemistry Frontiers*.

Hu, Q., Yao, B., Owyong, T. C., Prashanth, S., Wang, C., Zhang, X., Wong, W. W., Tang, Y., & Hong, Y. (2021). Detection of Urinary Albumin Using a "Turn-on" Fluorescent Probe with Aggregation-Induced Emission Characteristics. *Chemistry–An Asian Journal*, *16*(10), 1245-1252.

Hu, Y., Zhou, X., Lu, Y., Hu, C., & Hu, X. (2009). Novel biodegradable hydrogels based on pachyman and its derivatives for drug delivery. *International journal of pharmaceutics*, *371*(1-2), 89-98.

Huang, J., Li, J., Lyu, Y., Miao, Q., & Pu, K. (2019). Molecular optical imaging probes for early diagnosis of drug-induced acute kidney injury. *Nature materials*, *18*(10), 1133-1143.

Huang, Y., Lv, T., Qin, T., Xu, Z., Wang, L., & Liu, B. (2020). A DS2-specific flavonoid-based probe with a unique dual-emissive response to human serum albumin. *Chemical Communications*, *56*(75), 11094-11097.

Huang, Z., Wang, H., & Yang, W. (2015). Gold nanoparticle-based facile detection of human serum albumin and its application as an INHIBIT logic gate. *ACS Applied Materials & Interfaces*, *7*(17), 8990-8998.

Hubka, V. (2015). *Principles of engineering design*. Elsevier.

Irrera, A., Leonardi, A. A., Di Franco, C., Lo Faro, M. J., Palazzo, G., D'Andrea, C., Manoli, K., Franzo, G., Musumeci, P., & Fazio, B. (2018). New generation of ultrasensitive label-free optical Si nanowire-based biosensors. *Acs Photonics*, *5*(2), 471-479.

Iwanaga, M. (2016). *Plasmonic Resonators: Fundamentals, Advances, and Applications*. Jenny Stanford Publishing.

Iwanaga, M. (2018). All-dielectric metasurfaces with high-fluorescence-enhancing capability. *Applied Sciences*, *8*(8), 1328.

Iwanaga, M. (2020). All-dielectric metasurface fluorescence biosensors for high-sensitivity antibody/antigen detection. *ACS nano*, *14*(12), 17458-17467.

Iwanaga, M. (2021). Highly sensitive wide-range target fluorescence biosensors of high-emittance metasurfaces. *Biosensors and Bioelectronics*, *190*, 113423.

Iwanaga, M. (2022). Rapid detection of attomolar SARS-CoV-2 nucleic acids in all-dielectric metasurface biosensors. *Biosensors*, *12*(11), 987.

Iwanaga, M. (2023). Robust Detection of Cancer Markers in Human Serums Using All-Dielectric Metasurface Biosensors. *Biosensors*, *13*(3), 377.

Iwanaga, M., Choi, B., Miyazaki, H. T., & Sugimoto, Y. (2016). The artificial control of enhanced optical processes in fluorescent molecules on high-emittance metasurfaces. *Nanoscale*, *8*(21), 11099-11107.

Iwanaga, M., Hironaka, T., Ikeda, N., Sugasawa, T., & Takekoshi, K. (2023a). Metasurface Biosensors Enabling Single-Molecule Sensing of Cell-Free DNA. *Nano letters*.

Iwanaga, M., Hironaka, T., Ikeda, N., Sugasawa, T., & Takekoshi, K. (2023b). Metasurface biosensors enabling single-molecule sensing of cell-free DNA. *Nano Letters*, *23*(12), 5755-5761.

Iwanaga, M., & Tangkawsakul, W. (2022). Two-way detection of COVID-19 spike protein and antibody using all-dielectric metasurface fluorescence sensors. *Biosensors*, *12*(11), 981.

Jager, K. J., Kovesdy, C., Langham, R., Rosenberg, M., Jha, V., & Zoccali, C. (2019). A single number for advocacy and communication—worldwide more than 850 million individuals have kidney diseases. In (Vol. 34, pp. 1803-1805): Oxford University Press.

James, M. T., Hemmelgarn, B. R., & Tonelli, M. (2010). Early recognition and prevention of chronic kidney disease. *The lancet*, *375*(9722), 1296-1309.

Jha, V., Garcia-Garcia, G., Iseki, K., Li, Z., Naicker, S., Plattner, B., Saran, R., Wang, A. Y.-M., & Yang, C.-W. (2013). Chronic kidney disease: global dimension and perspectives. *The lancet*, *382*(9888), 260-272.

Ji, J., Lu, W., Zhu, Y., Jin, H., Yao, Y., Zhang, H., & Zhao, Y. (2019). Porous hydrogel-encapsulated photonic barcodes for multiplex detection of cardiovascular biomarkers. *ACS sensors*, *4*(5), 1384-1390.

Kabashin, A. V., Evans, P., Pastkovsky, S., Hendren, W., Wurtz, G. A., Atkinson, R., Pollard, R., Podolskiy, V. A., & Zayats, A. V. (2009). Plasmonic nanorod metamaterials for biosensing. *Nature materials*, *8*(11), 867-871.

Kalantar-Zadeh, K., Jafar, T. H., Nitsch, D., Neuen, B. L., & Perkovic, V. (2021). Chronic kidney disease. *The lancet*, *398*(10302), 786-802.

Kamijo, A., Sugaya, T., Hikawa, A., Yamanouchi, M., Hirata, Y., Ishimitsu, T., Numabe, A., Takagi, M., Hayakawa, H., & Tabei, F. (2005). Clinical evaluation of urinary excretion of liver-type fatty acid-binding protein as a marker for the monitoring of chronic kidney disease: a multicenter trial. *Journal of Laboratory and Clinical Medicine*, *145*(3), 125-133.

Kamijo, A., Sugaya, T., Hikawa, A., Yamanouchi, M., Hirata, Y., Ishimitsu, T., Numabe, A., Takagi, M., Hayakawa, H., & Tabei, F. (2006). Urinary liver-type fatty acid binding protein as a useful biomarker in chronic kidney disease. *Molecular and cellular biochemistry*, *284*, 175-182.

Kangas, M. J., Burks, R. M., Atwater, J., Lukowicz, R. M., Williams, P., & Holmes, A. E. (2017). Colorimetric sensor arrays for the detection and identification of chemical weapons and explosives. *Critical reviews in analytical chemistry*, *47*(2), 138-153.

Kapingidza, A. B., Kowal, K., & Chruszcz, M. (2020). Antigen–antibody complexes. *Vertebrate and Invertebrate Respiratory Proteins, Lipoproteins and other Body Fluid Proteins*, 465-497.

Karadağ, E., & Saraydın, D. (2002). Swelling studies of super water retainer acrylamide/crotonic acid hydrogels crosslinked by trimethylolpropane triacrylate and 1, 4-butanediol dimethacrylate. *Polymer Bulletin*, *48*, 299-307.

Kassirer, J. P. (1971). Clinical evaluation of kidney function: Glomerular function. *New England Journal of Medicine*, *285*(7), 385-389.

Keay, G., & Doxey, D. (1984). A study of the interaction between bromocresol green dye and bovine, ovine and equine serum globulins. *Veterinary Research Communications*, *8*, 25-32.

Kim, M. S. (1988). Proteinuria. *Clinics in Laboratory Medicine*, *8*(3), 527-540.

Kirsch, P. (2002). Carrageenan: a safe additive. *Environmental health perspectives*, *110*(6), A288-A288.

Klymchenko, A. S. (2017). Solvatochromic and fluorogenic dyes as environment-sensitive probes: design and biological applications. *Accounts of chemical research*, *50*(2), 366-375.

Kobayashi, H., Ogawa, M., Alford, R., Choyke, P. L., & Urano, Y. (2010). New strategies for fluorescent probe design in medical diagnostic imaging. *Chemical reviews*, *110*(5), 2620-2640.

Kragh-Hansen, U. (2013). Molecular and practical aspects of the enzymatic properties of human serum albumin and of albumin–ligand complexes. *Biochimica et Biophysica Acta (BBA)-General Subjects*, *1830*(12), 5535-5544.

Kragh-Hansen, U. (2016). Human serum albumin: a multifunctional protein. In *Albumin in medicine* (pp. 1-24). Springer.

Ksenofontov, A. A., Bocharov, P. S., Ksenofontova, K. V., & Antina, E. V. (2022). Water-Soluble BODIPY-Based fluorescent probe for BSA and HSA detection. *Journal of Molecular Liquids*, *345*, 117031.

Kubihal, S., Goyal, A., Gupta, Y., & Khadgawat, R. (2021). Glucose measurement in body fluids: A ready reckoner for clinicians. *Diabetes & Metabolic Syndrome: Clinical Research & Reviews*, *15*(1), 45-53.

Kuo, Y.-C., Yeh, W.-L., Wu, T.-K., & Chan, K.-C. (2018). Urinary N-Acetyl-β-D-Glucosaminidase May Identify Faster Progression in Diabetic Patients With Late-Stage Chronic Kidney Disease. *Acta Nephrologica*, *32*(1), 3-11.

Kuznetsova, K., Pashynska, V., & Eremenko, Z. (2024). Numerical modeling of metal-dielectric metasurface as an element of microwave sensors for biomedical applications. *Low Temperature Physics*, *50*(1), 15-20.

Kuznetsova, K. S., Eremenko, Z. E., Pashynska, V. A., Martynov, A. V., Kulish, S. M., & Voloshyn, Y. A. (2023). Metasurface design for determination of protein concentration in enzymatic reaction mixture.

Kwok, R. T., Leung, C. W., Lam, J. W., & Tang, B. Z. (2015). Biosensing by luminogens with aggregation-induced emission characteristics. *Chemical Society Reviews*, *44*(13), 4228-4238.

Lad, U., Khokhar, S., & Kale, G. M. (2008). Electrochemical creatinine biosensors. In: ACS Publications.

Laffel, L. (1999). Ketone bodies: a review of physiology, pathophysiology and application of monitoring to diabetes. *Diabetes/metabolism research and reviews*, *15*(6), 412-426.

Lambers Heerspink, H. J., Brantsma, A. H., de Zeeuw, D., Bakker, S. J., de Jong, P. E., Gansevoort, R. T., & Group, P. S. (2008). Albuminuria assessed from first-morning-void urine samples versus 24-hour urine collections as a predictor of cardiovascular morbidity and mortality. *American journal of epidemiology*, *168*(8), 897-905.

Lange, T., Artelt, N., Kindt, F., Stracke, S., Rettig, R., Lendeckel, U., Chadjichristos, C. E., Kavvadas, P., Chatziantoniou, C., & Endlich, K. (2019). MiR-21 is up-regulated in urinary exosomes of chronic kidney disease patients and after glomerular injury. *Journal of Cellular and Molecular Medicine*, *23*(7), 4839.

Lee, P., & Wu, X. (2015). Modifications of human serum albumin and their binding effect. *Current pharmaceutical design*, *21*(14), 1862-1865.

Lee, S. A., Choi, C., & Yoo, T.-H. (2021). Extracellular vesicles in kidneys and their clinical potential in renal diseases. *Kidney Research and Clinical Practice*, *40*(2), 194.

Lee, S. W., Cheon, S. A., Kim, M. I., & Park, T. J. (2015). Organic–inorganic hybrid nanoflowers: types, characteristics, and future prospects. *Journal of nanobiotechnology*, *13*(1), 1-10.

Lei, Z., Gao, C., Chen, L., He, Y., Ma, W., & Lin, Z. (2018). Recent advances in biomolecule immobilization based on self-assembly: organic–inorganic hybrid nanoflowers and metal–organic frameworks as novel substrates. *Journal of Materials Chemistry B*, *6*(11), 1581-1594.

Lepowsky, E., Ghaderinezhad, F., Knowlton, S., & Tasoglu, S. (2017). based assays for urine analysis. *Biomicrofluidics*, *11*(5), 051501.

Levey, A. S., & Coresh, J. (2012). Chronic kidney disease. *The lancet*, *379*(9811), 165-180.

Levey, A. S., Eckardt, K.-U., Tsukamoto, Y., Levin, A., Coresh, J., Rossert, J., Zeeuw, D. D., Hostetter, T. H., Lameire, N., & Eknoyan, G. (2005). Definition and classification of chronic kidney disease: a position statement from Kidney Disease: Improving Global Outcomes (KDIGO). *Kidney international*, *67*(6), 2089-2100.

Levitt, D. G., & Levitt, M. D. (2016). Human serum albumin homeostasis: a new look at the roles of synthesis, catabolism, renal and gastrointestinal excretion, and the clinical value of serum albumin measurements. *International journal of general medicine*, 229-255.

Li, A., Singh, S., & Sievenpiper, D. (2018). Metasurfaces and their applications. *Nanophotonics*, *7*(6), 989-1011.

Li, H., Yao, Q., Fan, J., Du, J., Wang, J., & Peng, X. (2016). An NIR fluorescent probe of uric HSA for renal diseases warning. *Dyes and Pigments*, *133*, 79-85.

Li, J., Ji, C., Lu, B., Rodin, M., Paradies, J., Yin, M., & Kuckling, D. (2020). Dually crosslinked supramolecular hydrogel for cancer biomarker sensing. *ACS applied materials & interfaces*, *12*(33), 36873-36881.

Li, J., Wang, J., Li, H., Song, N., Wang, D., & Tang, B. Z. (2020). Supramolecular materials based on AIE luminogens (AIEgens): construction and applications. *Chemical Society Reviews*, *49*(4), 1144-1172.

Li, J., Wu, J., Cui, F., Zhao, X., Li, Y., Lin, Y., Li, Y., Hu, J., & Ju, Y. (2017). A dual functional fluorescent sensor for human serum albumin and chitosan. *Sensors and Actuators B: Chemical*, *243*, 831-837.

Li, L., Jun Cui, T., Ji, W., Liu, S., Ding, J., Wan, X., Bo Li, Y., Jiang, M., Qiu, C.-W., & Zhang, S. (2017). Electromagnetic reprogrammable coding-metasurface holograms. *Nature communications*, *8*(1), 197.

Li, W., Chen, D., Wang, H., Luo, S., Dong, L., Zhang, Y., Shi, J., Tong, B., & Dong, Y. (2015). Quantitation of Albumin in Serum Using "Turn-on" Fluorescent Probe with Aggregation-Enhanced Emission Characteristics. *ACS Appl Mater Interfaces*, *7*(47), 26094-26100. https://doi.org/10.1021/acsami.5b07422

Li, W., Chen, D., Wang, H., Luo, S., Dong, L., Zhang, Y., Shi, J., Tong, B., & Dong, Y. (2015). Quantitation of albumin in serum using "turn-on" fluorescent probe with aggregation-enhanced emission characteristics. *ACS Applied Materials & Interfaces*, *7*(47), 26094-26100.

Liang, J., Tang, B. Z., & Liu, B. (2015). Specific light-up bioprobes based on AIEgen conjugates. *Chemical Society Reviews*, *44*(10), 2798-2811.

Liang, J., Tang, B. Z., & Liu, B. (2015). Specific light-up bioprobes based on AIEgen conjugates. *Chem Soc Rev*, *44*(10), 2798-2811. https://doi.org/10.1039/c4cs00444b

Liang, R., Das, D., & Bakhtiiari, A. (2021). Protein confinement fine-tunes aggregation-induced emission in human serum albumin. *Physical Chemistry Chemical Physics*, *23*(46), 26263-26272.

Liang, Y., Ridzon, D., Wong, L., & Chen, C. (2007). Characterization of microRNA expression profiles in normal human tissues. *BMC genomics*, *8*(1), 1-20.

Liangos, O., Perianayagam, M. C., Vaidya, V. S., Han, W. K., Wald, R., Tighiouart, H., MacKinnon, R. W., Li, L., Balakrishnan, V. S., & Pereira, B. J. (2007). Urinary N-acetyl-β-(D)-glucosaminidase activity and kidney injury molecule-1 level are associated with adverse outcomes in acute renal failure. *Journal of the American Society of Nephrology*, *18*(3), 904-912.

Liao, C., Li, F., Huang, S., Zheng, B., Du, J., & Xiao, D. (2016). A specific and biocompatible fluorescent sensor based on the hybrid of GFP chromophore and peptide for HSA detection. *Biosensors and Bioelectronics*, *86*, 489-495.

Ligler, F. (2008). Fluorescence-based optical biosensors. In *Biophotonics* (pp. 199-215). Springer.

Lin, C.-H., Chang, Y.-C., & Chuang, L.-M. (2016). Early detection of diabetic kidney disease: Present limitations and future perspectives. *World journal of diabetes*, *7*(14), 290.

Ling, X., Xie, L., Fang, Y., Xu, H., Zhang, H., Kong, J., Dresselhaus, M. S., Zhang, J., & Liu, Z. (2010). Can graphene be used as a substrate for Raman enhancement? *Nano letters*, *10*(2), 553-561.

Liow, S. S., Dou, Q., Kai, D., Li, Z., Sugiarto, S., Yu, C. Y. Y., Kwok, R. T. K., Chen, X., Wu, Y. L., & Ong, S. T. (2017). Long-term real-time in vivo drug release monitoring with AIE thermogelling polymer. *Small*, *13*(7), 1603404.

Liu, B., Zhuang, J., & Wei, G. (2020). Recent advances in the design of colorimetric sensors for environmental monitoring. *Environmental Science: Nano*, *7*(8), 2195-2213.

Liu, J., Zhong, Y., Lam, J. W., Lu, P., Hong, Y., Yu, Y., Yue, Y., Faisal, M., Sung, H. H., & Williams, I. D. (2010). Hyperbranched conjugated polysiloles: synthesis, structure, aggregation-enhanced emission, multicolor fluorescent photopatterning, and superamplified detection of explosives. *Macromolecules*, *43*(11), 4921-4936.

Liu, L., Mo, H., Wei, S., & Raftery, D. (2012). Quantitative analysis of urea in human urine and serum by 1 H nuclear magnetic resonance. *Analyst*, *137*(3), 595-600.

Liu, R., Ye, X., & Cui, T. (2020). Recent progress of biomarker detection sensors. *Research*.

Liu, X., Qi, S., Mao, J., Zhang, Y., Dong, B., Song, B., & Ji, L. (2024). A supramolecular ratiometric fluorescent probe for the detection of human serum albumin. *Dyes and Pigments*, 112054.

Liu, Y., Deng, C., Tang, L., Qin, A., Hu, R., Sun, J. Z., & Tang, B. Z. (2011). Specific detection of D-glucose by a tetraphenylethene-based fluorescent sensor. *Journal of the American Chemical Society*, *133*(4), 660-663.

Loh, K. P., Bao, Q., Eda, G., & Chhowalla, M. (2010). Graphene oxide as a chemically tunable platform for optical applications. *Nature chemistry*, *2*(12), 1015-1024.

Lü, T., Zhu, K., & Liu, B. (2019). Recent advances of organic fluorescent probes for detection of human serum albumin. *Chinese Journal of Organic Chemistry*, *39*(10), 2786.

Lu, W., Wei, S., Shi, H., Le, X., Yin, G., & Chen, T. (2021). Progress in aggregation-induced emission-active fluorescent polymeric hydrogels. *Aggregate*, *2*(3), e37.

Luo, X., Mohammed Al-Antaki, A. H., Igder, A., Stubbs, K. A., Su, P., Zhang, W., Weiss, G. A., & Raston, C. L. (2020). Vortex fluidic-mediated fabrication of fast gelated silica hydrogels with embedded laccase nanoflowers for real-time biosensing under flow. *ACS applied materials & interfaces*, *12*(46), 51999-52007.

Luo, Z., Liu, B., Zhu, K., Huang, Y., Pan, C., Wang, B., & Wang, L. (2018). An environment-sensitive fluorescent probe for quantification of human serum albumin: Design, sensing mechanism, and its application in clinical diagnosis of hypoalbuminemia. *Dyes and Pigments*, *152*, 60-66.

Luo, Z., Lv, T., Zhu, K., Li, Y., Wang, L., Gooding, J. J., Liu, G., & Liu, B. (2020). Paper-Based Ratiometric Fluorescence Analytical Devices towards Point-of-Care Testing of Human Serum Albumin. *Angew Chem Int Ed Engl*, *59*(8), 3131-3136. https://doi.org/10.1002/anie.201915046

Luo, Z., Lv, T., Zhu, K., Li, Y., Wang, L., Gooding, J. J., Liu, G., & Liu, B. (2020). Paper-based ratiometric fluorescence analytical devices towards point-of-care testing of human serum albumin. *Angewandte Chemie*, *132*(8), 3155-3160.

Ma, X., Sun, R., Cheng, J., Liu, J., Gou, F., Xiang, H., & Zhou, X. (2016). Fluorescence aggregation-caused quenching versus aggregation-induced emission: a visual teaching technology for undergraduate chemistry students. *Journal of Chemical Education*, *93*(2), 345-350.

Mahoney, E., Kun, J., Smieja, M., & Fang, Q. (2019). Point-of-care urinalysis with emerging sensing and imaging technologies. *Journal of The Electrochemical Society*, *167*(3), 037518.

Majcher, M. J., & Hoare, T. (2019). Hydrogel synthesis and design. *Functional Biopolymers*, 1-41.

Mambatta, A. K., Jayarajan, J., Rashme, V. L., Harini, S., Menon, S., & Kuppusamy, J. (2015). Reliability of dipstick assay in predicting urinary tract infection. *Journal of family medicine and primary care*, *4*(2), 265.

Marimuthu, A., O'Meally, R. N., Chaerkady, R., Subbannayya, Y., Nanjappa, V., Kumar, P., Kelkar, D. S., Pinto, S. M., Sharma, R., & Renuse, S. (2011). A comprehensive map of the human urinary proteome. *Journal of proteome research*, *10*(6), 2734-2743.

Martin, H. (2011). Laboratory measurement of urine albumin and urine total protein in screening for proteinuria in chronic kidney disease. *The Clinical Biochemist Reviews*, *32*(2), 97.

Maruyama, H., Matsumoto, H., Fukuda, T., & Arai, F. (2008). Functionalized hydrogel surface patterned in a chip for local pH sensing. 2008 IEEE 21st International Conference on Micro Electro Mechanical Systems,

Mathew, M., Rad, M., Mata, J., Mahmodi, H., Kabakova, I., Raston, C., Tang, Y., Tipper, J., & Tavakoli, J. (2022). Hyperbranched polymers tune the physicochemical, mechanical, and biomedical properties of alginate hydrogels. *Materials Today Chemistry*, *23*, 100656.

Mei, J., Huang, Y., & Tian, H. (2017). Progress and trends in AIE-based bioprobes: a brief overview. *ACS Applied Materials & Interfaces*, *10*(15), 12217-12261.

Mei, J., Leung, N. L., Kwok, R. T., Lam, J. W., & Tang, B. Z. (2015). Aggregation-induced emission: together we shine, united we soar! *Chemical reviews*, *115*(21), 11718-11940.

Mei, J., Leung, N. L., Kwok, R. T., Lam, J. W., & Tang, B. Z. (2015). Aggregation-Induced Emission: Together We Shine, United We Soar! *Chem Rev*, *115*(21), 11718-11940. https://doi.org/10.1021/acs.chemrev.5b00263

Mihaila, S. M., Gaharwar, A. K., Reis, R. L., Marques, A. P., Gomes, M. E., & Khademhosseini, A. (2013). Photocrosslinkable kappa-carrageenan hydrogels for tissue engineering applications. *Advanced healthcare materials*, *2*(6), 895-907.

Miller, W. G., Bruns, D. E., Hortin, G. L., Sandberg, S., Aakre, K. M., McQueen, M. J., Itoh, Y., Lieske, J. C., Seccombe, D. W., & Jones, G. (2009). Current issues in measurement and reporting of urinary albumin excretion. *Clinical chemistry*, *55*(1), 24-38.

Mir, S. H., Nagahara, L. A., Thundat, T., Mokarian-Tabari, P., Furukawa, H., & Khosla, A. (2018). Organic-inorganic hybrid functional materials: An integrated platform for applied technologies. *Journal of The Electrochemical Society*, *165*(8), B3137.

Mishra, V., & Heath, R. J. (2021). Structural and biochemical features of human serum albumin essential for eukaryotic cell culture. *International journal of molecular sciences*, *22*(16), 8411.

Mundt, L., & Shanahan, K. (2020). *Graff's textbook of urinalysis and body fluids*. Jones & Bartlett Learning.

Murphy, D., McCulloch, C. E., Lin, F., Banerjee, T., Bragg-Gresham, J. L., Eberhardt, M. S., Morgenstern, H., Pavkov, M. E., Saran, R., & Powe, N. R. (2016). Trends in prevalence of chronic kidney disease in the United States. *Annals of internal medicine*, *165*(7), 473-481.

Muzammil, S., Kumar, Y., & Tayyab, S. (2000). Anion-induced stabilization of human serum albumin prevents the formation of intermediate during urea denaturation. *Proteins: Structure, Function, and Bioinformatics*, *40*(1), 29-38.

Narayanan, S., & Appleton, H. (1980). Creatinine: a review. *Clinical chemistry*, *26*(8), 1119-1126.

Narva, A. S. (2008). The National Kidney Disease Education Program and other related efforts in the United States. *Scandinavian Journal of Clinical and Laboratory Investigation*, *68*(sup241), 12-15.

Negm, A., Howlader, M. M., Bakr, M., & Ali, S. (2023). Biomarker detection using GST-based permittivity-asymmetric metasurface. *Materials & Design*, *227*, 111747.

Nicholson, J., Wolmarans, M., & Park, G. (2000). The role of albumin in critical illness. *British journal of anaesthesia*, *85*(4), 599-610.

Nie, R., Huang, J., Xu, X., & Yang, L. (2020). Immunoassays using optical-fiber sensor with all-directional chemiluminescent collection. *Analytical chemistry*, *92*(9), 6257-6262.

Nimse, S. B., Sonawane, M. D., Song, K.-S., & Kim, T. (2016). Biomarker detection technologies and future directions. *Analyst*, *141*(3), 740-755.

Oguntoye, I. O., Simone, B. K., Padmanabha, S., Hartfield, G. Z., Amrollahi, P., Hu, T. Y., Ollanik, A. J., & Escarra, M. D. (2022). Silicon nanodisk Huygens metasurfaces for portable and low-cost refractive index and biomarker sensing. *ACS Applied Nano Materials*, *5*(3), 3983-3991.

Ohta, N., & Robertson, A. (2006). *Colorimetry: fundamentals and applications*. John Wiley & Sons.

Organization, W. H. (2022). *Non-communicable diseases*. World Health Organization. https://www.who.int/health-topics/noncommunicable-diseases#tab=tab_1

Papale, M., Di Paolo, S., Magistroni, R., Lamacchia, O., Di Palma, A. M., De Mattia, A., Teresa Rocchetti, M., Furci, L., Pasquali, S., & De Cosmo, S. (2010). Urine proteome analysis may allow noninvasive differential diagnosis of diabetic nephropathy. *Diabetes care*, *33*(11), 2409-2415.

Pape, P. T., Sharp, V. J., & Rockafellow, J. (2020). Urine Dipstick: An Approach to Glucosuria, Ketonuria, pH, Specific Gravity, Bilirubin and Urobilinogen–Undeniable Chemistry. In *Urine Tests* (pp. 117-141). Springer.

Park, H.-M., Lee, S.-H., Chung, H., Kwon, O.-H., Yoo, K.-Y., Kim, H.-H., Heo, S.-C., Park, J.-S., & Tae, G.-S. (2007). Immunochromatographic analysis of hippuric acid in urine. *Journal of analytical toxicology*, *31*(6), 347-353.

Patel, H. P. (2006). The abnormal urinalysis. *Pediatric Clinics*, *53*(3), 325-337.

Peters Jr, T. (1995). *All about albumin: biochemistry, genetics, and medical applications*. Academic press.

Pham, A. T. T., Tohl, D., Hu, Q., Li, J., Reynolds, K. J., & Tang, Y. (2022). Portable Colorimetric Device with Commercial Microplates for Quantitative Detection of Urine Biomarkers: Design, Development, and Clinical Evaluation. *Biosensors*, *12*(9), 723.

Pham, A. T. T., Tohl, D., Wallace, A., Hu, Q., Li, J., Reynolds, K. J., & Tang, Y. (2022). Developing a fluorescent sensing based portable medical open-platform-a case study for albuminuria measurement in chronic kidney disease screening and monitoring. *Sensing and Bio-Sensing Research*, *37*, 100504.

Pisitkun, T., Johnstone, R., & Knepper, M. A. (2006). Discovery of urinary biomarkers. *Molecular & cellular proteomics*, *5*(10), 1760-1771.

Pollak, M. R., Quaggin, S. E., Hoenig, M. P., & Dworkin, L. D. (2014). The glomerulus: the sphere of influence. *Clinical Journal of the American Society of Nephrology*, *9*(8), 1461-1469.

Prakash, S. (2017). Role of human serum albumin and oxidative stress in diabetes. *J. Appl. Biotechnol. Bioeng*, *3*(1), 57.

Pundir, C. S. (2015). *Enzyme nanoparticles: preparation, characterisation, properties and applications*. William Andrew.

Rahman, M. A., Lee, K.-S., Park, D.-S., Won, M.-S., & Shim, Y.-B. (2008). An amperometric bilirubin biosensor based on a conductive poly-terthiophene–Mn (II) complex. *Biosensors and Bioelectronics*, *23*(6), 857-864.

Raj, C. R., & Ohsaka, T. (2003). Voltammetric detection of uric acid in the presence of ascorbic acid at a gold electrode modified with a self-assembled monolayer of heteroaromatic thiol. *Journal of Electroanalytical Chemistry*, *540*, 69-77.

Revete, A., Aparicio, A., Cisterna, B. A., Revete, J., Luis, L., Ibarra, E., Segura González, E. A., Molino, J., & Reginensi, D. (2022). Advancements in the use of hydrogels for regenerative medicine: properties and biomedical applications. *International Journal of Biomaterials*, *2022*.

Richter, A., Kuckling, D., Howitz, S., Gehring, T., & Arndt, K.-F. (2003). Electronically controllable microvalves based on smart hydrogels: magnitudes and potential applications. *Journal of microelectromechanical systems*, *12*(5), 748-753.

Robinson, S., & Dhanlaksmi, N. (2017). Photonic crystal based biosensor for the detection of glucose concentration in urine. *Photonic Sensors*, *7*(1), 11-19.

Rose, C., Parker, A., Jefferson, B., & Cartmell, E. (2015). The characterization of feces and urine: a review of the literature to inform advanced treatment technology. *Critical reviews in environmental science and technology*, *45*(17), 1827-1879.

Rosenoer, V. M., Oratz, M., & Rothschild, M. A. (2014). *Albumin: Structure, function and uses*. Elsevier.

Sahoo, S., Shaikh, S. A., Priyadarsini, K. I., & Choudhary, S. (2024). Interaction of curcumin and its derivatives with the carrier protein human serum albumin: Biophysical and thermodynamic approach. *The Journal of Chemical Thermodynamics*, *193*, 107273.

Sakamoto, S., Putalun, W., Vimolmangkang, S., Phoolcharoen, W., Shoyama, Y., Tanaka, H., & Morimoto, S. (2018). Enzyme-linked immunosorbent assay for the quantitative/qualitative analysis of plant secondary metabolites. *Journal of natural medicines*, *72*, 32-42.

Salazar, J. H. (2014). Overview of urea and creatinine. *Laboratory medicine*, *45*(1), e19-e20.

Sanchez, C., Julián, B., Belleville, P., & Popall, M. (2005). Applications of hybrid organic–inorganic nanocomposites. *Journal of Materials Chemistry*, *15*(35-36), 3559-3592.

Sanders, E. C., Sen, S. R., Gelston, A. A., Santos, A. M., Luo, X., Bhuvan, K., Tang, D. Y., Raston, C. L., & Weiss, G. A. (2022). Under-5-Minute Immunoblot Assays by Vortex Fluidic Device Acceleration. *Angewandte Chemie*, e202202021.

Santucci, L., Candiano, G., Petretto, A., Bruschi, M., Lavarello, C., Inglese, E., Righetti, P. G., & Ghiggeri, G. M. (2015). From hundreds to thousands: Widening the normal human Urinome (1). *Journal of proteomics*, *112*, 53-62.

Sarigul, N., Korkmaz, F., & Kurultak, İ. (2019). A new artificial urine protocol to better imitate human urine. *Scientific reports*, *9*(1), 20159.

Sasaki, S., Drummen, G. P., & Konishi, G.-i. (2016). Recent advances in twisted intramolecular charge transfer (TICT) fluorescence and related phenomena in materials chemistry. *Journal of Materials Chemistry C*, *4*(14), 2731-2743.

Schaub, S., Wilkins, J., Weiler, T., Sangster, K., Rush, D., & Nickerson, P. (2004). Urine protein profiling with surface-enhanced laser-desorption/ionization time-of-flight mass spectrometry. *Kidney international*, *65*(1), 323-332.

Schubert, U. (2011). Cluster-based inorganic–organic hybrid materials. *Chemical Society Reviews*, *40*(2), 575-582.

Shaikh, A., Seegmiller, J. C., Borland, T. M., Burns, B. E., Ladwig, P. M., Singh, R. J., Kumar, R., Larson, T. S., & Lieske, J. C. (2008). Comparison between immunoturbidimetry, size-exclusion chromatography, and LC-MS to quantify urinary albumin. *Clinical chemistry*, *54*(9), 1504-1510.

Shang, J., Le, X., Zhang, J., Chen, T., & Theato, P. (2019). Trends in polymeric shape memory hydrogels and hydrogel actuators. *Polymer Chemistry*, *10*(9), 1036-1055.

Sharp, K. G. (1998). Inorganic/organic hybrid materials. *Advanced Materials*, *10*(15), 1243-1248.

Shaykhutdinov, R. A., MacInnis, G. D., Dowlatabadi, R., Weljie, A. M., & Vogel, H. J. (2009). Quantitative analysis of metabolite concentrations in human urine samples using 13 C {1 H} NMR spectroscopy. *Metabolomics*, *5*(3), 307-317.

Sheira, G., Noreldin, N., Tamer, A., & Saad, M. (2015). Urinary biomarker N-acetyl-β-D-glucosaminidase can predict severity of renal damage in diabetic nephropathy. *Journal of Diabetes & Metabolic Disorders*, *14*, 1-5.

Shikha, S., Zheng, X., & Zhang, Y. (2018). Upconversion nanoparticles-encoded hydrogel microbeads-based multiplexed protein detection. *Nano-Micro Letters*, *10*, 1-16.

Shrestha, Y. K., & Shrestha, S. K. (2023). Fundamentals of Colorimetry.

Shustova, N. B., McCarthy, B. D., & Dinca, M. (2011). Turn-on fluorescence in tetraphenylethylene-based metal–organic frameworks: an alternative to aggregation-induced emission. *Journal of the American Chemical Society*, *133*(50), 20126-20129.

Simerville, J. A., Maxted, W. C., & Pahira, J. J. (2005). Urinalysis: a comprehensive review. *American family physician*, *71*(6), 1153-1162.

Slagle, K. M., & Ghosn, S. J. (1996). Immunoassays: tools for sensitive, specific, and accurate test results. *Laboratory medicine*, *27*(3), 177-183.

Song, S. H., Oh, T. R., Choi, H. S., Kim, C. S., Ma, S. K., Oh, K. H., Ahn, C., Kim, S. W., & Bae, E. H. (2020). High serum adiponectin as a biomarker of renal dysfunction: Results from the KNOW-CKD study. *Scientific reports*, *10*(1), 5598.

Stamp, R. J. (1988). Measurement of albumin in urine by end-point immunonephelometry. *Annals of clinical biochemistry*, *25*(4), 442-443.

Stanifer, J. W., Muiru, A., Jafar, T. H., & Patel, U. D. (2016). Chronic kidney disease in low-and middle-income countries. *Nephrology Dialysis Transplantation*, *31*(6), 868-874.

Strasinger, S. K., & Di Lorenzo, M. S. (2014). *Urinalysis and body fluids*. FA Davis.

Streppel, U., Dannberg, P., Wächter, C., Bräuer, A., Fröhlich, L., Houbertz, R., & Popall, M. (2003). New wafer-scale fabrication method for stacked optical waveguide interconnects and 3D micro-optic structures using photoresponsive (inorganic–organic hybrid) polymers. *Optical Materials*, *21*(1-3), 475-483.

Sun, J.-Y., Zhao, X., Illeperuma, W. R., Chaudhuri, O., Oh, K. H., Mooney, D. J., Vlassak, J. J., & Suo, Z. (2012). Highly stretchable and tough hydrogels. *Nature*, *489*(7414), 133-136.

Taurino, I., Van Hoof, V., De Micheli, G., & Carrara, S. (2013). Superior sensing performance of multi-walled carbon nanotube-based electrodes to detect unconjugated bilirubin. *Thin Solid Films*, *548*, 546-550.

Tavakoli, J., Ghahfarokhi, A. J., & Tang, Y. (2021). Aggregation-induced emission fluorescent gels: Current trends and future perspectives. *Aggregation-Induced Emission*, 247-286.

Tavakoli, J., Raston, C. L., & Tang, Y. (2020). Tuning surface morphology of fluorescent hydrogels using a vortex fluidic device. *Molecules*, *25*(15), 3445.

Tavakoli, J., & Tang, Y. (2017). Hydrogel based sensors for biomedical applications: An updated review. *Polymers*, *9*(8), 364.

Teppo, A.-M. (1982). Immunoturbidimetry of albumin and immunoglobulin G in urine. *Clinical chemistry*, *28*(6), 1359-1361.

Thongboonkerd, V. (2020). Roles for exosome in various kidney diseases and disorders. *Frontiers in pharmacology*, *10*, 1655.

Thongboonkerd, V., & Kanlaya, R. (2022). The divergent roles of exosomes in kidney diseases: pathogenesis, diagnostics, prognostics and therapeutics. *The International Journal of Biochemistry & Cell Biology*, *149*, 106262.

Tohl, D., Teferra, M. N., Wallace, A., Pham, A. T. T., & Tang, Y. (2022). Re-referencing and calibration for robust ratiometric light intensity measurement. *IEEE Transactions on Instrumentation and Measurement*, *71*, 1-8.

Tong, H., Hong, Y., Dong, Y., Häussler, M., Li, Z., Lam, J. W., Dong, Y., Sung, H. H.-Y., Williams, I. D., & Tang, B. Z. (2007). Protein detection and quantitation by tetraphenylethene-based fluorescent probes with aggregation-induced emission characteristics. *The Journal of Physical Chemistry B*, *111*(40), 11817-11823.

Tong, J., Hu, T., Qin, A., Sun, J. Z., & Tang, B. Z. (2017). Deciphering the binding behaviours of BSA using ionic AIE-active fluorescent probes. *Faraday Discussions*, *196*, 285-303.

Truong, M., Yang, B., & Jarrard, D. F. (2013). Toward the detection of prostate cancer in urine: a critical analysis. *The Journal of urology*, *189*(2), 422-429.

Tsai, D. M., Lin, K. W., Zen, J. M., Chen, H. Y., & Hong, R. H. (2005). A new fabrication process for a microchip electrophoresis device integrated with a three-electrode electrochemical detector. *Electrophoresis*, *26*(15), 3007-3012.

Tseng, M. L., Jahani, Y., Leitis, A., & Altug, H. (2020). Dielectric metasurfaces enabling advanced optical biosensors. *Acs Photonics*, *8*(1), 47-60.

Tu, Y., Yu, Y., Zhou, Z., Xie, S., Yao, B., Guan, S., Situ, B., Liu, Y., Kwok, R. T., & Lam, J. W. (2019). Specific and quantitative detection of albumin in biological fluids by tetrazolate-functionalized water-soluble AIEgens. *ACS Applied Materials & Interfaces*, *11*(33), 29619-29629.

Turin, T. C., Coresh, J., Tonelli, M., Stevens, P. E., De Jong, P. E., Farmer, C. K., Matsushita, K., & Hemmelgarn, B. R. (2013). Change in the estimated glomerular filtration rate over time and risk of all-cause mortality. *Kidney international*, *83*(4), 684-691.

Uchino, S. (2010). Creatinine. *Current opinion in critical care*, *16*(6), 562-567.

Ueno, T., Hirayama, S., Sugihara, M., & Miida, T. (2016). The bromocresol green assay, but not the modified bromocresol purple assay, overestimates the serum albumin concentration in nephrotic syndrome through reaction with α2-macroglobulin. *Annals of clinical biochemistry*, *53*(1), 97-105.

Umpierrez, G. E., Murphy, M. B., & Kitabchi, A. E. (2002). Diabetic ketoacidosis and hyperglycemic hyperosmolar syndrome. *Diabetes spectrum*, *15*(1), 28-36.

Van Laere, F., Claes, T., Schrauwen, J., Scheerlinck, S., Bogaerts, W., Taillaert, D., O'Faolain, L., Van Thourhout, D., & Baets, R. (2007). Compact focusing grating couplers for silicon-on-insulator integrated circuits. *IEEE Photonics Technology Letters*, *19*(23), 1919-1921.

Viswanathan, G., & Upadhyay, A. (2011). Assessment of proteinuria. *Advances in chronic kidney disease*, *18*(4), 243-248.

VS, A. P., Joseph, P., SCG, K. D., Lakshmanan, S., Kinoshita, T., & Muthusamy, S. (2017). Colorimetric sensors for rapid detection of various analytes. *Materials Science and Engineering: C, 78*, 1231-1245.

Walcarius, A. (2001). Electrochemical applications of silica-based organic− inorganic hybrid materials. *Chemistry of Materials*, *13*(10), 3351-3372.

Wallace, T., & Matthews, D. (2004). Recent advances in the monitoring and management of diabetic ketoacidosis. *Qjm*, *97*(12), 773-780.

Wan, Q. J., Kubáň, P., Tanyanyiwa, J., Rainelli, A., & Hauser, P. C. (2004). Determination of major inorganic ions in blood serum and urine by capillary electrophoresis with contactless conductivity detection. *Analytica chimica acta*, *525*(1), 11-16.

Wang, D., & Tang, B. Z. (2019). Aggregation-induced emission luminogens for activity-based sensing. *Accounts of Chemical Research*, *52*(9), 2559-2570.

Wang, G., Bonkovsky, H. L., de Lemos, A., & Burczynski, F. J. (2015). Recent insights into the biological functions of liver fatty acid binding protein 1. *Journal of lipid research*, *56*(12), 2238-2247.

Wang, Y., Ali, M. A., Chow, E. K., Dong, L., & Lu, M. (2018). An optofluidic metasurface for lateral flow-through detection of breast cancer biomarker. *Biosensors and Bioelectronics*, *107*, 224-229.

Wang, Y., Huo, F., & Yin, C. (2024). Development of human serum albumin fluorescent probes in detection, imaging, and disease therapy. *The Journal of Physical Chemistry B*, *128*(5), 1121-1138.

Weber, J. A., Baxter, D. H., Zhang, S., Huang, D. Y., How Huang, K., Jen Lee, M., Galas, D. J., & Wang, K. (2010). The microRNA spectrum in 12 body fluids. *Clinical chemistry*, *56*(11), 1733-1741.

Wen, J., Chen, X., Wei, S., Ma, X., & Zhao, Y. (2022). Research progress and treatment status of liver cirrhosis with hypoproteinemia. *Evidence-based Complementary and Alternative Medicine*, *2022*.

Whicher, J., Price, C., Spencer, K., & Ward, A. M. (1982). Immunonephelometric and immunoturbidimetric assays for proteins. *CRC Critical Reviews in Clinical Laboratory Sciences*, *18*(3), 213-260.

Wu, M. T., Lam, K. K., Lee, W. C., Hsu, K. T., Wu, C. H., Cheng, B. C., Ng, H. Y., Chi, P. J., Lee, Y. T., & Lee, C. T. (2012). Albuminuria, proteinuria, and urinary albumin to protein ratio in chronic kidney disease. *Journal of clinical laboratory analysis*, *26*(2), 82-92.

Wu, W., & Liu, B. (2021). Aggregation-induced emission: challenges and opportunities. *National Science Review, 8*(6), nwaa222.

Würthner, F. (2020). Aggregation-induced emission (AIE): a historical perspective. *Angewandte Chemie International Edition*, *59*(34), 14192-14196.

Xi, X., Li, T., Huang, Y., Sun, J., Zhu, Y., Yang, Y., & Lu, Z. J. (2017). RNA biomarkers: frontier of precision medicine for cancer. *Non-coding RNA*, *3*(1), 9.

Xiao, C., & Yang, M. (2006). Controlled preparation of physical cross-linked starch-g-PVA hydrogel. *Carbohydrate polymers*, *64*(1), 37-40.

Xie, S., Wong, A. Y., Chen, S., & Tang, B. Z. (2019). Fluorogenic detection and characterization of proteins by aggregation-induced emission methods. *Chemistry–A European Journal*, *25*(23), 5824-5847.

Xie, S., Wong, A. Y., Kwok, R. T., Li, Y., Su, H., Lam, J. W., Chen, S., & Tang, B. Z. (2018). Fluorogenic Ag+–tetrazolate aggregation enables efficient fluorescent biological silver staining. *Angewandte Chemie International Edition*, *57*(20), 5750-5753.

Xie, Y., Bowe, B., Mokdad, A. H., Xian, H., Yan, Y., Li, T., Maddukuri, G., Tsai, C.-Y., Floyd, T., & Al-Aly, Z. (2018). Analysis of the Global Burden of Disease study highlights the global, regional, and national trends of chronic kidney disease epidemiology from 1990 to 2016. *Kidney international*, *94*(3), 567-581.

Xu, J.-F., Yang, Y.-S., Jiang, A.-Q., & Zhu, H.-L. (2022). Detection methods and research progress of human serum albumin. *Critical reviews in analytical chemistry*, *52*(1), 72-92.

Yalow, R. S. (1980). Radioimmunoassay. *Annual review of biophysics and bioengineering*, *9*(1), 327-345.

Yamakado, S., Cho, H., Inada, M., Morikawa, M., Jiang, Y.-H., Saito, K., Nakaishi, K., Watabe, S., Takagi, H., & Kaneda, M. (2019). Urinary adiponectin as a new diagnostic index for chronic kidney disease due to diabetic nephropathy. *BMJ Open Diabetes Research and Care*, *7*(1), e000661.

Yang, F., Zhang, Y., & Liang, H. (2014). Interactive association of drugs binding to human serum albumin. *International journal of molecular sciences*, *15*(3), 3580-3595.

Yang, Y., Zhang, Y., Xie, S., Tang, Y., Zeng, Z., & Tang, B. Z. (2021). Hydrogel-derived luminescent scaffolds for biomedical applications. *Materials Chemistry Frontiers*, *5*(9), 3524-3548.

Yao, B., Giel, M.-C., & Hong, Y. (2021). Detection of kidney disease biomarkers based on fluorescence technology. *Materials Chemistry Frontiers*, *5*(5), 2124-2142.

Yasmin, L., Chen, X., Stubbs, K. A., & Raston, C. L. (2013). Optimising a vortex fluidic device for controlling chemical reactivity and selectivity. *Scientific reports*, *3*(1), 1-6.

Yesilkoy, F., Arvelo, E. R., Jahani, Y., Liu, M., Tittl, A., Cevher, V., Kivshar, Y., & Altug, H. (2019). Ultrasensitive hyperspectral imaging and biodetection enabled by dielectric metasurfaces. *Nature Photonics*, *13*(6), 390-396.

Yu, Y., Huang, Y., Hu, F., Jin, Y., Zhang, G., Zhang, D., & Zhao, R. (2016). Self-Assembled Nanostructures Based on Activatable Red Fluorescent Dye for Site-Specific Protein Probing and Conformational Transition Detection. *Anal Chem*, *88*(12), 6374-6381. https://doi.org/10.1021/acs.analchem.6b00774

Yu, Y., Huang, Y., Hu, F., Jin, Y., Zhang, G., Zhang, D., & Zhao, R. (2016). Self-assembled nanostructures based on activatable red fluorescent dye for site-specific protein probing and conformational transition detection. *Analytical chemistry*, *88*(12), 6374-6381.

Yuk, H., Zhang, T., Lin, S., Parada, G. A., & Zhao, X. (2016). Tough bonding of hydrogels to diverse non-porous surfaces. *Nature materials*, *15*(2), 190-196.

Zangheri, M., Di Nardo, F., Mirasoli, M., Anfossi, L., Nascetti, A., Caputo, D., De Cesare, G., Guardigli, M., Baggiani, C., & Roda, A. (2016). Chemiluminescence lateral flow immunoassay cartridge with integrated amorphous silicon photosensors array for human serum albumin detection in urine samples. *Analytical and bioanalytical chemistry*, *408*, 8869-8879.

Zhang, A., & Huang, S. (2012). Progress in pathogenesis of proteinuria. *International journal of nephrology*, *2012*(1), 314251.

Zhang, S., Wong, C. L., Zeng, S., Bi, R., Tai, K., Dholakia, K., & Olivo, M. (2020). Metasurfaces for biomedical applications: imaging and sensing from a nanophotonics perspective. *Nanophotonics*, *10*(1), 259-293.

Zhang, X., Yao, B., Hu, Q., Hong, Y., Wallace, A., Reynolds, K., Ramsey, C., Maeder, A., Reed, R., & Tang, Y. (2020). Detection of biomarkers in body fluids using bioprobes based on aggregation-induced emission fluorogens. *Materials Chemistry Frontiers*, *4*(9), 2548-2570.

Zhang, Z., Deng, Z., Zhu, L., Zeng, J., Cai, X. M., Qiu, Z., Zhao, Z., & Tang, B. Z. (2023). Aggregation-induced emission biomaterials for anti-pathogen medical applications: detecting, imaging and killing. *Regenerative Biomaterials*, *10*.

Zhao, F., Wang, Z., Wang, H., & Ding, M. (2011). Determination of hippuric acid in human urine by ion chromatography with conductivity detection. *Journal of Chromatography B*, *879*(3-4), 296-298.

Zhao, M., Li, M., Yang, Y., Guo, Z., Sun, Y., Shao, C., Li, M., Sun, W., & Gao, Y. (2017). A comprehensive analysis and annotation of human normal urinary proteome. *Scientific reports*, *7*(1), 1-13.

Zhao, Z., He, B., & Tang, B. Z. (2015). Aggregation-induced emission of siloles. *Chemical Science*, *6*(10), 5347-5365.

Zhao, Z., Zhang, H., Lam, J. W., & Tang, B. Z. (2020). Aggregation-induced emission: new vistas at the aggregate level. *Angewandte Chemie International Edition*, *59*(25), 9888-9907.

Zheng, P., & Wu, N. (2017). Fluorescence and sensing applications of graphene oxide and graphene quantum dots: a review. *Chemistry–An Asian Journal*, *12*(18), 2343-2353.

Zhu, H., Cheung, S., Chung, K. L., & Yuk, T. I. (2013). Linear-to-circular polarization conversion using metasurface. *IEEE transactions on antennas and propagation*, *61*(9), 4615-4623.

Zhu, J., Wen, M., Wen, W., Du, D., Zhang, X., Wang, S., & Lin, Y. (2018). Recent progress in biosensors based on organic-inorganic hybrid nanoflowers. *Biosensors and Bioelectronics*, *120*, 175-187.

Zhu, K., Lv, T., Qin, T., Huang, Y., Wang, L., & Liu, B. (2019). A flavonoid-based fluorescent probe enables the accurate quantification of human serum albumin by minimizing the interference from blood lipids. *Chemical Communications*, *55*(93), 13983-13986.

Zhu, Y., Murali, S., Cai, W., Li, X., Suk, J. W., Potts, J. R., & Ruoff, R. S. (2010). Graphene and graphene oxide: synthesis, properties, and applications. *Advanced materials*, *22*(35), 3906-3924.

Zorzi, A., Linciano, S., & Angelini, A. (2019). Non-covalent albumin-binding ligands for extending the circulating half-life of small biotherapeutics. *MedChemComm*, *10*(7), 1068-1081.

Zsila, F. (2013). Subdomain IB is the third major drug binding region of human serum albumin: toward the three-sites model. *Molecular pharmaceutics*, *10*(5), 1668-1682.